

Università degli Studi di Torino  
Facoltà di Scienze Matematiche Fisiche e Naturali



Tesi di Laurea Magistrale in Fisica delle Interazioni Fondamentali

**A STUDY OF LOW MASS  
HIGGS BOSON DECAY  
 $H \rightarrow 2\mu 2e$  WITH THE CMS  
EXPERIMENT**

Relatore  
dott. Ernesto Migliore

Candidato  
Marco Musich

Anno Accademico 2006-2007

# Contents

<b>Introduction</b>	<b>iv</b>
<b>1 Higgs boson physics at LHC</b>	<b>1</b>
1.1 Standard Model . . . . .	2
1.1.1 The Glashow-Weinberg-Salam Model . . . . .	7
1.1.2 The Higgs boson and the mass term introduction . . . . .	9
1.2 Higgs Properties and Searches . . . . .	14
1.2.1 Higgs Decays . . . . .	14
1.2.2 Lower Limit on SM Higgs . . . . .	16
1.2.3 Upper Limit on SM Higgs . . . . .	18
1.2.4 Higgs decay processes . . . . .	20
1.2.5 Higgs searches . . . . .	24
1.2.6 Direct searches at Tevatron . . . . .	26
1.2.7 Beyond the Standard Model . . . . .	27
1.3 Basic phenomenology of proton-proton collisions . . . . .	28
1.4 Standard Model Higgs searches at LHC . . . . .	31
1.4.1 SM Higgs Production mechanisms . . . . .	31
1.4.2 SM Higgs Search . . . . .	34
<b>2 The CMS Experiment</b>	<b>38</b>
2.1 The LHC . . . . .	38
2.1.1 LHC Experiments . . . . .	42
2.2 CMS Overall Design . . . . .	44
2.3 The Magnet . . . . .	47
2.4 The Tracker . . . . .	48
2.5 ECAL . . . . .	53
2.6 HCAL . . . . .	55
2.7 The Muon System . . . . .	56

<b>3</b>	<b>The CMS trigger</b>	<b>60</b>
3.1	The Level-1 trigger . . . . .	62
3.1.1	The Calorimeter Trigger . . . . .	63
3.1.2	The Muon Trigger . . . . .	66
3.1.3	The Level-1 Trigger table . . . . .	69
3.2	The High Level Trigger . . . . .	71
3.2.1	Electron and photon High Level Trigger . . . . .	71
3.2.2	Muon High Level Trigger . . . . .	75
<b>4</b>	<b>Studies of <math>H \rightarrow ZZ^* \rightarrow 2\mu 2e</math> channel at generator level</b>	<b>79</b>
4.1	Definition of the signal and of the background . . . . .	80
4.2	Signal and background generation . . . . .	81
4.2.1	Higgs boson signal . . . . .	82
4.2.2	Z boson kinematics . . . . .	84
4.2.3	Lepton kinematics . . . . .	86
4.2.4	Higgs production mechanism . . . . .	87
4.2.5	Backgrounds . . . . .	93
4.3	Study of the kinematics of $H \rightarrow ZZ^* \rightarrow 2\mu 2e$ . . . . .	106
4.3.1	Z boson reconstruction algorithm . . . . .	106
4.3.2	Considered kinematical variables . . . . .	108
4.4	Rejection of $ZZ^*$ background . . . . .	116
<b>5</b>	<b>HLT performance for <math>H \rightarrow ZZ^* \rightarrow 2\mu 2e</math></b>	<b>123</b>
5.1	Maximum event rate and thresholds . . . . .	123
5.2	Trigger implementation in CMSSW . . . . .	125
5.3	Electron/photon and muon HLT paths . . . . .	126
5.3.1	Electron HLT path . . . . .	127
5.3.2	Photon HLT path . . . . .	128
5.3.3	Muon HLT path . . . . .	128
5.3.4	Detailed thresholds for low luminosity . . . . .	129
5.4	Efficiencies for Egamma trigger-paths . . . . .	131
5.5	Trigger efficiencies for combined Egamma-muon paths . . . . .	136
5.6	Resolution on selected observables . . . . .	139
	<b>Summary</b>	<b>143</b>
<b>A</b>	<b>Electroweak Lagrangian and spontaneous symmetry breaking</b>	<b>144</b>
A.1	Electroweak Symmetry Breaking . . . . .	148
A.2	S.M. couplings . . . . .	156

---

<b>B CMS Software and computing tools</b>	<b>158</b>
B.1 Priority and Challenges for CMS software . . . . .	158
B.2 CMSSW Application Framework . . . . .	159
B.2.1 Modular Architecture . . . . .	160
B.2.2 Events . . . . .	161
B.3 The Processing Model . . . . .	164
B.4 CMS computing Model . . . . .	165
B.4.1 Tier architecture of computing resources . . . . .	165
B.4.2 Data Organization . . . . .	168
B.5 Event Simulation . . . . .	169
B.5.1 Monte Carlo event generators . . . . .	170
B.5.2 Detector simulation . . . . .	171
B.5.3 Digitization . . . . .	171
B.5.4 Pile-up simulation . . . . .	172
B.5.5 Reconstruction . . . . .	172
B.6 CRAB . . . . .	173
B.6.1 CRAB Workflow . . . . .	173
<b>Bibliography</b>	<b>175</b>
<b>List of Tables</b>	<b>178</b>
<b>List of Figures</b>	<b>180</b>
<b>Acknowledgements</b>	<b>187</b>

# Introduction

The Standard Model (SM) of electroweak interactions is one of the most successful theories of modern physics. It provides a simple and elegant description of the basic components of matter and of their interactions.

The present belief is that all known matter can be described through twelve fundamental particles, the *fermions*, which can be divided into two groups: *quarks* and *leptons*. The fermions interact through three types of interactions: electromagnetic, weak and strong interactions, which are mediated by another kind of particles: the *vector bosons*. A fourth force, the *gravitation*, the closest to our everyday experience, is needed to describe the Universe, but it is negligible in the subnuclear environment because of its very low intensity at these scales.

The SM was extensively tested with high precision by recent experiments, and no relevant discrepancy from the theoretical predictions has been found yet. The theory, however, still lacks a final test. Particle masses are introduced in the Standard Model using the so called Electroweak Spontaneous Symmetry Breaking mechanism which predicts the existence of a scalar particle, the Higgs boson, which up to now has not been experimentally observed. There are also other aspects of the theory which induce to think the Standard Model more like an effective theory valid in a low energy approximation, rather than a fundamental one. Several possible extensions of the Standard Model have been proposed.

Though the existence of the Higgs boson still has to be proved, direct and indirect searches for the Higgs have been carried out at LEP-2 and Tevatron and have fixed a lower bound ( $m_H > 114.4 \text{ GeV}/c^2$  at 95% *C.L.*) and an upper bound ( $m_H < 237 \text{ GeV}/c^2$  at 95% *C.L.*) to its mass, indicating a value of  $\sim 114 \text{ GeV}/c^2$  as the best fit to experimental data.

The ultimate tests of the Standard Model and the possibility to search for new physics have led to the design of the Large Hadron Collider (LHC), a high-energy, high-luminosity proton-proton collider, installed at the European Laboratory for Nuclear Research (CERN) in Geneva (Switzerland). The first proton-proton collisions at LHC are planned for 2008.

---

By providing proton-proton collisions at a center of mass energy  $\sqrt{s}=14$  TeV, at an expected instantaneous luminosity as high as  $\mathcal{L}(t) = 10^{34} \text{cm}^{-2} \text{s}^{-1}$ , LHC will allow the search of the Higgs boson in the whole expected mass range, from the present LEP limit  $\sim 114$  GeV up to  $\sim 1$  TeV. Four experiments will collect data at LHC: two general-purpose ones (ATLAS and CMS), one dedicated to b-physics (LHC-b), and one dedicated to heavy ion collisions (ALICE). The search strategy of the Higgs boson at LHC will exploit different decay channels, according to the varying decay properties of the Higgs Boson with its mass. One of the most relevant channels is the Higgs decay into 4 leptons through a  $ZZ^{(*)}$  intermediate state, which can be used as a discovery channel in a wide Higgs mass range.

The work presented in this thesis has been carried out within the Torino CMS group during 2006/2007 academical year. The subject of the thesis is a study of the Higgs decay channel  $H \rightarrow ZZ^{(*)} \rightarrow 4\ell$ , which is expected to be one of the most important channels for the Higgs discovery at the LHC because of its very clear signature. Furthermore this channel is remarkably important for the determination of Higgs properties (e.g. spin,  $CP$ -parity, couplings to gauge bosons).

This study was focused on the first three years of running of LHC at low luminosity ( $2 \cdot 10^{33} \text{cm}^{-2} \text{s}^{-1}$ ), resulting in a total integrated luminosity of  $\sim 60 \text{fb}^{-1}$  concentrating on the  $2\mu 2e$  final state and the range of mass  $M_H < 2 \cdot M_Z$ .

After a general introduction to electroweak physics, spontaneous symmetry breaking and Higgs mechanism (chapter 1) and a description of the CMS detector (chapter 2), the CMS trigger algorithms (chapter 3) will be described in more detail. The last two chapters deal with the specific work performed in Torino about the Higgs decay into four leptons: a preliminary analysis at generator level (chapter 4) and a validation study of the CMS High Level Trigger on the considered signal (chapter 5).

# Chapter 1

## Higgs boson physics at LHC

Our current understanding of the subatomic world is summarized in the so called Standard Model (SM) of particle physics, a local gauge quantum field theory based on the  $SU(3)_C \otimes SU(2)_L \otimes U(1)_Y$  symmetry group.

Extensive consistency and precision tests have been performed so far yielding stringent constraints on the Standard Model over a wide range of energies.

However the Standard Model has not been completely confirmed: in particular, it predicts an additional scalar field, the Higgs field, whose corresponding particle has not been experimentally observed yet. The Higgs field has been introduced, in the so called *Higgs mechanism* to break  $SU(2)_L \otimes U(1)_Y$  electroweak symmetry to give masses to particles described by the Standard Model.

Direct searches for the Higgs boson, performed at LEP and Tevatron accelerators, have not given evidence yet, while setting a lower limit on its mass at about 114 GeV.

Apart from electroweak symmetry breaking still to be confirmed, there are several reasons to think the Standard Model only as an effective description, and to foresee a more fundamental theory. Several models proposing a wider symmetry than that of SM have been proposed in order to solve the theoretical drawbacks affecting it.

The ultimate tests of the Standard Model and the possibility to search for new physics beyond have led the scientific community to design the Large Hadron Collider (LHC), a high energy, high luminosity proton-proton collider, that will be installed at the European Laboratory for Nuclear Research (CERN) in Geneva. The first proton-proton collisions are planned for 2008 and at that time LHC will be the most powerful particle accelerator ever built.

In this chapter the basic concepts of Standard Model are overviewed, focusing on the electroweak symmetry breaking mechanism, in order to introduce the Higgs boson properties. The different searches conducted for Higgs boson are then reviewed together with the current theoretical and experimental limits on the determination of the Higgs boson mass.

## 1.1 The Standard Model

The Standard Model is a local gauge quantum field theory describing three of the four fundamental interactions: electromagnetic, weak interaction and strong interaction.

The SM is a gauge theory based upon the  $SU(3)_C \otimes SU(2)_L \otimes U(1)_Y$  symmetry group, the direct product of color symmetry group (C), weak isospin ( $T_L$ ) and hypercharge (Y). This gauge group includes the symmetry group of strong interactions  $SU(3)_C$  and the symmetry group of electroweak interactions,  $SU(2)_L \otimes U(1)_Y$ . The symmetry group associated to electromagnetic interactions,  $U(1)_{EM}$  appears in the SM as a sub-group of  $SU(2)_L \otimes U(1)_Y$  and it is in this sense that the weak and electromagnetic interactions are said to be unified. Associated to the gauge symmetry groups there are 12 vector (spin-1) gauge bosons: 8 bosons ( $g_i$ ) for  $SU(3)_C$ , 3 ( $W_i$ ) for  $SU(2)_L$  and 1 (B) for  $U(1)_Y$ . The Z boson and the photon  $\gamma$  are seen as linear combinations of  $W_3$  and B.

Since  $SU(3)_C$  gauge invariance is not broken, the eight associated force-carriers (the gluons  $g_i$ ) remain massless. The strong interactions do not have an infinite range, in spite of the gluon being massless, because of confinement. The theory of quarks interacting by exchange of gluons is called Quantum Chromodynamics (or QCD), to stress the parallel with Quantum Electrodynamics (or QED), which also has an unbroken gauge invariance and an associated massless gauge boson: the photon.

The  $SU(2)_L$  group describes the left-hand isospin, a "spin-like" algebra group associated to a weak charge carried by left-chirality fermions (in the ultra-relativistic limit ( $\beta = \frac{v}{c} \sim 1$ ) chirality is equivalent to helicity  $e = \frac{\Sigma \cdot p}{|p|}$ ). The subscript Y in  $U(1)_Y$  refers to "weak hypercharge", related to electric charge and left isospin by the relation:

$$Q = t_L^3 + \frac{Y}{2} \quad (1.1)$$

Unlike the  $SU(3)_C$  one, the  $SU(2)_L \otimes U(1)_Y$  gauge invariance is broken down to  $U(1)_{EM}$  the unbroken gauge symmetry of QED. As a result three of

the four gauge bosons,  $W^\pm$  and  $Z^0$  of  $SU(2)_T \otimes U(1)_Y$  acquire mass, while the fourth, the photon ( $\gamma$ ), remains massless.

From the phenomenological point of view, this is not a little effect. The W and Z masses<sup>1</sup>:

$$M_W = 80.423 \pm 0.039 \text{ GeV}$$

$$M_Z = 91.1876 \pm 0.0021 \text{ GeV}$$

are responsible for the subnuclear range of the weak forces  $r_{weak} \sim \hbar c / m_W c^2 \sim 10^{-16}$  cm. In contrast. Therefore the symmetry-breaking mechanism produces a mass hierarchy of at least 26 orders of magnitude, being the state of the art measurement of the  $M_W/M_\gamma$  ratio  $> 10^{26}$ .

Actually, the fact that the weak gauge bosons are massive particles indicates that  $SU(2)_L \otimes U(1)_Y$  is *not* a good vacuum state symmetry. In contrast, the photon being massless reflects the fact that  $U(1)_{EM}$  is a good symmetry of the vacuum state (state of lowest possible energy). Therefore, the symmetry breaking pattern of the Standard Model must be:

$$SU(2)_L \otimes U(1)_Y \longrightarrow U(1)_{EM}$$

The dynamics of the symmetry breaking mechanism is unknown. There are good reasons to believe that a general framework is the spontaneous symmetry breaking. The term "spontaneous" here means that the symmetry is not broken explicitly by terms violating gauge symmetry in the Lagrangian (i.e. field interactions), but rather by an asymmetry of the state of the vacuum state. In the absence of an associated gauge symmetry, each spontaneously broken direction in the global (i.e. space-time independent) symmetry space gives rise to a massless, spin-zero un-physical Goldstone boson in the theory spectrum. If the direction in that abstract space corresponding to the broken symmetry corresponds also to a gauge symmetry (i.e. a space-time dependent symmetry) then the associated Goldstone boson and the massless gauge boson combine to form a massive gauge bosons. In this process the extra degree of freedom provided by the scalar Goldstone field is absorbed in the longitudinal component of the gauge vector boson. This procedure is known as Higgs mechanism. The Higgs mechanism provides the proper masses to the W and Z gauge bosons and to the fermions, and leaves as a consequence the prediction of a new particle: the Higgs boson. This must be scalar and electrically neutral. This particle has not yet been observed in experiments.

---

<sup>1</sup>In the following natural units  $\hbar = c = 1$  will be used.

The Higgs mechanism preserves the number of states. A massless gauge boson occurs in two transverse polarization<sup>2</sup> states. On the contrary, since a massive gauge boson can be brought to rest by a Lorentz transformation, and since there is no preferred direction in the rest frame, spatial isotropy requires three spin states. As specified by an *Equivalence Theorem*, at energies large compared to gauge bosons mass the longitudinal mode can be identified with the underlying Goldstone boson from symmetry-breaking sector. In this sense we can say that three particles from the otherwise unknown symmetry-breaking sector have already been discovered: the longitudinal gauge modes  $W_L^\pm$  and  $Z_L$ .

In the Standard Model matter fields are represented by spin- $\frac{1}{2}$  particles, fermions, divided into two categories, leptons and quarks. Both leptons and quarks have their charge conjugate partner (antiparticles) which have identical mass and spin, but opposite additive quantum numbers (with respect to the vacuum).

**Table 1.1:** Fermion features

Fermions	1 <sup>st</sup> gen	2 <sup>nd</sup> gen.	3 <sup>rd</sup> gen.	Charge	Interactions
<i>Quarks</i>	$\begin{pmatrix} u \\ d \end{pmatrix}$	$\begin{pmatrix} c \\ s \end{pmatrix}$	$\begin{pmatrix} t \\ b \end{pmatrix}$	$+\frac{2}{3}$ $-\frac{1}{3}$	All
<i>Leptons</i>	$\begin{pmatrix} \nu_e \\ e \end{pmatrix}$	$\begin{pmatrix} \nu_\mu \\ \mu \end{pmatrix}$	$\begin{pmatrix} \nu_\tau \\ \tau \end{pmatrix}$	0 -1	Weak,E.M.

All the elements of the three generations have been directly observed and up to now there is no experimental evidence of the existence of a further generation.

Fermionic matter-fields of the SM are classified in specific representations of the gauge group, and therefore have specific transformation properties with respect to the  $SU(3)_C \otimes SU(2)_T \otimes U(1)_Y$  gauge group. Fermions fields are written as two components left- an right-handed Weyl spinors.

$$Q_L^i = \begin{pmatrix} u_L^i \\ d_L^i \end{pmatrix} = (3, 2, \frac{1}{6}), \quad u_R^i = (3, 1, \frac{2}{3}), \quad d_R^i = (3, 1, -\frac{1}{3})$$

$$L_L^i = \begin{pmatrix} \nu_L^i \\ l_L^i \end{pmatrix} = (1, 2, -\frac{1}{2}), \quad l_R^i = (1, 1, -1), \quad i = 1, 2, 3$$

<sup>2</sup>The terms transverse and longitudinal refer to the polarization of three-vectors:  $\varepsilon_T$  is transverse to the momentum  $\mathbf{p}$  while  $\varepsilon_L$  is parallel to it

where the indicated numbers are the dimensions of the representation respectively for  $SU(3)_C$ ,  $SU(2)_T$  and the value of the hypercharge  $Y$ ; the index  $i$  runs over the three generations, while the  $\nu_R^i$  is not shown since it is a singlet with respect to gauge group transformation.

Electric charge (in unit of elementary charge  $e=1.602176462 \times 10^{-19}C$ ) can be written as:  $Q = T_3 + \frac{Y}{2}$  indicating with  $T_3$  the diagonal generator of  $SU(2)_L$ .

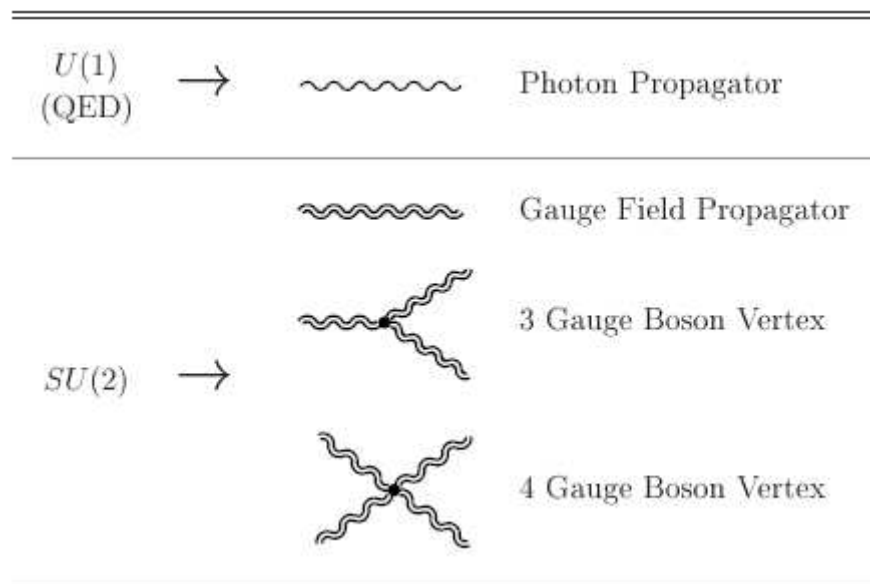
So the elementary constituents of matter are of two types, the basic building blocks of matter themselves known as matter particles and the intermediate interaction particles, quanta of the gauge fields. The first ones are fermions of spin  $s=1/2$  and are classified into leptons and quarks. The known leptons are: the electron  $e^-$ , the muon  $\mu^-$  and the tau  $\tau^-$ , all with electric charge  $Q=-1$  (all charges are given in units of the elementary charge  $e$ ); and the corresponding neutrinos  $\nu_e$ ,  $\nu_\mu$  and  $\nu_\tau$  with  $Q=0$ . The known quarks are of six different flavours u,d,s,c,b, and t and have fractional charge  $Q=2/3$  for up-like quarks  $u^i$   $i=1,2,3$  (u,c,t) and  $Q=1/3$  for down-like quarks  $d^i$   $i=1,2,3$  (d,s,b).

The quarks have an additional quantum number (a charge that comes from  $SU(3)_C$  invariance of QCD lagrangian), which comes in three types. We know that colour is not directly observable and therefore quarks must be confined into experimentally observed colourless strongly interacting *hadrons*. These colourless composite particles are classified into baryons and mesons. The baryons are fermions made by three valence quarks, while mesons are bosons made of one quark and one antiquark.

The second type of elementary particles are the intermediate interaction particles. Leaving aside gravitation, which plays a minor role at subatomic scales, all relevant interactions in elementary particle physics are known to be mediated by the exchange of a spin  $s = 1$  vector boson. The photon,  $\gamma$ , is the exchanged particle in electromagnetic interactions, the eight gluons  $g_\alpha$ ,  $\alpha=1,\dots,8$ , mediate the strong interactions among quarks, while the weak bosons  $W^\pm$  and  $Z^0$ , are the corresponding intermediate bosons of the weak interactions. The main features of both the two kinds of elementary constituents of matter are summarized in Tables 1.1 and 1.2.

**Table 1.2:** Gauge Bosons features

	Electromagnetic	Weak	Strong
Quantum	Photon( $\gamma$ )	$W^\pm$ and Z	$g_\alpha$
Number of quanta	1	3	8
Mass ( $GeV/c^2$ )	0	$80 \div 90$	0
Coupling constant	$\alpha(\mu = m_e) \simeq \frac{1}{137}$	$G_F = 1.167 \times 10^{-5} GeV^{-2}$	$\alpha_S(M_Z) \simeq 0.1$
Range(cm)	$\infty$	$10^{-16}$	$10^{-13}$

**Figure 1.1:** Examples of couplings prescribed by an Abelian gauge symmetry (U(1)) and a non abelian SU(2)

### 1.1.1 The Glashow-Weinberg-Salam Model

In physics, the dynamics of any system could be described through the lagrangian formalism. In such representation symmetries of the lagrangian function play a capital role: as an example one can think about invariance of the Lagrangian with respect to temporal translations or spatial translations and rotations and the resulting conservation laws of four-momentum and angular momentum of the system.

In order to implement a theory able to describe fundamental interactions of elementary particles, lagrangian formalism of Quantum Field Theory (QFT) is used. In particle physics, one of the fundamental principles of QFT is local gauge symmetry of the Lagrangian. This invariance as a matter of fact predicts the nature of the interactions between particles and ensures the existence of conserved physical quantities; in substance the conserved quantities are the observables associated to the symmetry group generators.

Another required feature of a QFT is renormalizability of the Lagrangian. Theoretical predictions of whatever physical observable are obtainable only through a perturbative computation: in the case of a non-renormalizable theory this approach fails and therefore the theory itself loses any predictive power. It has been demonstrated that in a QFT local gauge invariance is an essential requirement to ensure the renormalizability of the Lagrangian. The third foundation of of QFT, beyond local gauge invariance and renormalizability is unitarity. Given the probabilistic meaning of the the matrix element inherent to any physical process, the integral of whatever amplitude over the kinematically accessible interval (eventually infinite) has to be finite and therefore such to ensure that the sum over all the possibilities can be normalized to the unit.

The Glashow-Weinberg-Salam Model [1], which formalizes electroweak interactions is based upon a quantum field theory invariant under local gauge transformations. The Lie group of transformations under which there is invariance is the direct product of weak left-handed isospin  $SU(2)_L$  with the weak hypercharge group  $U(1)_Y$ :  $SU(2)_L \otimes U(1)_Y$ . Noether theorem ensures, for that symmetry group, the existence of 4 conserved currents: two weak charged currents, one weak neutral current and one electromagnetic neutral current.

#### Gauge Invariance

Quarks and leptons, grouped in families, are further on organized in weak interactions doublets and singlets (representation of  $SU(2)_L$ ). Weak interactions, in fact, act only upon the negative helicity components of fermions

(*left*) corresponding to the projection of spin opposite to particle's motion, while electromagnetic interaction couples itself indistinctly with positive helicity (*right*) and negative projections of the field, provided that it is charged. Since neutrino has only negative helicity and therefore negative helicity, one has:

$$l_{eL} = \begin{pmatrix} \nu_{eL} \\ e_L \end{pmatrix}, \quad e_R \quad / \quad q_L = \begin{pmatrix} u_L \\ d_L \end{pmatrix}, \quad q_R \quad (1.2)$$

Starting from free Dirac Lagrangian and requiring only invariance under global  $SU(2) \otimes U(1)$  gauge transformations, one obtains a Lagrangian ( $\mathcal{L}$ ) of the type:

$$\mathcal{L} = \bar{\nu}_L i \gamma^\alpha \partial_\alpha \nu_L + (\bar{e}_L + \bar{e}_R) i \gamma^\alpha \partial_\alpha (e_L + e_R) \quad (1.3)$$

where  $\alpha$  is a lorentzian index and mass terms are not present since they would break global  $SU(2)_L$  symmetry.

In order to render  $\mathcal{L}$  invariant also under global gauge transformations, the introduction of the *covariant derivative* is needed.

$$\partial_\alpha \rightarrow D_\alpha = \partial_\alpha - i g t^a A_\alpha^a + \frac{1}{2} i g' Y B_\alpha \quad (1.4)$$

where  $A_\alpha^a$  and  $B_\alpha$  are gauge fields ( $a = 1, 2, 3$ ) associated respectively to generators of  $SU(2)$  and  $U(1)$  which in a non-abelian theory take the name of Yang-Mills fields. The fields thus appearing in  $\mathcal{L}$  are not yet real physical fields. By applying a rotation to  $B_\alpha$  and  $A_\alpha^{(3)}$ , of an angle  $\theta_W$ , called *Weinberg angle*, one obtains the electromagnetic field  $A_\alpha$  and a neutral field  $Z_\alpha$ :

$$\begin{cases} Z_\alpha = \cos \theta_W A_\alpha^{(3)} + \sin \theta_W B_\alpha \\ A_\alpha = -\sin \theta_W A_\alpha^{(3)} + \cos \theta_W B_\alpha \end{cases} \quad (1.5)$$

Now linearly combining  $A_\alpha^1$  and  $A_\alpha^2$  one obtains:

$$\begin{cases} W_\alpha^+ = \frac{1}{\sqrt{2}} A_\alpha^+ = \frac{1}{\sqrt{2}} (A_\alpha^{(1)} + i A_\alpha^{(2)}) \\ W_\alpha^- = \frac{1}{\sqrt{2}} A_\alpha^- = \frac{1}{\sqrt{2}} (A_\alpha^{(1)} - i A_\alpha^{(2)}) \end{cases}$$

introducing transformation 1.4 e and making the physical gauge fields  $A, Z, W^\pm$  appear,  $\mathcal{L}$  becomes:

$$\mathcal{L} = \frac{1}{2\sqrt{2}} g (J_\alpha^{(+)} W^{\alpha(+)} + J_\alpha^{(-)} W^{\alpha(-)}) - e J_\alpha^{EM} A^\alpha + \frac{\sqrt{g^2 + g'^2}}{2} J_\alpha^{(Z)} Z^\alpha \quad (1.6)$$

where:

$$\begin{aligned}
J_\alpha^+ &= \bar{\nu}_L \gamma_\alpha e_L \\
J_\alpha^- &= e_L \gamma_\alpha \bar{\nu}_L \\
J_\alpha^Z &= J_\alpha^3 - 2 \sin^2 \theta_W J_\alpha^{EM} \\
J_\alpha^{EM} &= -(\bar{e}_R \gamma_\alpha e_R + \bar{e}_L \gamma_\alpha e_L)
\end{aligned}$$

In order to obtain a Lagrangian in which appears the electromagnetic current  $J_\alpha^{EM}$  it has been necessary to impose the conditions:

$$-g \sin \theta_W + g' \cos \theta_W = 0$$

$$\frac{g' g}{\sqrt{g'^2 + g^2}} = e$$

The Lagrangian so obtained predicts the existence of two charged gauge fields ( $W_\alpha^+$  and  $W_\alpha^-$ ) which couple themselves only with left-handed fermions ( $J_\alpha^+$  and  $J_\alpha^-$  are purely weak) and two neutral fields ( $Z_\alpha$  and  $A_\alpha$ ) which interact with both left and right components.

### 1.1.2 The Higgs boson and the mass term introduction

In order to make a theory describe a real phenomenology of fundamental interactions it is required that matter-fields (fermions) and gauge fields (bosons) acquire a mass. *Spontaneous symmetry breaking*, which happens through *Higgs mechanism*[2] has been introduced in order to explain the origin of masses, without breaking the underlying local gauge symmetry of the Lagrangian, essential requirement to ensure renormalizability of SM.

The mechanism requires the introduction in the Lagrangian of a weak isodoublet of complex scalar fields, the Higgs field  $\phi$  and of a potential depending on the latter:

$$\phi = \begin{pmatrix} \phi^+ \\ \phi^0 \end{pmatrix} = \frac{1}{\sqrt{2}} \begin{pmatrix} \phi^1 + i\phi^2 \\ \phi^3 + i\phi^4 \end{pmatrix} \quad (1.7)$$

$$V(\phi^\dagger \phi) = \mu^2 \phi^\dagger \phi + \lambda (\phi^\dagger \phi)^2 \quad \mu^2 < 0, \lambda > 0$$

The Higgs term Lagrangian is written as:

$$\mathcal{L}_{EWSB} = (D^\mu \phi)^\dagger (D_\mu \phi) + V(\phi^\dagger \phi) \quad (1.8)$$

The functional form of Higgs potential is shown in figure 1.2

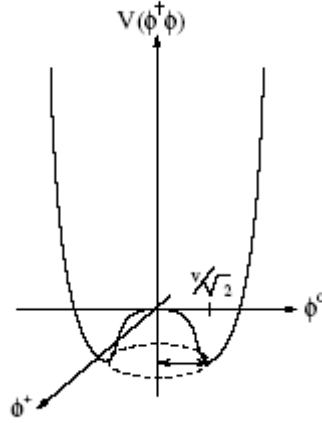


**Figure 1.2:** Functional form of Higgs potential

Higgs potential  $V(\phi^\dagger\phi)$  being invariant under  $SU(2)$  transformations, i.e. rotations on the plane  $(\phi^+, \phi^0)$  owns a degenerate minimum state. That minimum is equal to the void expectation value (v.e.v.) of the Higgs field  $\phi$ . The locus of minima is itself invariant under  $SU(2)$  transformations. It is therefore chosen arbitrarily a minimum along the  $\phi_0$  axis:

$$\langle \phi \rangle = \frac{1}{\sqrt{2}} \begin{pmatrix} 0 \\ v \end{pmatrix}, \quad v^2 = -\frac{\mu^2}{2\lambda} \quad (1.9)$$

Thanks to this process symmetry is spontaneously broken and one of the two complex scalar fields of the Higgs field remains massless (Goldstone boson), while the other is endowed with mass and is baptized Higgs boson.

In fact  $\phi$  can be re-written in a generic gauge starting from its v.e.v. under the form:

$$\phi = \frac{1}{\sqrt{2}} e^{i\phi^a t_a} \begin{pmatrix} 0 \\ H + v \end{pmatrix}, \quad a = 1, 2, 3$$

where it could be observed the presence of three fields  $\phi^a$  e il  $\phi^4 = H + v$ . So four extra degrees of freedom are added to the six degrees of freedom coming from transversal polarizations of the three original gauge fields ( $W^+, W^-, Z$ ) not yet massive.

The unitary gauge is fixed applying the gauge transformation:

$$\phi' = e^{-\frac{i}{v}\phi^a t_a} \phi = \frac{1}{\sqrt{2}} \begin{pmatrix} 0 \\ H + v \end{pmatrix} = \frac{1}{\sqrt{2}} \begin{pmatrix} 0 \\ \phi^4 \end{pmatrix} \quad (1.10)$$

So it is possible to define the only remaining field, the Higgs field, in order to let it have a vanishing v.e.v.

If now one considers the extra lagrangian term 1.8 and expands it introducing the value of  $\phi$  in the unitary gauge, one obtains a sum of three terms.

$$\mathcal{L}_{\text{EWSB}} = \mathcal{L}_{\mathcal{H}} + \mathcal{L}_{\mathcal{HW}} + \mathcal{L}_{\mathcal{HZ}} \quad (1.11)$$

where not considering higher orders and approximating the Higgs potential as  $V \sim \mu^2 H^2 + \text{cost}$  one has:

$$\begin{aligned} \mathcal{L}_{\mathcal{H}} &= \frac{1}{2} \partial_\alpha H \partial^\alpha H + \mu^2 H^2 & (1.12) \\ \mathcal{L}_{\mathcal{HW}} &= \frac{1}{4} v^2 g^2 W_\alpha W^{\alpha\dagger} + \frac{1}{2} v g^2 H W_\alpha W^{\alpha\dagger} = M_W^2 W_\alpha W^{\alpha\dagger} + \frac{1}{2} g_{HW} H W_\alpha W^{\alpha\dagger} \\ \mathcal{L}_{\mathcal{HZ}} &= \frac{1}{8} v^2 (g^2 + g'^2) Z_\alpha Z^\alpha + \frac{1}{4} v (g^2 + g'^2) H Z_\alpha Z^\alpha = \frac{1}{2} M_Z^2 Z_\alpha Z^\alpha + \frac{1}{2} g_{HZ} H Z_\alpha Z^\alpha \end{aligned}$$

The three gauge bosons of Glashow-Weinberg-Salam model become massive and acquire an extra polarization degree (the longitudinal one). The original ten degrees of freedom are restored, since three Goldstone bosons have yielded their degrees of freedom to gauge boson, which therefore acquire mass.

The masses of  $W$  and  $Z$  depend on the electroweak coupling constants  $e$  on the  $v$  parameter:

$$\begin{cases} M_W = \frac{1}{2} v g \\ M_Z = \frac{1}{2} v (g^2 + g'^2)^{1/2} \end{cases} \rightarrow \frac{M_W}{M_Z} = \frac{g}{(g^2 + g'^2)^{1/2}} = \cos\theta_W \quad (1.13)$$

and the coupling between Higgs and gauge bosons are proportional to the square of their masses:

$$g_{HW} = \frac{1}{2} v g^2 = \frac{2}{v} M_W^2 \quad (1.14)$$

$$g_{HZ} = \frac{1}{2} v (g^2 + g'^2) = \frac{2}{v} M_Z^2 \quad (1.15)$$

So the following relationship between branching ratios holds:

$$\frac{BR(H \rightarrow W^+W^-)}{BR(H \rightarrow ZZ)} = \left( \frac{g_{HW}}{g_{HZ}} \right)^2 = 4 \frac{M_W^2}{M_Z^2} \sim 3$$

Finally it is possible to determine the energy scale of electroweak spontaneous symmetry being the parameter  $v$  linked to Fermi constant by the relationship:

$$v = \left( \frac{1}{\sqrt{2}G_F} \right)^{\frac{1}{2}} = 246 \text{ GeV} \quad (1.16)$$

Higgs mechanism is used also to give masses to fermions, by inserting in the SM lagrangian an interaction term between Higgs field and matter quanta such to maintain  $SU(2) \times U(1)$  symmetry. Fermions are divided in left-handed doublets and right-handed singlets, and Higgs field is a doublet of  $SU(2)$ : the interaction term to preserve gauge invariance has to be of the form:

$$\bar{l}_e \phi e_R$$

Since in the unitary gauge the first component of  $\phi$  is vanishing, only the second left component of  $l_e$ ; this results perfectly adequate in the case of leptons for whom the first component of  $l_e$  is occupied by the neutrino field, that does not have a right component. For leptons and quark fields of type down (the ones occupying the second component of  $l_e$ ), the extra term in the Lagrangian is:

$$\mathcal{L}_l = -G_{lH}(\bar{l}_e \phi e_R + \bar{e}_R \phi^\dagger l_e) = -\frac{G_{lH}}{\sqrt{2}} v \bar{e} e - \frac{G_{lH}}{\sqrt{2}} H \bar{e} e \quad (1.17)$$

with the lepton mass and the Higgs coupling given by:

$$M_e = \frac{G_e}{\sqrt{2}} v \quad (1.18)$$

$$g_{He} = \frac{G_{lH}}{\sqrt{2}} = \frac{M_e}{v} \quad (1.19)$$

in order to give mass to the positive isospin quarks (u,c,t) it is necessary to introduce the charge-conjugate field  $\phi^c$ :

$$\phi^c = -i\tau_2 \phi^* = \frac{1}{\sqrt{2}} \begin{pmatrix} \phi^3 - i\phi^4 \\ -\phi^1 + i\phi^2 \end{pmatrix} \quad (1.20)$$

which in the unitary gauge becomes:

$$\phi^c = \frac{1}{\sqrt{2}} \begin{pmatrix} \eta + v \\ 0 \end{pmatrix}$$

In the case of quarks a further lagrangian term is therefore needed:

$$\mathcal{L}_u = -G_{Hu} \bar{l} \phi^c u_R + h.c. \quad (1.21)$$

Also in this case the coupling constant is proportional to the fermion mass. The mass of all matter quanta remain free parameters of the lagrangian which cannot justify neither their values nor the enormous mass range in which they are distributed.

Nevertheless the SM is extremely predictive for what concerns the Higgs coupling, which is described only by the parameter  $v$ , since the two initial terms  $\mu$  and  $\lambda$  are related by eq. 1.9.

### Experimental success of SM

The Standard model has been successfully tested at the LEP collider, at SLC, at the Tevatron and at HERA. Precision tests were performed on the most important observables predicted by the S.M. The main lesson of the precision tests can be summarized as follows. It has been checked that coupling of quarks and leptons to gauge bosons  $W$  and  $Z$  are indeed precisely those prescribed by the gauge symmetry. The accuracy of a few 0.1% for these tests implies that, not only the tree-level expectation values, but also higher order quantum corrections have been verified. Even if not with comparable precision triple gauge vertexes  $\gamma W^+ W^-$  and  $Z W^+ W^-$  have been measured and found in agreement with the predicted non-abelian structure of the theory. This means that the gauge symmetry is indeed unbroken in the vertexes of the theory: the weak currents are indeed conserved. Yet there is an obvious evidence that the symmetry is otherwise broken in the masses. In fact the  $SU(2)_L \otimes U(1)_Y$  gauge symmetry forbids masses for all the particles that have been so far observed, quark, leptons and gauge bosons. But of all these particles only the photon and the gluons are massless (protected by the  $SU(3)_C \otimes U(1)_{EM}$  unbroken colour and electric charge gauge symmetry), all other are massive. The Higgs particle, responsible for the EWSB (Electroweak Symmetry Breaking) and the particle masses, has not been found but its mass can well be heavier than the present direct lower limit  $m_H < 114.4 GeV$  (95% C.L.) obtained at LEP2.

## 1.2 Higgs Properties and Searches

Higgs boson is a particle hard to discover, since it couples itself with fermion fields through a constant proportional to their masses, therefore direct decays in electrons and muons, which provide the cleanest signatures are heavily suppressed. In the following the main production mechanisms and decay modality which determine search strategies at LHC will be described.

### 1.2.1 Higgs Decays

The Standard Model is extremely predictive in the Higgs sector, giving all couplings, decay widths and production cross sections at a given Higgs boson mass, a parameter which instead should be experimentally determined.

In figure 1.3 and 1.4 the total decay width and decay branching ratios of the SM Higgs boson are reported as a function of the mass for a large range of values, from  $50 \text{ GeV}$  to  $1 \text{ TeV}$ . The curves shown include effects of next to leading order radiative corrections.[3]

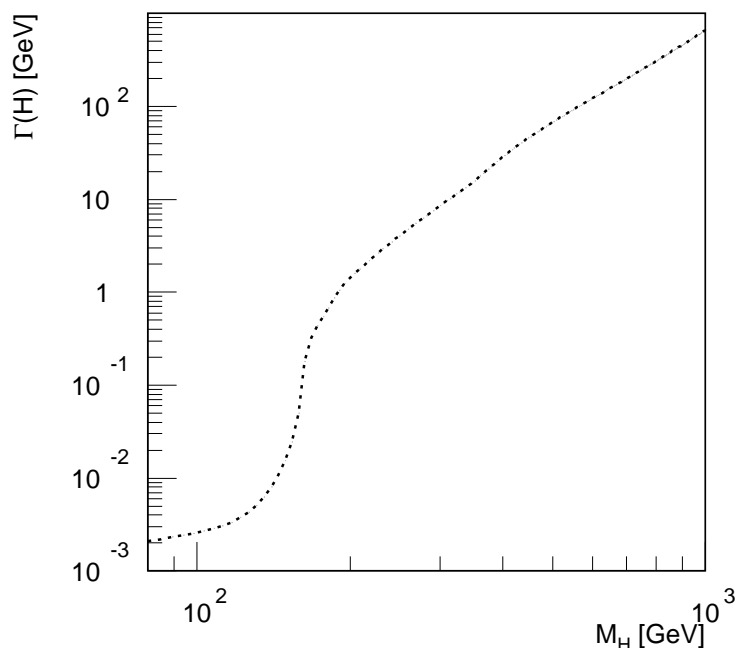
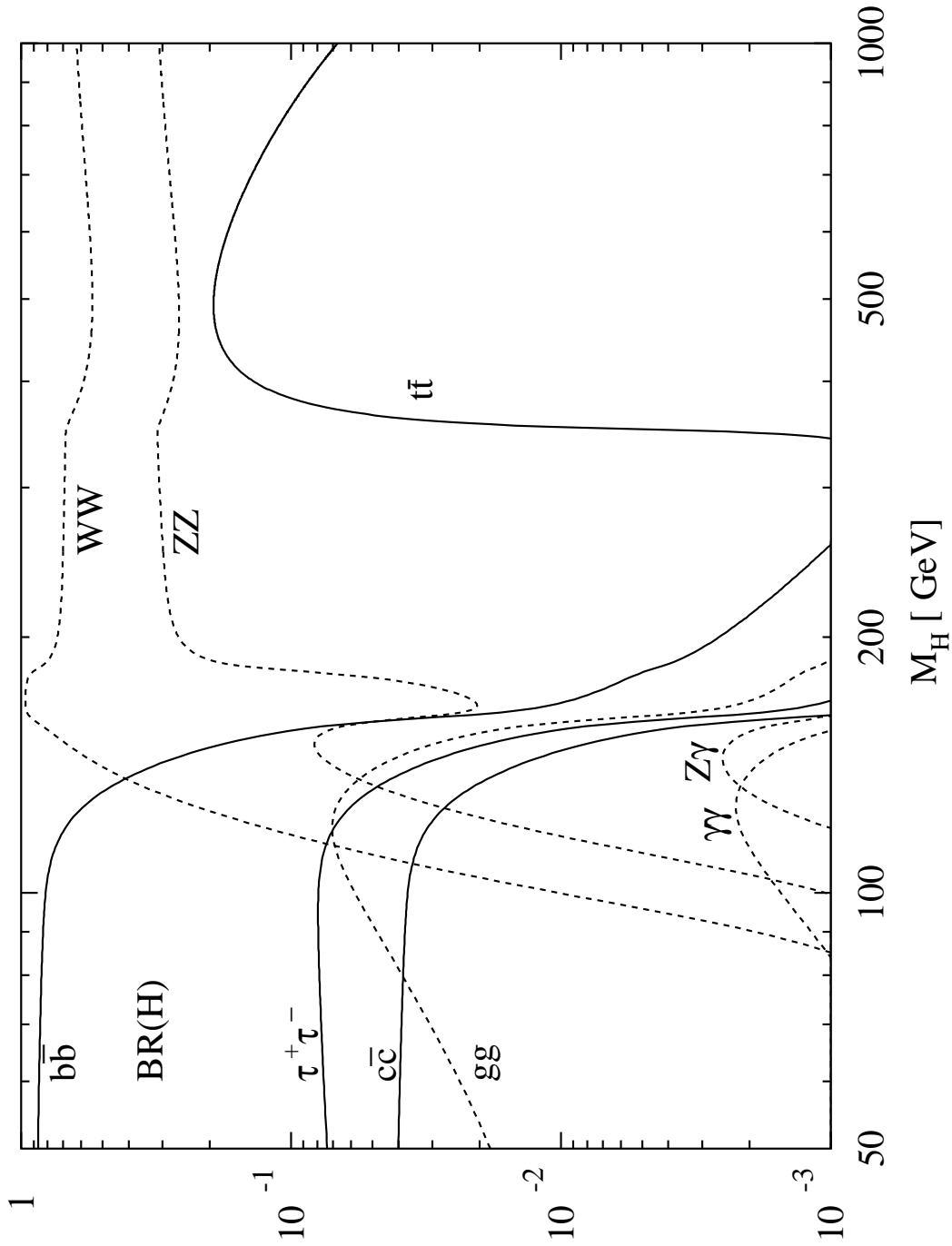


**Figure 1.3:** Total decay width  $\Gamma_H$  of Standard Model Higgs Boson in function of its mass

**Figure 1.4:** Decay branching ratios of the Standard Model Higgs boson as a function of the mass. Decays into fermion-antifermion pairs are represented by solid lines, decays into vector bosons with dashed lines



The trend of the branching ratios in function of the Higgs mass  $M_H$  suggests to divide the range of possible masses (50  $GeV$  up to  $\mathcal{O}(1 TeV)$ ) into three distinct regions: a *light Higgs region* ( $M_H < 130 GeV$ ), an *intermediate region* ( $130 GeV < 180 GeV$ ) and finally a *heavy Higgs region* ( $M_H > 180 GeV$ ), being the value of mass of two on shell  $Z$  bosons the threshold between the latter two regions. As it will be seen in subsection 1.7.2 each region has specific dominant channels, that can be exploited in a SM Higgs search at the LHC.

The Higgs mass depends on the unknown coupling constant  $\lambda$  in the Higgs potential, and therefore cannot be predicted. However some constraints can be fixed from theory [4],[5]. A lower bound can be set requiring that the theory is stable up to a certain scale: the Higgs potential is affected by radiative corrections (which depend on the renormalization scale) and the potential itself can change its shape until it loses an absolute minimum, generating a spectrum without lower bounds and therefore unphysical. At the same time, the coupling  $\lambda$  increases with the energy scale; the requirement that it remains finite up to a scale (triviality) corresponds on putting an upper bound on  $M_H$ . The theoretical bounds on  $M_H$  as a function of the scale up to which the Standard Model is assumed to be valid are shown in figure 1.6.

For a Standard Model remaining valid up to the Planck scale  $\Lambda_P (= 10^{19} GeV)$ , the Higgs mass must be in the range 130-200  $GeV$ . Nevertheless it is important to understand that even if the Higgs boson is found, the SM, for internal consistency, predicts an energy scale at which new physics must appear.

Assuming the validity of the Standard Model only up to 1  $TeV$ , the Higgs mass can be as large 700  $GeV$ . In any case, the main indication is that the Higgs boson should be searched in a range of masses below 1  $TeV$ . More stringent limits are in fact coming from the direct experimental searches which will be reviewed in the following.

### 1.2.2 Lower Limit on SM Higgs

A lower limit on the Higgs mass  $M_H$  can be derived from the requirement of vacuum stability. The limit is a function of the top quark mass  $m_t$  and of the energy scale  $\Lambda$  where the model breaks down and new physics appears. The possible instability of the Higgs potential  $V(\phi\phi^\dagger)$  is generated by quantum loop corrections to classical expression of  $V(\phi\phi^\dagger)$ . At large values of  $\phi$  the derivative of the potential could become negative and the potential unbounded from below. It has been demonstrated that the stability of the potential for  $\langle 0|\phi(x)|0\rangle \sim \Lambda \gg m_Z$  practically coincides with the requirement that the running coupling constant  $\lambda(\mu)$  never becomes negative up to

the break down scale  $\Lambda$ .

The one-loop renormalization group equation (RGE) for  $\lambda(\mu)$  is:

$$\frac{d\lambda(\mu)}{d\ln(\mu)} = \frac{1}{8\pi^2} \left[ 12\lambda^2 + \frac{3}{8}g^4 + \frac{3}{16}(g^2 + g'^2)^2 - 12\left(\frac{m_t}{v}\right)^4 - \lambda g^2 - \frac{3}{2}\lambda(g^2 + g'^2) + 12\lambda\left(\frac{m_t}{v}\right) \right] \quad (1.22)$$

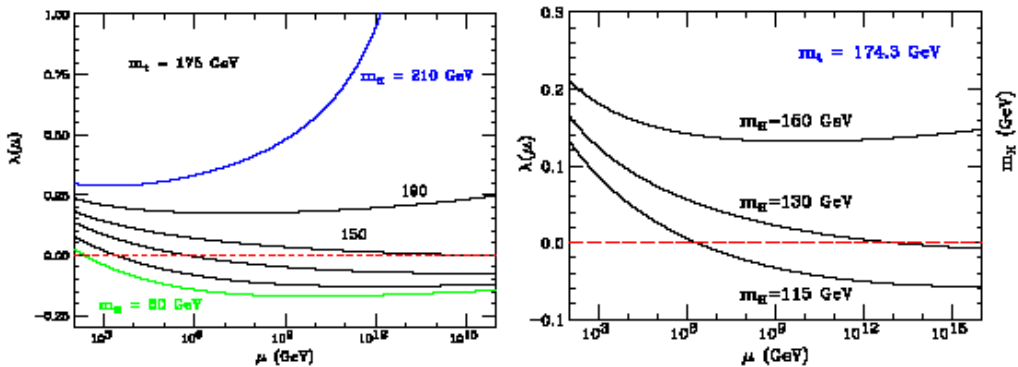
This equation must be solved together with one-loop RGE for the gauge and Yukawa couplings.

For small  $m_H$  with respect to  $m_t$ , it is possible that:

$$\frac{d\lambda(t)}{dt} < 0 \quad t = \ln\left(\frac{\Lambda}{\mu}\right);$$

thus  $\lambda$  becomes negative. In figure 1.5 the dependences of  $\lambda(\mu)$  on  $\mu$  for two different Higgs masses are shown. One can also invert the curves in figure 1.5, obtaining the  $M_H$  limits as a function of  $\Lambda$ . It is remarkable that if  $m_t \sim (174 \div 178)$  GeV and  $\Lambda \sim \Lambda_P$  then  $M_H$  must be larger than 130 GeV. On the other side, if  $M_H < 130$  GeV (and  $m_t$  is in the range indicated) the SM breaks down well below  $\Lambda_P$ : new physics must appear at the scale where SM breaks down.

**Figure 1.5:** Dependence of quartic coupling constant  $\lambda$  on the energy scale  $\mu$



### 1.2.3 Upper Limit on SM Higgs

An upper bound on  $m_H$  (with mild dependence on  $m_t$ ) can be obtained from the requirement that up to a scale  $\Lambda$  no Landau poles appear in the Higgs self-couplings. In fact if we consider the renormalization group equation for  $\lambda$  in the simplified case when gauge and Yukawa couplings were neglected, we can find:

$$\beta(\lambda) = \frac{3\lambda^2}{2\pi^2} \quad (1.23)$$

with the  $\beta$ -function giving the variation of the coupling with the scale:

$$\beta(\lambda) = \mu \frac{d\lambda}{d\mu} \quad (1.24)$$

combining equations 1.23 and 1.24, it possible to compute the behaviour of the coupling constant as a function of the scale:

$$\frac{1}{\lambda(\mu)} = \frac{1}{\lambda(\Lambda) + \frac{3}{2\pi^2} \ln \frac{\Lambda}{\mu}}$$

or in function of  $\Lambda(\lambda)$ :

$$\lambda(\Lambda) = \frac{\lambda(\mu)}{1 - \lambda(\mu) \frac{3}{2\pi^2} \ln \left( \frac{\Lambda}{\mu} \right)}$$

We can see that  $\lambda(\Lambda)$  has a Landau pole for:

$$\Lambda = \mu \exp \left( \frac{2\pi^2}{3\lambda(\mu)} \right) \quad (1.25)$$

vacuum stability requirement forces Eq. 1.25 to be:

$$\Lambda < \mu \exp \left( \frac{2\pi^2}{3\lambda(\mu)} \right) \quad (1.26)$$

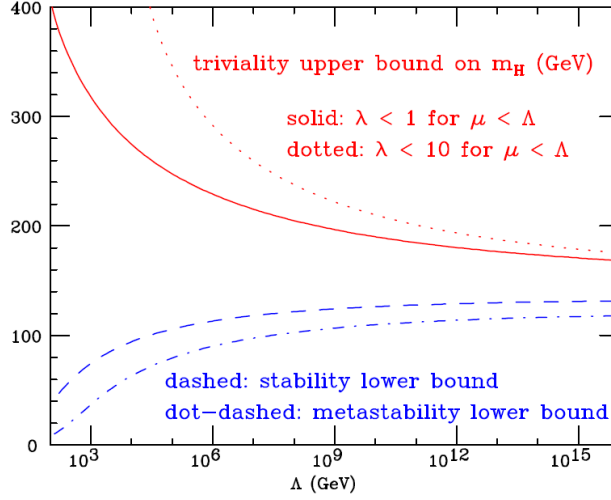
Thus for the energy scale <sup>3</sup>  $\mu = M_H$  and remembering that  $m_H^2 \sim 2\lambda(m_H)v^2$ , at tree level, an upper bound on Higgs mass is obtained:

$$\Lambda < M_H \exp \left( \frac{4\pi^2 v^2}{3M_H^2} \right) \quad (1.27)$$

---

<sup>3</sup>The Higgs mechanism has to be valid, at least, up to this scale of energy, in order to perform its task

**Figure 1.6:** Theoretical limits on Standard Model Higgs boson mass. The allowed region, as a function of the energy scale  $\Lambda$  at which the Standard Model breaks down, is between the two curves, obtained assuming  $m_t = 175 \text{ GeV}/c^2$  and  $\alpha(M_Z) = 0.118$



The relation 1.27 implies that for a given Higgs boson mass, there is a finite cutoff energy at which the description of the theory as a fundamental theory stops making sense. This means that the Standard Model can only be regarded as an effective theory valid below this cutoff. The theory of a relatively light weakly coupled Higgs boson can be self-consistent to a very high energy. Conversely, Higgs mass has not to be too large. For example, if the theory has to be valid up to a typical Grand Unified Theory scale energy,  $10^{16}$  GeV, then the Higgs boson mass has to be less than about 170 GeV. Since we have computed the  $\beta$ -function in perturbation theory, this answer is only reliable at energy scales at which  $\lambda(\mu)$  as well as the Higgs boson mass is small. Non-perturbative lattice calculations are available. Estimates indicated that if the theory has to be valid up to 4 TeV, the mass of the Higgs boson has to be less than about 800 GeV. The upper limit is the so-called "triviality bound", in fact from Eq. 1.41 it is easy to find that:

$$\lambda(\mu) < \frac{2\pi^2}{3 \ln\left(\frac{\Lambda}{\mu}\right)} \quad (1.28)$$

which shows that for  $\Lambda \rightarrow \infty$ ,  $\lambda \rightarrow 0$ . So if the SM is valid up to the Grand Unification Theory scale, Higgs sector interactions are weak.

### 1.2.4 Higgs decay processes

The magnitude of Higgs boson interactions with fermions and vector gauge bosons  $V$  ( $V=W,Z$ ) scales with their masses ( $M_V, m_f$ ):

$$g_{VVH} = 2\sqrt{\sqrt{2}G_F}M_V^2 \quad g_{f\bar{f}H} = 2\sqrt{\sqrt{2}G_F}m_f \quad (1.29)$$

Therefore Higgs boson couples preferentially with the heaviest kinematically available particles of the Standard Model (top quark,  $Z$ ,  $W$ , bottom quark). Decays into these particles will be dominant as soon as they become kinematically allowed. The measurement of this different decay channels should, in principle, allow to distinguish a Standard Model Higgs and a more complicated Higgs Sector.

#### Decay in a fermion-antifermion pair

To the lowest perturbative order partial decay width for Higgs boson in a lepton-antilepton pair is given by:

$$\Gamma(H^0 \rightarrow l^+l^-) = \frac{G_F M_l^2}{4\pi\sqrt{s}} M_H \beta^3 \quad (1.30)$$

where  $\beta = \sqrt{1 - 4M_l^2/M_H^2}$  is the speed of the leptons. The fraction of Higgs decays into  $\tau$  leptons is roughly 10% in the intermediate mass range, while decay in muon reaches a level of  $10^{-4}$ ; all other leptonic decays are not phenomenologically important. In Fig. 1.7 is shown the diagram which contributes to this process at the lowest order.

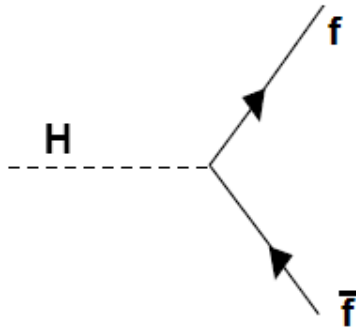


**Figure 1.7:** Lowest order Feynman diagram for Higgs decay into two fermions

The partial decay width in a couple of quarks has an additional colour factor ( $N_C = 3$ ), besides other important QCD corrections:

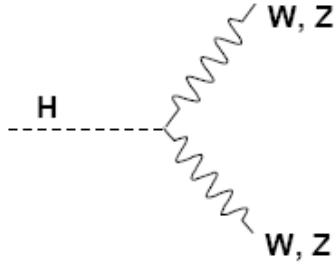
$$\Gamma(H^0 \rightarrow q\bar{q}) = \frac{3G_F m_q^2}{4\pi\sqrt{s}} M_H \beta^3 \left( 1 + \frac{4\alpha_s}{3\pi} \Delta_H^{QCD} \right) \quad (1.31)$$

where  $\alpha_s$  is strong interactions coupling constant<sup>4</sup>. To understand the importance of these corrections, it suffice to consider that, for a 100 GeV Higgs, the fraction of decays into a  $b$  couple diminish of a factor 2, when one includes order  $\alpha_s$  corrections. The most part of corrections for Higgs decay in a couple of quarks can be absorbed in the definition of a variable mass for the quark in the final state  $m_q(\mu)$ , calculated at energy scale  $\mu = M_H$ . Electroweak corrections for Higgs decay into heavy quarks and in leptons are very little and therefore can be neglected.

## Decay into a pair of gauge bosons

Beyond the WW and ZZ threshold these channels become the main way of decay of Higgs boson. In the following Fig. 1.8 is shown a typical decay of this type.

**Figure 1.8:** Lowest order Feynman diagram of Higgs decay into a vector boson pair



Partial decay width for this decay is given by:

$$\Gamma(H^0 \rightarrow VV) = \delta_V \frac{G_F M_H^3}{16\pi\sqrt{2}} \beta(1 - 4x + 12x^2) \quad (1.32)$$

<sup>4</sup>Most recent measured value for it at Z peak mass is  $\alpha_s(M_Z) = 0.1185(20)$

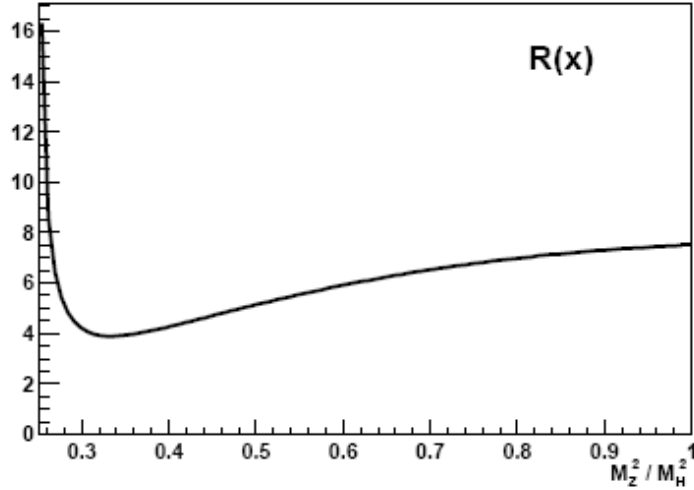
where ( $V = Z^0, W^\pm$ ),  $\delta_W = 2$ ,  $\delta_Z = 1$ ,  $x = \frac{M_V^2}{M_H^2}$  and  $\beta = \sqrt{1 - 4x}$

Electroweak corrections are about 5% in the intermediate mass range and therefore negligible. Slightly under WW and ZZ thresholds, of course become important decay in two gauge bosons whereof one is off-shell. Partial decay width for these decays has the following expression:

$$\Gamma(H^0 \rightarrow VV^*) = \delta'_V \frac{G_F M_H M_V^4}{16\pi^3} R\left(\frac{M_V^2}{M_H^2}\right) \quad (1.33)$$

where  $\delta'_W = 1$ ,  $\delta'_Z = \frac{7}{12} - \frac{10}{9}\sin^2\theta_W + \frac{40}{27}\sin^4\theta_W$ .  $R(x)$  trend in the interesting interval of masses is reported in figure 1.9:

**Figure 1.9:** Trend of function  $R(x)$  in the interval  $(\frac{1}{4} < x < 1)$   $x = \left(\frac{M_Z}{M_H}\right)^2$ , corresponding to  $(M_Z < M_H < 2M_Z)$



For a Higgs mass slightly larger than the corresponding gauge boson one, the fraction of decays into two off-shell bosons  $W^*W^*$  and  $Z^*Z^*$  becomes important. Both fractions reach the percent level for Higgs boson masses equal to 100(110) GeV for  $W^*(Z^*)$ .

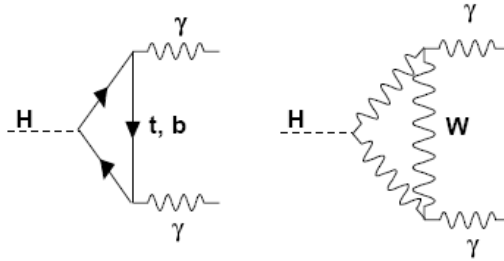
## Decays into two photons

Higgs boson decay into two photons proceeds via a heavy fermion loop, or W loop. The partial decay width can be written in the following form:

$$\Gamma(H^0 \rightarrow \gamma\gamma) = \frac{G_F \alpha^2 M_H^3}{128 \pi^3 \sqrt{2}} \left| \sum_f N_{cf} e_f^2 A_f^H + A_W^H \right|^2 \quad (1.34)$$

In figure 1.10 are reported the two lowest order diagrams contributing to two photon final state decay.

**Figure 1.10:** Typical lowest order diagrams contributing to  $H^0 \rightarrow \gamma\gamma$



If particles in the loop have very large  $Q^2$  form factors can be approximated with constant values:

$$A_f^H \longrightarrow \frac{4}{3} (M_H^2 \ll 4m_Q^2) \quad (1.35)$$

$$A_W^H \longrightarrow -7 (M_H^2 \ll 4M_W^2) \quad (1.36)$$

QCD corrections simply re-scale lowest order amplitude by a factor which depends on the ratio of Higgs and quark masses.

Electroweak corrections bring to a rise of photonic decay width of less than 1% and therefore can be neglected.

When the mass of the Higgs boson becomes large, electroweak corrections begin to depend heavily on the longitudinal component of Z and W, while transverse contributions are suppressed. This electroweak corrections are important in the region around  $M_H = 600 \text{ GeV}$ , where lowest order decay width has a minimum due the large cancellation of top quark and W loop contributions, and around very high masses  $M_H \simeq 1 \text{ TeV}$ . Since photon decay fraction becomes important in the intermediate and low range of masses, where it reaches the maximum value of  $10^{-3}$ , electroweak corrections can always be neglected.

### 1.2.5 Higgs searches

The present knowledge of the Higgs boson comes from two different sources: the direct searches at leptonic or hadronic colliders and the indirect limits, relying on the internal consistency of the SM and of the proposed electroweak symmetry breaking mechanism.

#### Indirect limit

The precision of the electroweak measurements has reached such a sensitivity to be able to probe higher order loops corrections of the Standard Model to tree level expectation values. At higher orders, all electroweak parameters have at most logarithmic dependence on  $M_H$  [6],[7]; other corrections are due to top quark loops, which depend on  $(m_t/m_W)^2$ . Measurements of electroweak parameters coming from different experiments, mainly from LEP and SLC, are used in a global  $\chi^2$  fit with the aim to find the best constraints on  $M_H$ . The results of the global fit are shown in figure 1.5 where  $\Delta\chi^2 = \chi^2 - \chi_{min}^2$  is plotted as a function of  $M_H$ .

The 95% confidence level upper limit on  $M_H$  is:

$$m_H < 219 \text{ GeV} \quad (1.37)$$

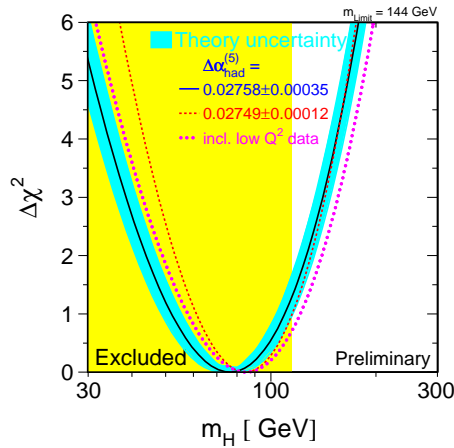


**Figure 1.11:**  $\Delta\chi^2$  of the fit to electroweak precision observables as a function of Higgs Mass  $M_H$ . The line is the result of the fit using all data, and the blue band represents the uncertainty due to neglecting higher order corrections. Vertical band delimits the region excluded by direct searches[8]

### Direct searches at LEP

The tightest constraints on the Higgs boson mass come from the combined results of the four LEP[9] (*Large Electron Positron Collider*) experiments. The four collaborations ALEPH, DELPHI, L3 and OPAL collected 2461  $pb^{-1}$  of  $e^+e^-$  collision data at a center of mass energy  $\sqrt{s}$  between 189 and 209 GeV. At LEP the Higgs boson was expected to be produced mainly in association with the  $Z^0$  boson, through the so-called *Higgsstrahlung process* ( $e^+e^- \rightarrow HZ$ ). Inputs from the four experiments are provided for all the channels and are combined together to define a variable sensitive to the signal-to-background ratio  $Q$ . One can divide the invariant mass spectrum into  $N_{bins}$  bins,  $i = 1, 2, \dots, N_{bins}$  each containing  $N_i$  observed candidates. The likelihood ratio tells how much the outcome of an experiment is signal-like. It is given by:

$$Q(M_H) = \frac{P_{poisson}(Data|s+b)}{P_{poisson}(Data|b)} = \frac{L(s+b)}{L(b)} = \frac{e^{-(s_{tot}(M_H)+b_{tot})}}{e^{-(b_{tot})}} \prod_{i=1}^{N_{bins}} \left( \frac{s(M_H)_i + b_i}{b_i} \right) \quad (1.38)$$

which can be easily simplified taking the logarithm:

$$-2\ln Q(M_H) = 2s_{TOT} - 2 \sum_{i=1}^{N_{bins}} N_i \ln \left( 1 + \frac{s_i(M_H)}{b_i} \right) \quad (1.39)$$

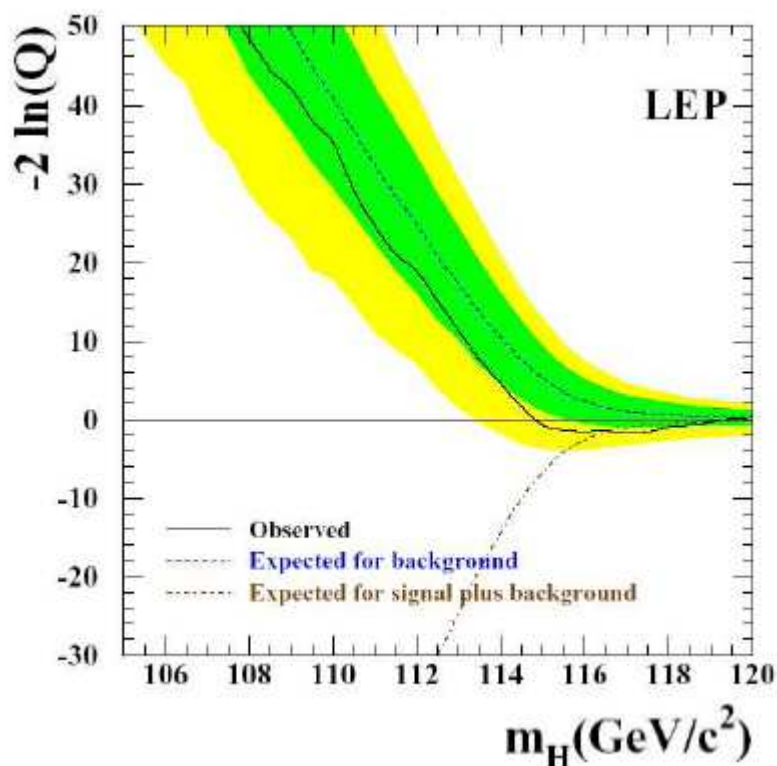
where  $b$  is the expected distribution for *background* only, and  $s+b$  the distribution for *signal+background*.

Its value is shown in figure 1.12 as a function of  $M_H$  (Higgs-like events have large  $Q$  value). The lower bound on  $M_H$  at 95% C.L. is:

$$m_H > 114.4 \text{ GeV} \quad (1.40)$$

while the preferred mass value is  $m_H = 115.6$  GeV corresponding to the maximum of the Likelihood  $-2\ln(Q)_{max} = 2.88$  (minimum of the solid line in figure 1.6). The minimum is 1.74 standard deviations away from the only background hypothesis, and it is consistent with the signal+background expectation for the same test mass. The signal-like behaviour mainly originates from the four-jet ALEPH data.

**Figure 1.12:** Observed and expected behaviour of test statistics  $-2\ln(Q)$  as a function of the test mass  $m_H$ , obtained combining the data of the four LEP experiments. The solid line is the observed curve, the dashed (dot-dashed) is the median expectation in the hypothesis of background only (signal+background)



### 1.2.6 Direct searches at Tevatron

The Higgs boson can be produced via several mechanisms at the Tevatron proton-proton collider at a center of mass energy  $\sqrt{s} = 1.96$  TeV.

The most promising discovery mode at the Tevatron is the production of the Higgs Boson in association with either a W or a Z boson: possible final states are  $\nu b \bar{b}, l^+ l^- b \bar{b}, \nu \bar{\nu} b \bar{b}, q \bar{q} b \bar{b}$ . The integrated luminosity required for each experiment (D0 and CDF)[10] to exclude a 115 GeV SM Higgs boson at 95% C.L. is  $1.5 \text{ fb}^{-1}$ , while observation at  $3\sigma$  requires instead about  $2 \text{ fb}^{-1}$ .

### 1.2.7 Beyond the Standard Model

Despite the remarkable agreement between the precision measurements of electroweak observables and Standard Model predictions, there are strong theoretical arguments that the Standard Model is not the *ultimate* theory of the fundamental particles and their interactions. It has 17 free arbitrary parameters, which may seem too many for a fundamental theory and leaves several unanswered questions. Some of them concern the problems of unification of interactions, number of fermion families, neutrino masses, naturalness/hierarchy problem. Therefore, the Standard Model is generally considered as an effective field theory, valid up to some energy scale.

Among these problems, the naturalness-hierarchy problem is considered to be one of the most serious theoretical drawbacks of the Standard Model. There are two ways that propose to solve it: one is to avoid the scalar field and construct a new strong force with new vector bosons, the other is to introduce a new symmetry and new particles that cancel exactly and naturally the divergences. Each of these proposals would have some experimental observables at the energy scale of 1 TeV.

In the case of a new strong force, the electroweak symmetry could be broken by a condensate of new fermions that are attracted by the new strong force like in the technicolour theories. Such a mechanism for the symmetry breaking is also offered for example in the BESS (Breaking Electroweak Symmetry Strongly) model. It would result new vector bosons and the Higgs would not be a physical particle. Composite models where the vector bosons and the Higgs are not elementary particles would result in a spectrum of new particles.

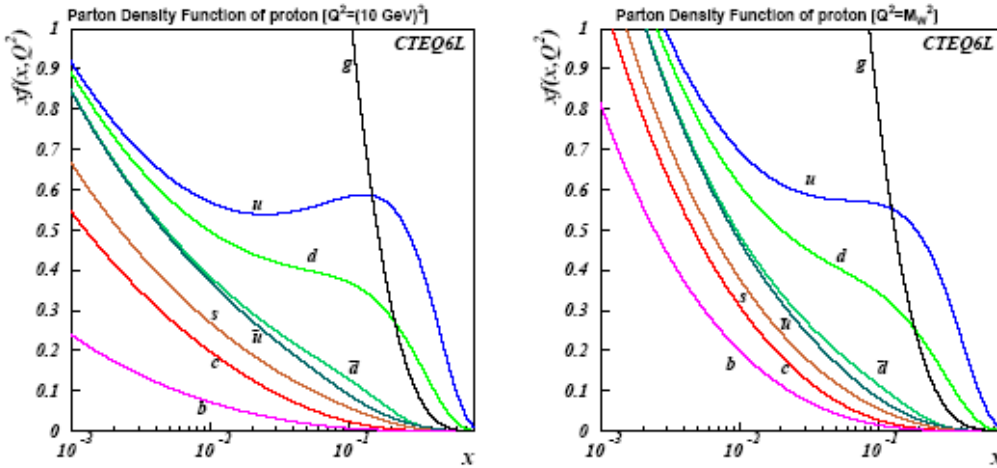
Models proposing a new symmetry are extensions of the Standard Model. In  $E_6$  (from the symmetry group  $E_6$ ) gauge models there is an additional U(1) symmetry arising from the superstring theories. The most popular theory extending the Standard Model is the Minimal Supersymmetric Standard Model (MSSM) that introduces a symmetry between bosons and fermions. Each SM particle should have a SUSY (Supersymmetric) partner, a *sparticle*, with a spin differing by 1/2. At least two Higgs doublets are required resulting in five observable particles. The naturalness problem is solved by an exact cancellation between the particle and sparticle contributions. There is no experimental evidence of any of these models and their validity would be confirmed, or ruled out with experiment.

## 1.3 Basic phenomenology of proton-proton collisions

In the next decade the electroweak symmetry breaking mechanism and the existence of an Higgs sector in the SM will be investigated at the LHC[11]. Since this machine is a proton proton collider it is necessary to introduce some basic concepts about proton proton collision at an hadronic collider such as LHC.

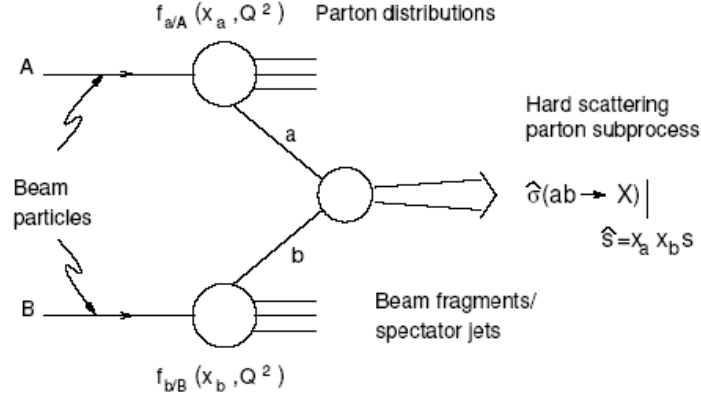
When two protons collide at high energies (several hundreds of GeV), the interaction involves their constituents, since the proton is resolved into its partons (quark and gluons), carrying only a fraction  $x$  of the total momentum of protons. The distributions of the  $x$  variable for different constituents are called *Parton Density Functions*  $f(x, Q^2)$ . They depend on  $x$  and on  $Q^2$ , the exchanged four momentum during the interaction: at low  $Q^2$  the major contributions come from the valence quarks, while at high  $Q^2$ , the PDFs are shifted towards lower values of  $x$ , equalizing the contribution of valence and sea quarks. In figure 1.13 the CTEQ6L PDFs at thoo different values of  $Q^2$  are shown.

A schematization of a p-p interaction is shown in figure 1.14.



**Figure 1.13:** Parton density function for a proton with  $Q^2 = 10\text{GeV}^2$  (left) and  $Q^2 = m_W^2$  (right)

The energy available for interaction of the di-parton system is  $\sqrt{\hat{s}} = \sqrt{x_a x_b s}$ , and in general the two fractions  $x_a$  and  $x_b$  are different. In the factorization hypothesis the cross-section of a generic p-p interaction can be written as:

**Figure 1.14:** A proton proton interaction, at partonic level

$$\sigma = \sum_{a,b} \int dx_a dx_b f_a(x_a, Q^2) f_b(x_b, Q^2) \hat{\sigma}_{ab}(x_a, x_b) \quad (1.41)$$

where  $\hat{\sigma}_{ab}$  is the cross-section for the elementary interaction between partons  $a$  and  $b$ , and  $f_{a/b}(x_{a/b}, Q^2)$  represents the PDF for fraction  $x_a(x_b)$ .

The p-p total cross-section, estimated from results of the experiments UA4, UA5 and E710, is equal to:

$$\sigma_{tot} = (100 \pm 20) mb$$

where the purely elastic contribution (30%) has been included. The inelastic interactions, around 60-70 mb, are due to two classes of processes:

- Large distance collisions between the two incoming protons, where only a small momentum is transferred during the interaction. They are soft collisions with productions of particles with large longitudinal momentum ( $p_T$  around 500 MeV). The scattering at large angle is suppressed, most of the particles escaping along the beam pipe. This kind of processes are usually referred as *Minimum Bias* and represents the vast majority of p-p collision events
- Head-on collisions at small distances between parton  $a$  from one proton and parton  $b$  from the other. In this hard scattering there is a transferred momentum larger than in *Minimum Bias* and massive particles could be created, with higher  $p_T$  and large angles with respect to the

beam line. These are the interesting physics event, but unfortunately they are rare. For example, the inclusive W(Z) production cross section is 140 nb (43 nb), which results in an interesting event every about 2 millions (8 millions) p-p interactions

In the following Tab. 1.3 are reported the rates ( $R_i = \mathcal{L}\sigma_i$ ) for some important processes at LHC (Low Luminosity)

**Table 1.3:** Event rates for some processes at LHC

Process	Events/s	Events/year
$W \rightarrow e\nu$	20	$5 \cdot 10^8$
$Z \rightarrow ll$	2	$5 \cdot 10^7$
$t\bar{t}$	4	$10^8$
$b\bar{b}$	$10^5$	$10^{12}$
$H(M_H \simeq 800 GeV)$	0.002	$10^4$
QCD jet ( $p_T > 200 GeV$ )	$10^2$	$10^9$

It is convenient to introduce boost invariant quantities to define the kinematics of the process:

- transverse momentum,  $p_T$ , the projection of particle momenta on a plane perpendicular to the beam axis
- rapidity,  $y$ , defined as:

$$y = \frac{1}{2} \ln \frac{E + p_z}{E - p_z} = \tanh^{-1} \left( \frac{p_z}{E} \right) \quad (1.42)$$

indicating with E the energy and with  $p_z$  the projection of momentum p along the beam axis.

Under a boost in z direction with velocity  $\beta$ ,  $y \rightarrow y - \tanh^{-1}\beta$ ; the rapidity differential distributions  $\frac{dN}{dy}$  are invariant under a boost along the z direction. In the ultrarelativistic approximation  $\frac{v}{c} \simeq 1$ , the rapidity may be expanded to obtain:

$$y = \frac{1}{2} \ln \frac{1 + \cos\theta + \frac{1}{2}(\frac{m}{p})^2 + O((\frac{m}{p})^2)}{1 - \cos\theta + \frac{1}{2}(\frac{m}{p})^2 + O((\frac{m}{p})^2)} \simeq -\ln \left( \tan \frac{\theta}{2} \right) = \eta \quad (1.43)$$

with  $\cos\theta = \frac{p_z}{p}$ . This equation defines the quantity  $\eta$  pseudorapidity, approximatively equal to  $y$  if  $\frac{m}{p} \ll 1$  and  $\theta \ll \frac{1}{\gamma}$  and in any case measurable when either the mass or the momentum of a particle are unknown.

## 1.4 Standard Model Higgs searches at LHC

### 1.4.1 SM Higgs Production mechanisms

In the following the different production processes for the Standard Model Higgs at LHC will be reviewed.

The cross section of the various Higgs production mechanisms at the LHC are presented in the following as a function of the Higgs mass. All known QCD and QED corrections are included in the calculations.

Over the entire mass range, the gluon fusion is the dominant production mode, vector boson fusion becoming competitive only around  $1\text{ TeV}$ . In the intermediate mass range,  $100\text{ GeV} < m_H < 200\text{ GeV}$ , several combination of production and decay are accessible at LHC, giving the possibility to measure Standard Model Higgs coupling.

#### **Gluon fusion:** $gg \rightarrow H$

The gluon fusion process is the dominant Higgs production mode at the LHC over the entire accessible mass range, that is up to about  $1\text{ TeV}$ . The diagram at leading order is presented in the figure 1.15:

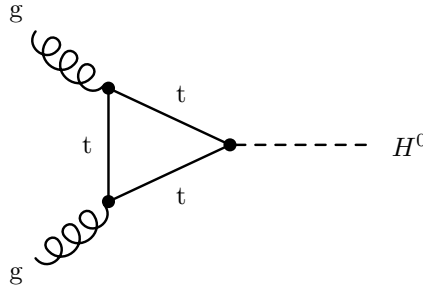


**Figure 1.15:** Leading order Feynman diagram for gluon fusion

A more precise calculation should take in account the 2 loop QCD radiative corrections.

Usually the higher order corrections are expressed in terms of K-factor defined as the ratio of the higher orders cross-section over the leading-order one, which considering only next-to-leading order is written as:

$$K = \frac{\sigma_{NLO}}{\sigma_{LO}} \quad (1.44)$$

The total correction K in this channel is large, ranging from 1.6 up to 1.9 for different values of  $m_H$ . The most important theoretical uncertainties come

from the parametrization of the parton distribution functions, especially the gluon one, and from the contributions of higher orders, still unknown.

### Vector Boson Fusion $qq \rightarrow H qq$

The cross section of the Higgs boson production through the fusion of virtual W or Z bosons is one order of magnitude smaller than the gluon fusion in the intermediate mass range ( $130 < m_H < 180$  GeV), only becoming competitive for Higgs masses around 1 TeV. The leading order Feynman diagram for the process is shown in Fig. 1.16:

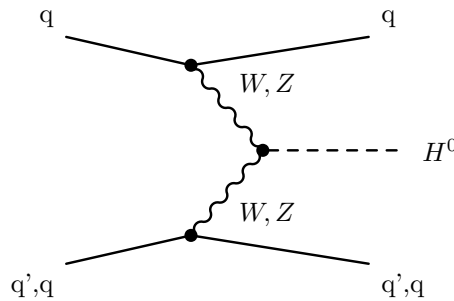


**Figure 1.16:** Leading order Feynman diagram for vector boson fusion

The radiative NLO QCD corrections for these processes are known; the K factor for these processes are smaller than the gluon fusion one, roughly in the interval 1.08-1.1. The most important topological feature of these production processes is the presence of two forward jets, with high invariant mass, and the suppression of hadronic production in the central region. Despite the lower cross-section, the particular features of these channels can be exploited to increase the signal-to-background ratio in the search for an intermediate Higgs Mass at LHC.

### *Higgs-strahlung* $qq \rightarrow VH$

The Higgs production through the Higgs-strahlung, or associated production with a Z or W boson, presents the interesting feature that one can tag on the vector boson decay products. Cross-section for these processes is about one to two orders of magnitude smaller than gluon fusion process in the range  $m_H < 200$  GeV. The Higgs-strahlung process at leading order is presented in Fig. 1.17:

QCD corrections are identical to the ones for the Drell-Yan process. K factor for this process ranges from 1.25 to 1.40.

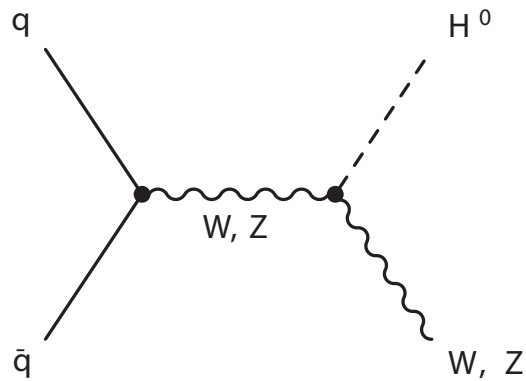


**Figure 1.17:** Leading order Feynman diagram for *Higgs-strahlung*

### Associated production with a $t \bar{t}$ pair

In the intermediate mass range, the cross section for the production of a Higgs boson in association with top quarks becomes similar to *Higgs-strahlung* cross-section. With the detection of the associated pair of  $t\bar{t}$  and in the decay channel, this process gives an additional possibility to search for the Higgs boson in the mass region below  $130 \text{ GeV}$ . The process at leading order is presented on the diagrams in Fig. 1.18:

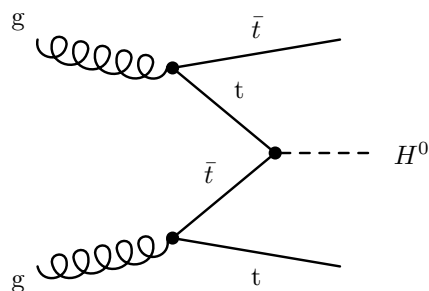


**Figure 1.18:** Leading order Feynman diagram for associated top production

The calculation of QCD corrections is rather involved and only recently has been made available. K factors are around 1.2

### 1.4.2 Search strategy at LHC

The Higgs decays into fully hadronic final states are the most copious at LHC. However it would be very difficult to detect them when embedded in higher QCD background. Therefore topologies with leptons or photons in the final states are preferred, even if disfavored by their smaller branching ratios. The associated production with a leptonically decaying particle or with forward jets can be exploited as well.

The different search strategies at LHC depend on the Higgs mass since the Higgs decay channels branching ratios depend on it. It is possible to define according to the Higgs decay properties three regions:

- Low Mass Region  $M_H < 130 \text{ GeV}$  where the  $b\bar{b}$  decay mode dominates
- Intermediate Mass Region ( $130 \text{ GeV} < M_H < 2 M_Z$ ) where fermionic final states decrease and vector boson final states start to rise and dominate  $H \rightarrow VV^{(*)}$  ( $V=W^\pm$ ) or  $Z$ .
- High Mass Region  $M_H > 2 M_Z$  where the Higgs boson decays mainly into on-shell  $W^+W^-$  or  $ZZ$  pairs

In the following the Higgs searches at LHC in these three different regions will be discussed, introducing the subject to which the last part of this thesis will be devoted, the Higgs search in the leptonic channel  $H \rightarrow ZZ^* \rightarrow 2e2\mu$ .

#### Low Mass Region ( $M_H < 130 \text{ GeV}$ )

The dominant decay channel in this mass region is  $H \rightarrow b\bar{b}$ . Difficulties arise for this channel when one considers the overwhelming background due to QCD di-jet rates. To make things worse the inclusive  $H \rightarrow b\bar{b}$  decay lacks any useful trigger signature for CMS, since neither the jet trigger neither the leptonic trigger can be used. A more favorable situation can be obtained restricting the search to the associate production channels, where the decay products of the top quark pair or the vector boson produced together with the Higgs, allow both to trigger the events, searching for a high energy lepton (also mixed triggers can be used, e.g. lepton+b-tagged jets) and to enhance the S/B ratio, adopting tagging techniques. The HZ channel seems to be of little interest, being already suppressed in comparison with the HW, and taking into account the leptonic branching ratios of the Z. So with a lepton, missing energy and two/four tagged b-jets, the Higgs search in the  $H \rightarrow b\bar{b}$  decay can be feasible.

Another possibility is to select rare decays, with a favorable S/B ratio: the "golden channel" in this region is  $H \rightarrow \gamma\gamma$ . The requirements for a good

$\gamma\gamma$  invariant mass reconstruction are an excellent energy and direction resolution, hence an excellent electromagnetic calorimeter is required. To achieve a good event reconstruction and to suppress pile-up, the primary vertex associated with the Higgs production should be identified and reconstructed: at high luminosity algorithms for vertex finding and reconstruction using tracks are under study, but a good knowledge of high luminosity pile-up is needed. The background for this channel has an irreducible component due to prompt  $pp \rightarrow \gamma\gamma + X$  and  $pp \rightarrow \gamma + jet + X$ , with a hard bremsstrahlung coming from the quark jet, and a reducible component due to QCD multi-jets production or  $\gamma + jet$ , the latter background being about 40% of the irreducible one. A good  $\pi^0/\gamma$  discrimination is needed in order to minimize the reducible background. This decay channel can be studied also in the exclusive production process  $pp \rightarrow H + jet + X$ , where the Higgs boson is produced at large  $p_T$ , and in associated WH production channel with an isolated lepton from W. The search in these processes is less sensitive to  $\gamma\gamma$  mass resolution and the backgrounds can be significantly reduced with the requirements of a lepton or a jet, yielding a S/B  $\simeq 1$ .

Another promising channel in this region is the  $H \rightarrow \tau^+\tau^-$  decay, with a branching ratios of about 8%, using in particular the vector boson fusion process, where the energetic quark jets in the forward and backward direction allow to suppress the background processes, coming mainly from QCD and Zjj.

### Intermediate Mass Region ( $130 \text{ GeV} < M_H < 180 \text{ GeV}$ )

In this mass region the Higgs boson starts decaying into pairs of vector bosons WW or ZZ. The most promising channels are  $pp \rightarrow H \rightarrow WW \rightarrow l^+\nu l'^-\bar{\nu}$  or  $pp \rightarrow H \rightarrow ZZ \rightarrow l^+l^-l'^+l'^-$  with  $l, l' = e, \mu$ . The WW decay mode has to be extracted from a background mainly due to  $qq \rightarrow WW$  continuum or  $t\bar{t} \rightarrow bW\bar{b}W$  and W-t(b) associated production.

The fully leptonic decay  $H \rightarrow ZZ \rightarrow 4l$  has a very clean experimental signature. In particular a good lepton identification and reconstruction is required in this mass range, where the invariant mass resolution of the Higgs resonance is dominated by experimental resolution, being the natural Higgs boson width negligible (around 20 MeV). The signal selection is based on the identification of two opposite charged lepton pairs coming from a common vertex. The invariant mass of at least one pair should be compatible with  $m_Z$ . The main irreducible background is continuum  $ZZ^*$  production together with reducible background  $t\bar{t} \rightarrow 4l + X$  and  $Zb\bar{b} \rightarrow 4l + X$ . In the first case leptons come from  $t \rightarrow Wb$  decay followed by  $W \rightarrow l\nu$  and semileptonic b decay, in the second case two leptons are from the real  $Z \rightarrow ll$  and the other

two from b quark decay chains. A sharp decrease of the branching ratio  $H \rightarrow ZZ$  can be noticed around 160-170 GeV due to a kinematic threshold effect when the decay in two on mass shell W bosons become possible.

### High Mass Region( $M_H > 180$ GeV)

In this region the dominant decay channels are  $H \rightarrow W^+W^-$  and  $H \rightarrow ZZ$  with both bosons on shell. The  $H \rightarrow ZZ \rightarrow 4l$  channel has a smaller ZZ irreducible background than in the intermediate mass region, requiring both pairs of invariant mass being close to  $M_Z$ . Furthermore, the Higgs width  $\Gamma_H$  is larger than the achievable experimental mass resolution, being in the tens of GeV, therefore the detector performance is less critical. For all these reasons, the  $H \rightarrow ZZ \rightarrow 4l$  channel is a gold plated Higgs boson signature at LHC in this mass region. For very large masses,  $M_H > 600$  GeV, other decay modes are used to supplement  $H \rightarrow ZZ \rightarrow 4l$ , because of the production cross section decreases significantly and the resonance peak of the four leptons become, due to very large  $\Gamma_H$ , no longer visible:  $H \rightarrow Z(\ell^+\ell^-)Z(\nu\nu)$  or  $H \rightarrow Z(\ell^+\ell^-)Z(q\bar{q})$

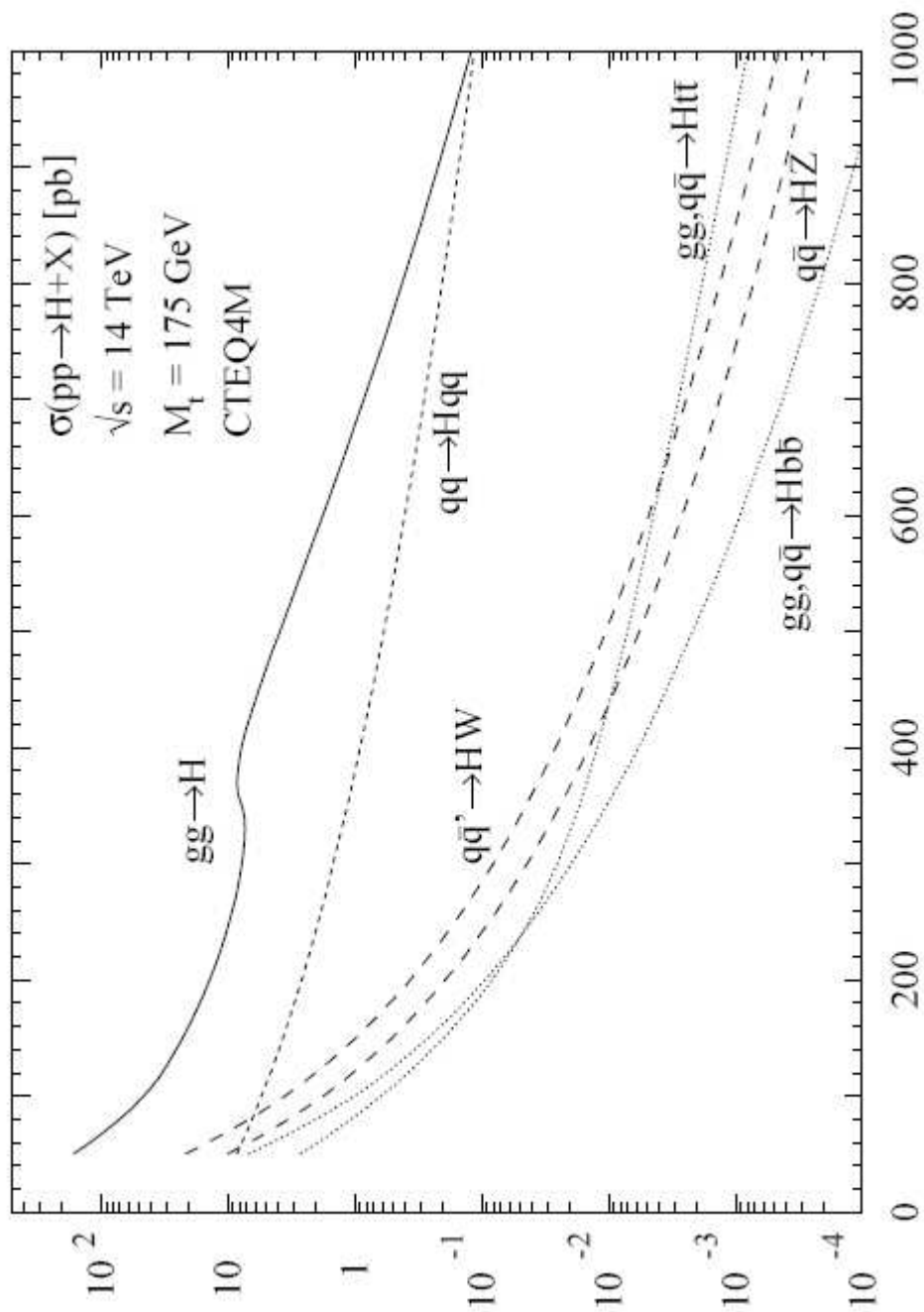


Figure 1.19: Cross sections for all Higgs production channels

# Chapter 2

## The CMS Experiment

### 2.1 The Large Hadron Collider

It has been shown how the main goal of particle physics for the years to come will be the understanding of the electroweak symmetry breaking mechanism and the search for possible new physics. These are the reasons that led the particle physics community to design and build a new more powerful accelerator, the Large Hadron Collider (LHC). In this section the physics requirements and feasibility will be reviewed.

In a circular collider of radius  $R$ , the energy loss per turn due to synchrotron radiation is proportional to the fourth power of the energy-mass ratio and inversely proportional to the collider's radius:

$$\Delta E \sim \left(\frac{E}{m}\right)^4 \cdot \frac{1}{R} \quad (2.1)$$

where  $E$  and  $M$  are respectively the energy and mass of the particles accelerated; it then follows that a circular electron collider would need enormous dimension to maintain energies of the order of 500 GeV per beam, therefore the natural choice for a collider with current technologies is to use beams of protons, which are almost 2000 times heavier than electrons, and proportionally, at the same energy, radiate a  $(1/2000)^4$  of synchrotron light than electrons. In a proton-proton collider the basic interactions involve the proton constituents (quarks, anti-quarks and gluons), which carry only a fraction of proton momentum. A drawback of this is that the center-of-mass energy and the rest frame for the hard scattering are unknown, but an advantage is that a wider range of energies can be explored with respect to with fixed energy beams experiments.

The event rate  $R_i$ , of a process  $i$  ( $pp \rightarrow X_i$ ) can be defined as the number

of events per unit time occurring with cross section  $\sigma_i$ :

$$\frac{dN_i}{dt} = R_i = \sigma_i \cdot \mathcal{L}(t) \quad (2.2)$$

The event rate is proportional to the cross section via the *luminosity*  $\mathcal{L}$ , which depends only on the accelerating machine parameters. Assuming a small crossing angle between beams and a gaussian shape of beam transverse density, the luminosity at a collider can be expressed as:

$$\mathcal{L} = f \frac{n_b N_1 N_2}{4\pi \sigma_x \sigma_y} \quad (2.3)$$

where  $f$  is the revolution frequency of the  $n_b$  proton bunches,  $N_1$  and  $N_2$  numbers of protons in the colliding bunches,  $\sigma_x$  and  $\sigma_y$  the beam profiles in horizontal (bend) and vertical directions at the interaction point.

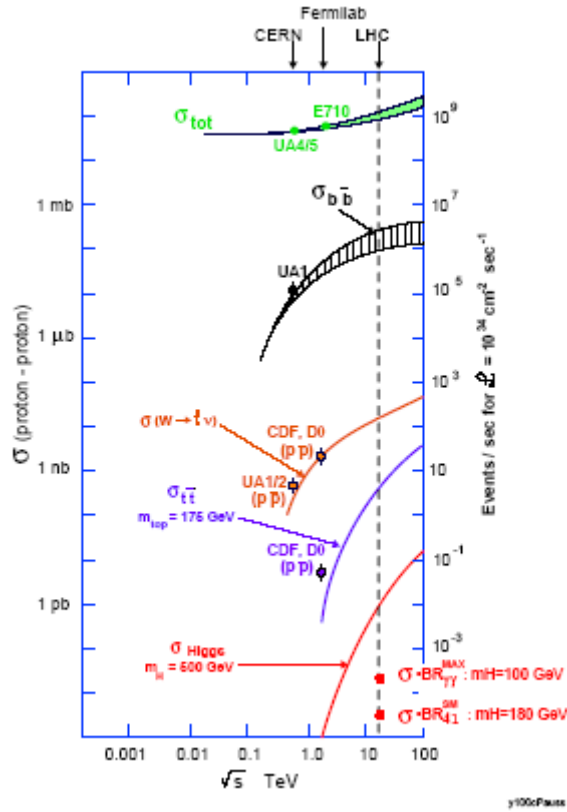


**Figure 2.1:** Cross sections for different processes as a function of the center of mass energy in p-p collisions

In the figure 2.1 cross-sections for different processes are given as a function of center of mass energy in p-p collisions, in particular it can be noticed how the inclusive Higgs production cross-section steeply increases with the center of mass energy, while the background, the total inelastic non-diffractive p-p cross section approximatively remains constant over a wide range of energies. Therefore, it can be argued that, at an hadronic collider, to increase Higgs event statistics, the highest possible center of mass energy should be used.

One of the basic ideas behind the LHC design is to install a new hadron collider into the existing 27 km long tunnel previously occupied by LEP (sited 100 m deep under CERN laboratories in Geneva). This gives also the possibility to reuse several infrastructures, including preaccelerating machines. In the LHC design, 1232 main magnetic dipoles operating at 1.9 K and generating a magnetic field up to 8.33 T will be used to steer proton beams into curvilinear trajectories together with 836 quadrupoles for focusing, 360 sextupoles and 336 octupoles for stability control.

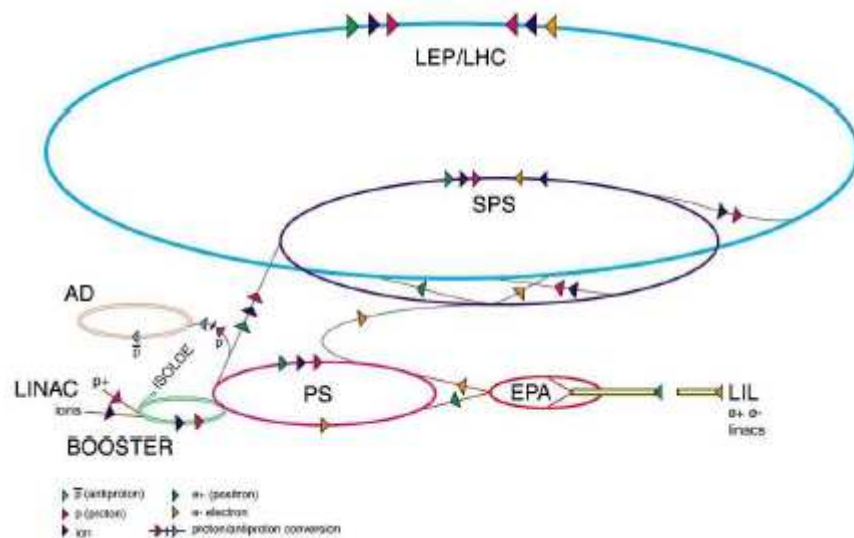
The other important feature to care about, when maximizing the production rate for a given process, is the luminosity. This has its drawback, however, since the total event rate for inclusive p-p collisions can become so high that several interactions will overlap in the same bunch-crossing (*pile-up*). The LHC will operate at a bunch crossing frequency of 40 MHz and at a design luminosity of  $10^{34} \text{cm}^{-2} \text{s}^{-1} = 10 \text{nb}^{-1} \text{s}^{-1}$ . The bunch structure is such that only about 80% of the bunches will be filled; since the predicted total non-diffractive inelastic p-p cross section is 55 mb, on average 17.3 events will occur at every bunch crossing. With about 50 charged tracks per interaction, this pile-up poses several experimental problems. In the first three years of data-taking, the LHC will run at a reduced luminosity of  $2 \cdot 10^{33} \text{cm}^{-2} \text{s}^{-1}$ ; only afterwards it will run at design luminosity. The two luminosity regimes are commonly called *High Luminosity* and *Low Luminosity*.

The LHC will also be able to accelerate and collide beams of heavy ions such as Lead (Pb) at 2.76 ATev to study deconfined hadronic phase of matter (QGP, Quark Gluon Plasma). The parameters of LHC are summarized in Tab. 2.1.

**Table 2.1:** LHC design parameters

	p-p	Pb-Pb
Beam energy at injection	450 GeV	73.8 TeV
Beam energy at collision	7 TeV	574 TeV(2.76ATev)
Maximum luminosity	$1 \times 10^{34} \text{ cm}^{-2} \text{ s}^{-1}$	$2 \times 10^{27} \text{ cm}^{-2} \text{ s}^{-1}$
Number of Bunches	2808	1608
Bunch spacing	7.84 cm	5.3 cm
Bunch separation	24.95 ns	124.75 ns
Number of particles per bunch	$1.1 \times 10^{11}$	$8 \times 10^7$
Total crossing angle	$300 \mu\text{rad}$	$\approx 100 \mu\text{rad}$
Bunch Length	7.5 cm	7.5 cm
Transverse beam size at Impact Point	$15 \mu\text{m}$	$15 \mu\text{m}$
Luminosity lifetime	10 h	4.2 h
Filling time per ring	4.3 min	9.8 min

**Figure 2.2:** Overview of the accelerator complex at CERN. Protons will be accelerated up to 50 MeV by a linear accelerator LINAC. A Booster raises the beam energy up to 1.4 GeV injecting proton beam in the old circular protosynchrotron PS. The 25 GeV energy beams extracted at PS are injected into a bigger circular accelerator SPS, which introduces 450 GeV proton beams in the LHC ring



### 2.1.1 LHC Experiments

LHC detectors will operate in a very difficult environment: the high bunch crossing frequency, the high event rate and the pile-up of several events in the same bunch-crossing dictate strict requirements on the design of the detectors. To cope with a bunch crossing rate of 25 ns and a pile-up of about 20 events per crossing (at design luminosity), the detectors should have a very fast time response and read-out electronics.

Regarding the challenge given by the particle density, a typical minimum bias collision at LHC will produce on average 5.5 charged particles with mean transverse momentum around 0.5 GeV and 8 primary photons per unit of pseudorapidity. An interesting event, which typically contains high  $p_T$  leptons, high  $E_T$  hadron jets,  $b$ -jets, large missing transverse momentum, will always be superimposed on this pile-up

Due to the presence of this pile-up, high granularity and sophisticated reconstruction algorithms are required to avoid the overlap of particles in the same sensitive element. High granularity means a large number of electronic channels, and therefore high costs. LHC detectors will also have to stand an extremely high radiation dose, and therefore special radiation-hard electronics must be used. Additional requirements apply to the online trigger selection that has to deal with a background rate several orders of magnitude higher than the signal rate.

Moreover, to extract as much information as possible from an interesting signal, multi-purpose detectors should fulfill the following requirements:

- full hermeticity to allow for an accurate measurement of the missing transverse energy and momentum (coming from almost non interacting particles like neutrinos and supersymmetric neutralinos)
- capability to reconstruct leptons in a wide range of transverse momenta and rapidity (to reconstruct gauge bosons, tag b-jets etc.);
- capability to reconstruct tracks with a good precision on their transverse momentum and impact point position (to efficiently reconstruct and tag  $B$  particles and  $\tau$ )
- capability to reconstruct hadron jets from QCD process and heavy particles decays

A very high particle flux traversing each component of the detector also imposes restrictive requirements on the material that can be used for the detector's construction: the best results will be obtained with the optimal compromise between detector performance and particle radiation resistance.

Four experiments, will be installed at the LHC. Their location in the accelerating ring is shown in figure 2.1.

Two of them are devoted to specific topics: ALICE [12] to heavy ions collisions and LHC-b [13] to b-physics. The other two are general-purpose experiments: ATLAS [14] and CMS [15].

Since their physical goals are similar, the latter two detectors share many common features.

The main differences between these two detectors are related to the magnetic field configuration. The *Compact Muon Solenoid* (CMS) uses a big superconducting solenoid which generates a strong solenoidal field, while *A Toroidal LHC ApparatuS* (ATLAS) uses a toroidal field produced by three sets of air-core toroids complemented by a small inner solenoid. The CMS solenoidal magnet produces a very intense field (4T) and the resulting system is very compact: calorimeters can be installed inside the magnet improving electron and photon energy measurement. Precise tracking exploits both the constant field within the magnet and the field inside the return yoke. Among the disadvantages of this kind of setup we have to consider that multiple scattering within the yoke degrades the muon measurement. On the other hand ATLAS, using a toroidal magnetic field, has the advantage that  $p_T$  resolution does not have any dependence on pseudorapidity. Moreover an air-core toroid together with excellent detector alignment resolution allows a good momentum resolution even without the inner tracker.

In the following the CMS experiment and its subdetectors are described in detail.

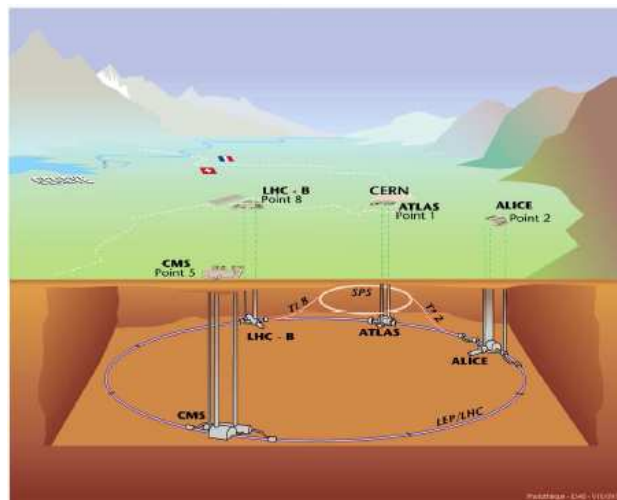
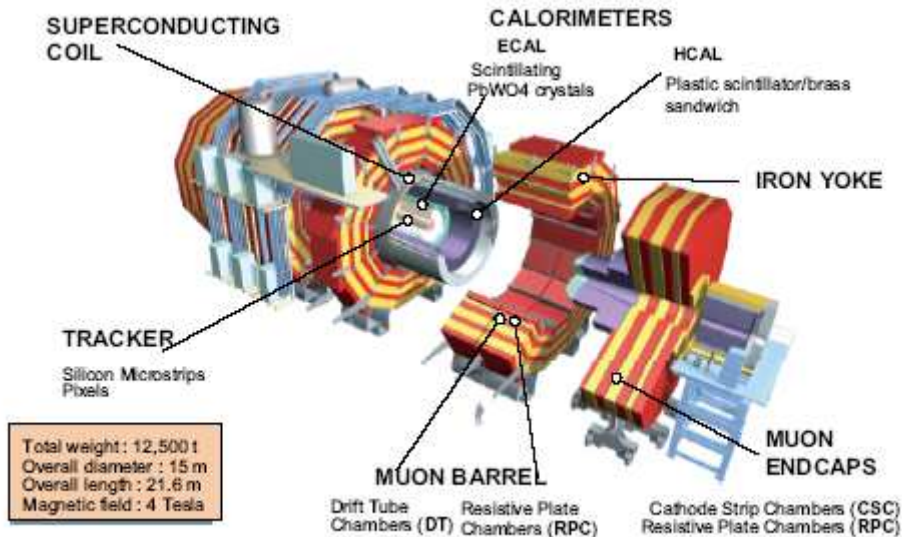


**Figure 2.3:** Map of LHC and related experiments

## 2.2 CMS Overall Design

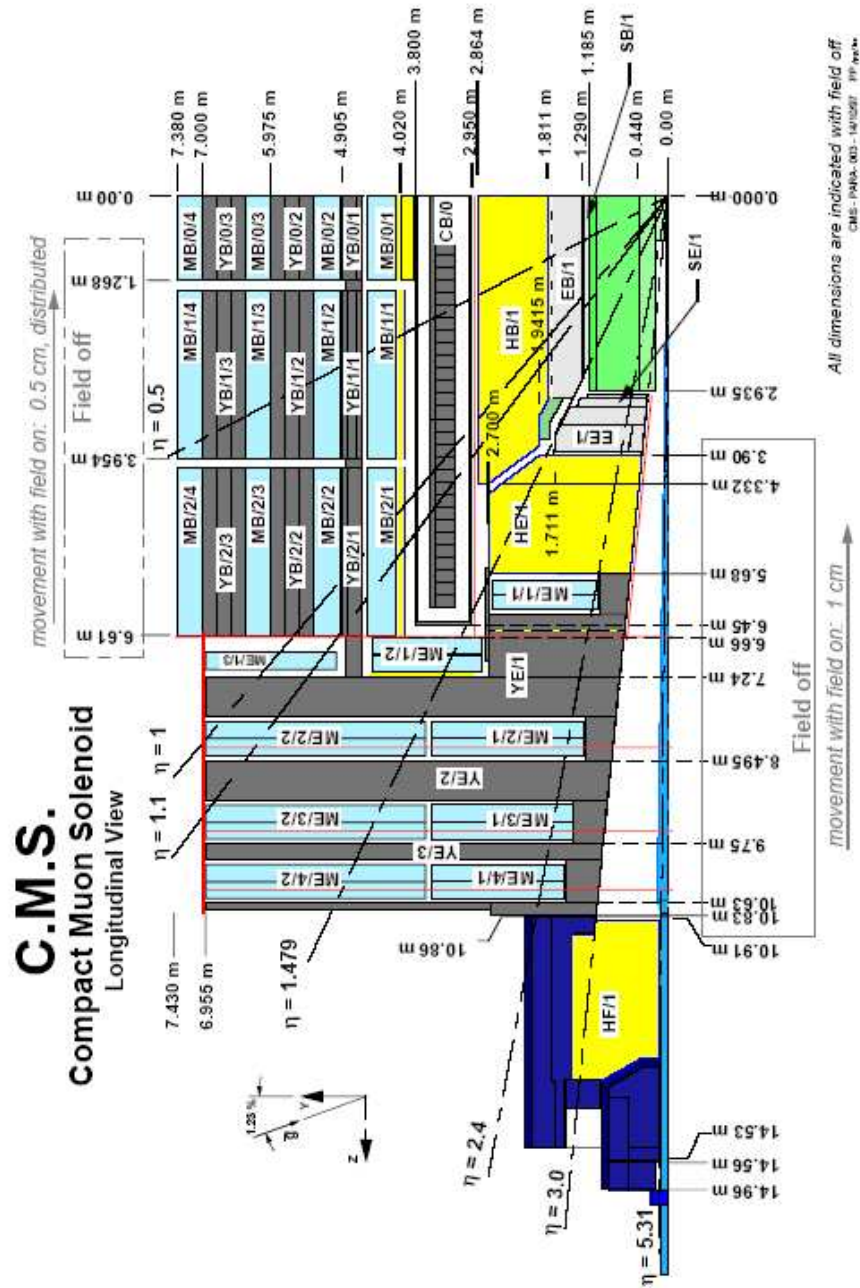
CMS design has a cylindrical symmetry around the beam axis and has a typical structure of collider based physics experiment: several cylindrical layers coaxial to the beam direction, referred to as *barrel* layers, closed at both ends by detector disks orthogonal to the beam pipe, the *endcaps*, to ensure detector hermeticity. In figure 2.4 a schematic view of CMS is shown. The full length of the detector is 21.6 m, diameter is 15 m for a total weight of  $\simeq 1200$  t.

Figure 2.4: Schematic picture of CMS experiment at LHC



The coordinate frame used by the CMS collaboration is a right-handed cartesian system with the  $x$  axis pointing to the center of LHC ring, the  $z$  axis coincident with the CMS cylinder axis and the  $y$  axis directed upwards along the vertical. Cylindrical symmetry of CMS design drives the use of a pseudo-angular reference frame, given by the triplet  $(r, \phi, \eta)$ , with  $r$  distance from  $z$  axis,  $\phi$  azimuthal coordinate with respect to  $x$  axis and pseudorapidity  $\eta$  defined as in equation 1.43.

The longitudinal view of one quarter of the CMS detector is shown in figure 2.5. The transverse view of the barrel region is shown in figure 2.6. Detectors and non-sensitive volumes are indicated with a standard defined by two-letter code.



**Figure 2.5:** Longitudinal view of a quarter of CMS experiment. Detectors and non-sensitive volumes are indicated by two letter code: the first letter indicates the subdetector (S=Silicon tracker, E =Electromagnetic calorimeter, H=Hadron Calorimeter, C=magnetic Coil, Y= magnet iron Yoke, M=MMuon chambers), the second letter refers to the position (B=Barrel,E=Endcap,F=Forward region)



The CMS design is driven by the choice of its magnet (**CB**) a 13 m long superconducting solenoid with a diameter of 5.9 m. Cooled with liquid helium, it will generate a magnetic field of 4 T, which is kept uniform by a massive iron return yoke (**YB, YE**). The yoke also hosts the muon system (**MB, ME**), composed by drift tube (**DT**) detectors in the barrel region and cathode strip chambers (**CSC**) in the endcaps (up to  $|\eta| < 2.4$ ), complemented by a system of resistive plate chambers (**RPC**) with a coverage of  $|\eta| < 2.1$ .

The calorimeters and the inner tracker are installed inside the coil. Very fine segmentation is crucial for the innermost detectors to deal with a very high density, therefore a silicon pixel and microstrips detectors were chosen. In the baseline design it consists of barrel layers and 2 forward disks. Outside the pixel detector, a silicon strip detector is installed, extending up to a radius of about 1.2 m. The full silicon tracker allows charged tracks reconstruction in the acceptance region of  $|\eta| < 2.5$ .

Photons and electrons are measured by a homogeneous electromagnetic calorimeter (**ECAL**), composed by lead tungstate  $PbWO_4$  scintillating crystals covering the region  $|\eta| < 3.0$  (**EE, EB**). In the endcaps, it will be supplemented by a lead/silicon preshower detector, to improve the resolution in the determination of electron and photon direction and to help pion rejection.

Jets and energy imbalance are measured by a sampling hadronic calorimeter (**HCAL**) installed just before the coil. It is composed of copper alloy and stainless steel instrumented with plastic scintillators. The barrel and endcap parts (**HB, HE**) have the same  $\eta$  coverage of the **ECAL**, and are complemented by a very forward calorimeter (**HF**), which extends the coverage up to  $|\eta| < 5.3$ .

## 2.3 The Magnet

The choice of a compact design for the CMS detector drives to the choice of a strong solenoidal magnetic field in order to achieve the needed resolution on the muon momentum measure. The magnet system provides a uniform magnetic field of 4 T using a 13 m long superconducting coil with a diameter of 5.9 m. The magnetic flux is returned via a 1.8 m thick saturated iron yoke. The solenoid is composed by the winding (divided in four parts) with its structural support, the thermal radiation shields and the vacuum tank. The conductor consists of three concentric parts: the central flat superconducting cable (Rutherford type NbTi) with high purity aluminium stabilizer and two external aluminium-alloy reinforcing slabs.

The cooling system was chosen to be extremely reliable to protect against

sudden power failure, since a complete re-cooling from a non superconducting state needs twelve days.

Being the largest element of the CMS detector, the magnet is also providing the principal support structure for all the barrel detector components (tracking and calorimetry inside the coil, muons stations outside). The magnet system includes the cryogenic system, power supply, quench protection, vacuum pumping and control system.

## 2.4 The Tracker

The tracker[16] is the CMS sub-detector closest to the interaction point and is devoted to reconstruction of charged tracks and vertices.

The design goal of the central tracking system is the reconstruction of isolated leptons with an efficiency better than 95% and of high  $p_T$  tracks within jets with an efficiency better than 90% over the pseudo-rapidity range  $|\eta| < 2.5$ .

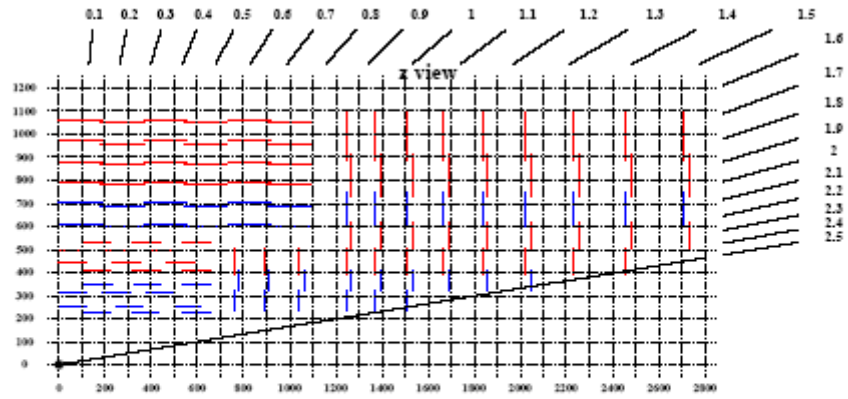
Track and vertex finding at LHC will be an important tool for identifying signal events and rejecting background. Efficient track reconstruction provides electron-photon separation, and it is helpful in identifying W and Z bosons which will be involved in many signatures of new physics at LHC. Track isolation is another important tool because it can be used to suppress jet backgrounds to isolated high energy leptons and photons.

The tracking system consists of three silicon pixel layers close to the interaction point, surrounded by a large silicon microstrip tracking detector. A major constraint on the design of the tracking detector is to limit as much as possible the material budget in front of the calorimeters. Early conversions of photons degrade sensitivity to  $H \rightarrow \gamma\gamma$ , and bremsstrahlung in the tracker material and high magnetic field deteriorates the energy resolution for electrons.

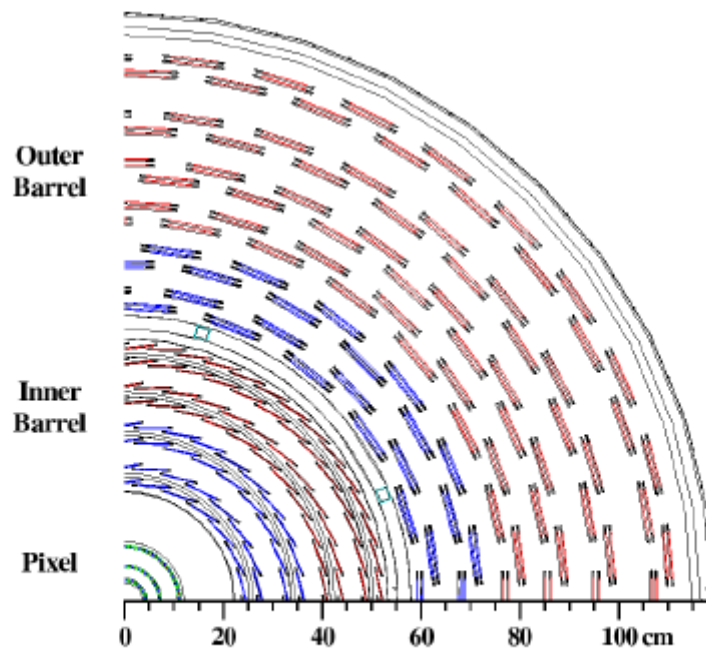
In addition to accurate track reconstruction, the tracker will provide vertex identification. In the case of  $H \rightarrow \gamma\gamma$ , charged recoil tracks can be used to identify the Higgs vertex, for example. Massive particle decays at LHC will frequently involve B hadrons, with markedly displaced secondary vertices. An important role of the tracking system will be the identification of these secondary vertices in order to tag b-jets in CMS.

The tracker extends in the region  $|\eta| < 2.5$ ,  $r < 120$  cm,  $|z| < 270$  cm and it is completely based on semiconductor detectors made of silicon covering the largest ever designed detector surface of  $\sim 200$  m<sup>2</sup>.

To better solve the pattern recognition problem, the tracker is designed to fulfill two basic properties: low cell occupancy ( $1 \div 2\%$ ) and large hit



(a)



(b)

**Figure 2.7:** Schematic longitudinal (pixel detector layers are not shown) (a) and transverse (b) view of a quarter of the tracker layout. Red lines represent single modules, blue lines double modules

redundancy. The low occupancy is obtained by high granularity detectors, mainly those closest to the interaction point because they have to cope with higher particle fluxes, and a fast primary charge collection.

The redundancy is guaranteed by the overall design shown in Fig. 2.8 which allows many measured points per track within an acceptable material budget.

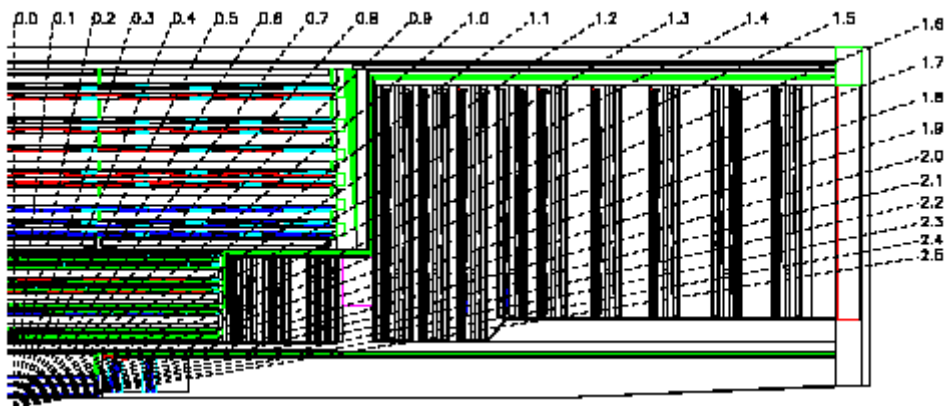


**Figure 2.8:** Schematic view of a quarter of the CMS silicon tracker comprehensive of the supporting structures, cables and services

An average of 12-14 points (hits) per track are guaranteed to permit a high tracking efficiency and a low rate ( $10^{-3}$  or less) of fake tracks (reconstructed tracks not corresponding to any real track). Because of the high *dark current* developed after exposure to ionizing radiation, both pixel and microstrips detectors have to be kept cold at a working temperature of about  $-10^{\circ}C$  for the whole tracker volume.

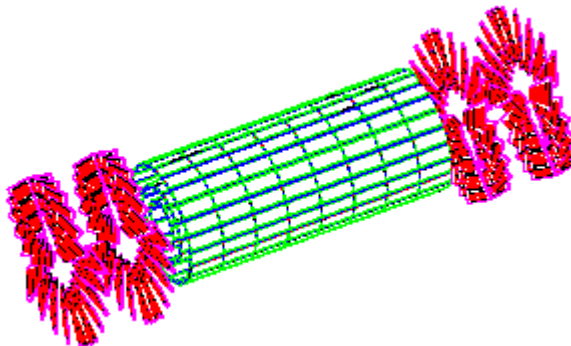
The tracker will reconstruct high energy electrons (from W or Z decays, for example) with an efficiency better than 90%. Simulations of single muons within the tracker show that an efficiency close to 100% is reachable in the range  $|\eta| < 2.0$  (see figure 2.8). The standalone tracker performance for isolated muons over a range of pseudorapidities and for several different muon transverse momenta is shown in figure 2.10.

Charged leptons and hadrons which are produced in the central region are reconstructed with a momentum precision given by equation 2.6:

$$\frac{\Delta p_T}{p_T} \approx 0.005 + 0.15 p_t \quad p_t \text{ in } TeV \quad (2.4)$$

**The Pixel Detector** The pixel detector, thanks to its high-resolution three-dimensional measurement, will allow excellent track reconstruction and impact parameter measurement, identification of  $\tau$  and  $b$ -jets and three dimensional vertex reconstruction. The pixel detector is composed of three barrel layers at mean radii of 4.4 cm, 7.3 cm and 10.2 cm, extending for a total length of 53 cm and two endcap disks extending in radius from 6 to 15 cm placed on each side, at  $|z| = 34.5$  cm and 46.5 cm. This layout will guarantee at least two pixel hits for tracks originating within  $2 \sigma_z$  of the nominal collision point, up to about  $|\eta| < 2.2$ . Figure 2.9 shows a three-dimensional representation of the pixel detector. The full detector consists in total of 4.4 millions of square  $n$ -type silicon pixels with a size of  $100 \mu\text{m} \times 150 \mu\text{m}$  on a  $n$ -type substrate. A spatial resolution of  $\simeq 14 \mu\text{m}$  is obtained. With this kind of layout, stand-alone track seeding, that requires three hits per track, will also be possible with good efficiency. However, in the initial low-luminosity phase only two barrel layers and one endcap disk will be installed. The standalone track seeding will therefore not be possible and the region where each track gives two hits will be limited to  $|\eta| < 2$ .

**Figure 2.9:** Three-dimensional view of the pixel subdetector



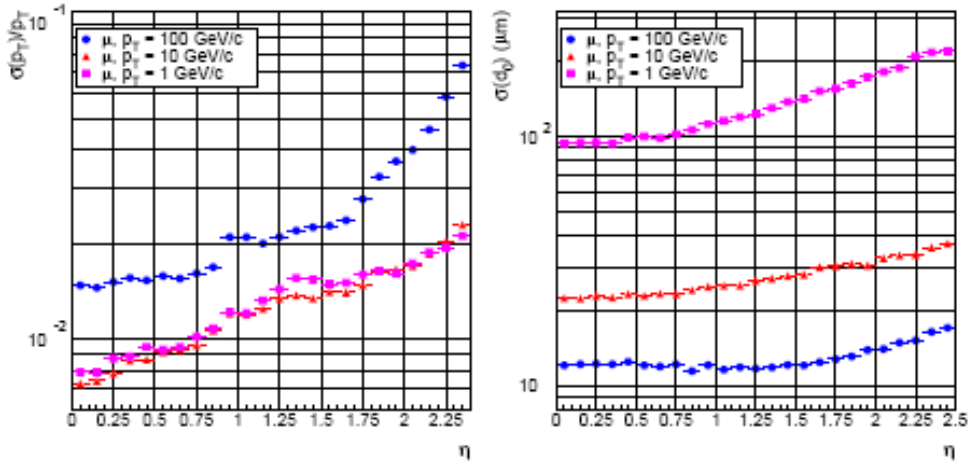
**The Silicon Microstrip Detector** Together with the pixel detector the tracker is composed of several layers of silicon microstrip detectors; they provide high spatial precision and time resolution combined with adequate radiation hardness. There are about 15000 microstrip detectors, with an interstrip pitch size from 80 to 180  $\mu\text{m}$ . In the inner part they are organized in four barrel layers and three small forward disks while in the outer part there are six barrel layers and nine forward disks. Some of the modules are "stereo" modules, composed by two detectors mounted back-to-back with the strip rotated by 10 mrad ( $6^\circ$ ) to reduce ambiguities in the hits association.

Fig. 2.10 shows the resolution of the full tracker for the transverse momentum and the impact parameter.

The general tracking performance is here summarized:

- the  $p_t$  resolution is better than  $\Delta p_T/p_T \sim (15p_T \oplus 0.5)\%$  ( $p_T$  in TeV) in the pseudorapidity range  $|\eta| < 0.7$ , slightly worse in the forward region;
- the efficiency for single muons reconstruction is greater than 98% over the whole  $\eta$  coverage and for single electrons reconstruction around 95% in the central region;
- the efficiency for the reconstruction of hadrons inside jets is around 80% for  $p_T > 1 \text{ GeV}$  and around 95% for  $p_T > 10 \text{ GeV}$ ;
- the resolution in the transverse impact parameter for the reconstructed tracks is about  $20 \mu\text{m}$  for 10 GeV particles

Furthermore, the possibility to read a single region of the tracker allows both to lower the time needed to perform the reconstruction and the use of the tracker detector in a quite early stage of the trigger system.



**Figure 2.10:** Resolution on the transverse momentum (left) and transverse impact parameter measured by the tracker (right) as a function of pseudorapidity, for single muons with transverse momentum of 1, 10, 100 GeV

## 2.5 The Electromagnetic Calorimeter

The physics process that imposes the strictest requirements on the electromagnetic calorimeter (ECAL) [17] performance is the intermediate mass Higgs decay into two photons. The goal is a 1% resolution on the invariant mass of two photon. The Calorimeter system should also be able to distinguish between showers initiated by neutral pions and photons, or charged pions and electrons, which require good granularity. The natural choice to achieve this task is a homogeneous calorimeter. The CMS collaboration chose a crystal calorimeter composed of about 80000 lead tungstate ( $PbWO_4$ ) crystals. Lead tungstate is a fast, intrinsically radiation hard scintillator, characterized by a small Moliere radius ( $R_M=21.9$  mm) and short radiation length ( $X_0=8.9$  mm). In the barrel the crystals are 230 mm long while in the endcaps they are 220 mm long, corresponding to 25.8 and 24.7 radiation lengths, respectively; the short radiation length allows a good shower containment in the limited space available for the ECAL.

Crystals are trapezoidal with a square front face of  $22 \times 22$  mm<sup>2</sup> in the barrel and  $30 \times 30$  mm<sup>2</sup> in the endcaps, matching the Moliere radius. This granularity is not large enough in the endcap regions where a preshower device with higher granularity will be used, consisting of two lead radiators and two planes of silicon strip detectors with a total radiation length of  $3 X_0$ . This detector will allow rejection of photon pairs from  $\pi^0$  decays which may fake a single photon.

In the barrel light is collected by silicon avalanche photo-diodes (APD) while, in the endcaps, vacuum photo-triodes are used.

As shown in Fig. 2.11 the geometric coverage of the ECAL extends up to  $|\eta| < 3.0$ .

Usually the energy resolution of a calorimeter is parametrized as:

$$\left(\frac{\sigma_E}{E}\right)^2 = \left(\frac{a}{\sqrt{E}}\right)^2 + \left(\frac{\sigma_n}{E}\right)^2 + c^2 \quad (2.5)$$

where  $a$  is called stochastic term, corresponding to the statistical fluctuations in the number of primary processes that generate the signal,  $\sigma_n$  is the noise term including the energy equivalent of the electronic noise and pile-up effects and  $c$  is a constant term related to the calibration of the calorimeter. The different contributions as a function of the measured energy are shown in Fig. 2.12.

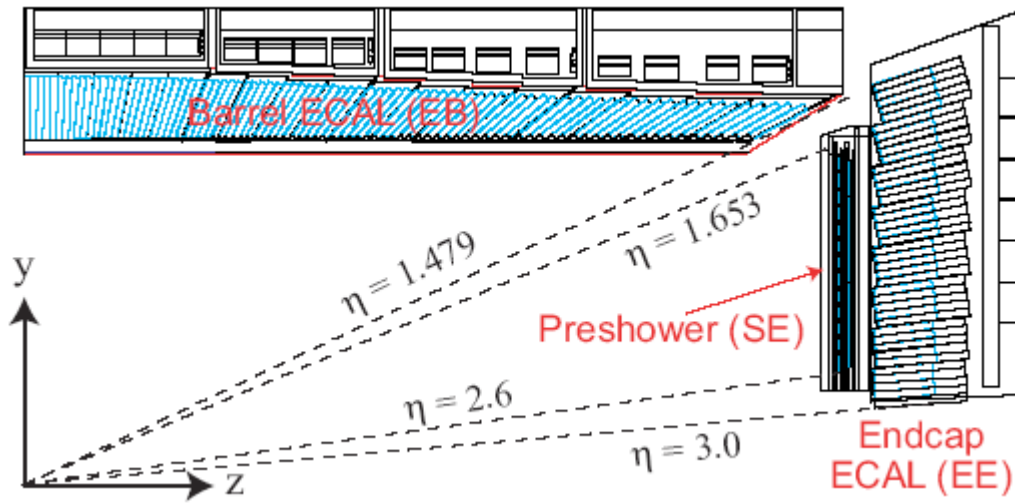


Figure 2.11: Longitudinal view of one quarter of the ECAL

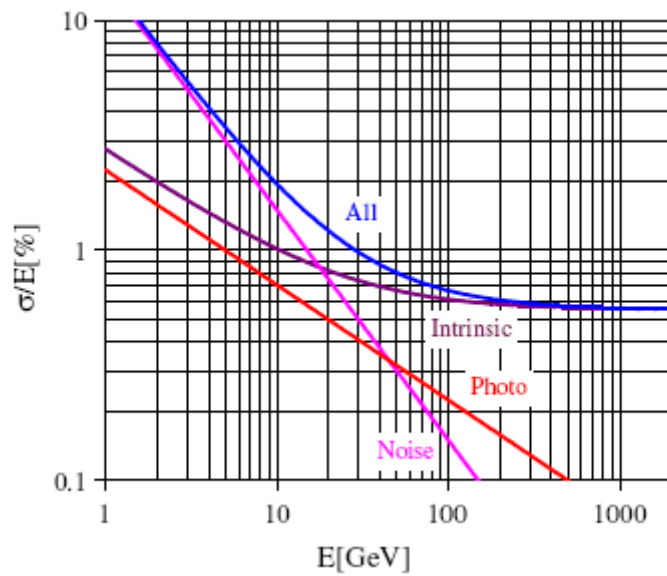
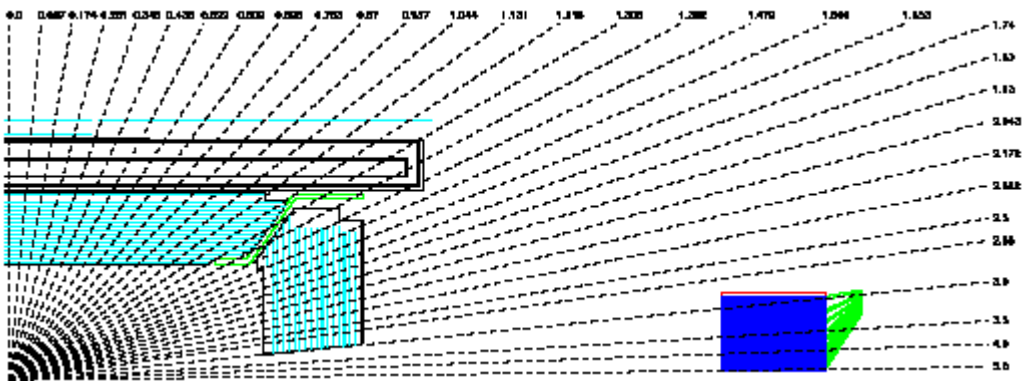


Figure 2.12: Different contributions to the energy resolution of the ECAL. The curve labeled "intrinsic" includes the shower containment and a constant term of 0.55%

## 2.6 The Hadron Calorimeter

The Hadron calorimeter (HCAL) [18] surrounds the ECAL and contributes to measure direction and energy of jets and transverse missing energy. One of the main requirements for the HCAL is therefore a high hermeticity. Moreover, the identification of forward jets is very important for the rejection of the main backgrounds to the typical signatures of new physics. For these reasons, the barrel and the endcap parts, which extends the coverage up to  $|\eta|=3.0$ , are complemented by a very forward calorimeter which extends the coverage up to  $|\eta|=5.3$ . The barrel and the endcap calorimeters consist of active plastic scintillator layers interleaved with brass absorber plates; the light coming out is collected by wavelength-shifting fibers. Only the first layer is read out separately while all others are read out together in towers of size  $\Delta\eta \times \Delta\phi = 0.087 \times 0.087$ . In the barrel region full shower containment is not possible within the magnet volume and an additional "tail catcher" is placed outside the magnet.

The very forward calorimeter is placed outside the magnet yoke, 11 *m* far from the interaction point. It uses quartz fibers parallel to the beam, inserted in steel absorber plates. The energy resolution is  $\sigma/E \sim 65\%\sqrt{E} \oplus 5\%$  in the barrel,  $\sigma/E \sim 85\%\sqrt{E} \oplus 5\%$  in the endcaps and  $\sigma/E \sim 100\%\sqrt{E} \oplus 5\%$  ( $E$  in GeV) in the very forward calorimeter.



**Figure 2.13:** Longitudinal view of a quarter of CMS hadron calorimeter, subdivided into barrel and endcap HCAL, placed inside the magnetic coil, the outer barrel tail-catcher and the very forward calorimeter HF

## 2.7 The Muon System

The muon detection system [19] is placed outside the magnetic coil. Its purposes are multiple: muon reconstruction and identification, trigger for events with muon as well as precise time measurements of the bunch crossings.

The muon detector are integrated in the iron return yoke of the magnet. Both barrel and end-caps are made out of four active layers and three layers of absorber.

The barrel region extends up to  $|\eta| < 1.3$ . It is divided longitudinally into five segments (*Wheels*). Each wheel houses four active layers of Drift Tube (DT) chambers called *Stations*. According to which cylinder they belong these stations are called MBX, where  $X = 1, 2, 3, 4$ .

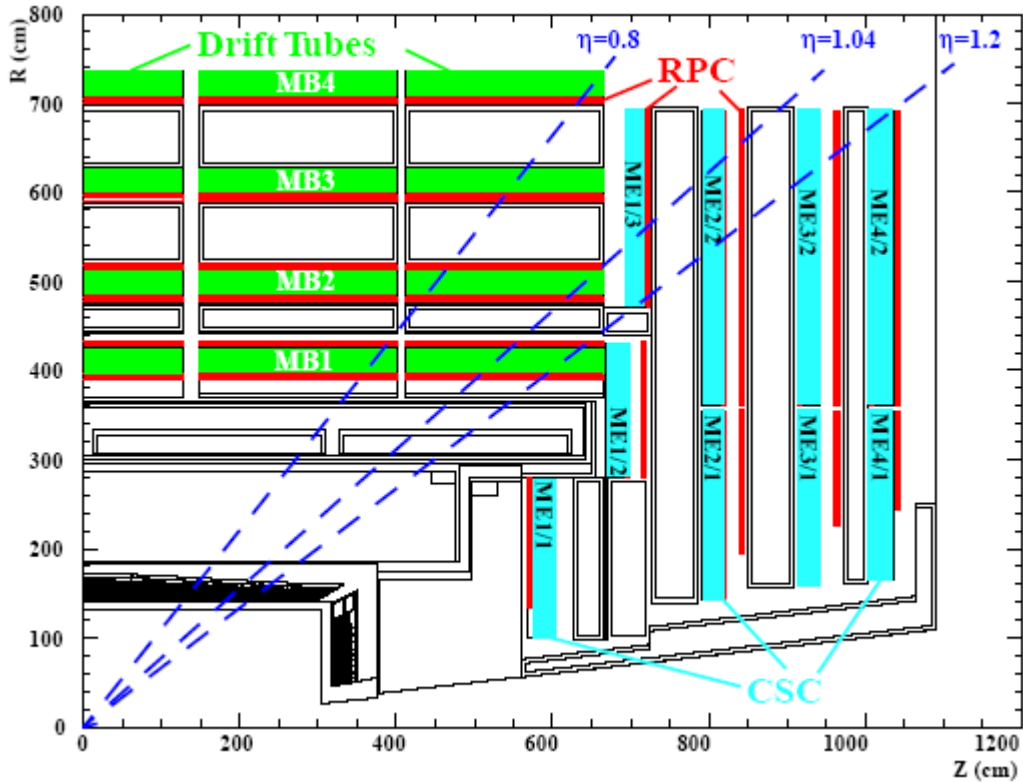


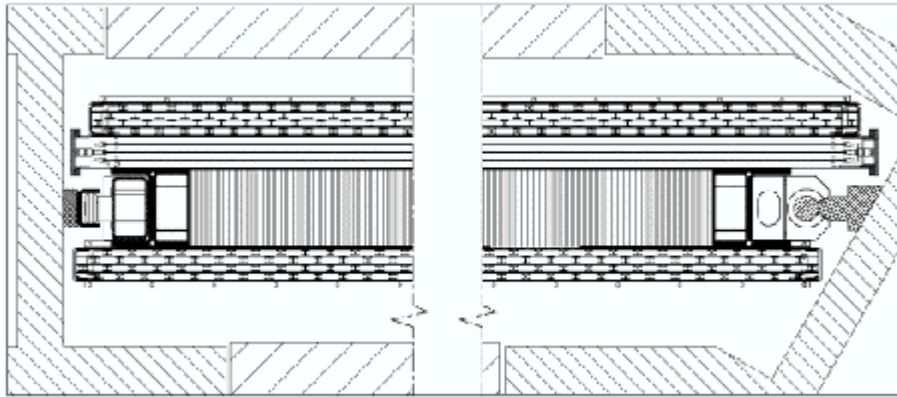
**Figure 2.14:** Longitudinal view of the muon system, subdivided into barrel, with drift tubes (DT) and resistive plate chambers (RPC), and endcap with cathode strip chambers (CSC) and RPCs

Stations MB1, MB2, MB3 house 12 layers of Drift Tubes, while MB4

hosts only 8 layers.

In a station layers are clustered in group of four, each group called a SuperLayer (SL) as can be seen in Fig. 2.15.

**Figure 2.15:** Transverse section of a DT in its definitive position inside the iron return yoke of the magnetic field



Stations MB1,MB2,MB3 have 3 superlayers, two of them are glued together and are separated from the third by a honeycomb structure. Station MB4 has only 2 superlayers.

As said, each superlayer has four layers of single-wired drift cells. All the wires are parallel and those positioned in odd layers are shifted by an half-cell with respect to the wires of the adjacent layers, in order to resolve the left-right ambiguity in track reconstruction.

Two SL (of type  $\phi$ ) have wires oriented along the direction of the beam and therefore measure the coordinate in the curvature plane, while the remaining SL (of type  $\theta$ ) consists of wires orthogonal to those of  $\phi$  SL, in order to measure the coordinate in the plane containing the beam axis.

Chambers of the MB4 type do not possess the  $\theta$  SL.

A DT has approximately 400 ns of drift time and a time resolution of 5 ns. The DT spatial resolution is  $180 \mu\text{m}$  per tube and an overall resolution of  $100 \mu\text{m}$  in  $R-\phi$  and  $150 \mu\text{m}$  in  $z$  is expected.

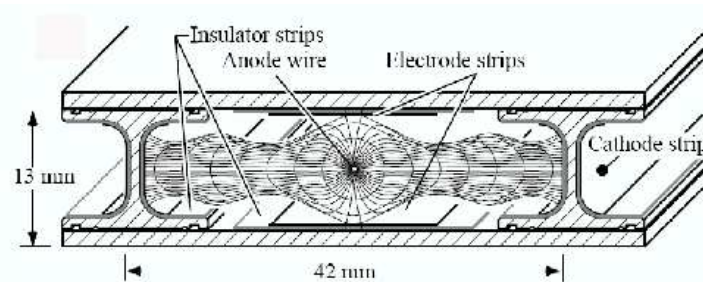
Endcaps extend the coverage up to  $|\eta| < 2.4$ . The active layers are equipped with trapezoidal shaped Cathode Strip Chamber (CSC) detectors. Each chamber is made of 6 sandwiches of cathode strips and wires which provide 3-dimensional hit reconstruction. The CSCs are designed to operate in non uniform magnetic field ranging from 1 to 3 T. The spatial resolution

varies from  $75\ \mu\text{m}$ , for the first two inner layers, to  $150\ \mu\text{m}$  for the outer ones.

To complement DT and CSC measurements at trigger level, the information provided by the Resistive Plate Chambers (RPC) is used. RPC detectors have very prompt time response and excellent time resolution ( $\sigma < 1 \div 2\ \text{ns}$ ). There is a plane of RPC detectors for each layer of CSC detectors in the endcaps, and the first, second and fourth layers of DT detectors in the barrel. Each RPC chamber in the barrel is made of two phenolic resin plates separated by a gap of a few  $\text{mm}$  filled with gas. Planes are coated by a conductive graphite paint in the shape of electrodes. Read-out is made by plastic insulated aluminium strips outside the resin plates. The spatial resolution of RPC is of the order of the strip size ( $10\text{-}40\ \text{mm}$  in  $R\text{-}\phi$ ) and  $100\text{-}300\ \text{mm}$  in  $z$ . These devices operate in avalanche mode, instead of more common streamer mode, to cope with LHC high rate.

In the barrel region **drift tube chambers** are used, since the chamber occupancy is low ( $10\ \text{Hz cm}^{-2}$ ), the neutron presence negligible and the residual magnetic field not too high thanks to the presence of the magnet return yoke. The basic element of a drift tube chamber is the drift cell, which is shown in figure 2.16. A stainless steel anode wire is placed between 2 parallel aluminium layers; two "I"-shaped electrodes, which define the boundaries of the cell, work as cathodes and shape the electric field.

**Figure 2.16:** Transverse view of a drift tube cell



The distance of the track from the wire is measured by the drift time of the ionization electrons and the chosen mixture of 80% Ar and 20 %  $\text{CO}_2$  ensures a good space-time linearity. The single cell, which works in condition of saturated drift velocity, has efficiency around 99.8% and spatial resolution at the level of  $180\ \mu\text{m}$ . Despite the long drift time of a single layer, the combination of the responses of the 4 layers ensures a good time resolution.

The **cathode strip chambers** are multi-wire proportional chambers able to work also in a high radiation environment and in presence of non-homogenous magnetic field chosen as detectors for the endcaps. The chambers are composed of six layers, each consisting of an array of anode wires between two cathode planes, one of which is segmented in the radial direction to provide the  $\phi$  measurements. The region among the cathodes is filled with a mixture of Ar,  $CO_2$ , and  $CF_4$  (30%,50%,20%). The passage of a particle induces a signal on many wires and strips and the particle position is obtained by an interpolation, with a resolution between 50 and 100  $\mu\text{m}$  for the  $\phi$  measurement performed by the strips and about 5 mm for  $r$  measured by the wires. In each endcap station, the presence of 6 layers of cathode strip chambers improves the timing and gives an efficiency better than 99%.

The **resistive plate chambers** are used both in the barrel and in the endcaps to provide a fast answer which is suitable for triggering purposes. The main feature of the RPCs is their excellent time resolution, which is better than 2 ns. The RPCs have four bakelite electrodes forming 2 coupled gaps. They are filled with a gas mixture of freon ( $C_2H_2F_4$ , 94%) and Isobutane ( $i-C_4H_{10}$ , 5%). The outer face of the bakelite planes is covered with graphite to distribute the high voltage over the whole surface. The RPCs operate in the avalanche mode instead of the streamer mode, to better sustain the high flux of particles; the amplitude of the signal is smaller since the gas multiplication is reduced, but this is compensated by an electronic amplification. The read-out is made by aluminium strips.

# Chapter 3

## The CMS trigger

At the LHC nominal luminosity, the total event rate is  $1\text{ GHz}$ . As the raw data event has a typical size of  $\sim 1\text{ MB}$ , the resulting amount of data, if totally recorded will be prohibitive to processed in later off-line analysis. This rate has therefore to be reduced to the order of  $100\text{ Hz}$ , which is the upper limit for storing and processing the data.

This reduction corresponds to a selection of the interesting physical events: in fact the rate is dominated by low  $p_T$  processes, while physics channels of interest represent only a small fraction of total events (see fig. 3.1). This fraction must fit as closely as possible the allowed output rate. This task is not easy, because QCD high- $p_T$  process alone can reach the upper limit and saturate the output rate. The trigger system is therefore required to provide a huge rejection factor ( $\sim 10^7$ ) and at the same time to keep the efficiency for interesting events high. This means that events must be selected on the basis of their physics content and that online selection has a level of complexity comparable to that of offline reconstruction.

In addition the trigger algorithms must run fast. In fact, the time available in the interval between two bunch-crossings,  $25\text{ ns}$ : is too small even to read out all the RAW data from the detector. Hence the final decision must be divided into several subsequent steps of increasing refinement and length. Each step (*level*) accesses and uses only a part of the available data in order to take its *accept/reject* decision within the required time constraints. The following levels have a lower rate of events to process and more time available, so they can use larger sets of data and more refined algorithms.

The event rate reduction thus takes place via different sequential trigger levels. The first level, *Level-1* (*L1*), must be hardware implemented, due to the strict timing constraints. It accesses data from the calorimeters and the muon detectors with coarse granularity and performs low level analysis in custom trigger processors. On the basis of this limited information, it

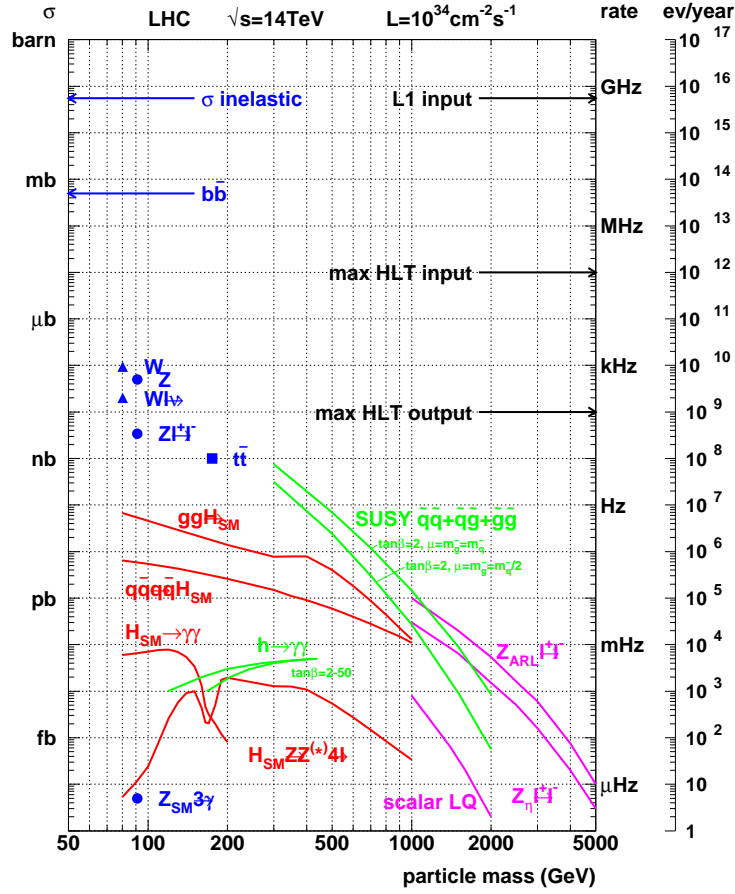


**Figure 3.1:** Cross sections and event rates at high luminosity ( $10^{34}; cm^{-2}s^{-1}$ ) as a function of particle masses.

has to reduce the data rate to  $\sim 100 kHz$ , which is the maximum input accepted by the *Data Acquisition System (DAQ)* at high luminosity. At low luminosity, when the dedicated farm to on line selection will not be completed yet, instead, the DAQ will not be able to handle an input rate higher than 50 kHz.

The subsequent levels of the trigger (*High Level Trigger* or *HLT*) are fully implemented on software running on a farm of commercial processors: this ensures more flexibility and the possibility to improve the selection algorithms. The HLT performs the final selection and achieves the output rate of  $\mathcal{O}(100 Hz)$ . Only data accepted by the HLT are recorded for offline physics analysis. Additionally, small samples of the rejected data are retained for monitoring the HLT performances. The HLT can be subdivided into several

logical levels (*Level-2, Level-3* and an intermediate *Level-2.5*), each one using a different set of data from different subdetectors. Anyway such classification is somehow arbitrary, as there is not a sharp distinction between these trigger steps, apart from the order in which they are applied: all events accepted by the L1 trigger are processed by the HLT in a single processor farm.

### 3.1 The Level-1 trigger

The L1 trigger receives events at the total LHC production rate ( $1\text{ GHz}$ ) and must select them in order to obtain an accept/reject decision for each bunch crossing, i.e. every  $25\text{ ns}$ . To achieve this, all detector data are temporarily stored in pipeline memories which can contain simultaneously up to 128 events. In the meanwhile, the event data are analyzed in pipelines of processing elements, each one taking less than  $25\text{ ns}$  to complete. At every bunch crossing, each element passes its results to next one and receives a new event to process. The L1 trigger decision must therefore be taken every 128 bunch crossing, i.e. every  $3.2\text{ }\mu\text{s}$ . Taking into account the time needed to transmit data from the detector to the counting room (through fibers up to  $90\text{ m}$  long) and, in the case of Drift Tubes detectors, the electron drift time (up to  $400\text{ ns}$ ), taking into account front-end electronic dead time, the time remaining for calculation can be as low as  $1\text{ ns}$ .

The L1 trigger is organized into three major subsystem: the Calorimeter Trigger, the Muon Trigger and the Global Trigger. The Muon Trigger is further divided into three independent sections representing the three different muon detectors: the Drift Tube trigger in the barrel, the Cathode Strip Chamber trigger in the endcap and the Resistive Plate Chamber trigger covering both barrel and endcap. The Muon Trigger also includes a Global Muon Trigger which combines the information from the DT, CSC and RPC trigger systems and sends this to the L1 Global Trigger.

The Calorimeter and Muon Trigger do not perform any selection themselves. They identify "trigger objects": *isolated/not isolated e.m. objects (electrons/photons), forward/central/ $\tau$  jets, muons*. The four best candidates of each type are sent to Global Trigger, together with a measurement of their position, transverse energy/momentum and a quality word. The Global Trigger also receives the total and missing energy measured by the Calorimeter.

The Global Trigger performs the event selection on the basis of the information provided by the trigger subsystems. To be accepted, an event must satisfy some programmable trigger conditions, such as the presence of certain object(s) with energies or momenta above predefined thresholds, topological

conditions and correlations between different objects. Up to 128 of these conditions can be tested in parallel, and each one can be *prescaled* to accept only a fraction of selected events.

A schematic view of the L1 trigger system with its components and their relationships is shown in fig. 3.2. The input data to the Global Calorimeter Trigger and Global Trigger are transmitted to the DAQ for storage along with event readout data. In addition, all trigger objects found, whether they were responsible for the L1 trigger decision or not, are also sent. The decision whether to accept or reject a specific bunch crossing is transmitted to all subdetector front-end and readout systems.

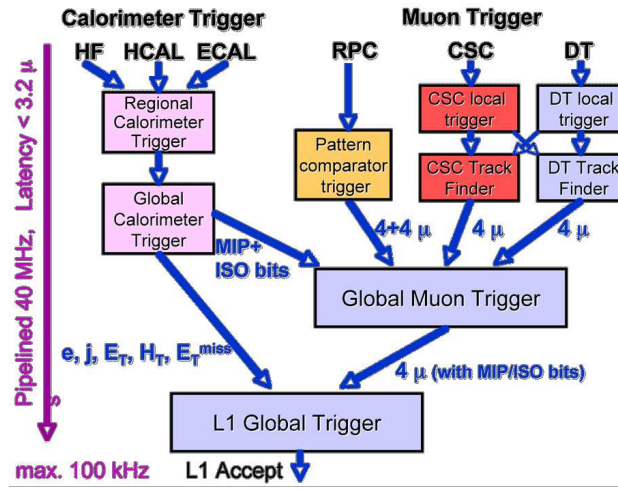


**Figure 3.2:** Components of the L1 trigger system and their relationships.

### 3.1.1 The Calorimeter Trigger

The L1 Calorimeter Trigger identifies five types of trigger objects and measures their positions and transverse energies: isolated electrons/photons, non-isolated electrons/photons, central jets, forward jets and  $\tau$ -jets.

The Calorimeter Trigger is divided into 4176 *trigger towers* (2448 in the barrel, 1584 in the endcap and 144 in the forward calorimeters). These have a size of  $\Delta\eta \times \Delta\phi = 0.087 \times 0.087$  up to  $\eta \sim 1.74$ , while at higher pseudorapidity the  $\eta$ -size of towers increases up to  $\Delta\eta = 0.35$ .

In the ECAL barrel, a trigger tower is formed by  $5 \times 5$  crystals, while in the ECAL endcap crystals are arranged in a  $x - y$  geometry, so the towers do not follow exact  $\eta - \phi$  boundaries. and the number of crystals per tower varies between 25 at  $\eta \sim 1.5$  and 10 at  $\eta \sim 2.8$ . Anyway, both in the barrel

and in the endcap, the boundaries of ECAL trigger towers match the HCAL ones.

In the barrel, each ECAL trigger tower corresponds to the  $\eta - \phi$  size of a HCAL physical tower. In the endcap ( $\eta > 1.479$ ), instead, two ECAL trigger towers along  $\phi$  correspond to one HCAL physical tower. In this region, the HCAL energy of one tower is equally divided between the two corresponding ECAL towers.

The forward hadron calorimeter does not participate in the electron/photon triggers and can therefore have a coarser  $\phi$ -binning ( $4 \times 0.087 = 20^\circ$ ): trigger towers, in this region, have a size of  $\Delta\eta \times \Delta\phi = 0.5 \times 0.348$ . The forward calorimeter takes part in the jets and missing energy triggers and allows a seamless coverage up to  $|\eta| = 5$  for these objects.

The trigger towers are further organized in calorimeter regions, each one formed by  $4 \times 4$  towers, with a size of about  $\Delta\eta \times \Delta\phi = 0.35 \times 0.35$ . In the forward calorimeter, each tower is treated as a trigger region by itself, because of its size.

The data of each ECAL and HCAL trigger tower is first processed by the Trigger Primitive Generator, integrated in the readout electronics, which provides the bunch crossing identification and calculates the *trigger primitives* of each tower, i.e. the sum of transverse energy and a *fine grain veto bit* (FG). The ECAL FG bit reflects the lateral extension of the electromagnetic shower and is used to improve the rejection of background in the electron trigger. The HCAL fine grain veto bit identifies the passage of a minimum ionizing particle requiring the HCAL energy to be within a programmable range, of the order of  $1.5 \div 2.5 \text{ GeV}$ .

These data are sent to the *Regional Calorimeter Trigger* (RCT), which finds the candidate physics objects (e.m. objects both isolated and non-isolated, taus and jets) and transmits them along with the sums of transverse energy to the *Global Calorimeter Trigger* (GCT). The GCT sorts by  $E_T$  the candidate electrons/photons, taus and jets and forwards the top four of each type to the Global Trigger. It also calculates and transmits the total transverse energy and the total missing energy vector.

The RCT transmits to the Muon Trigger a  $(\eta, \phi)$  grid of the activity in the whole calorimeter system to determine if there are energy deposits compatible with the passage of a muon “*MIP bits*” and if they are below a programmable threshold (*Quiet bit*) for muon isolation cuts.

## Photon and electron trigger

At L1, electrons and photons cannot be distinguished because of the absence of any tracker information, so they are treated together as more general iso-

lated and non-isolated electrons/photons “electromagnetic objects”. Electron/photon candidates are found using a sliding window algorithm on  $3 \times 3$  towers and their identification is based on the presence of a relevant energy deposition in one or two adjacent trigger towers. Requirements on the spatial extension of the shower are also imposed: the lateral profile information is provided by the ECAL FG bit, while the longitudinal profile is indicated by the *HAC veto bit*, which is set depending on the HCAL/ECAL energy ratio.

The Calorimeter Trigger separates isolated and non-isolated electrons / photons into two different streams. To be labeled as isolated, an e.m. candidate is required to pass conditions on  $E_T$  threshold and on FG and HAC bits not only in the central hit tower, but also in the eight neighboring towers of the  $3 \times 3$  window.

In each calorimeter region ( $4 \times 4$  trigger towers) the highest  $E_T$  non-isolated and isolated electron/photon candidates are separately found. The 16 candidates of both streams are further sorted by  $E_T$  and the Global Calorimeter Trigger sends the four most energetic ones of each type to the L1 Global Trigger.

### Jet and $\tau$ -jet triggers

The jet trigger uses energy sums (electromagnetic plus hadronic) computed in calorimeter regions. Jet candidates are found using a sliding window algorithm on  $3 \times 3$  regions, requiring the central region to have an  $E_T$  value higher than the eight neighbour regions and, in addition, higher than a fixed threshold value, in order to suppress noise.

The  $\tau$ -jets are characterized by their narrow profile. A jet is identified as “ $\tau$ -like” if each of the nine trigger regions of the  $3 \times 3$  window has no more than two towers exceeding a programmable  $E_T$  threshold.

$\tau$ -jets are expected only in the central calorimeter region ( $|\eta| < 3$ ), while the other jets are separately identified as central ( $|\eta| < 3$ ) or forward ( $3 < |\eta| < 5$ ) jets. As well as for e.m. objects, jet candidates are sorted by their  $E_T$  measures and the Global Calorimeter Trigger forwards the top four candidates of each type to the Global Trigger, together with the number of jets above some programmable threshold.

### Total and missing transverse energy

The total energy is obtained by summing the transverse energy of all ECAL and HCAL regions. The missing transverse energy ( $\cancel{E}_T$ ) is calculated from the vector sum of the  $E_x$  and  $E_y$  components of the deposit in each region, using the coordinates of the center of the region. The total and the missing

transverse energy (absolute value and  $\phi$  direction) are then sent to the Global Trigger.

### Quiet and MIP bits

For each calorimeter region, a *Quiet bit* is set if the sum of transverse energy of deposits in ECAL and HCAL is below a programmable threshold. The *MIP bit* is set if the quiet bit is active and the HCAL fine grain bit is set in at least one of the 16 HCAL trigger towers of that region. The quiet and MIP bits are transmitted to the Global Muon Trigger and can be used for muon selection.

### 3.1.2 The Muon Trigger

The goal of the Muon Trigger is to identify muons, reconstruct their position and transverse momentum and provide bunch crossing assignment.

As previously mentioned, each of the three components of the muon system (DT, CSC and RPC) contributes separately to the L1 trigger: such redundancy ensures a robust trigger with high efficiency and good background rejection. The features of the three detectors complement each other: the good spatial resolution of the wire chambers (DT+CSC) and the excellent time resolution of the RPC. Inefficiencies and sensitivity to backgrounds are also complementary in different detectors: the RPC suffer from the low energy background particles and the intrinsic noise, which can cause ghost triggers, while the layer structure of DT and CSC protects from this drawback. Moreover, such complementarity can be used for cross-checks and to improve the understanding of the performance of each system.

The information from each DT and CSC station is first processed by a Local Trigger, which reconstructs track segments. The DT and CSC Regional Track Finders then collect and combine segments of different stations to form muon tracks and estimate their  $p_T$ . In the region where the chambers overlap, DT and CSC Track Finders (TF) exchange segment information to reconstruct full tracks in each of the two subsystems.

In the RPC, instead, there is no local processing. Hits from all stations are collected by a Pattern Comparator Trigger (PACT), which detects muon candidates on the basis of predefined hit patterns.

The top four candidates from each subsystem (DT, CSC, barrel-RPC and endcap-RPC) are sent to the Global Muon Trigger, together with a word indicating their quality. The GMT compares the information from the TF's and the PACT and attempts to correlate DT/CSC tracks with RPC ones, then looks for MIP and Quiet bits delivered by the calorimeter to confirm

muon trigger and determine isolated muons. Finally, the four candidates with highest  $p_T$  are sent to the Global Trigger.

The acceptance of the Muon Trigger system does not cover that of the whole spectrometer, as trigger electronics will not be installed in the most forward CSC station, thus covering only up to  $|\eta| < 2.1$ .

A schematic view of the Muon Trigger structure is provided in fig. 3.3 and a short description of the different subsystems in the following paragraphs.

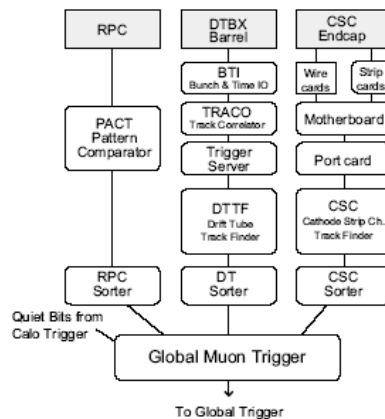


**Figure 3.3:** Structure of the L1 Muon Trigger system

### The DT Trigger

The first step of the DT trigger is the *local* trigger and is performed by the *Bunch and Track Identifier* (BTI), directly connected to the read-out electronics. For each superlayer, made up of four layers of drift cells, the BTI fits at least three hits to a straight segment and returns the unknown bunch crossing originating the track. In  $r-z$  superlayer, only tracks pointing to the interaction point are selected. In  $r-\phi$  superlayers, the reconstructed segments are matched by the Track Correlator (TRACO). The Trigger Server (TS) selects, among all the segment pairs in a chamber, the two with highest  $p_T$  and transmits them to the DT Track Finder (DTTF).

The DTTF is responsible for the second step of L1 muon trigger, the *regional* trigger. Here the segments produced by the four stations are combined in a single muon track candidate, with assigned  $p_T$ ,  $\eta$ ,  $\phi$  and a quality word. The segments between the stations are extrapolated using precomputed Look-Up Tables (LUT). The reconstructed track parameters are estimated using other LUT's, on the basis of the  $\phi$  directions of the two innermost

stations. Finally, the tracks are sorted by  $p_T$  and the four best candidates are sent to the GMT.

### The CSC Trigger

The local segment reconstruction in the CSC chambers is performed using independently the strips and the wires of the six layers of each chamber.

Cathode strips are used to reconstruct the binding coordinate  $\phi$  by a simple interpolation. The hits in the six layers are then searched for patterns compatible with high  $p_T$  tracks.

The anode wires instead are used to determine the  $\eta$  coordinate and the muon bunch crossing. A coincidence of two hits in different layers is needed to assign the bunch crossing, while the reconstruction of a segment requires at least four hits out of the six layers. To reduce the number of channels, wires are read-out in groups of 5 to 16.

### The RPC Trigger

Since the measurements in a single RPC are simple points, no local reconstruction is possible. The hits of the different stations are directly collected by the PACT which looks for correlations in space and time. Hits are matched with predefined patterns stored in a LUT to provide an estimation of the muon  $p_T$ . Muons can be identified using at least three hits in four stations. For the barrel, where six stations are present, the search is done independently for low- $p_T$  muons in the first four layers (in MB1 and MB2) and for high- $p_T$  ones using one layer in each station.

A ghost suppression algorithm is applied to reduce the effect of accidental coincidences due to background hits. The four highest  $p_T$  candidates in the barrel and endcaps are then separately sent to the GMT.

### The Global Muon Trigger

The GMT has the task to match the four muon candidates provided by the DT and CSC regional triggers with the 4+4 candidates from the RPC's. The matching is performed by comparing the spatial coordinates of the candidates in the  $(\eta, \phi)$  space and it needs to be tuned to reach an optimal balance between efficiency and background rejection. The highest efficiency is achieved selecting all candidates, even if they have been found by only one subsystem, while the maximum background rejection can be obtained requiring all candidates to be reconstructed by both subsystems (DT/CSC + RPC). In the current implementation, a candidate is accepted if it is reconstructed by two complementary systems, otherwise it is selected on the basis of its quality word.

Low-quality candidates from problematic  $\eta$  regions are discarded. If two candidates are matched, the parameters of the tracks are combined according to a programmable logic to achieve optimum precision.

The GMT also extrapolates the tracks back to the calorimeter and assigns each candidate the corresponding MIP and Quiet bits, which can be used to confirm the muon selection and to determine its isolation.

The parameters of the four best muon tracks in the whole CMS detector are sent to the L1 Global Trigger, which takes the Level-1 decision.

The simplest possible L1 muon selection is based on a threshold on the GMT  $p_T$ . The L1  $p_T$  threshold is defined at 90% efficiency.

The resolution on the inverse of transverse momentum,  $\frac{1}{p_T}$ , is about 17% in the barrel, 20% in the endcaps and 22% in the overlap region. Such limited resolution and the presence of non-gaussian tails cause the so-called “feed-through” of low- $p_T$  muons which are reconstructed at high momenta. This effect is important as the muon rate increases steeply at low  $p_T$ , so that the contribution of feed-through muons to the L1 trigger is dominant even for moderately high thresholds. This effect can be reduced by improving the  $p_T$  resolution, and this task is performed by the High Level Trigger.

### 3.1.3 The Level-1 Trigger table

The simplest triggers usually applied are based on the presence of one object with  $p_T$  or  $E_T$  above a predefined threshold (*single-object triggers*), two objects of the same type (*di-object triggers*) or even of different type (*“mixed” triggers*) with symmetric or asymmetric thresholds. However, the L1 Trigger allows to define more complex and “exclusive” selection algorithms, based on the presence of several, different objects and on topological conditions and correlations. These are usually required by special channels that are not efficiently selected by simple criteria.

The choice of the L1 trigger thresholds is determined by the maximum event rate that can be accepted by the DAQ system ( $\sim 50$  kHz at start-up,  $\sim 100$  kHz later). This bandwidth is then subdivided among the L1 objects described in the previous sections and for each of them between the single- and multiple-object streams. The resulting set of thresholds is called trigger table. The present Level-1 trigger tables at low and high luminosity are shown in 3.1 and 3.2 respectively.

**Table 3.1:** L1 trigger table at low luminosity

Trigger	Threshold (GeV)	Rate (kHz)	Cumulative Rate (kHz)
Inclusive isolated electron/photon	29	3.3	3.3
Di-electrons/di-photons	17	1.3	4.3
Inclusive muon	14	2.7	7.0
Di-muons	3	0.9	7.9
Single tau-jet trigger	86	2.2	10.1
Two tau-jets	59	1.0	10.9
1-jet, 3-jets, 4-jets	177,86,70	3.0	12.5
Jet $\times$ MET	88 $\times$ 46	2.3	14.3
Electron $\times$ Jet	21 $\times$ 45	0.8	15.1
Minimum-bias (calibration)		0.9	16.0
Total			16.0

**Table 3.2:** L1 trigger table at high luminosity

Trigger	Threshold (GeV)	Rate (kHz)	Cumulative Rate (kHz)
Inclusive isolated electron/photon	34	6.5	6.5
Di-electrons/di-photons	19	3.3	9.4
Inclusive muon	20	6.2	15.6
Di-muons	5	1.7	17.3
Single tau-jet trigger	101	5.3	22.6
Two tau-jets	67	3.6	25.0
1-jet, 3-jets, 4-jets	250,110,95	3.0	26.7
Jet $\times$ MET	113 $\times$ 70	4.5	30.4
Electron $\times$ Jet	25 $\times$ 52	1.3	31.7
Muon $\times$ Jet	15 $\times$ 40	0.8	32.5
Minimum-bias (calibration)		1.0	33.5
Total			33.5

Minimum bias rates are prescaled.

## 3.2 The High Level Trigger

The HLT is the second level of trigger in CMS: the input is given by the L1, so it is  $\sim 100\text{ kHz}$ , while the output will be sent to persistent storage, and it's limited to  $\sim 100\text{ Hz}$ . The reduction factor of  $\mathcal{O}(10^3)$  is achieved in several steps, often referred to as L2, L3..., but since the HLT is implemented on software programs running on commercial processors, it's very flexible, and so the boundary between the various levels of HLT is not so sharp.

The main difference among the HLT levels (and with the L1) is the amount of data to be handled at each step. The first step, L2, receives the maximum rate of events in input and has the task to confirm the L1 decision. Hence it has to perform a “regional” and fast reconstruction, using only information from the calorimeter and muon detectors. In contrast, L3 refers to selection that includes the reconstruction of full tracks in the tracker: because of the high number of channels, the complex pattern recognition and the higher combinatorics, track reconstruction is a process that demands large amounts of CPU time. As previously mentioned, intermediate levels between L2 and L3 triggers, often called L-2.5 triggers, refer to algorithms that use partial tracker information, e.g. pixel hits, for a fast confirmation of the electron candidate.

The decision on whether an event should be accepted by the HLT, in most cases, involves the reconstruction of quantities in only a limited region of the detector. The HLT reconstruction of physics objects is driven by the corresponding candidates identified by the L1 trigger. This approach leads to significant CPU savings, however it also leads to rejecting events that contain objects that did not pass the L1 trigger.

In the following sections, the electron, photon and muons High Level Triggers, which are the most relevant for the present work, will be described in some more detail.

### 3.2.1 Electron and photon High Level Trigger

The HLT selection of electrons and photons proceeds in three steps. The first step (L2) uses the calorimeter information alone. The next step (L2.5) demands hits in the pixel detectors consistent with an electron candidate. Presence or absence of hits in the Pixel detector matching the energy deposits in the ECAL towers, splits the electromagnetic triggers into two categories: *electron candidates* (single and double), and, above significantly higher thresholds, *photon candidates*. In the final step (L3) the selection of electrons uses full track reconstruction, seeded from the pixel hits obtained at the matching step.

Preliminary essential operations, of course, are the clustering of the energy deposits in the ECAL and the estimate of the electron/photon energy and position from this information [20]. For the calorimeter reconstruction, anyway, the emphasis is mostly on the reconstruction of electrons, because the transverse momentum thresholds for triggering on electrons are much lower than those for photons. Since the amount of material traversed in the tracker volume is almost  $1 X_0$  for certain polar angles, the first challenge for ECAL clustering is to include all energy radiated by electrons. Photons that have converted in the tracker material, instead, are adequately reconstructed by the electron algorithms, using the tracker information to assist the clustering.

## **L2: selection of electrons and photons**

Using only calorimeter information, the Calorimeter L2 Trigger has to reconstruct an ECAL super-cluster in a region specified by the Level-1 trigger. The super-cluster is first required to fall within the precision physics fiducial region of the ECAL, defined by removing the barrel/endcap transition region, strongly shadowed by tracker cables, from the overall coverage of  $|\eta| < 2.5$ . The excluded region is  $1.4442 < |\eta| < 1.5660$ .

The super-cluster is then required to have  $E_T$  above a threshold which is chosen to give 95% efficiency for electrons at the same point on the  $E_T$  scale at which the L1 trigger has 95% efficiency. The same threshold is required for both objects in the di-electron trigger. At  $\mathcal{L} = 2 \cdot 10^{33} \text{ cm}^{-2}\text{s}^{-1}$ , the thresholds are  $26 \text{ GeV}$  for the single and  $14.5 \text{ GeV}$  for the double electron trigger. The corresponding thresholds at  $\mathcal{L} = 10^{34} \text{ cm}^{-2}\text{s}^{-1}$ , are  $31 \text{ GeV}$  and  $16.9 \text{ GeV}$ . This cut on the transverse energy reconstructed in the ECAL increases the rejection of fake electrons by about a factor 2.

### **L2.5: matching of super-clusters to hits in the Pixel detector**

The L2.5 trigger searches for hits in the Pixel detector matching the position  $(\eta, \phi)$  of the Calorimeter Super-Cluster (SC). This task takes advantage of the fact that the position of an electron candidate is estimated as the energy-weighted average of the deposits (i.e. the energy-weighted average impact point of the electron and the bremsstrahlung photons it has radiated), and that is exactly where a non-radiating electron would have impacted. Such point can be propagated back to obtain an estimate of the direction of the electron at the vertex and the hit position expected in the pixel detector. Since most of the tracker material lies after the Pixel detector, most electrons and photons are expected not to radiate or convert before it.

The method to find Pixel hits matching a SC proceeds as follows.

- The electromagnetic cluster gives the energy and the position of the electron candidate, so that its transverse momentum can be computed. The expected hit position on the pixel layers is estimated by propagating the electron inwards to the nominal vertex using the magnetic field map. A search area is defined in the innermost pixel layer (typically  $40\text{mrad}$  wide in  $\phi$ , unrestricted in  $z$ ) and the  $\phi$ -width is the main parameter used to control the tightness of the pixel matching.
- If a compatible hit is found within the search area on the innermost pixel layer, a better estimate of the longitudinal vertex position  $z$  is obtained by interpolating the line from the cluster through the corresponding hit to the beam line. Nominal values (0,0) for  $x$  and  $y$  coordinates of the vertex are assumed. If no hit is found in the search area of the innermost pixel layer, the search is repeated in the next layer.
- The track is propagated from the newly estimated vertex to the second (or third) pixel layer through the compatible hit in the first (or second) layer. The dominating uncertainty, in the  $r - \phi$  plane, results from the estimate of the  $E_T$  value of the SC, and thus the radius of curvature of the electron track. But this is a very small uncertainty since the distance from one pixel layer to the next is short. In the  $r - z$  plane, the main uncertainty comes from the vertex  $z$ .
- If a second compatible hit is found, the cluster is identified as an electron; if not, it is considered as a jet. If there are no compatible hits in the current layer, there may be one more pixel layer left, and the search is repeated there.

The search is made twice, once for each charge assignment. In the first step of the search, the electron and positron search areas can overlap, but in the second step, when a compatible hit is propagated to another pixel layer, the  $p_T$  needed for the search areas of different charges to overlap is almost  $1\text{TeV}$ .

### **L3: inclusion of full tracking information**

The L3 performs the final selection and includes all further requirements needed to reach an acceptable rate to offline storage. At this stage, the full detector information is available, including tracks. Nevertheless, some purely calorimetric quantities are still used for selection and isolation cuts.

**Electrons** The L3 selection for electrons starts with electron track-finding, seeded by the L2.5 pixel match. To maintain high efficiency, track-finding is made with very loose cut parameters. Further cuts are applied on the following variables:

- $\frac{E}{p}$ , i.e. the SC energy and correspondent track momentum ratio;
- $\Delta\eta(\text{track} - SC)$ , i.e. the distance between the SC position and the extrapolated track position in the ECAL in the longitudinal coordinate;
- for the endcaps only  $\left(\frac{H}{E}\right)$  i.e. the energy found *behind* the SC (in the HCAL), expressed as a fraction of the SC energy.

Other useful cuts, especially at high luminosity, are the *isolation* cuts. Three isolation techniques have been studied:

- ECAL isolation;
- pixel-track isolation;
- full-track isolation.

All of the three techniques consider a “cone” around the electron/photon candidate, sum the  $E_T$  of deposits (or  $p_T$  of tracks or number of tracks) within this cone and compare it to a prefixed threshold. The cone is defined as

$$\Delta R = \sqrt{(\Delta\eta)^2 + (\Delta\phi)^2} < \Delta R_{max} ,$$

with  $\Delta\eta$  and  $\Delta\phi$  the distances from the candidate direction in pseudorapidity and azimuthal angle, respectively. The  $\Sigma E_T$  deposited in the cone in the case of ECAL isolation or the  $\Sigma p_T$  of tracks in the cone in the case of pixel and tracker isolation are computed after subtracting the contribution from the candidate itself, i.e. excluding a “*veto cone*”, so that  $\Delta R_{veto} < \Delta R < \Delta R_{max}$ .

Track isolation has the advantage that it is less sensitive to pileup, which is the dominant source of electron identification inefficiency at high luminosity, because only tracks associated with the primary vertex are selected for the isolation cuts.

**Photons** When a SC passes the L2 triggers but fails the L2.5 pixel matching, it is compared to further  $E_T$  thresholds. higher than those applied at L2. The events passing these cuts form the photon stream. The thresholds are chosen to give an acceptable rate. The di-photon thresholds are usually asymmetric. Backgrounds can be rejected using track isolation cuts and by

rejecting  $\pi^0$ 's based on the lateral shape of the shower. Defining the longitudinal coordinate of the vertex is a significant issue for the analysis of a  $H \rightarrow \gamma\gamma$  signal. For events where one or more of the photons has converted in the tracker, the track segment and the ECAL cluster can be used to locate the vertex. The vertices in the remaining events can be found using algorithms that choose the track vertex associated with the largest track activity.

### 3.2.2 Muon High Level Trigger

The Muon High Level Trigger is organized in two logical steps: the Level-2 and the Level-3 muon reconstruction. Selection criteria are applied at the end of each step, in order to reduce the event rate to a level acceptable by the following one. The Level-2 consists in the reconstruction of muon tracks in the standalone spectrometer (*Standalone Muon Reconstruction*), while the Level-3 uses both tracker and spectrometer data (*Global Muon Reconstruction*).

The tracking is based on a *Kalman Filter* technique, which is the same used also in the off-line reconstruction; the main differences will be in the seeding of the track fit. The HLT is seeded by the (up to four) muon candidates found by the L1 Global Muon Trigger, including those candidates that did not necessarily lead to a L1 trigger accept by the Global Trigger. In the L2 muon selection, the resulting trajectories are used to validate the L1 decision as well as to refine the muon measurement. The basis of the L3 muon selection is to add Tracker hits to the muon trajectory, thus greatly improving the muon momentum measurement.

Both at L2 and L3, the muon selection is based on thresholds on the  $p_T$  of reconstructed tracks. In addition, isolation criteria can be applied to the muon candidates to provide further rate reduction: at L2 using the calorimetric energy sum in a cone around the muon and at L3 using the number of pixel tracks in a region around the projected muon trajectory. This suppresses muons from  $b$ ,  $c$ ,  $\pi$ , and  $K$  decays.

#### **L2: muon standalone reconstruction**

The L2 step improves the L1 muon trigger response using the full resolution of the muon detectors. It consists in a track reconstruction based on the iterative Kalman Filter method. The selection is based on a cut on the  $p_T$  of reconstructed muons.

Track seeds are initially created using the segments reconstructed at L1 in the innermost chambers. Starting from these seeds, the hits to be included in

the fit are looked for iteratively, moving outwards in the muon spectrometer and through the iron yoke. At each step, the *state vector* (track position, direction and momentum) is propagated through the magnetic field, extrapolated to the next layer of chambers and compared to the results of L1 local reconstruction (track segments in the DT's or CSC's and three-dimensional hits for the RPC's). These are used to update the estimate of the trajectory parameters.

This procedure is iterated until the outermost measurement station in the muon system is reached. The result is a track state vector at the outermost muon station updated with all available measurements. This is used as seed to the actual fit, which is performed in a similar way using a backward Kalman Filter and assuming the muon candidate to originate from the interaction region (defined by the beam spot size:  $\sigma_{xy} = 15 \mu m$  and  $\sigma_z = 5.3 cm$ ). In both the forward and backward propagation, a hit is not added to the muon trajectory if its contribution to the total  $\chi^2$  exceeds 25. The resulting track parameters, propagated inward to the collision vertex, are used to reject or accept the event for further L3 processing.

The typical  $p_T$  resolution obtained by the L2 reconstruction, for muons coming from  $W \rightarrow \mu\nu$  decays, is about 10% in the barrel, 16% in the endcaps and 15% in the overlap regions. The improvement in the resolution with respect to the L1 trigger allows to reduce the muon rate by almost an order of magnitude.

### L3: inclusion of Tracker information

At L3, muon tracks are reconstructed using data from the full tracking system. The resulting improved resolution allows a much sharper  $p_T$  cut than at L2.

Starting from a L2 reconstructed muon, the muon trajectory is extrapolated from the innermost muon station to the outer Tracker surface and a region of interest (i.e. compatible with the muon trajectory) within the silicon layers is defined to perform regional track reconstruction. Here *regional seeds* are built from pairs of reconstructed hits in different layers, considering all combinations of compatible pixel and double-sided strip layers.

Starting from these seeds, tracks are reconstructed inside the region of interest using an algorithm based on the Kalman Filter method, which proceeds through the following steps:

- **trajectory building:** for each seed (pair of hits), a set of trajectories is built; starting from the innermost layer, the trajectory is propagated to the next tracker layer that is reachable, and updated with compatible measurements found on that layer;

- **trajectory cleaning:** ambiguities between multiple trajectories that may result from a single seed are resolved, on the basis of the number of hits and the  $\chi^2$  of the track fit;
- **trajectory smoothing:** all reconstructed tracks are fitted once again, including the hits in the muon chambers belonging to L2 reconstructed muons, and selected on the basis of a  $\chi^2$  cut.

The typical  $p_T$  resolution obtained by the L3 reconstruction, for muons coming from  $W \rightarrow \mu\nu$  decays, is about 1.0% in the barrel, 1.7% in the endcaps and 1.4% in the overlap region. This allows to eventually reduce the rate with respect to the L2.

### Muon isolation

In order to improve background rejection isolation cuts can be applied to  $\mu$  candidates. In particular, the integrated rate of muons at LHC is dominated by muons from  $b$ ,  $c$ ,  $\pi$  and  $K$  decays, which are usually accompanied by other nearby particles.

Three isolation techniques have been studied. Each of these is based on the standard technique of summing the  $E_T$  or  $p_T$  in a cone around the muon, excluding a veto cone to subtract the contribution of muon itself.

**Calorimeter isolation** The muon direction at the impact point is used to define the cone axis. The extraction of the energy deposits is done independently in the ECAL and the HCAL. The total energy is obtained as a weighted sum,  $E_T = \alpha E_T^{ECAL} + \beta E_T^{HCAL}$ , where  $\alpha \approx 1.5$  and  $\beta \approx 1$  are found to be an optimum value, due to the ECAL higher resolution with respect to HCAL. Typical values are 0.2 for cone sizes, 0.07 for veto cone sizes in ECAL (in HCAL, the energy of a single tower is subtracted),  $6.5 \div 9$  GeV for thresholds on summed  $E_T$  in a cone. This technique can be used with the standalone muon reconstruction at L2. However, as it is based on the calorimeter, this technique becomes less effective at high luminosity, as more pileup enter in the sum.

**Pixel isolation** In this case, isolation is determined on the basis of the summed  $p_T$  of tracks reconstructed in the Pixel detector within a prefixed cone. These track candidates are used to fit primary vertices. All pixel tracks contributing to the  $\Sigma p_T$  in the cone are required to come from the same primary vertex as the L3 muon, thus reducing the effect of pileup. The veto value is defined as the  $p_T$  of the pixel track closest in direction to the muon, within  $\Delta R < 0.015$ . Typical values are 0.2

for cone sizes and  $1.8 \div 3.8 \text{ GeV}$  for  $p_T$  thresholds. This method, which can be applied at L3, is less sensitive to pileup, but requires the reconstruction of three pixel hits out of the three layers in the pixel detector for every track and is thus sensitive to inefficiencies.

**Tracker isolation** This method uses full tracks reconstructed regionally. It is more robust than pixel isolation, but is more time consuming, especially at high luminosity. As well as for the pixel-based isolation, a cut is imposed on the  $\Sigma p_T$  of tracks reconstructed in a cone around the direction of the L3 muon, neglecting the contribution from the muon itself. Tracks are reconstructed using regional tracking, i.e. track seeds are created using pairs of pixel hits in a region of interest, defined by a vertex constraint. Thresholds on the summed  $p_T$  vary from 2.0 to 3.0  $\text{GeV}$  for typical cone sizes of 0.2.

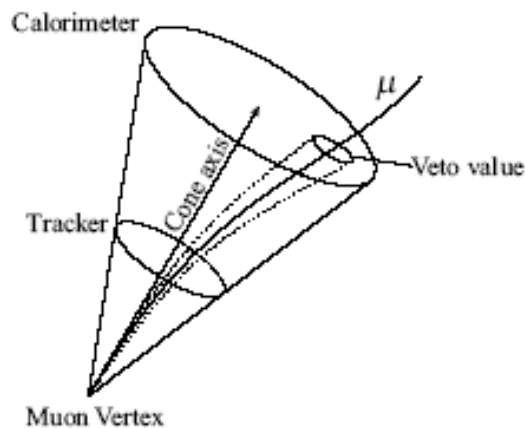


**Figure 3.4:** Schematic picture of Muon Isolation

# Chapter 4

## Studies of $H \rightarrow ZZ^* \rightarrow 2\mu 2e$ channel at generator level

For Higgs masses below twice the  $Z$  mass, the channel  $H \rightarrow ZZ^*$  is considered the "silver channel" after  $H \rightarrow \gamma\gamma$ . Despite that its branching ratio is lower than the corresponding  $H \rightarrow WW^{(*)}$  channel, it provides a cleaner experimental signature for the detection of the Higgs signal and allows a direct measure of the Higgs boson mass and width. Furthermore it is the best channel for characterizing the Higgs spin and CP quantum numbers from the angular correlations of the  $ZZ^*$  decay products in the fully leptonic final state. Used in conjunction with the information from the decay  $H \rightarrow WW^{(*)}$ , it also allows for the measurement of the Higgs couplings to weak gauge bosons.

In this chapter a preliminary analysis at MC generator level of the channel  $H \rightarrow ZZ^*$  when the two  $Z$  bosons decay into a couple of electrons and a couple of muons<sup>1</sup>, respectively, is described.

This channel presents several experimental challenges which are mainly related to the extraction of an electron signal from a very difficult environment. Indeed, the considerable amount of radiation emitted by bremsstrahlung can affect both the electron reconstruction efficiency and the measurement of their energy. In order to provide the best possible measurement of the 4-momentum of the four leptons produced in the Higgs decay, a combination of tracking and calorimetry information is required to cover the full spectrum of momenta from  $\mathcal{O}(1 \text{ GeV})$  to  $\mathcal{O}(10^2 \text{ GeV})$ .

In the following sections, signal and backgrounds for the  $H \rightarrow ZZ^* \rightarrow 2\mu 2e$  channel will be introduced and the kinematic distributions for some

---

<sup>1</sup>in the following, the charge conjugate states  $e^+/e^-$  and  $\mu^+/\mu^-$  are referred collectively to as electrons and muons, regardless of the charge sign.

interesting cut for further analysis are presented. The studies described in this chapter are performed at generator level, and so distributions deal with leptons four momenta at the interaction point. The effect of the detector will be considered only as far as the geometrical acceptance is concerned, while the experimental resolution will not be taken into account.

## 4.1 Definition of the signal and of the background

The signal considered in this analysis is characterized by the presence of two electrons and two muons in the final state. The background is thus constituted by all processes with at least two final state muons and two final state electrons, either prompt or from hadron misidentification, or cascade decays of beam remnants. The most important contributions to the background are:

- $ZZ^*$  events, with one  $Z$  decaying in to an electron-positron pair and the other in a muon-antimuon pair
- $Zb\bar{b}$ , where both the  $b$  hadrons decay semileptonically
- $t\bar{t}$ , where the top quark decays with branching ratio  $\sim 1$  into  $Wb$  and leptons in the final state may come from the decay  $W \rightarrow \ell\nu_\ell$  and from semileptonic decays in the  $b$  decay chain

Having two  $Z$  in the intermediate state, the  $ZZ^*$  background is called "irreducible", since it has many kinematical features similar to the signal. The two remaining backgrounds constitute the so-called "reducible" background.

Before starting an analysis it can be useful to look at the general properties of the signal and of the background.

The most important feature of the signal is that the four leptons come from the decay chain of a single particle, the Higgs boson. This implies that their invariant mass peaks at the Higgs mass, while for the other backgrounds a distribution without peaks is anticipated. The Higgs boson search would consist in looking for the appearance of a peak in the four leptons invariant mass distribution:

$$M_H^2 = P_H^2 = \left( \sum_l E_l \right)^2 - \left( \sum_l \mathbf{p}_l \right)^2 \quad (4.1)$$

Signal events can be also identified for the presence of two  $Z$  bosons in the intermediate state. Depending on the Higgs mass the two bosons could be either real or off mass shell (virtual), the fraction of virtual  $Z$  decreasing with the increase of the Higgs mass. This thesis will consider the case  $M_H < 2M_Z$ . Moreover assuming that the Standard Model Higgs is a CP-even scalar particle, the two  $Z$  bosons from the Higgs decay are mainly longitudinally polarized. This implies that differential cross section in the angle  $\theta^*$  between one lepton in the  $Z$  rest frame and the direction of its parent in the Higgs rest frame is of the form:

$$\frac{d\sigma}{d\cos\theta^*}(H \rightarrow ZZ^*) \sim \sin^2\theta^* \quad (4.2)$$

For the  $ZZ^*$  background, which also has two  $Z$  as intermediate state, the bosons are mainly transversely polarized. This polarization implies a differential cross section of the form:

$$\frac{d\sigma}{d\cos\theta^*}(q\bar{q} \rightarrow ZZ^*) \sim \cos^2\theta^* \quad (4.3)$$

which could be exploited to enhance the background rejection.

Reversing the argument, it is possible to identify the Higgs spin and CP quantum numbers from the angular distributions of its decay products. The channel  $H \rightarrow ZZ^* \rightarrow 4\ell$  is optimal for this purpose, since the final state can be completely reconstructed. Also the mass spectrum of the virtual  $Z$  boson could be used to discriminate different spin-CP hypothesis for the Higgs particle.

The analysis of the transverse momentum distributions of the four final state leptons would lead to the consideration that there are substantial differences for signal and background, especially for the two lowest  $p_T$  leptons. Furthermore the presence of neutrinos in the decay of both  $b$  and  $t$  quarks implies a larger missing energy for the reducible backgrounds with respect to the signal events. Finally, the tracks of the four leptons from the Higgs decay are compatible with a single vertex hypothesis, while for the  $Zb\bar{b}$  and  $t\bar{t}$  backgrounds, the electrons from the  $b$  and  $t$  decay chain come from secondary vertices.

## 4.2 Signal and background generation

In order to simulate signal and background for  $H \rightarrow ZZ^* \rightarrow \mu^+ \mu^- e^+ e^-$ , standard MC Generators in use by CMS collaboration have been used.

Leading-Order (LO) generator (mainly PYTHIA [21] and CompHEP [22] in the  $Zb\bar{b}$  background case) have been used to produce signal and background

events. In order to accelerate the event production without biasing the sample for the analysis, a preselection at the generator level has been applied. This permits to fully simulate in the detector only the events with four final state leptons, two electrons and two muons within the CMS angular acceptance for muons ( $|\eta_\mu| < 2.5$ ) and for electrons ( $|\eta_e| < 2.7$ ) and with a transverse momentum sufficiently high ( $p_T^\mu > 3$  GeV for muons and  $p_T^e > 10$  GeV for electrons) to allow a good efficiency in the lepton detection. In this thesis we will consider the case of Standard Model Higgs boson with  $M_H < 2M_Z$  and the LHC machine operating at low luminosity *low luminosity* scenario ( $\mathcal{L} = 2 \cdot 10^{33} \text{cm}^{-2} \text{s}^{-1}$ ).

### 4.2.1 Higgs boson signal

It has already been extensively described how the Higgs boson production cross section is dominated by gluon-gluon fusion (80%) over the mass range  $100 \text{ GeV} < M_H < 1 \text{ TeV}$ . At LHC, where  $\sqrt{s_{pp}} = 14 \text{ TeV}$ , the cross section for this process is around 45 pb at  $M_H = 120 \text{ GeV}$  and decreases monotonically to 5 pb at  $M_H = 500 \text{ GeV}$ .

The associated production processes,  $qq \rightarrow \text{HW}$ ,  $qq \rightarrow \text{HZ}$ ,  $gg/q\bar{q} \rightarrow t\bar{t}H$  and  $gg/q\bar{q} \rightarrow b\bar{b}H$  have cross sections lower by a factor of 20 at  $M_H \approx 100 \text{ GeV}$  and by a factor of 1000 at larger masses,  $M_H > 500 \text{ GeV}$ . The production cross section for the gauge boson fusion,  $VV \rightarrow H$ , is about 10% of the gluon fusion production cross section for  $M_H < 200 \text{ GeV}$ , and becomes comparable for  $M_H \approx 1 \text{ TeV}$ .

The QCD corrections for the  $gg \rightarrow H$  process are large, with a  $K$ -factor ranging from 1.5 to 1.8 [23]. The QCD corrections are smaller for the gauge boson fusion ( $K$ -factor  $\sim 1.1$ ) and for the associated production processes  $qq \rightarrow \text{HW}$ ,  $qq \rightarrow \text{HZ}$  ( $K$ -factor  $\sim 1.3$ ) and  $gg/q\bar{q} \rightarrow t\bar{t}H$  ( $K$ -factor  $\sim 1.2$ ) [24].

The numerical values of the Higgs boson cross sections can be predicted with **HIGLU 2.1**[23] and other programs which include the next-to-leading order correction so that the uncertainties are of the order of 15%.

The signal events have been generated with **PYTHIA 6.227** (using the **CTEQ5L** set of parton distribution functions) with a Higgs mass  $M_H = 150 \text{ GeV}$  with  $2 \cdot 10^5$  events. Events where the four leptons in the final state come from intermediate decay of  $Z^* \rightarrow \tau \rightarrow \ell\nu_\ell$  with  $\ell = e, \mu$  have been excluded from the analysis, since, due to the presence of neutrinos in the final state, they contribute to the tail of  $4\ell$  invariant mass distribution rather than to the peak.<sup>2</sup>

<sup>2</sup>the relative branching ratio of  $Z \rightarrow 2\mu 2e$  directly and through the chain decay of  $\tau$  is:  $R = B.R.(ZZ^* \rightarrow 4\tau \rightarrow 2\mu 2e)/B.R.(ZZ^* \rightarrow 2\mu 2e) \sim 1/300$

The expected number of events for an integrated luminosity  $\mathcal{L}_{int} = \int \mathcal{L}(t)dt = 20 \text{ fb}^{-1}$  (about one year of run at LHC at Low-Luminosity) is shown in figure 4.1 and the relevant cross sections and branching ratios are reported in table 4.1 for some masses of the Higgs boson.

As one can see, in the region  $m_H < 2m_Z$  the cross section  $\sigma(H \rightarrow ZZ^* \rightarrow 2\mu 2e)$  peaks around 150 GeV and therefore this value has been chosen in order to study this kinematical region.

**Table 4.1:** Cross sections for the Higgs boson production, branching ratio into  $ZZ^*$  and preselection efficiencies for different values of the Higgs mass. The cross section and branching ratios are obtained from Spira[23]

$m_H$ [GeV]	$\sigma(gg \rightarrow H)$ [pb]	$\sigma(qq \rightarrow Hqq)$ [pb]	$\sigma_{tot}$ [pb]	$B.R.$ ( $H \rightarrow ZZ^*$ )	$\epsilon_{kin}$	$\sigma_{tot} \cdot B.R.$ [fb]	$\sigma \cdot B.R. \cdot \epsilon_{kin}$ [fb]
115	39.3	4.65	47.73	0.008	0.54	0.43	0.23
120	36.5	4.47	44.30	0.015	0.56	0.74	0.41
130	31.7	4.14	38.44	0.039	0.61	1.70	1.04
140	27.8	3.83	33.69	0.068	0.65	2.59	1.68
<b>150</b>	<b>24.6</b>	<b>3.56</b>	<b>29.80</b>	<b>0.083</b>	<b>0.67</b>	<b>2.79</b>	<b>1.87</b>
160	21.9	3.32	26.50	0.043	0.69	1.29	0.89
170	19.7	3.09	23.88	0.023	0.71	0.62	0.44
180	17.8	2.88	21.59	0.058	0.73	1.41	1.03
190	16.2	2.71	19.67	0.219	0.74	4.88	0.61

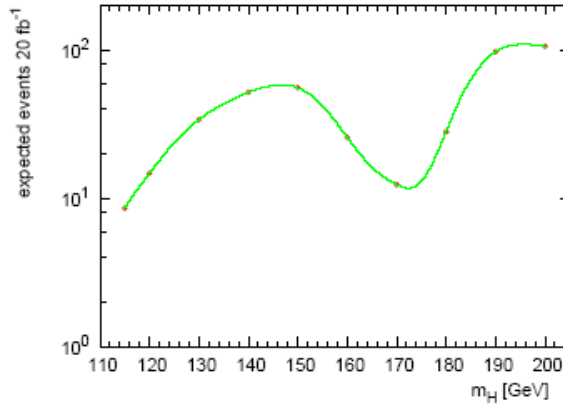


**Figure 4.1:** Expected number of signal events after one year of LHC running with an integrated luminosity of  $20 \text{ fb}^{-1}$

### 4.2.2 Z boson kinematics

One of the most important features of the signal events is the presence of two Z bosons in the intermediate state. In the mass region  $M_H < 2M_Z$  the Higgs boson will decay mainly into one real and one off-shell  $Z^3$ .

The fraction of events with both Z off-mass-shell is decreasing with increasing Higgs boson mass. There are about 40%, 26% and 20% of such events for Higgs boson masses of 120 GeV, 140 GeV and 160 GeV, respectively. This is illustrated in Fig. 4.2, where the mass distribution of the Z closest to the nominal Z boson mass, for three different Higgs boson masses, is shown. In Fig.4.2 and in the following Fig. 4.3 the number of events is rescaled in order to normalize to the same integrated luminosity ( $N_i = \mathcal{L}_{int} \cdot \sigma_i$ ).

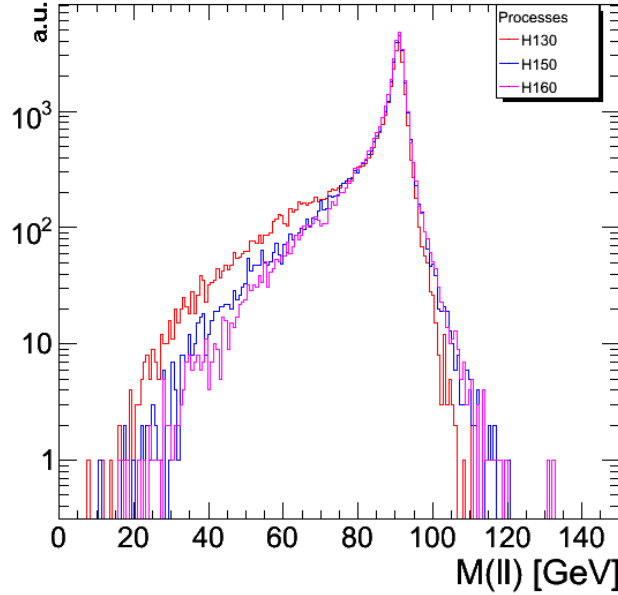


**Figure 4.2:** The mass distribution of the on-shell Z boson (the Z closer to the nominal Z boson mass) for three different Higgs masses.

In the following analysis the vector boson closest to the nominal Z mass  $\min|M(\ell\ell) - M_Z|$  is referred to as Z boson, and the other one as  $Z^*$ .

The  $Z^*$  mass distribution is shown in Fig. 4.3. A  $M_{Z^*}$  characteristic upper edge, at the position  $M_H - M_Z$  can be noticed, becoming more pronounced as the Higgs boson mass increases.

<sup>3</sup>A Z boson is considered off-shell if  $|M(\ell\ell) - M_Z| > 3\Gamma_Z$

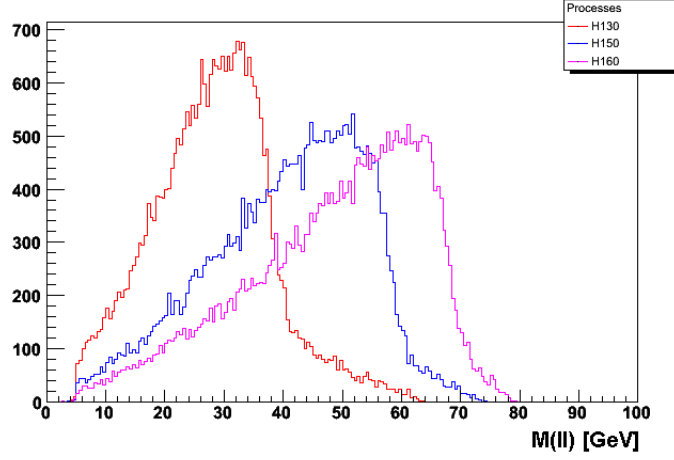


**Figure 4.3:** The mass distribution of the off-shell  $Z^*$  boson for three different Higgs masses.

In figure 4.4-*left* is shown the differential cross-section  $\sigma_c$ :

$$\sigma_c = \int_0^{M_Z - 3\Gamma_Z} \frac{d\sigma}{dM_{\ell\ell}} dM_{\ell\ell}$$

as a function of the Higgs mass, while in figure 4.4-*right* is shown the fraction of events with two off-shell  $Z$ , in function of the Higgs mass.

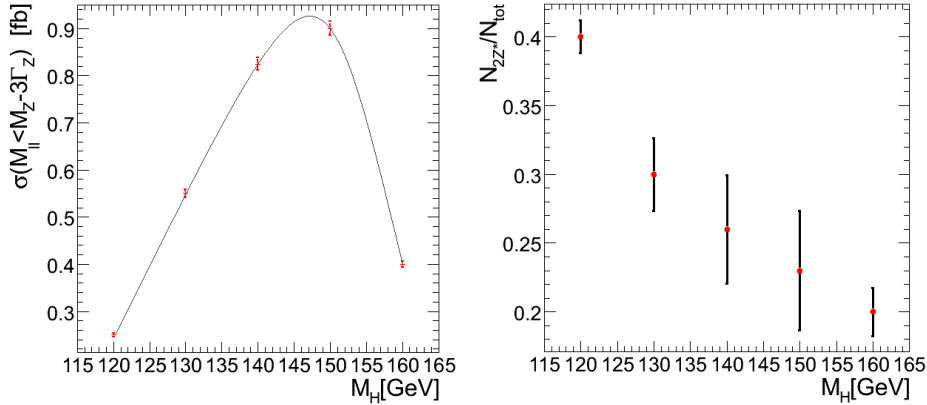


**Figure 4.4:** *Left:* Cross section for 2 off shell  $Z$  (see text) in function of  $M_H$ . *Right:* Fraction of events with two off-shell  $Z$

### 4.2.3 Lepton kinematics

A feature of the signal channel is the presence of four relatively isolated and high  $p_T$  leptons in the final state. This leptons' property is used to effectively reduce the backgrounds. As an illustration, in Fig. 4.5 the transverse momentum distributions of the four leptons from the  $Z$  and  $Z^*$  decays, sorted by decreasing  $p_T$ , for three values of the Higgs boson mass after the preselection cuts are shown. In order to better appreciate the difference in shape between the distributions, these are normalized to the unit area.

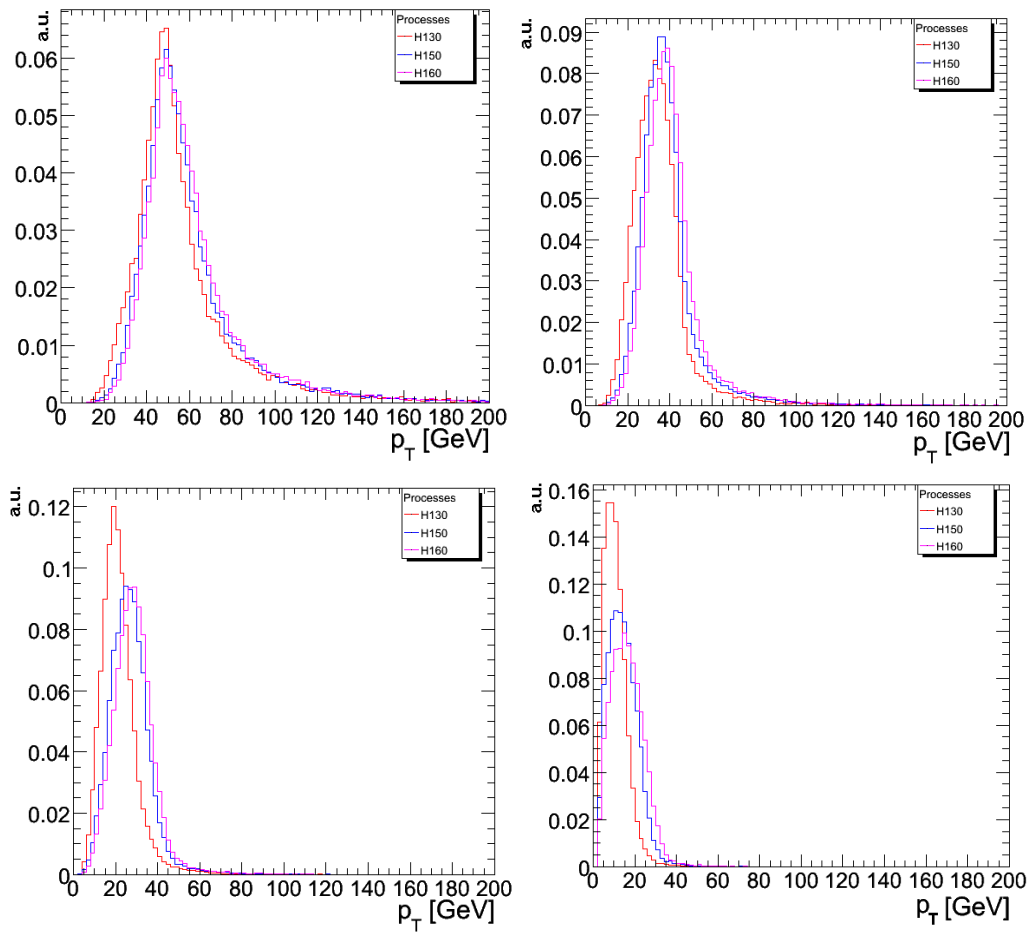


**Figure 4.5:** The  $p_T$  distributions of the four leptons in signal events for three different Higgs boson masses. In each event leptons are sorted according to  $p_T$  value. Distributions are normalized to unit area

The difference between the distributions for various Higgs boson masses becomes clear on the third and on the fourth lepton. From the distribution of

the softest lepton, which has a peak at about  $10 \text{ GeV}$  for  $M_H < 130 \text{ GeV}$ , it can be foreseen that the signal acceptance is very sensitive to the minimum  $p_T$  chosen. It has to be reminded that there is a minimal preselection on lepton transverse momenta in order to mimic detector acceptance. In this mass region, despite the higher cross section, the number of expected signal events is small due to the low branching ratio and it is very important to maximize the acceptance together with the reconstruction efficiency to optimize the low mass reach.

#### 4.2.4 Higgs production mechanism

The two main production processes involved in the creation of the Higgs Boson at the LHC will be the gluon-gluon fusion with Next-to-Leading (NLO) order cross-section  $\sigma_{NLO}(gg \rightarrow H) = 1.15 \text{ fb}$  and the vector boson fusion(VV-fusion) with NLO cross-section  $\sigma_{NLO}(VV \rightarrow H) = 0.33 \text{ fb}$ , whose leading order Feynman diagrams are shown in Fig. 4.6.

Since in the final state of the VV-fusion production process there are two forward jets, coming from the two quarks involved in the process, the kinematics of the two processes is different. Here is presented a brief study on the differences between some kinematical distributions of final state leptons, with the aim to determine whether it is possible to distinguish the two production mechanisms.

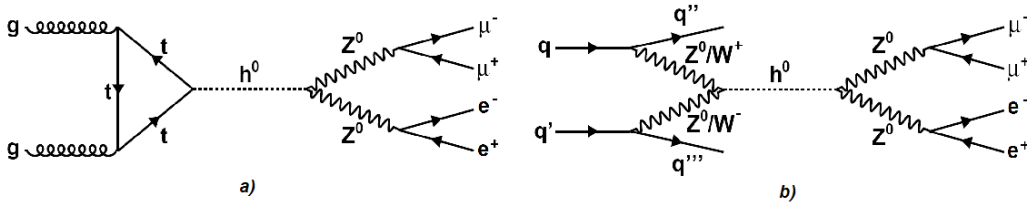


**Figure 4.6:** Leading order Feynman diagrams for gluon-gluon fusion and vector boson fusion.

In Fig. 4.7 are presented the transverse momentum spectra for the four final state leptons, divided by flavour and between the most and the least energetic one. The distributions are normalized to the same area in order to better appreciate the differences between the two processes considered.

As can be seen in the plots the distributions are quite different, mostly as far most energetic leptons are considered, and VV-fusion spectra are generally harder than gg-fusion correspondents.

In figure 4.8 are presented the transverse momentum for the reconstructed  $Z$ , (indistinctly from muons or electrons) and their pseudorapidity  $\eta$ .

As one can notice the reconstructed  $Z$  transverse momentum spectrum is harder for the VV-fusion process, and the pseudorapidity distribution shows that  $Z$ s are mostly produced at midrapidity for the VV-fusion, while there are two backward and forward peaks around  $|\eta| = 3$  in the gg-fusion process.

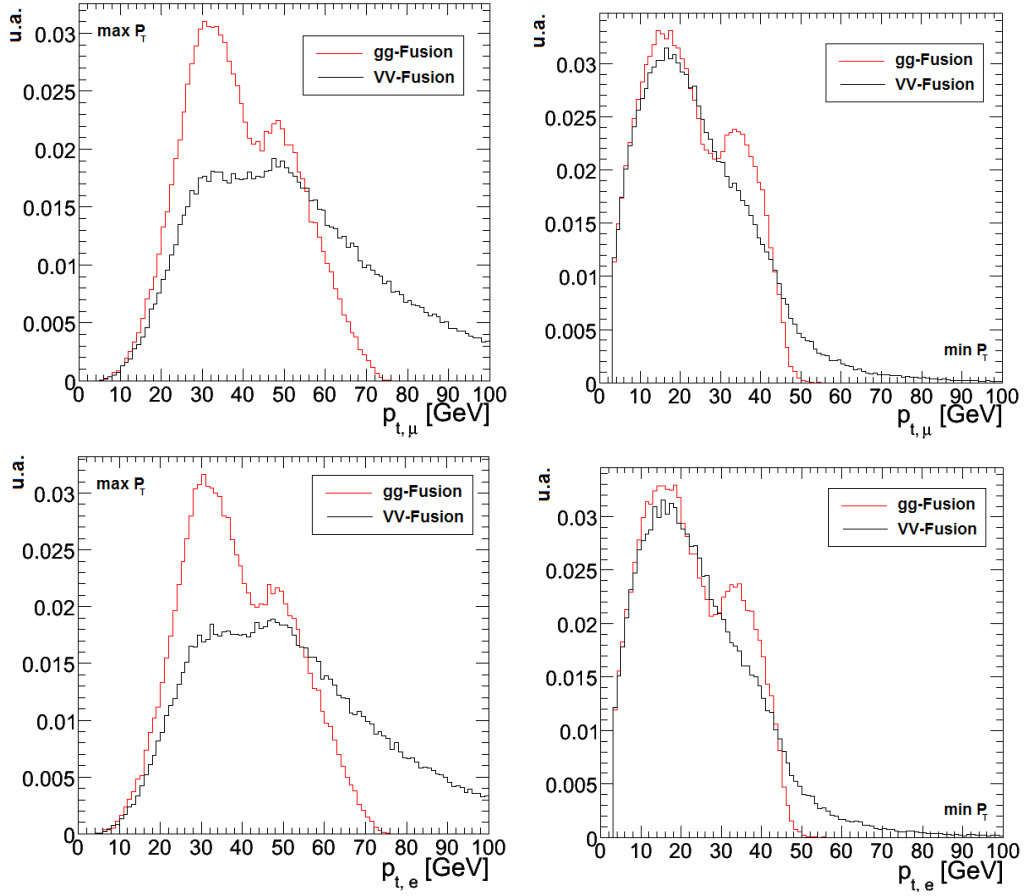


**Figure 4.7:** Transverse momentum distribution for final state leptons. *Top-Left:* leading muon  $p_T$ . *Top-Right:* softest muon  $p_T$ . *Bottom-Left:* leading electron  $p_T$ . *Bottom-Right:* softest electron  $p_T$

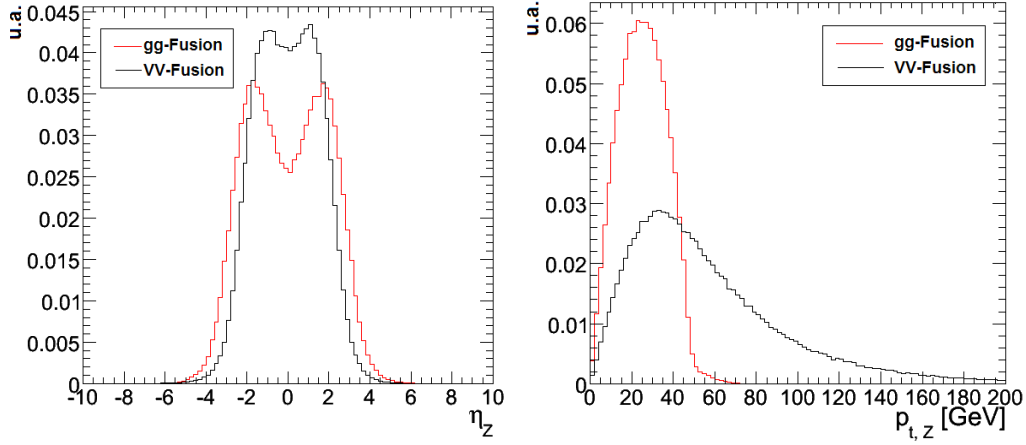


**Figure 4.8:** *Left* Pseudorapidity and (*right*) transverse momentum (right) of the reconstructed  $Z$

The invariant mass of each reconstructed  $Z$  is presented in Fig. 4.9, together with the pseudorapidity of the reconstructed Higgs, whose four-momentum has been defined as the sum of reconstructed  $Z$  four-momenta. The relative plots are presented in Fig. 4.9

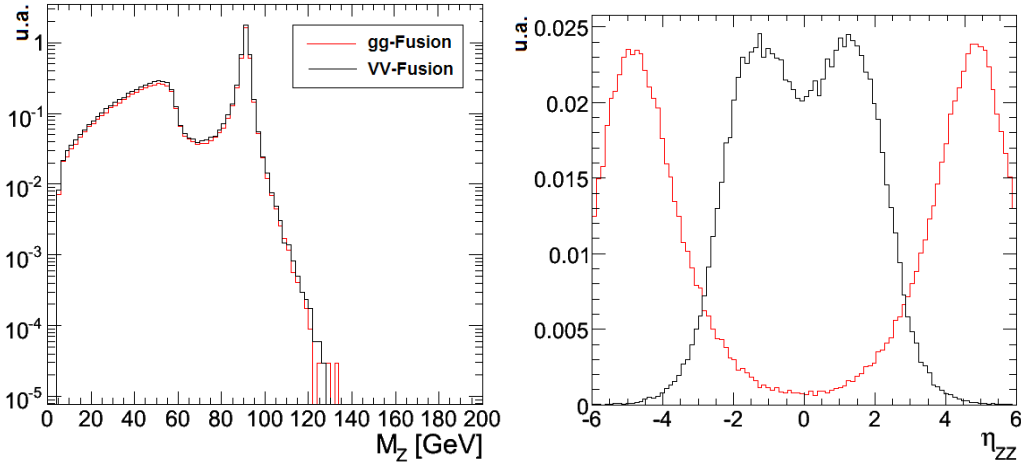


**Figure 4.9:** *Left:* Invariant mass of reconstructed  $Z$ . *Right:* Pseudorapidity of  $ZZ^*$  system

Finally some angular distributions are presented in Fig.4.10: the angle between two electrons from the same  $Z$ , the angle between the muon and

the electron with the largest transverse momentum, the angle between two like-sign leptons, and the angle between two reconstructed  $Z$ , all considered in the CMS reference frame.

In conclusion, there are some differences between the kinematic distributions of the four final state leptons, such that it could be possible to discriminate between the two production mechanisms. Anyway these differences are not so pronounced to justify a separate analysis between the gluon-gluon fusion and the vector boson fusion process. In the following when referring to the signal it is meant the incoherent sum of the two processes.

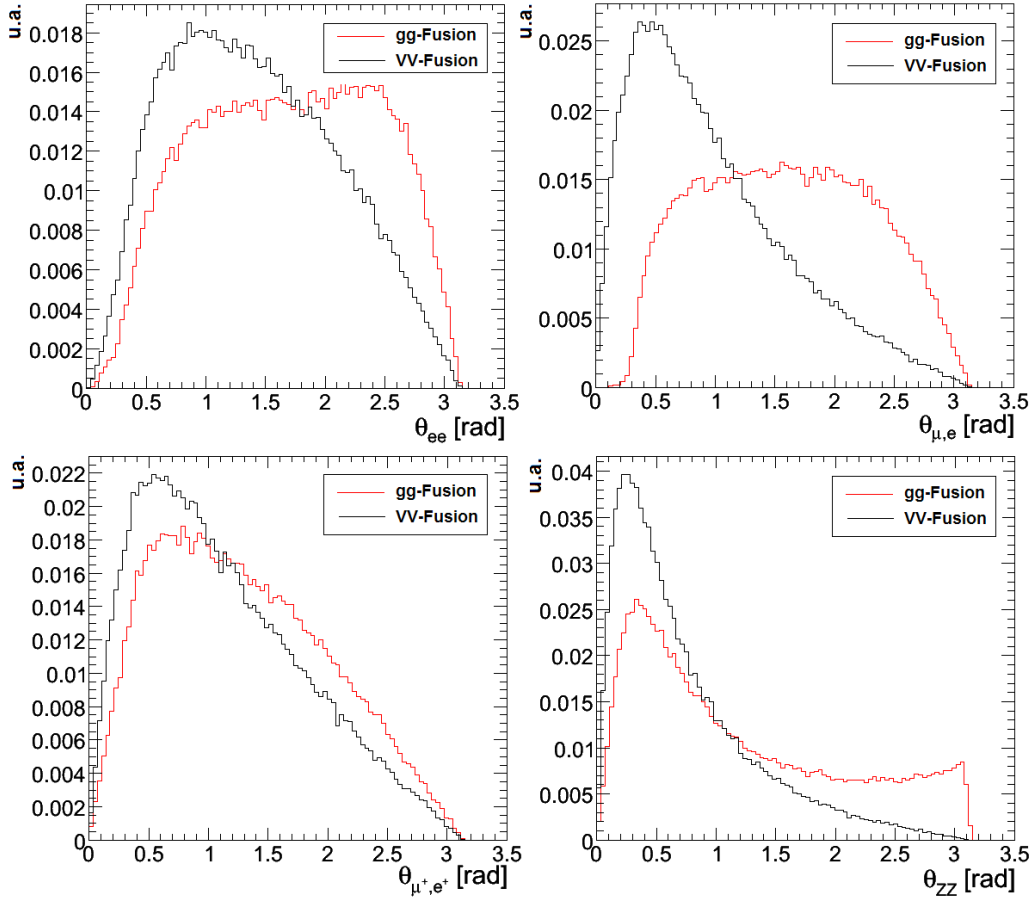


**Figure 4.10:** Top left: angle between two leptons from the same  $Z$ . Top right: angle between the highest  $p_T$  muon and the highest  $p_T$  electron. Bottom left: angle between two like-sign leptons. Bottom right: angle between the two reconstructed  $Z$

### Internal bremsstrahlung

Another feature of  $H \rightarrow 2\mu 2e$  channel is the radiation of photons in the Z decays, which is called *internal bremsstrahlung*. Photons are emitted by final state leptons as shown in Fig. 4.11.

From the experimental point of view these photons are difficult to find at the reconstruction level and thus can be lost.

This effect is investigated in order to evaluate possible consequences on the Higgs invariant mass measurement as events might indeed fall outside the mass peak if the internal bremsstrahlung photon is not properly reconstructed. Similar effects are irrelevant in background events, which exhibit a continuous spectrum for the invariant mass of the final state leptons.

The distribution of the angular distance ( $\Delta R = \sqrt{(\Delta\eta)^2 + (\Delta\phi)^2}$ ) between the emitted photon and the muon, as well as the photon  $p_T$  are shown in Fig. 4.12. Most of emitted photons have low energy ( $E_T < 1 \text{ GeV}$ ) but the fraction of events with highly energetic photons increases with the Higgs boson mass; for example it is respectively 18% and 37% with  $M_H = 130 \text{ GeV}$  and  $M_H = 500 \text{ GeV}$ . The mean angular distance between the photon and the muon ( $\langle \Delta R_{\mu\gamma} \rangle$ ) decreases instead monotonically from 0.57 when  $M_H = 130 \text{ GeV}$  to 0.27 at  $M_H = 500 \text{ GeV}$ . However, an important fraction of the photons are clearly separated from the leptons and have a non-negligible  $p_T$ . These photons can be important in improving the Higgs boson mass resolution especially at low mass.

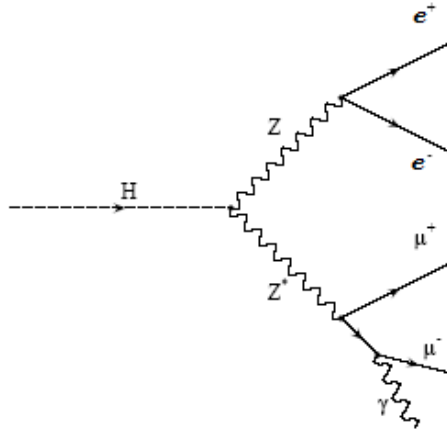


**Figure 4.11:** Feynman diagram showing the internal bremsstrahlung process.

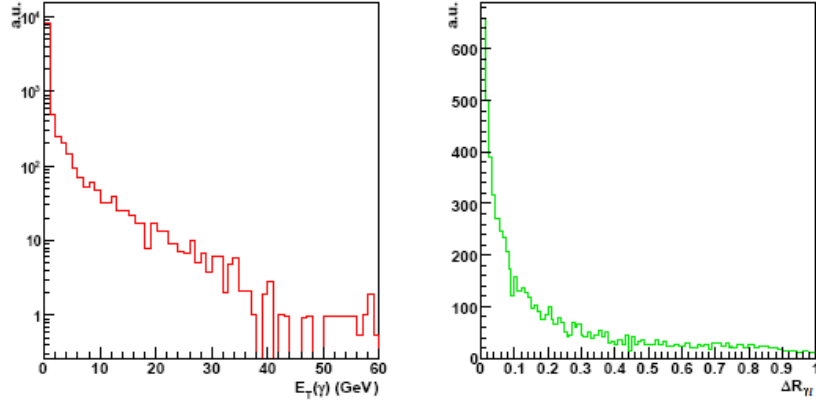


**Figure 4.12:** Transverse energy distribution of the final state radiation photons (left) and angular separation between the photon and the muon (right) in signal events for  $M_H = 150 \text{ GeV}$ .

The effect on the Higgs invariant mass resolution if the internal bremsstrahlung photon is not taken into account is shown in figure 4.13 for two Higgs boson masses:  $M_H = 120 \text{ GeV}$  and  $M_H = 150 \text{ GeV}$ . If the photon is not collected the effect is therefore not negligible. As can be seen these effect is rather independent on  $M_H$ .

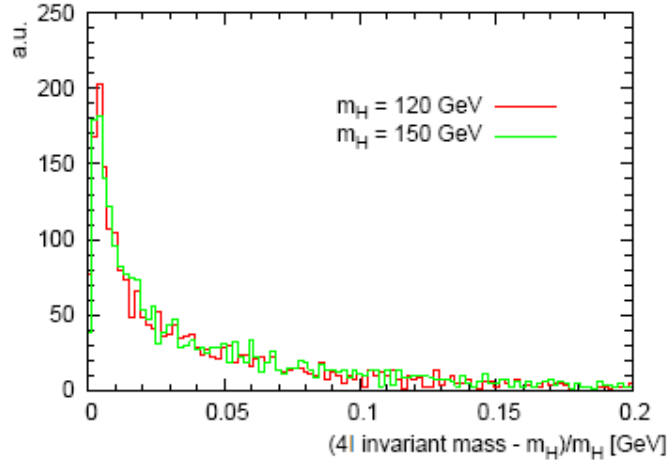


**Figure 4.13:** Effect on neglecting internal bremsstrahlung photons in the invariant mass computation: on the abscissa the normalized difference between the four leptons invariant mass computed with and without considering photons in the final state

### 4.2.5 Backgrounds

As already mentioned, the sources of background for the  $H \rightarrow ZZ^* \rightarrow 2\mu 2e$  channel are events with four high  $p_T$  leptons in the final state, mainly coming from  $ZZ^*$ ,  $Zb\bar{b}$ , and  $t\bar{t}$ . Other sources of backgrounds, consisting of events where jets can be misidentified as electrons (namely  $Z$ +jets events) can be reduced to a negligible level by adopting standard selections strategies [?].

There are two basic classes of background processes, called *reducible* and *irreducible* backgrounds. The reducible backgrounds have very pronounced kinematical and topological differences with respect to the signal, both in the final states as well as in the two and four leptons combinatorics. Therefore by applying appropriate kinematical and topological cuts, these backgrounds can be effectively suppressed. The largest reducible background processes are  $t\bar{t} \rightarrow W^+W^-b\bar{b} \rightarrow 2\mu 2e$  and  $Zb\bar{b} \rightarrow 2\mu 2e$ .

The only irreducible background is  $ZZ^*/\gamma^* \rightarrow 2\mu 2e$ , with final and intermediate state kinematics when compared similar to signal events. Nevertheless, adjusting properly the kinematical cuts and using some additional cuts, like the four-leptons overall transverse momentum, this background can also be suppressed to some extent.

#### Reducible background: $t\bar{t}$

The two main processes for  $t\bar{t}$  production in the  $p-p$  interactions are gluon fusion and quark annihilation (Fig. 4.15). The corresponding cross-section at the LHC for different choices of the renormalization scale and of the parton density function (*PDFs*) is shown in figure 4.14. The best current estimate for the cross-section is  $840^{+52}_{-39} pb$  with 5% of uncertainties coming from the scale and 3% from the *PDFs*.

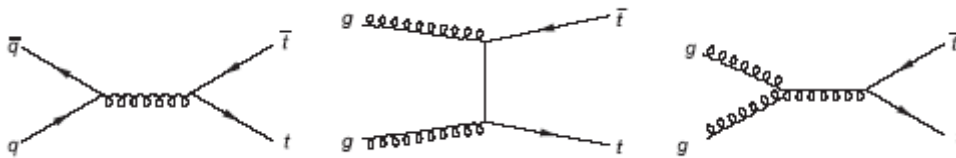


**Figure 4.14:** Leading order Feynman diagrams for the  $t\bar{t}$  production in hadronic collisions

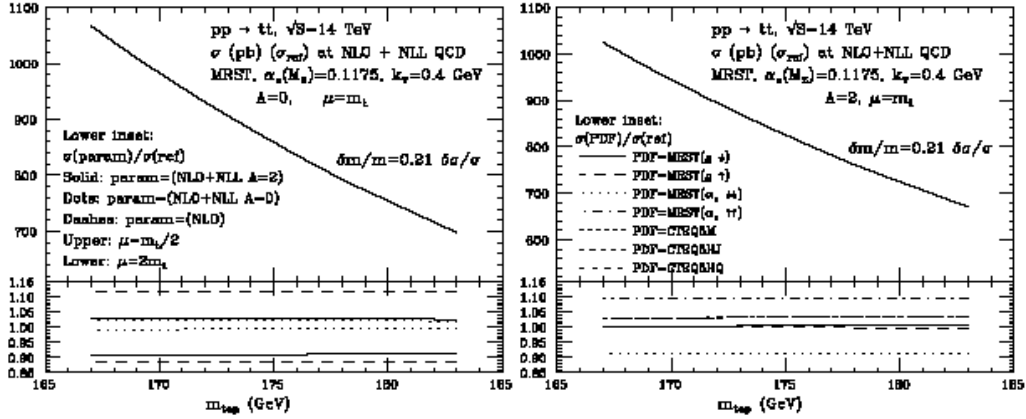


Figure 4.15:  $t\bar{t}$  production rates. *Left*: scale dependence at fixed order (NLO, dashed line in lower insert), and NLO+NLL (solid lines). *Right*: PDF dependence

Sources of leptons in the final state are the two top quark decay chains (Fig. 5.5). The decay process  $t \rightarrow Wb$  has a branching ratio of 99.8%; final state leptons arise from the semileptonic decays of the bottom quark and from the  $W$ , via direct decay  $W \rightarrow \ell\nu_\ell$  or  $W \rightarrow \tau\bar{\nu}_\tau \rightarrow \ell\nu_\ell\nu_\tau\bar{\nu}_\tau$ . Semileptonic decays of mesons produced in  $W \rightarrow hadrons$  give a negligible contribution to events with four high- $p_T$  leptons in the final state. The typical decay chain is schematically shown in Fig. 4.16.

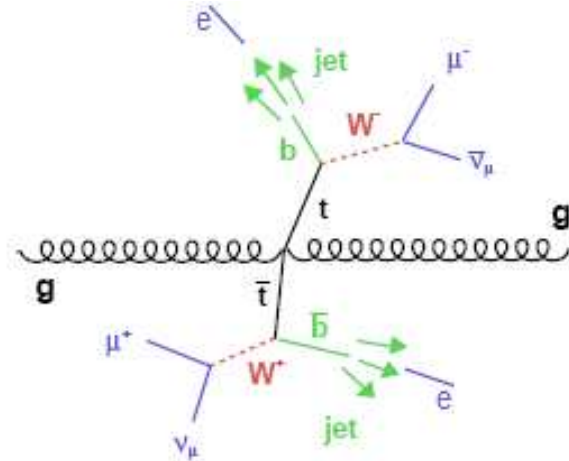
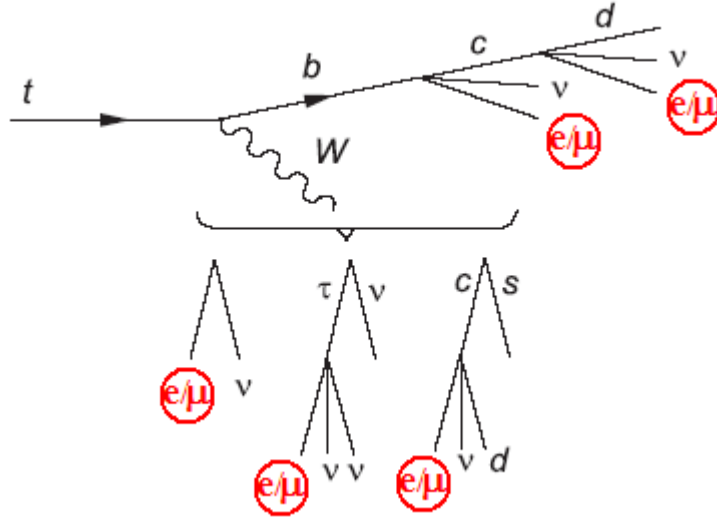


Figure 4.16: Typical decay chain of a  $t\bar{t}$  pair. Two leptons come from the  $W$  bosons decays, the other two come from the  $b$ -jet hadronization.

Anyhow at least two out of the four leptons belong to a hadronic jet and they are not isolated. The most probable scenario is given by two leptons produced directly from the  $W$  decays and the other two produced in the  $b$  semileptonic decay.

Total cross-section, branching ratios and pre-selection efficiency for this process are reported in table 4.2. The comparison of the values between the signal and the other background sources show that this channel is the largest source for a final state with two muons and two electrons, and its "visible" cross-section is around a factor  $\sim 100$  greater than the signal one. For the analysis, this number gives the order of magnitude of the rejection power needed to enhance the signal to  $t\bar{t}$  background ratio.



**Figure 4.17:** Sources of final state muons/electrons in the top quark decay chain

The sample of  $t\bar{t}$  have been generated with PYTHIA 6.227. The  $7 \cdot 10^5$   $t\bar{t}$  events have been produced with no requirements on the  $b$ -quark decay, but by imposing that the  $W$  boson decays leptonically. The events were generated with the same preselection cuts ( $|\eta_\mu| < 2.5$ ,  $p_T^\mu > 3.0$   $GeV$ ,  $|\eta_e| < 2.7$ ,  $p_T^e > 10.0$   $GeV$  and  $5 < M(\ell\ell) < 150$   $GeV$  as the Higgs boson sample. The  $W$  bosons are forced to decay into leptons while while all the decays of the  $b$  quark are allowed, but eventually only events with two muons and two electrons in the final state are selected. The generation of those events is very CPU time consuming being the acceptance of the preselection cuts only

1%.

In Fig. 4.18 the  $p_T$  of the four leptons is shown. These distributions and all the following, if not otherwise specified are normalized to unit area. The soft spectra of the third and fourth lepton explain the low acceptance of the generation cut and show the high rejection power of a  $p_T$  cut.

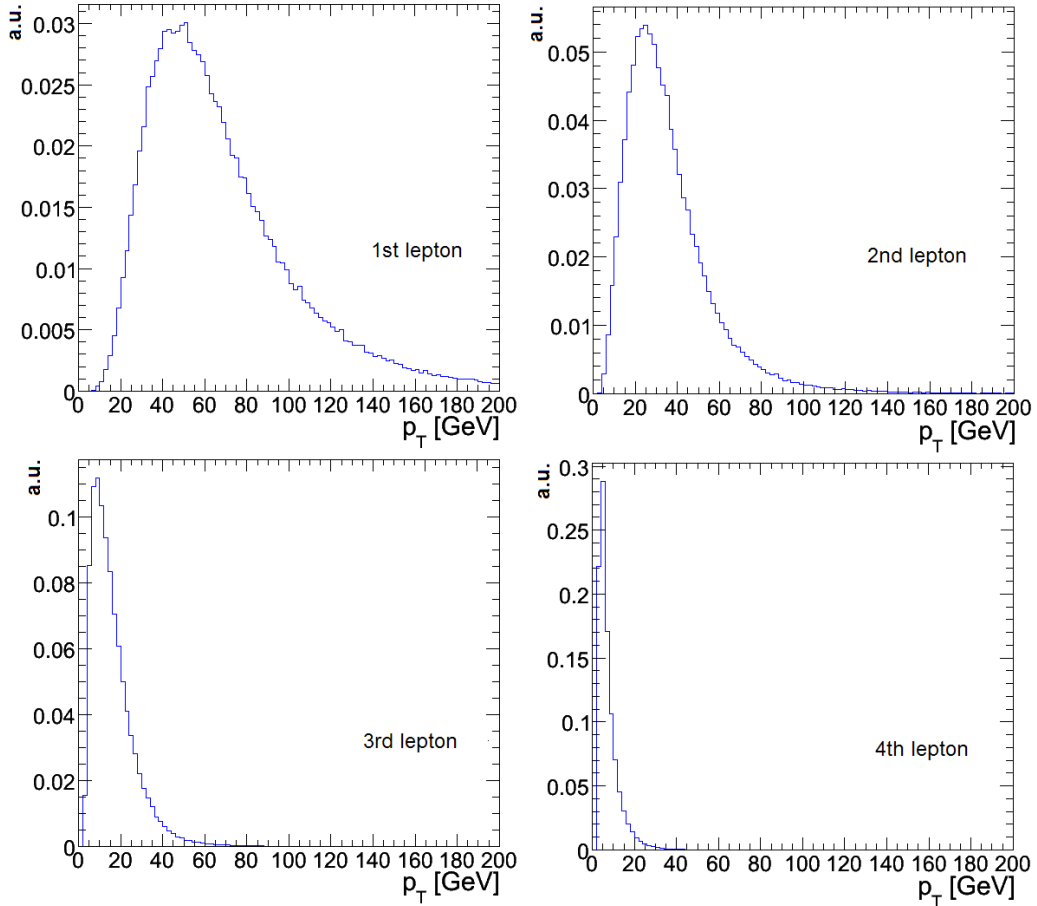


**Figure 4.18:**  $p_T$  distribution of the four leptons in  $t\bar{t}$  events. The muons are sorted by decreasing  $p_T$ .

Some interesting dilepton and four-lepton distributions are shown in Fig. 4.19 and 4.20. The first lepton pair is chosen as the one with the invariant mass closest to the nominal  $Z$  mass ( $\min|M(\ell\ell) - M_Z|$ ). From the two lepton invariant mass distribution the power of a  $Z$  mass cut is evident (requesting one  $\ell^+\ell^-$  pair to have an invariant mass compatible with the  $Z$  mass). Moreover, it is interesting to note a low mass peak in the second two-lepton

invariant mass distribution which is due to leptons originating from the same cascade. This peak will be effectively suppressed by a lower  $Z^*$  mass cut.

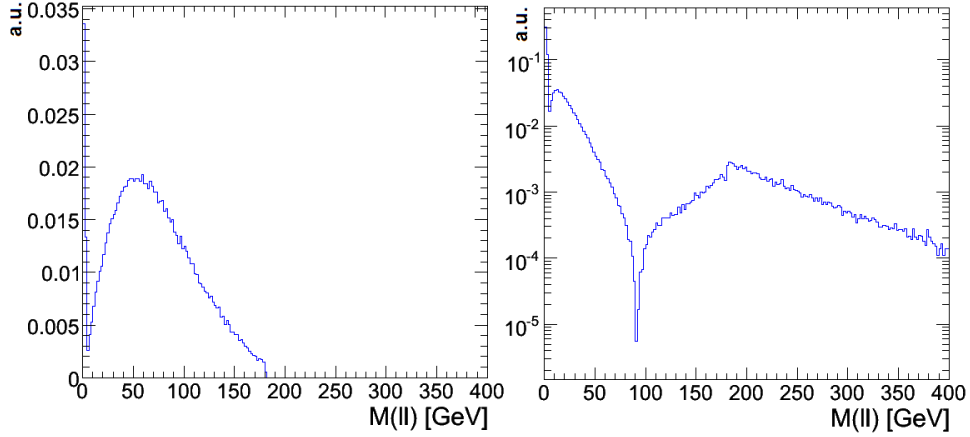


**Figure 4.19:** Invariant mass distributions of the two  $\ell^+\ell^-$  pairs in  $t\bar{t}$  background. The first lepton pair (left) is chosen as the one with the invariant mass closest to the nominal Z mass. The invariant mass of the remaining leptons is shown on the right

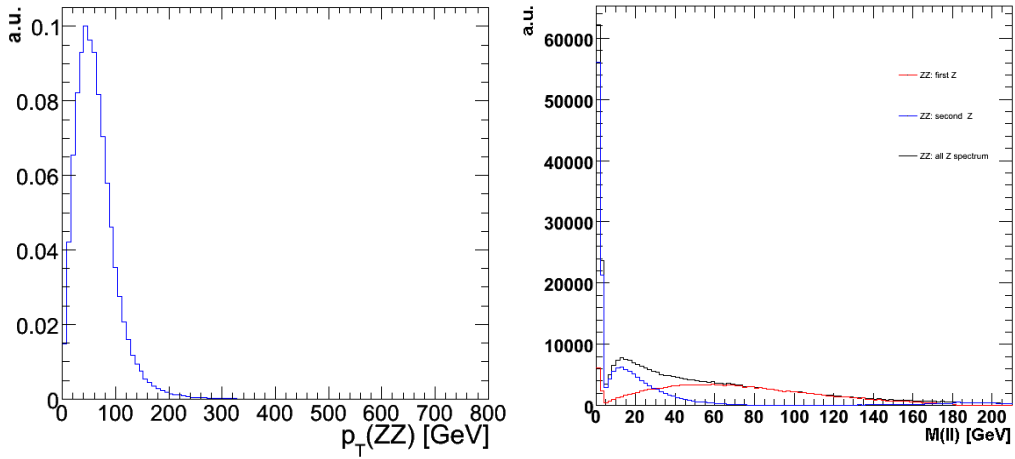


**Figure 4.20:** *Left:* Invariant mass distribution of the four leptons coming from  $t\bar{t}$  events. *Right:* Comparison between first and second candidate Z spectra

### Reducible background: $Zb\bar{b}$

The second source of reducible background consists in the  $Zjj$  production. In most of the cases, two leptons come from the  $Z$  decay while the other two originate from cascade decays of hadrons produced in the quark hadronization.

The presence of a real  $Z$  boson makes this background insensitive to a  $Z$  mass cut, unlike the  $t\bar{t}$  background. This background has also the distinctive feature of the presence of two non-isolated leptons, coming from the  $q$ -hadron cascade decays.

Particularly important is the case in which the  $Z$  boson is produced in association with two  $b$  quarks. The leading order diagrams corresponding to the two possible initial states producing  $Zb\bar{b}$  ( $q\bar{q}$  and  $gg$ ) are shown in figure 4.22.

The total cross section, about  $650 \text{ pb}$ , has been calculated using the CompHep Monte Carlo generator at LO.

The production of the  $4 \cdot 10^5$  hard scattering has been performed with CompHEP at partonic level, since PYTHIA is not adequate to produce this kind of background

As a matter of fact PYTHIA produces such final states starting from  $q\bar{q} \rightarrow Zg$  and  $gq \rightarrow Zq$ , then it generates additional  $b$  quarks with the parton showering. This approach significantly underestimates the final rates after selection cuts, since the quarks generated by the parton shower evolution have a softer spectrum than those generated using exact matrix elements. Then for the events generation, the CompHEP code has been used. In CompHEP the matrix elements of the  $Zb\bar{b}$  are calculated exactly at leading order.

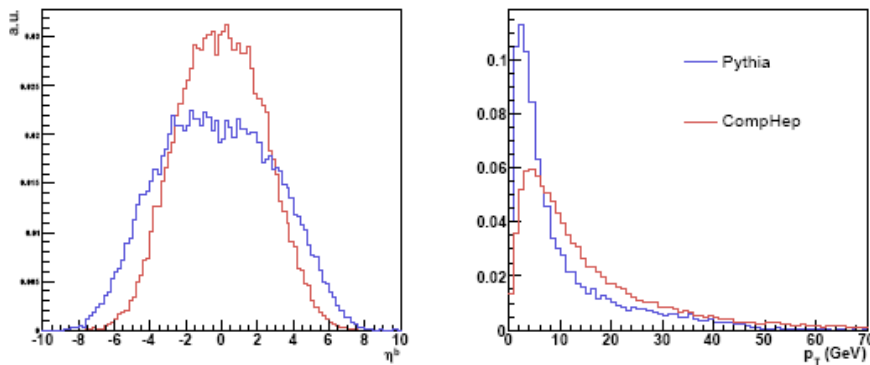


**Figure 4.21:** Comparison of the  $\eta$  (left) and  $p_T$  (right) distributions of the  $b$  quarks in  $Zb\bar{b}$  events generated by PYTHIA and CompHEP, distributions are normalized to the same integrated luminosity.

The  $p_T$  and  $\eta$  distributions of the  $b$  quarks generated by PYTHIA and CompHEP are shown in Fig. 4.21. Distributions are normalized to the same integrated luminosity: the softer  $p_T$  spectrum of the  $b$  quark produced by PYTHIA is evident.

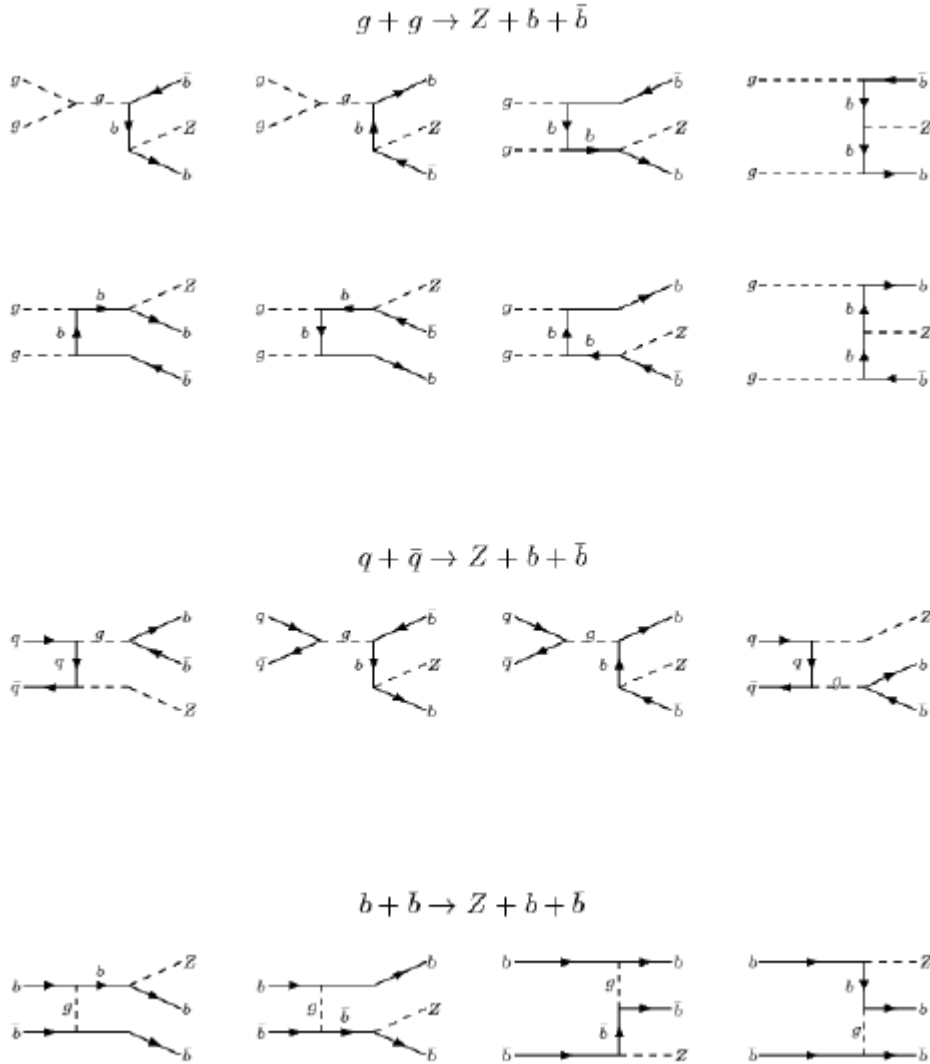


**Figure 4.22:** Leading order diagrams corresponding to the possible initial states producing  $Zb\bar{b}$

The partonic events generated by CompHEP are then passed through PYTHIA for the hadronization and the initial and final state parton showers genera-

tion. The Z boson is forced to decay into a couple of leptons while b-hadrons semileptonic decays are not forced to avoid biasing the sample. Furthermore the same preselection cut as above has been imposed demanding  $|\eta_\mu| < 2.5$ ,  $p_T^\mu > 3.0 \text{ GeV}$ ,  $|\eta_e| < 2.7$ ,  $p_T^e > 10.0 \text{ GeV}$  and  $5 < M_Z < 150 \text{ GeV}$ . The acceptance to these preselection cuts is  $\sim 0.02\%$ .

The invariant mass distributions of the two leptons pairs are shown in Fig. 4.23. The interesting property of the invariant mass distribution is a broad mass peak of the lighter di-lepton combination (leptons coming from the same cascade), which will allow a considerable reduction of this background.

The production of the  $4 \cdot 10^5$  events has dealt also with the case of a virtual Z boson and two b quarks, with a limit on the  $Z^*$  invariant mass as well as on the invariant mass of the  $b\bar{b}$  pair of  $5 \text{ GeV}$ . In this sense the background could be seen as  $\ell^+\ell^-b\bar{b}$  (and the cross-section reported in the following is after the requirements on the invariant masses of the lepton and b pairs).

The corresponding values for cross-section and branching ratio are reported in table 4.2.

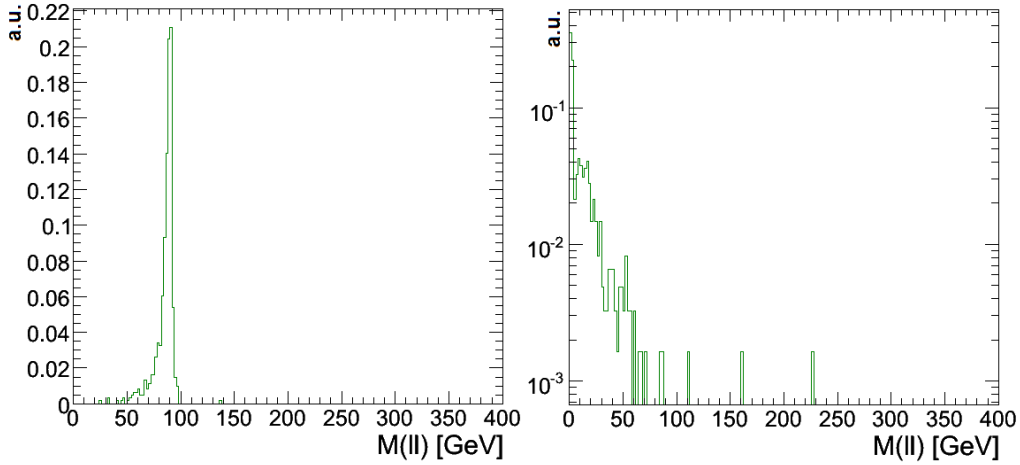


**Figure 4.23:** Invariant mass distribution of the the two  $\ell^+\ell^-$  pairs in  $Zb\bar{b}$  events. *Left:* Invariant mass of the best Z candidate. *Right:* invariant mass of the remaining two leptons

In Fig. 4.24 the four leptons mass distribution is shown. It clearly has a shape similar to that of the  $t\bar{t}$  background.

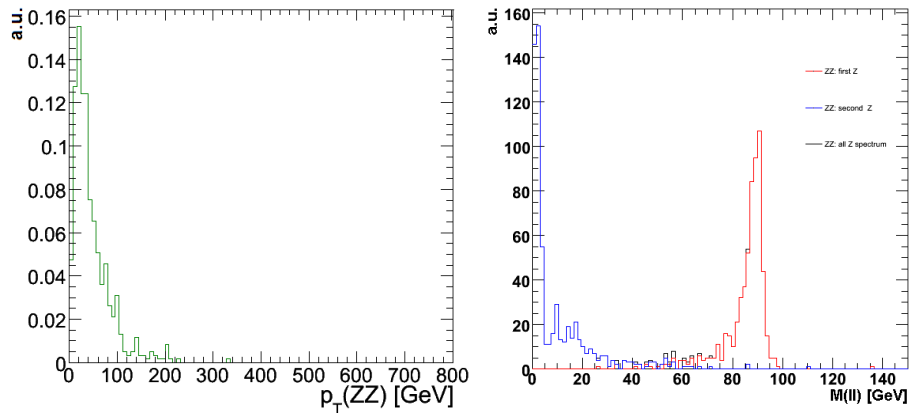


**Figure 4.24:** *Left* Invariant mass distribution of the four leptons coming from the  $Zb\bar{b}$  events. *Right* invariant mass of the two reconstructed "Z".

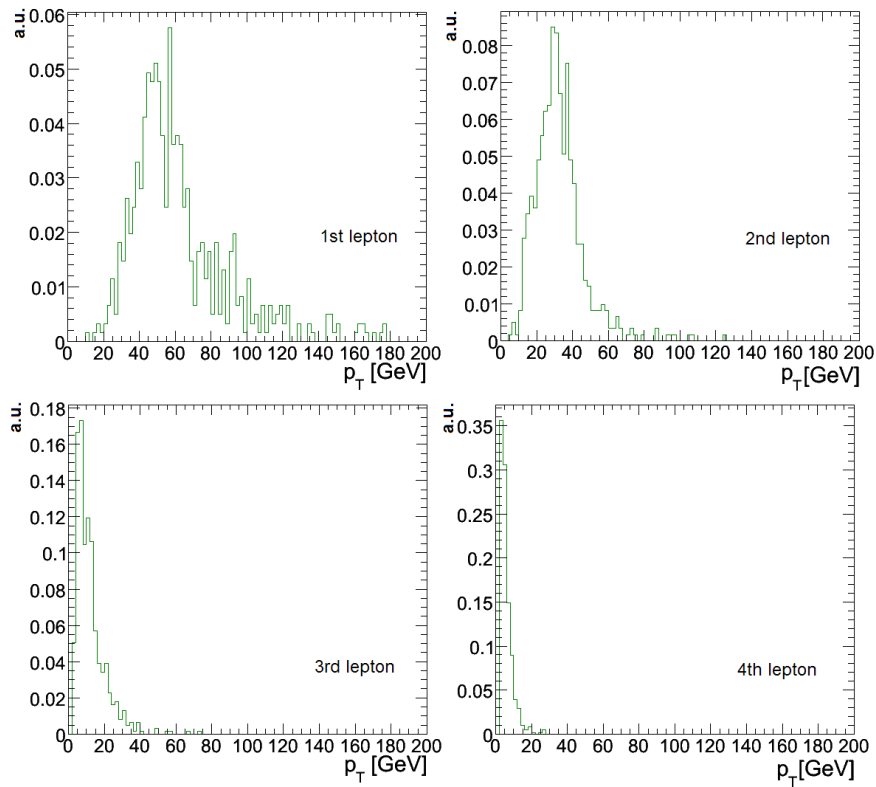


**Figure 4.25:**  $p_T$  distribution of the four leptons in  $Zb\bar{b}$  events. The muons are sorted by decreasing  $p_T$ .

The transverse momentum distribution of the four leptons, sorted in decreasing order, is given in Fig. 4.25. In comparison with the signal and the other backgrounds, a softer distribution of the two lightest lepton can be noticed, making this background particularly sensitive to this kinematical cut.

### Irreducible background : $ZZ^*/\gamma^*$

The leading order process for gauge bosons pair production in hadronic interactions at LHC is the  $q\bar{q}$  annihilation, shown in Fig. 4.26(a). An additional contribution, corresponding to 20% of the  $q\bar{q} \rightarrow ZZ^*$  process, comes from  $gg \rightarrow ZZ^*$  (Fig.4.26(b)). Indeed, the lower amplitude of the  $gg \rightarrow ZZ^*$  process, which is an higher order process in  $\alpha_S$  since it involves a quark box diagram, is balanced by the higher gluon luminosity with respect to the quark-antiquark at small values of  $x$ . NLO calculations are available only for the first process and predict a correction ( $K$  factor) of 1.33. The total production cross-section, branching ratio and preselection efficiency are reported in table 4.2.

The  $q\bar{q} \rightarrow ZZ^*$  cross section has been evaluated with the Monte Carlo generator MCFM, which performs the calculation in next-to-leading order in  $\alpha_S$ . The expected cross section has been calculated using CTEQ6m as parton distribution function set and the factorization and renormalization scales  $\mu$  are set equal to the average of the produced vector boson masses. The cross section results to be

$$\sigma_{LO}(ZZ) = 10.7 \text{ pb}, \quad \sigma_{NLO}(ZZ) = 15.3 \text{ pb}. \quad (4.4)$$

The uncertainty due to the PDFs is around 6%.

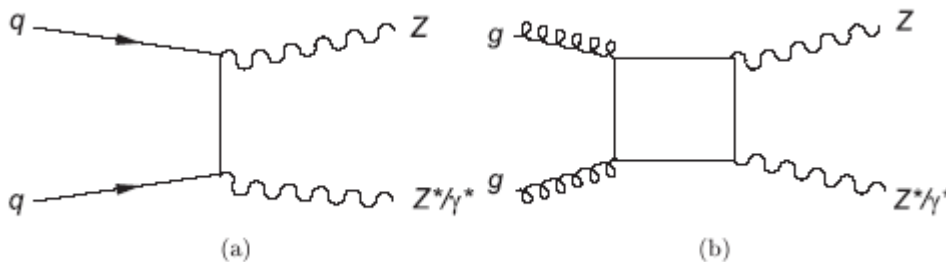


**Figure 4.26:** Leading order processes for the  $t$ -channel  $ZZ^*$  production in hadronic collisions

For this theses events were generated with PYTHIA 6.227, which only accounts for the  $q\bar{q}$  annihilation. The number of expected events was be re-scaled to the total cross-section, including the  $gg$  fusion process. This implies some systematic uncertainty, which is related to the kinematical difference between the two production processes.

The  $2 \cdot 10^5$  events were generated with PYTHIA, with the same preselection cuts ( $|\eta_\mu| < 2.5$ ,  $p_T^\mu > 3.0 \text{ GeV}$ ,  $|\eta_e| < 2.7$ ,  $p_T^e > 10 \text{ GeV}$  and  $5 < M_Z < 150 \text{ GeV}$ ) as the Higgs boson sample. In those events the Z bosons are allowed to decay only into a pair of leptons. Then only the events with two muons and two electrons in the final state are selected. The acceptance to these generation cuts is  $3.97\% \pm 0.01$ .

As an illustration of the PYTHIA generated Z's kinematics, in Fig.?? the invariant mass distributions of the Z and  $Z^*$  bosons are shown. The  $p_T(ZZ^{(*)})$  and the invariant mass  $M(ZZ^*)$  distributions are shown in Fig.4.28.

The  $p_T$  distributions of the four leptons from the Z decays are shown in Fig.4.29, sorted in decreasing order of  $p_T$ . The distribution stops at about  $50 \text{ GeV}$ , giving a potentially high rejection power by increasing the threshold.

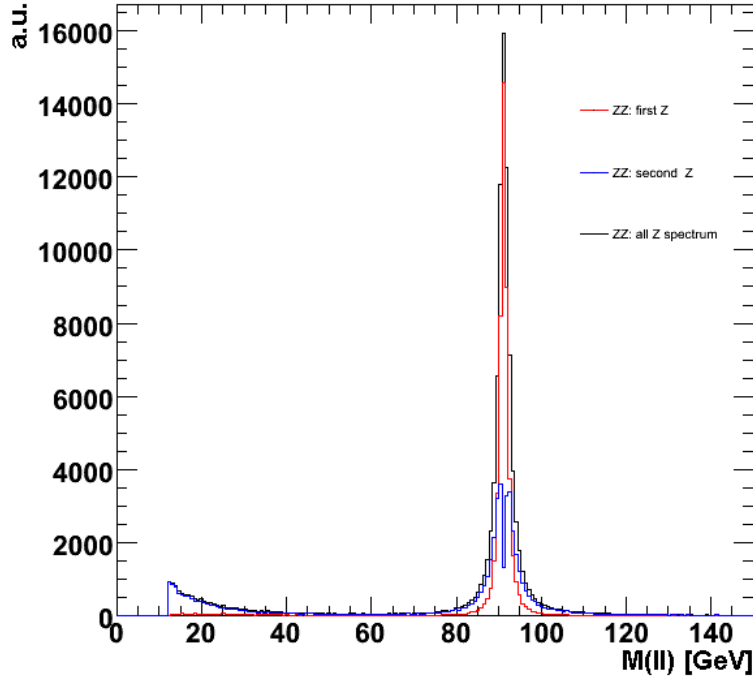


**Figure 4.27:** The Z and  $Z^{(*)}$  boson mass distribution as produced by PYTHIA.

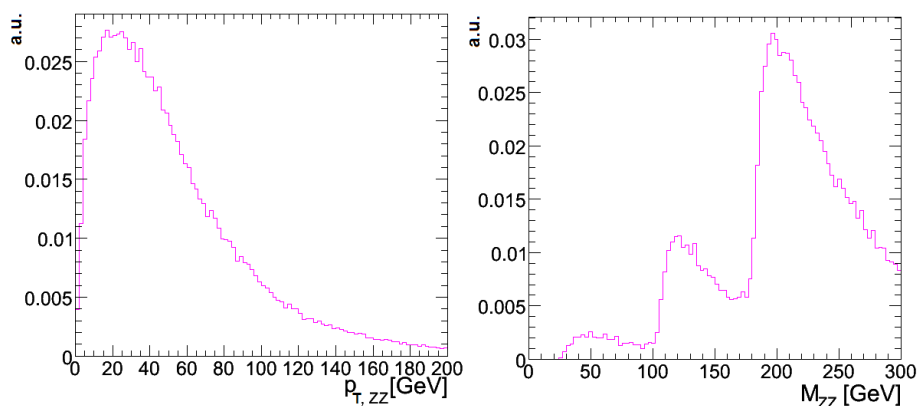


**Figure 4.28:** Transverse momentum (left) and invariant mass distribution (right) of the  $ZZ^{(*)}$  system.

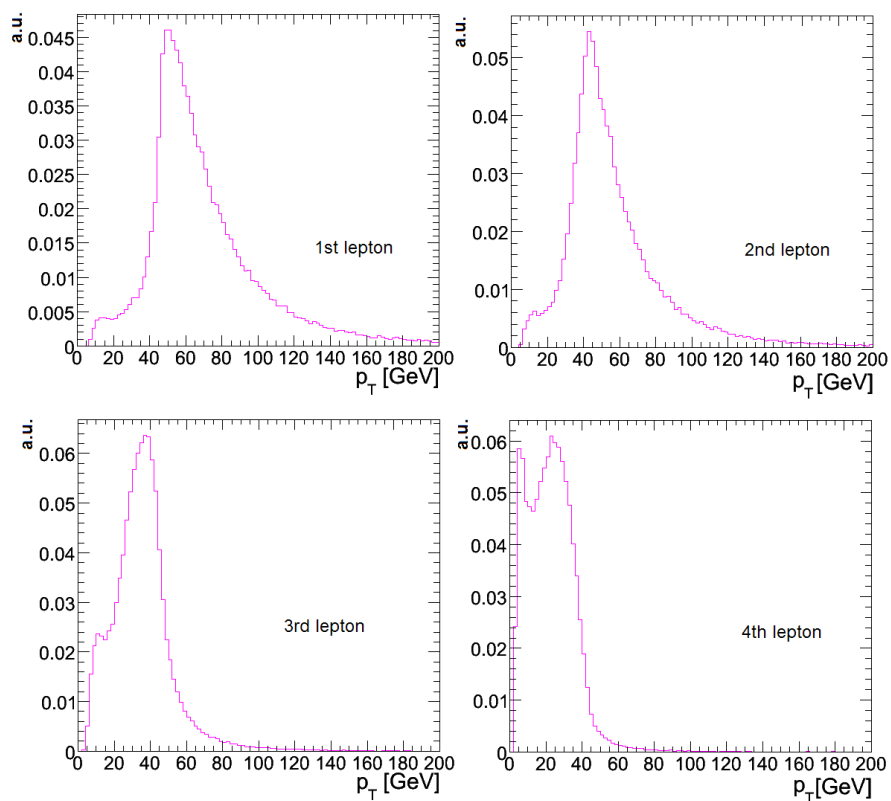


**Figure 4.29:** The  $p_T$  distributions of the four leptons in  $ZZ^*$  events. In each event leptons are sorted according to  $p_T$  value.

**Table 4.2:** Cross-section, branching ratio and preselection efficiency for the different backgrounds. A mass of 175 GeV for the top quark has been assumed

Background	$\sigma_{NLO}$ [pb]	B.R.	$\epsilon_{kin}$	$\sigma_{NLO} \times \text{B.R.}$ [fb]	$\sigma_{NLO} \times$ $\text{B.R.} \times \epsilon_{kin}$ [fb]
$ZZ^*$	35.1	$1.13 \cdot 10^{-3}$	$0.397 \pm 0.001$	39.6	15.72
$t\bar{t}$	840	$6.31 \cdot 10^{-2}$	$(0.9 \pm 0.03) \cdot 10^{-2}$	$56 \cdot 10^3$	504
$Zb\bar{b}$	115.1	1	$(0.2 \pm 0.02) \cdot 10^{-2}$	115.1	0.23

A summary of the cross section, preselection cut and B.R. for the backgrounds described above is reported in Tab. 4.2.

The expected number of events in the first year of data-taking at LHC (low-luminosity regime  $\mathcal{L} = 2 \cdot 10^{33} \text{cm}^{-2} \text{s}^{-1}$ ) is given by:

$$N_{events} = \mathcal{L}_{int} \times \sigma_{acc} \quad (4.5)$$

where:

$$\mathcal{L}_{int} = \int \mathcal{L}(t) dt = 20 \text{fb}^{-1}$$

and:

$$\sigma_{acc} = \int \sigma(\theta, \phi)_{pp \rightarrow X}^{NLO} \times \text{B.R.}(X \rightarrow e^+ e^- \mu^+ \mu^-) \times \epsilon_{kin} \times \mathcal{A}(\theta, \phi) d\Omega$$

where  $\sigma_{pp \rightarrow X(s/b_i)}^{NLO}$  is the Next-to-Leading Order cross section of the process  $pp \rightarrow X(s/b_i)$  ( $s$ =signal,  $b_i$  = backgrounds),  $\text{B.R.}$  is the branching ratio in the final state with two muons and two electrons,  $\mathcal{A}$  is the detector geometrical acceptance and  $\epsilon_{kin}$  the pre-selection efficiency.

## 4.3 Study of the kinematics of $H \rightarrow ZZ^* \rightarrow 2\mu 2e$

### 4.3.1 $Z$ boson reconstruction algorithm

For the channel under study, it is essential to be able to reconstruct the intermediate  $Z$  bosons and their properties from the particles in the final state. The first step is thus to define a criterion to select the lepton pairs coming from the same  $Z$ . This task is necessary not only for a final state with four leptons of the same flavour, but also for the  $H \rightarrow 2\mu 2e$  channel: as the final state almost always contains additional muons and/or electrons, due to the decay of particles generated in the hadronization of beam remnants. Moreover, the detector will introduce further sources of ambiguity as  $e/\mu$  misidentifications, photon conversions to  $e^+e^-$  pairs.

The variable which showed the most efficient selection of correct pair is the difference between the two-lepton invariant mass and the  $Z$  boson nominal mass,  $M_Z = 91.1876 \text{ GeV}$ :

$$\Delta_M = M(\ell^+\ell^-) - M_Z$$

where:

$$M(\ell^+\ell^-) \simeq 2\sqrt{p_+^\mu p_-^\mu} = 2\sqrt{E_+E_- - \mathbf{p}_+\mathbf{p}_-}.$$

As this study deals with a low mass Higgs, the two  $Z$ 's produced by its decay are not expected to have both masses near to  $M_Z$ . Therefore, the pairs selection algorithm consists the following steps:

1. all the possible same flavour of opposite-sign lepton pairs are formed and their invariant mass is computed;
2. these pairs are sorted by  $\Delta M$ ;
3. the pair with the lowest  $\Delta M$  is chosen as best candidate  $Z$ .
4. the other  $Z$  is formed pairing the 2 highest  $p_T$  lepton with different flavour from those of the best candidate.

This method has been tested for both  $4\mu$  and  $2\mu 2e$  final states, for signal samples ( $M_H = 150 \text{ GeV}$ ) and for  $ZZ^*$  background. To quantify its performance, two efficiencies have been defined:

$$\varepsilon_Z = \frac{\# \text{ identified } Z's}{\# \text{ generated } Z's}, \quad \varepsilon_{evt} = \frac{\# \text{ events with 2 identified } Z's}{\# \text{ generated events}}.$$

$\epsilon_Z$  is thus the fraction of  $Z$  bosons correctly identified (i.e. *selected pairs* that match *true Z's*) and  $\epsilon_{evt}$  is the fraction of events with both  $Z$ 's correctly identified. Results obtained in the signal sample for  $M_H = 150\text{GeV}$  are reported in tab. 4.3 (for  $ZZ^*$  identical values have been obtained).

	$\epsilon_{4\mu}$	$\epsilon_{2\mu 2e}$	$\sigma_\epsilon$
$\epsilon_Z$	0.970	0.980	0.001
$\epsilon_{evt}$	0.960	0.970	0.001

**Table 4.3:**  $Z$  selection algorithm efficiencies.

Considering that the four momenta of the leptons are those at generator level, the main inefficiency cause has been found to be the emission of high energy photons from the final state leptons.

The efficiency statistical errors have been calculated using the binomial distribution:

$$\sigma_\epsilon = \sqrt{\frac{\epsilon(1-\epsilon)}{N_{gen}}}$$

One can check if there is correlation between the two efficiencies and if it differs between the two considered channels. In principle if there is no correlations the relationship  $\epsilon_{evt} = \epsilon_Z^2$  should hold. Viceversa if there is correlation  $\rho$  one should expect that:

$$\epsilon_{evt} = \epsilon_Z^2 + 2\rho\epsilon_Z(1 - \epsilon_Z)$$

Since the two efficiencies are not compatible within the statistical error, one can calculate the correlation factor as:

$$\rho = \frac{\epsilon_{evt} - \epsilon_z^2}{2\epsilon_z(1 - \epsilon_z)}$$

Explicit calculation yields:

$$\rho_{4\mu} = 0.32 \quad \rho_{2\mu 2e} = 0.24$$

As expected the correlation between the  $\epsilon_Z$  of the two pairs is higher in the channel with four final state muons than in the channel with two muons and two electrons, due to the muon combinatorics in the former.

### 4.3.2 Considered kinematical variables

The main kinematical variables characterizing the events are listed in the following paragraphs. The plots shown are normalized to unit area, in order to enhance the differences in shape, or normalized to a total integrated luminosity of  $\sim 60 fb^{-1}$ , corresponding to the first three years of data taking: this normalization is obtained by weighting the events by a factor

$$W = \frac{\mathcal{L}_{int} \cdot \sigma}{N_{gen}}$$

where  $\mathcal{L}_{int}$  is the integrated luminosity,  $\sigma$  the cross-section for the considered process (in this case the LO cross section) and  $N_{gen}$  the number of MC generated events (and these plots are referred to as weighted). A Higgs mass  $M_H = 150 GeV$  is assumed.

Where there were not significant differences between the muon and electron spectra, such as in the transverse momenta  $p_T$ , results for one flavour only are shown, instead where there are significant differences both flavours are presented.

#### Leptons transverse momentum and pseudorapidity

The transverse momentum and the pseudorapidity  $p_T$  and  $\eta$  are typically the first variables measured and quoted to define the state of a particle. In particular, since the four final state leptons have different  $p_T$  distributions for each channel, they are always used for both *on-line* and *off-line* preselection and selection, together with  $\eta$  limits. Some examples are provided in the figures 4.30

Both leptons and  $Z$ 's  $p_T$  distributions allow a good rejection of reducible background, by imposing a lower  $p_T$  limit. For what concerns the final state leptons, in particular, separate cuts on  $p_T$ -ordered leptons seem to be possible. The efficiencies of these cuts, anyway, are  $M_H$ -dependent (e.g. see 4.36-*left*).

#### Invariant mass of leptons pairs

The invariant mass of leptons pairs is needed to reconstruct the intermediate  $Z$  boson, as explained in detail in section 4.3.1. In Fig. 4.31 plots are shown for the invariant mass of all possible  $\mu^+ \mu^-$  (or  $e^+ e^-$ ) pairs and for the pairs identified as product of a  $Z$  decay, and  $ZZ$  (i.e. Higgs) invariant mass.

Lower and upper cuts on  $\ell^+ \ell^-$  invariant mass (after the pair assignment described in sec. 4.3.1) can provide another way to suppress  $t\bar{t}$  and  $Zb\bar{b}$  back-

grounds. In particular, this cut provides a powerful rejection of  $t\bar{t}$  background where neither of the lepton pairs are expected to resonate on  $M_Z$ . Furthermore, these cuts are essentially mass-independent (see fig. 4.36-*right*).

### Angular variables

Another set of observables which are expected to provide a good selection power are the *angular variables*. All the angles considered here are expressed in the CMS laboratory reference frame. The variable distributions shown in 4.32 refer to angles between opposite-sign lepton pairs (coming from the same  $Z$ ), like-sign lepton pairs, electron-muon with higher  $p_T$ , electron-muon with lower  $p_T$  and the angle between the two  $Z$ 's.

The  $\ell^+\ell^-$ -angle distribution (first plot in fig. 4.32) shows a peak near 0 for  $t\bar{t}$  and  $Zb\bar{b}$  backgrounds, originated by the leptons produced in  $b$  quarks decays (in  $e^+e^-$  case, the peak is absent because of the higher  $p_T$  cut in generation, 10 GeV, which rejects part of the events with electrons coming from  $b$  decays). This angle represents another possible cut variable.

Finally, the angle between the two  $Z$ 's in the  $ZZ^*$  channel shows a different distribution with respect to the signal, and this could suggest a way to discriminate the signal from the irreducible background. Anyway, the shape of signal distribution is quite mass-dependent (see fig. 4.37).

### Collinearity

The *collinearity in  $p_z$*  refers to a correlation between the  $p_z$  component of the two leptons coming from the same  $Z$  decay, and thus is represented by a  $p_z(\ell^+) vs p_z(\ell^-)$ . This observable is expected to have allow a good rejection of  $t\bar{t}$  and  $Zb\bar{b}$  backgrounds (see Fig. 4.34)

As expected, the correlation between  $p_z$  component of lepton pairs offers another selection criterion with respect to the reducible background, by requiring the product  $p_z(\ell^+) \cdot p_z(\ell^-)$  to be above some threshold (usually a negative value, not to affect the signal efficiency).

The spikes on the  $Zb\bar{b} \rightarrow 2\mu 2e + X$  spectra are due to very low statistics available after the pre-selection cuts.

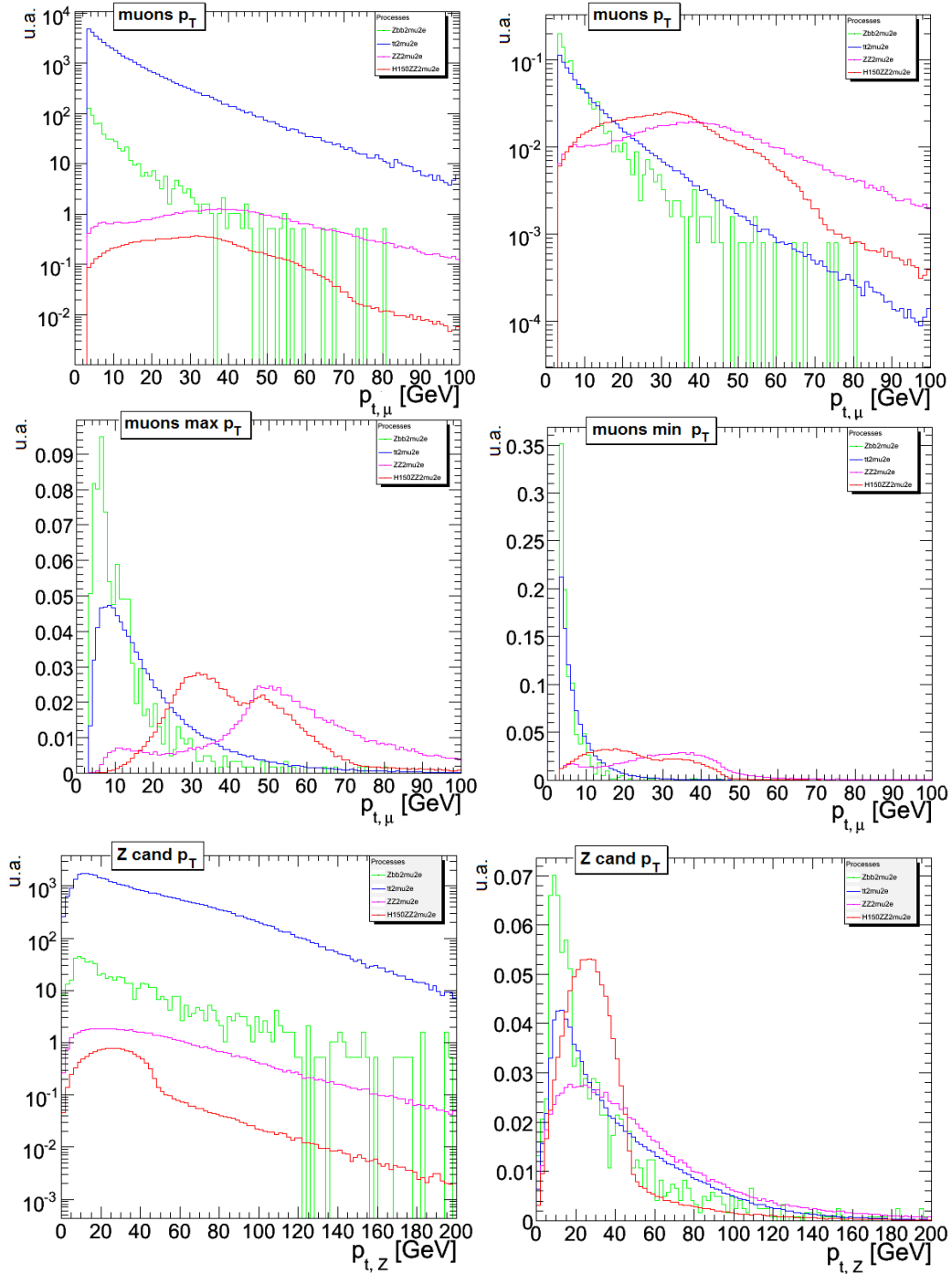


**Figure 4.30:**  $p_T$  distributions for muons and  $Z$ s. *Top left(right):* weighted (normalized) distribution of all muon momenta. *Center left(right):* Hardest (softest) muon  $p_T$  spectrum (normalized to the unit area). *Bottom-left:* weighted  $p_T$  distribution for  $Z$ . *Bottom-right:* normalized  $Z$   $P_T$  distributions

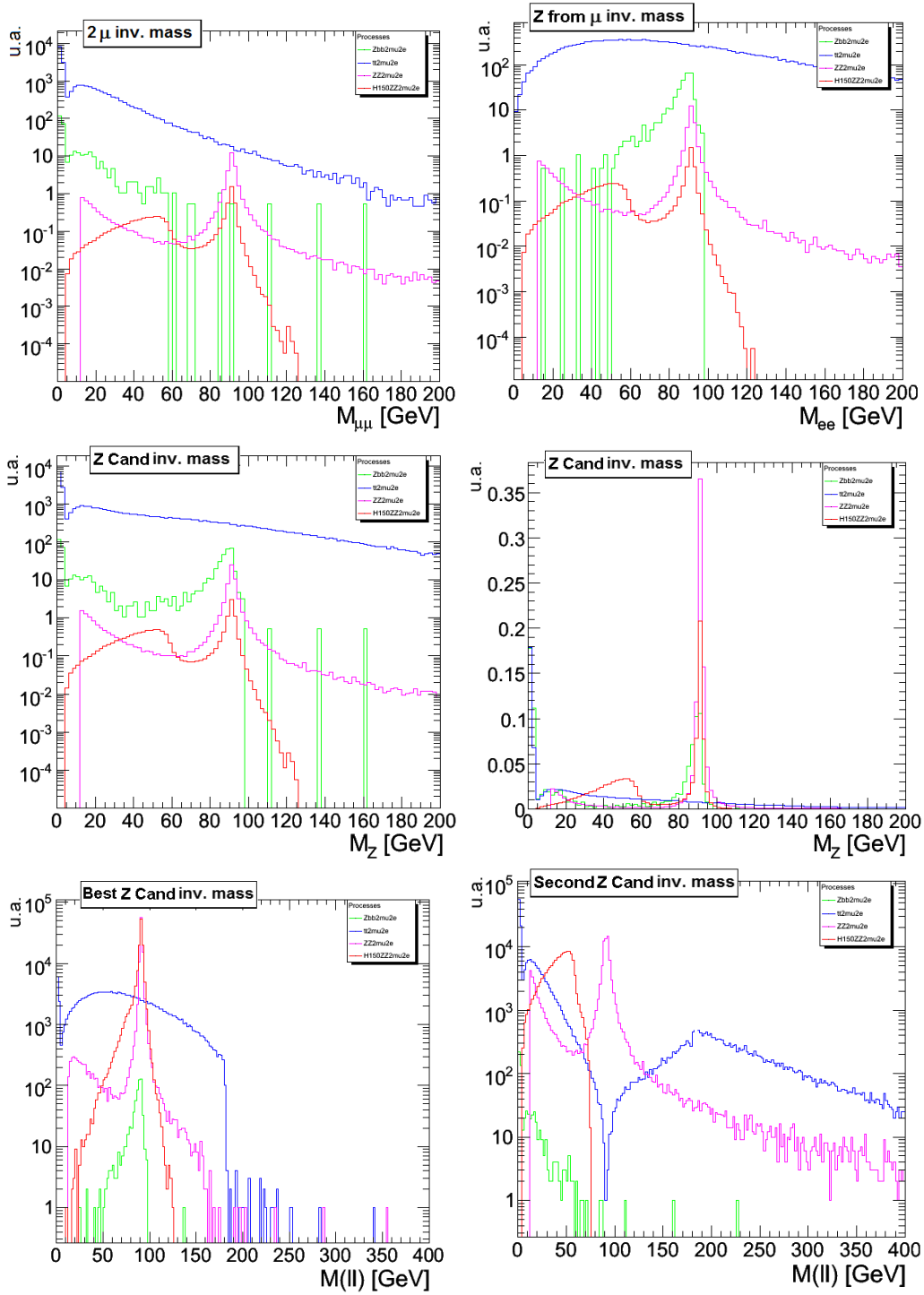


**Figure 4.31:** Invariant mass distributions. *Top:* muon-pairs (all combinations and selected pairs). *Center:* Z candidate invariant mass (weighted and normalized). *Bottom:* on-shell and off-shell Z

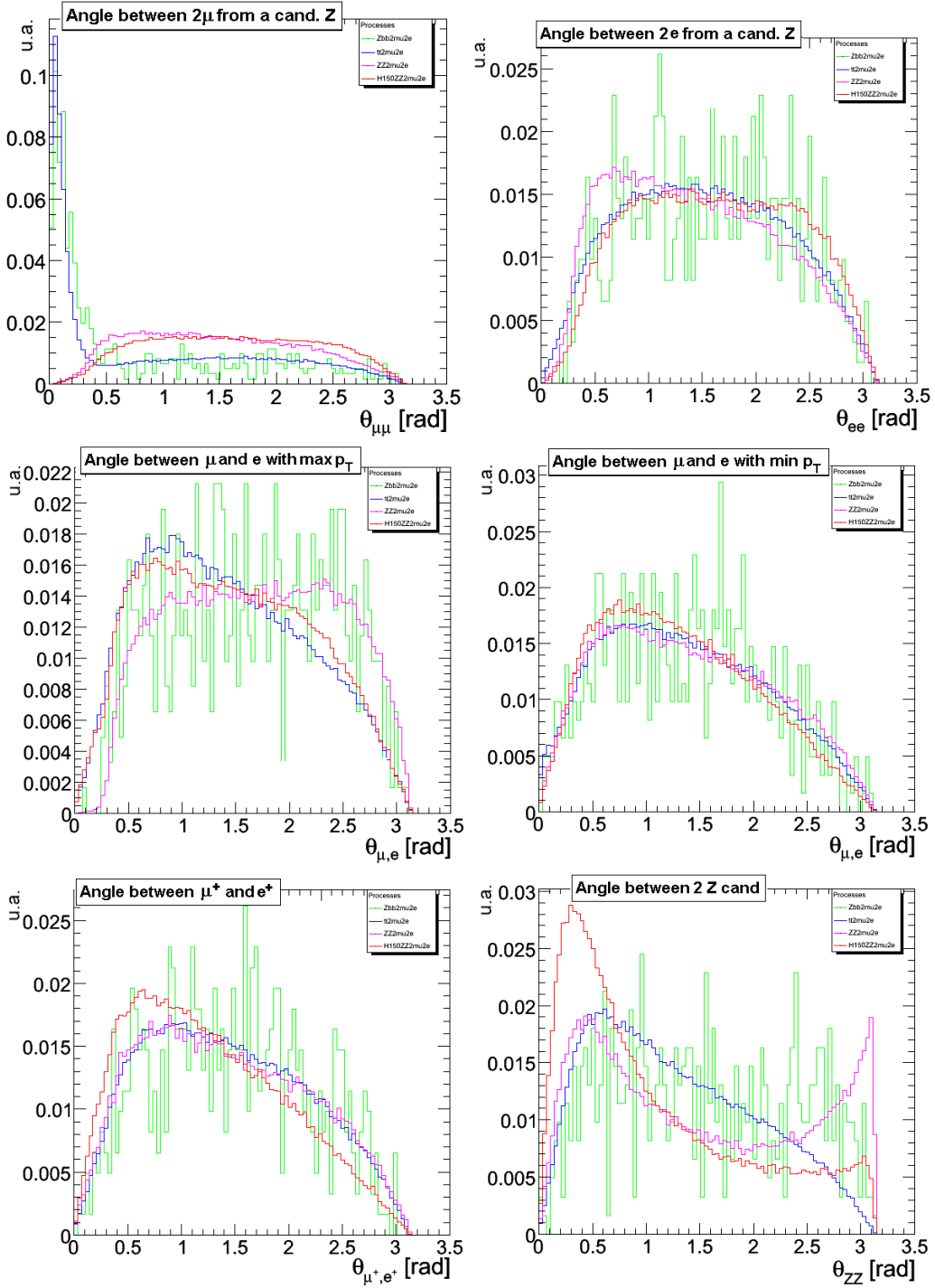


**Figure 4.32:** Angular variables distributions: angles between  $\mu^+\mu^-$  and  $e^+e^-$  pairs (from the same  $Z$  decay), between  $\mu - e$  pairs with higher and lower  $p_T$ , between  $\mu^+ - e^+$  and between two  $Z$ 's

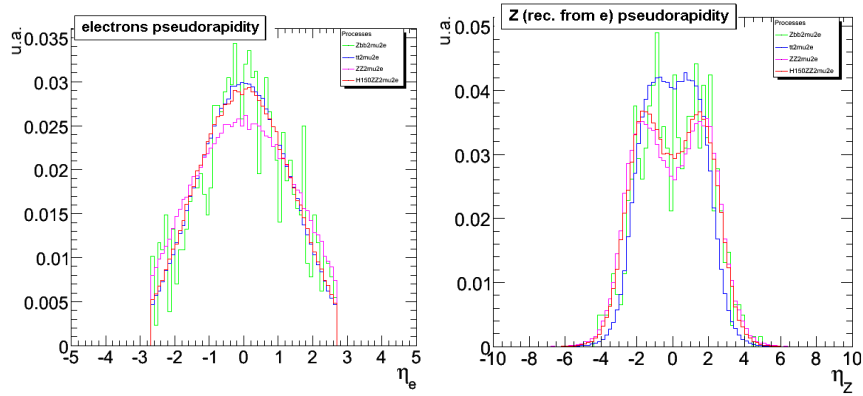


**Figure 4.33:** Pseudorapidity distributions. *Left:* Normalized distribution for electrons. *Right:* Normalized distribution for Zs from electrons

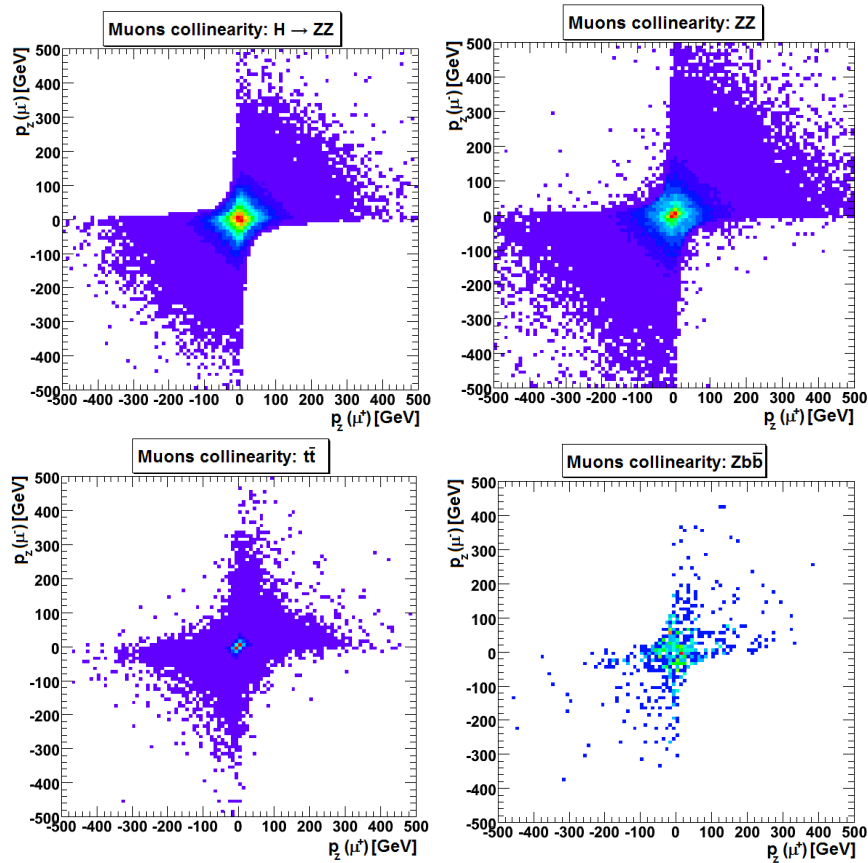


**Figure 4.34:** Muons collinearity in  $p_z$  for signal and backgrounds

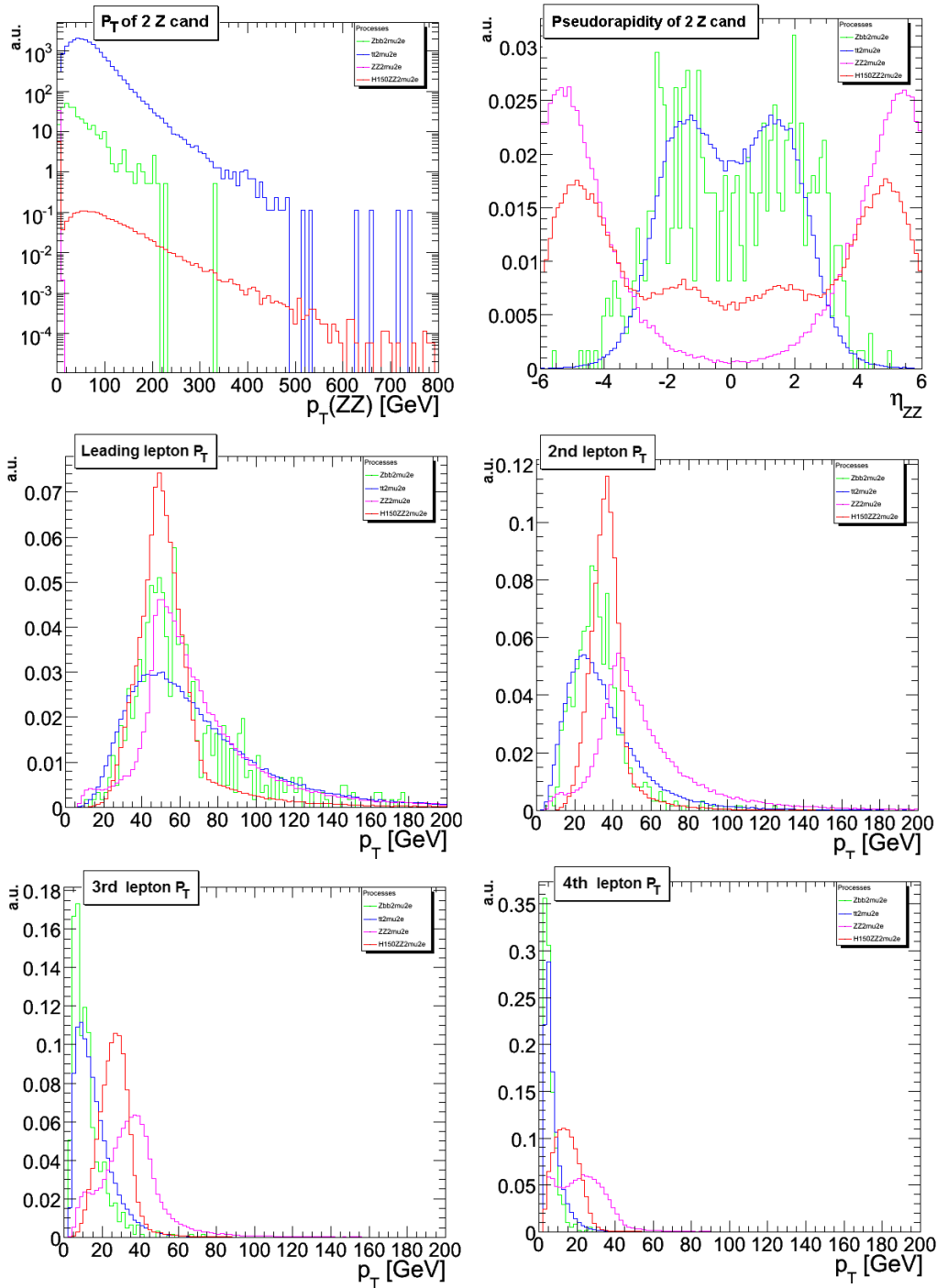


**Figure 4.35:** *Top-Left:*  $p_T$  of two candidate  $Z$ . *Top-Right:* Pseudorapidity of two candidate  $Z$ . *Center-Left:*  $p_T$  of leading lepton. *Center-Right:*  $p_T$  of second lepton. *Bottom-Left:*  $p_T$  of third lepton. *Bottom-Right:*  $p_T$  of softest lepton

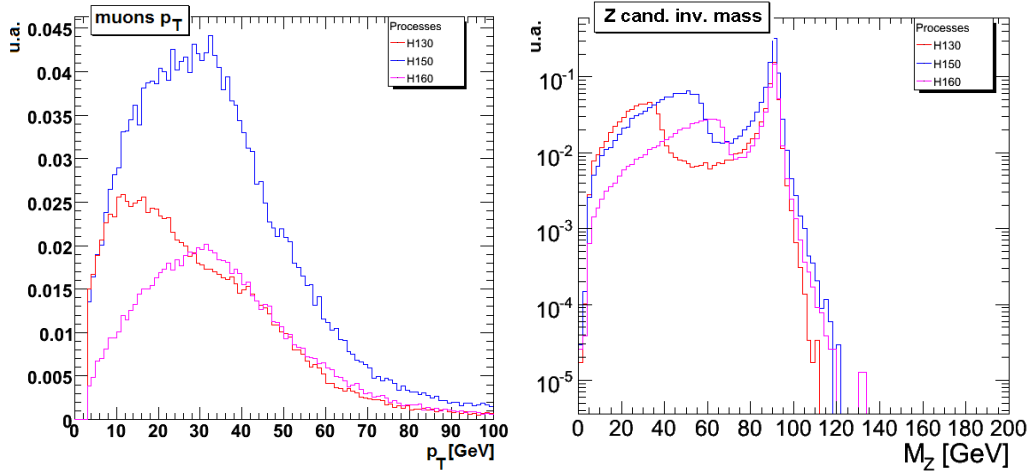


**Figure 4.36:** *Left:* muons  $p_T$  for different Higgs mass values. *Right:* lepton pairs invariant mass (i.e.  $Z$  boson mass) for different Higgs mass values)

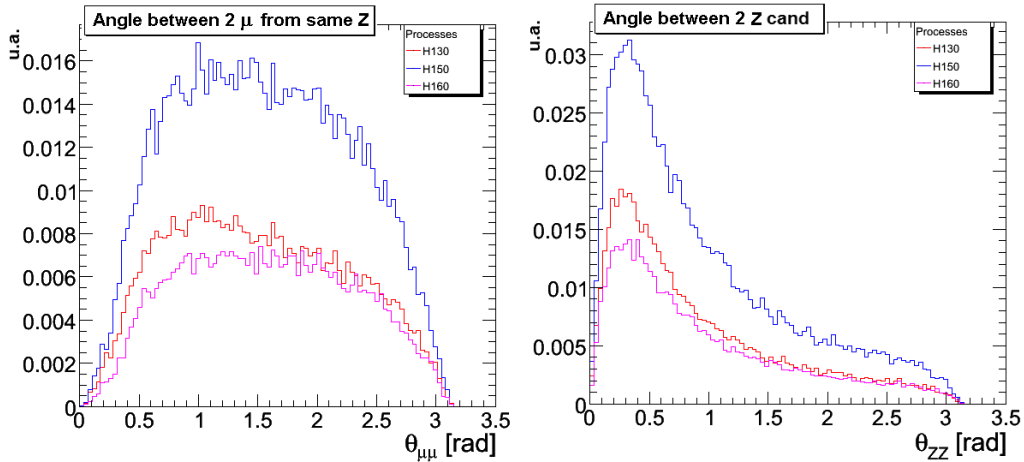


**Figure 4.37:** Distributions of  $\mu^+\mu^-$ -angle and  $ZZ$  angle for different Higgs mass values

All of these criteria, of course, need to be properly analyzed and tested after detector simulation and event reconstruction, and some of them could result to be correlated (e.g. cuts on  $p_T$  and  $\ell^+\ell^-$ -angle). In a complete analysis of course, not only kinematical variables are to be considered for signal selection, e.g. lepton *isolation* is expected to be an excellent discriminant between signal and reducible background.

However, this work on signal selection for further *offline* analysis cannot be carried out without taking into account the *online* selection performed by the trigger system, which is the subject of the next chapter.

## 4.4 Rejection of $ZZ^*$ background

In order to reduce the  $ZZ^*$  irreducible background, the scalar nature of the Higgs Boson can be exploited.

The Higgs signal process evolves in a s-channel while the  $ZZ^*$  background at LO in a t-channel as can be seen in the LO Feynman diagrams in Fig. 4.38.

Therefore one could expect that the angular distributions of the leptons could help in discriminating between the two processes.

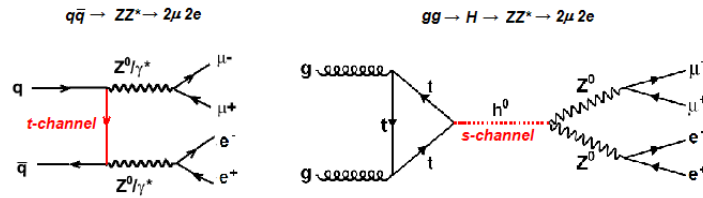


**Figure 4.38:** Leading order Feynman graphs for  $ZZ^*$  irreducible background and Higgs boson signal

To this aim we have introduced the angle  $\phi_D$  between the momentum  $\mathbf{p}_Z$  of the most energetic reconstructed  $Z$  and the direction of the  $H$  calculated in the  $H$  rest frame.

$$\phi_D = \phi_{H,Z}|_{H \text{ at rest}} = \arccos\left(\frac{\mathbf{P}_Z^{\mathbf{H} \text{ ref}} \cdot \mathbf{P}_H}{|\mathbf{P}_Z||\mathbf{P}_H|}\right) \quad (4.6)$$

In order to study this angular distribution two samples, one for the signal and one for the  $ZZ^*$  background have been generated with `Pythia 6.227`.

The kinematics of the  $ZZ^*$  sample is not completely correct as `Pythia` ignores the gluon-gluon fusion production mechanism described in sec. 4.2.6.

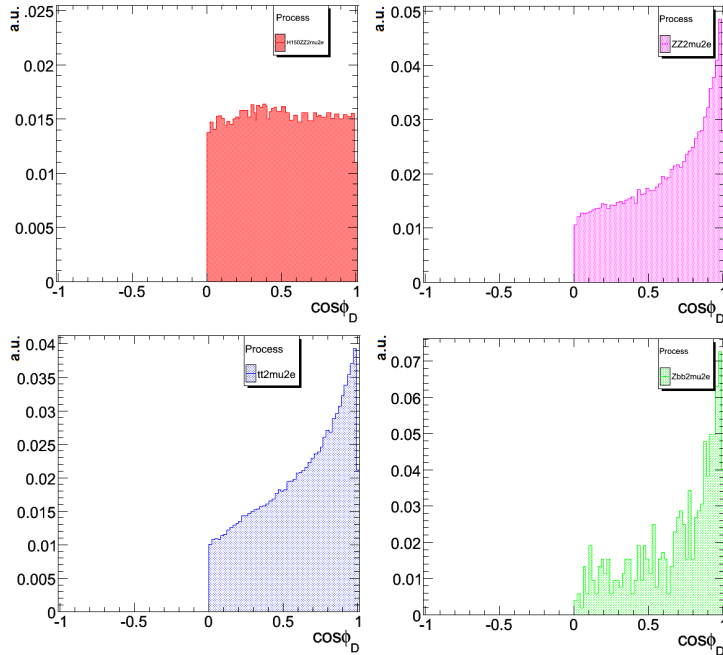
This angular variable was studied for  $H \rightarrow ZZ^* \rightarrow 4\mu$  samples as they were the only available at that time available. The study of this angular variable in the case of two muons and two electrons in the final state at a MC generation level is not significantly different from the four muons final state, since at the energies involved in the hard processes considered, the muon mass is for any analysis purpose comparable to that of the electron.

**Table 4.4:** Number of generated events and efficiencies for signal and background

Process	N generated events	$\epsilon_{kin}$ filter efficiency
S: $H \rightarrow ZZ^* \rightarrow 4\mu$	$1.0 \cdot 10^5$	$0.610 \pm 0.001$
B: $q\bar{q} \rightarrow ZZ^* \rightarrow 4\mu$	$1.0 \cdot 10^5$	$0.41 \pm 0.001$

The generated events were then passed through a CMSSW *EDFilter* which skimmed events with less than four muons, two positive, two negative, in the angular acceptance of CMS barrel  $|\eta_\mu| < 2.5$  (in the region where the DT+CSC subdetectors are placed) and with transverse momentum  $p_T > 3 \text{ GeV}$ . In table 4.4, the number of generated events and the filtering efficiencies for the two channels are shown.

The  $\cos\phi_D$  distribution is presented for signal and all three the main background in 4.39, while  $\phi_D$  and  $\cos\phi_D$  distributions for signal and for the  $ZZ^*$  background events are shown in Fig. 4.40.

**Figure 4.39:** Distribution of  $\cos\phi_D$ , for signal and backgrounds

The events are weighted to the same integrated luminosity  $\mathcal{L}_{int}$  with a

low luminosity scenario ( $\mathcal{L} = 2 \cdot 10^{-33} \text{cm}^{-2} \text{s}^{-1}$ ).

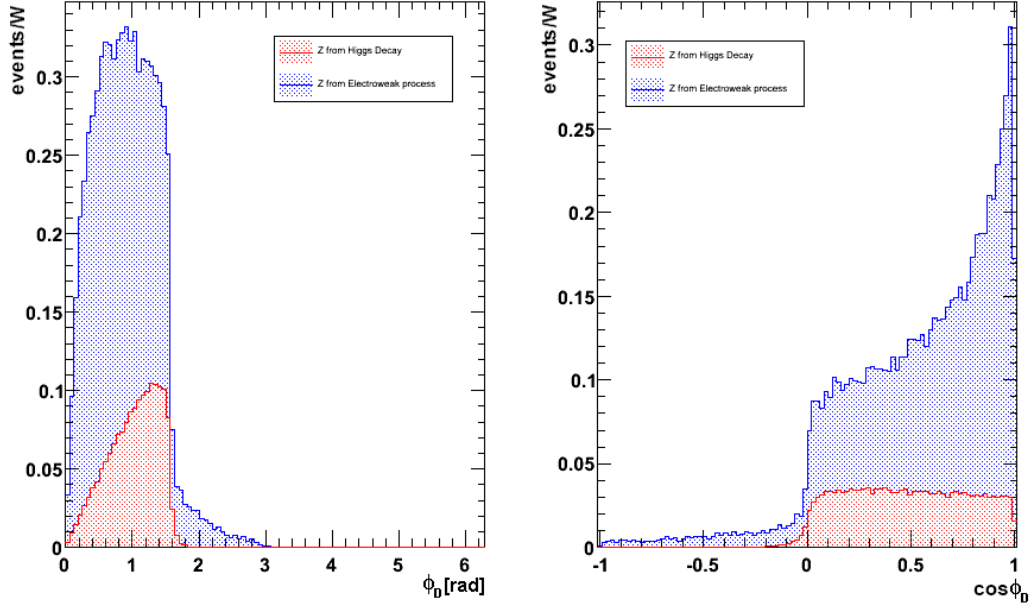


**Figure 4.40:** Distribution of  $\phi_D$  decay angle and  $\cos\phi_D$ , its cosine

Along with the angle of Higgs decay  $\phi_D$  some other angular variables has been considered: the angle between two muons with the same charge: ( $\theta_{ls}$ ):

$$\theta_{ls} = \theta_{\mu^\pm, \mu^\pm}|_{Lab} = \text{ArcCos} \left( \frac{\mathbf{P}_{\mu^\pm} \cdot \mathbf{P}_{\mu^\pm}}{|\mathbf{P}_{\mu^\pm}| |\mathbf{P}_{\mu^\pm}|} \right) \quad (4.7)$$

the angle between two muons from the same reconstructed candidate  $Z$  ( $\theta_{os}$ ):

$$\theta_{os} = \theta_{\mu^\pm, \mu^\mp}|_{Lab} = \text{ArcCos} \left( \frac{\mathbf{P}_{\mu^+} \cdot \mathbf{P}_{\mu^-}}{|\mathbf{P}_{\mu^+}| |\mathbf{P}_{\mu^-}|} \right) \quad (4.8)$$

and the angle between the two reconstructed  $Z$  ( $\theta_{ZZ}$ ):

$$\theta_{ZZ} = \text{ArcCos} \left( \frac{\mathbf{P}_{Z_1} \cdot \mathbf{P}_{Z_2}}{|\mathbf{P}_{Z_1}| |\mathbf{P}_{Z_2}|} \right) \quad (4.9)$$

All these other angular variables have been considered in the CMS reference frame.

A sketch of the considered angular variables is illustrated in Fig. 4.41.

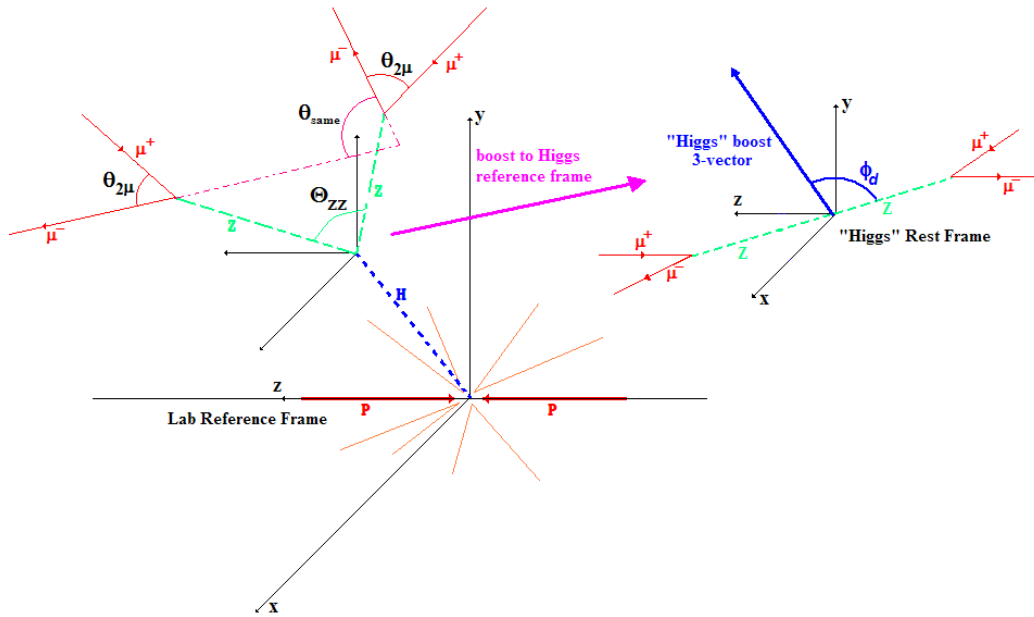


Figure 4.41: Sketch of considered angular variables

The distributions of the angles and of their cosines for the Higgs boson signal and the  $ZZ^*$  electroweak background are presented in Fig. 4.42.

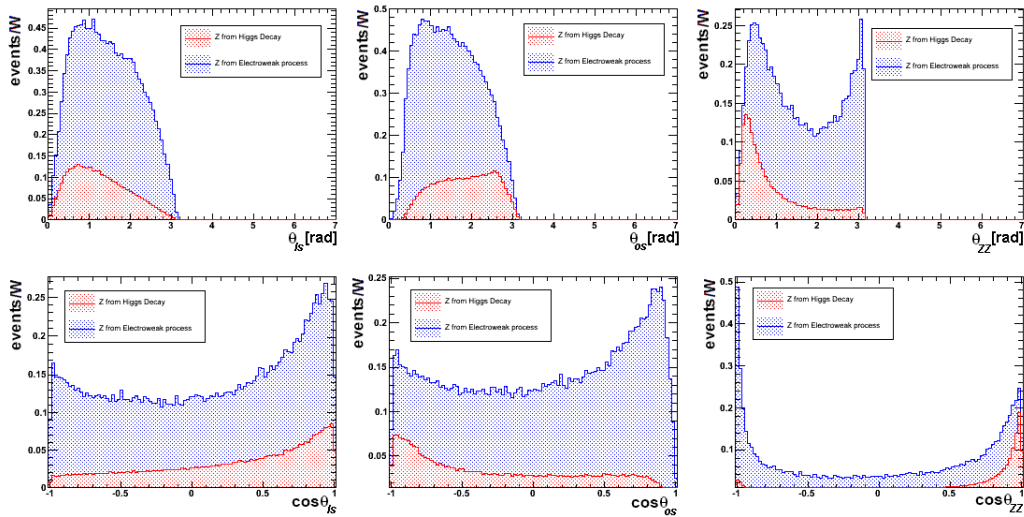
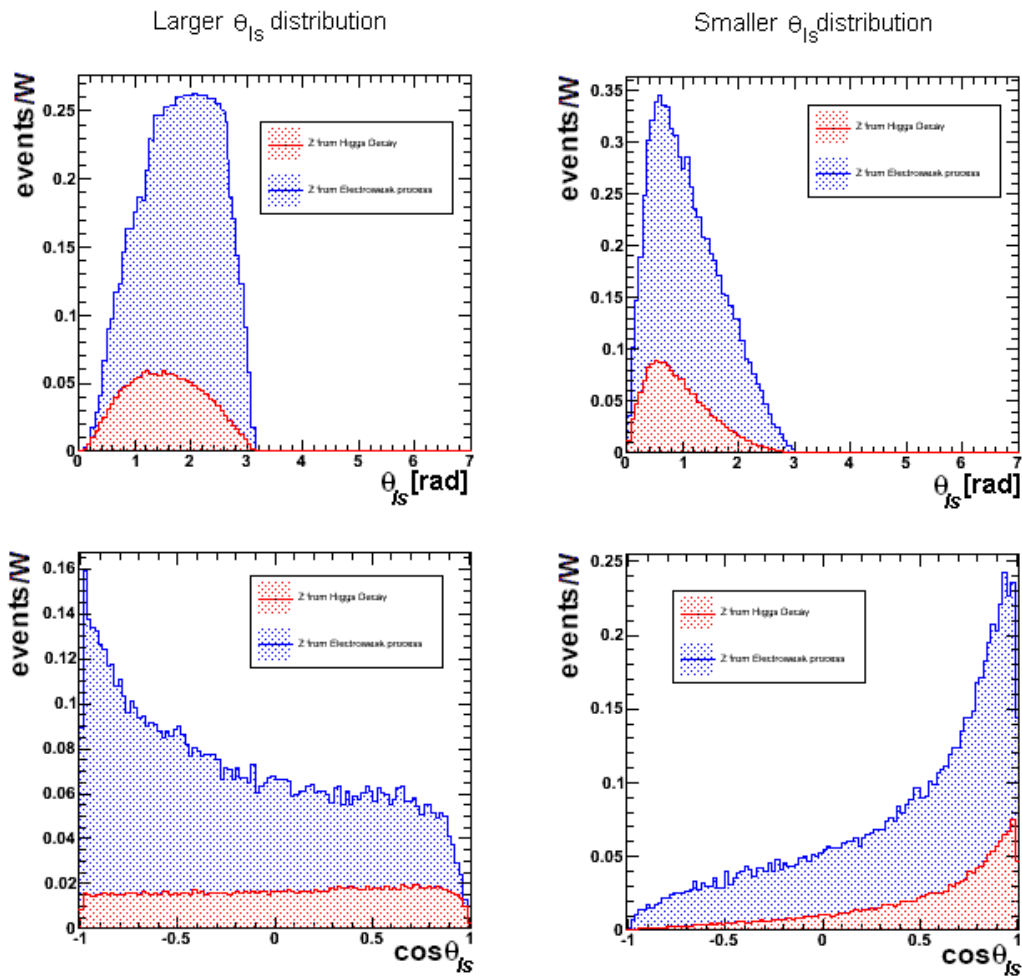


Figure 4.42: Angular distributions and cosine of considered angles. At the left  $\theta_{ls}$  distribution of like-sign muons. At the centre distribution of opposite sign muons  $\theta_{os}$  and at the right distribution of angle between  $Z$   $\theta_{ZZ}$

As far as the distributions of the angle between like-sign muons  $\theta_{ls}$  and opposite sign muons  $\theta_{os}$  are concerned, there are obviously two angles to be considered for each event. Since the angle between two muons from the same  $Z$  is heavily correlated to the invariant mass distribution, it will not be considered here. In order to have just one observable per event, the angular distribution of the angle between the two muon of the same charge has been split into two separate spectra, one for the larger angle and the other for the smaller. The plots for these two angular variables and their cosine is presented in Fig. 4.43



**Figure 4.43:** Angular distributions and cosine of considered angles. On the left the largest  $\theta_{ls}$ , on the right the smallest  $\theta_{ls}$

Starting from the distributions of the cosine of this angular variables ( $x_i = \text{Cos}\theta_i$ ), the following quantities were defined:

**Efficiency:**

$$\epsilon_C(\cos \phi_C) = \frac{\int_{\cos(\phi_C)}^1 \frac{dS}{dx} dx}{\int_{-1}^1 \frac{dS}{dx} dx} \quad (4.10)$$

**Purity:**

$$P(\cos \phi_C) = \frac{\int_{\cos(\phi_C)}^1 \frac{dS}{dx} dx}{\int_{\cos(\phi_C)}^1 \frac{dS}{dx} dx + \sum_k \int_{\cos(\phi_C)}^1 \frac{dB_k}{dx} dx} \quad (4.11)$$

**Signal to Background:**

$$\frac{N_S}{\sqrt{N_B}} = \frac{\int_{\cos(\phi_C)}^1 \frac{dS}{dx} dx}{\sqrt{\sum_k \int_{\cos(\phi_C)}^1 \frac{dB_k}{dx} dx}} \quad (4.12)$$

**Signal to Signal+Background:**

$$\frac{N_S}{\sqrt{N_S + N_B}} = \frac{\int_{\cos(\phi_C)}^1 \frac{dS}{dx} dx}{\sqrt{\int_{\cos(\phi_C)}^1 \frac{dS}{dx} dx + \sum_k \int_{\cos(\phi_C)}^1 \frac{dB_k}{dx} dx}} \quad (4.13)$$

where  $\frac{dS(x)}{dx}$  and  $\frac{dB_k(x)}{dx}$  are the differential distributions for the signal and the k-th background.

The quantities  $\frac{N_S}{\sqrt{N_B}}$  and  $\frac{N_S}{\sqrt{N_S + N_B}}$  are simplifications of the likelihood variables used in complex cut-based analysis. A part from a scale factor the last statistical observable is the product efficiency  $\times$  purity.

In measuring a cross-section for a process where the background is known, the best precision is obtained when choosing the maximum of the product efficiency times purity. Chosen the angular variable which maximizes the product efficiency times purity, the best choice for the cut position is the one corresponding to the global maximum of the curve  $\epsilon \times P(\cos(\phi_C))$ .

In Fig. 4.44 the plots for efficiency vs purity, efficiency times purity vs the cut on  $\cos \phi_i$ , signal to background ratio vs the cut on  $\cos \phi_i$ , and signal to signal plus background vs the cut cosine  $\cos \phi_i$  are presented.

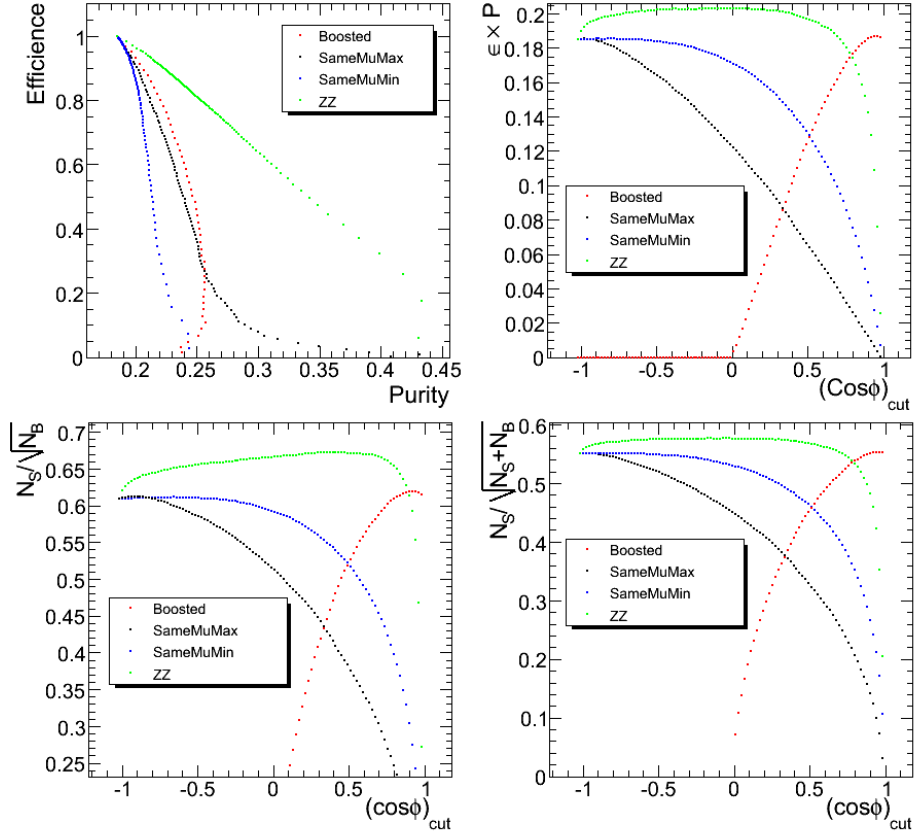


**Figure 4.44:** Top-left: Efficiency vs Purity for each cut position. Top-right: Efficiency times Purity Vs the cut cosine. Bottom-Left: Signal to Background ratio vs the cut cosine. Bottom-right: Signal to Signal plus Background ratio vs the cut cosine

Among the considered angular variables, the one maximizing the product efficiency times purity is the angle  $\theta_{ZZ}$  between the two reconstructed  $Z$ , and the best value for the cut is  $\cos\theta_{ZZ} > 0.75$ .

In principle one would have expected that the most promising cut variable should be the Higgs decay angle  $\phi_D$  because of the very forward events in the  $ZZ^*$  background distribution.

That should be indeed the most performing cut variable, but most of the forward peak due to  $ZZ^*$  in which the  $Z$  vector bosons are produced forward and backward in the lab reference frame lay outside of the geometrical acceptance of the muon system and are therefore already rejected by the generation filter.

# Chapter 5

## HLT performance for $H \rightarrow ZZ^* \rightarrow 2\mu 2e$

This chapter describes the performance of the CMS High Lever Trigger selection described in chapter 3 on the channel under study,  $H \rightarrow ZZ^* \rightarrow 2\mu 2e$ . Different L1 and HLT paths were applied to signal Monte Carlo samples of events to determine the trigger selection efficiencies. This study was carried out for the low luminosity scenario ( $\mathcal{L} = 2 \cdot 10^{33} \text{ cm}^{-2}\text{s}^{-1}$ ). The aim is to investigate the effect of the HLT selection with the currently implemented algorithms on this “silver-plated” channel and verify that the efficiency is not highly affected.

As the final state is characterized by the presence of two muons and two electrons, the corresponding triggers were considered: first electron and photon triggers alone and then combined with muon trigger.

### 5.1 Maximum event rate and thresholds

The choice of both L1 and HLT thresholds is determined by the maximum event rate (and the corresponding *bandwidth*) that can be accepted at each trigger level. In particular, the L1 bandwidth depends on the DAQ system, which can handle up to 50 *kHz* at start-up and 100 *kHz* at full luminosity, while the HLT bandwidth (i.e. the final rate of events written on disk) is required to be about  $\mathcal{O}(100 \text{ Hz})$ . At both levels, the total bandwidth is shared among different trigger objects (muons, electrons, photons, tau jets and so on), each subdivided into single- and multiple-object streams. The selection thresholds are thus determined by the study of the rate reduction on *minimum bias* events and of the signal efficiency for some high- $p_T$  benchmark channel (for electrons and muons, e.g., these channels can be  $Z$  or  $W$  decays).

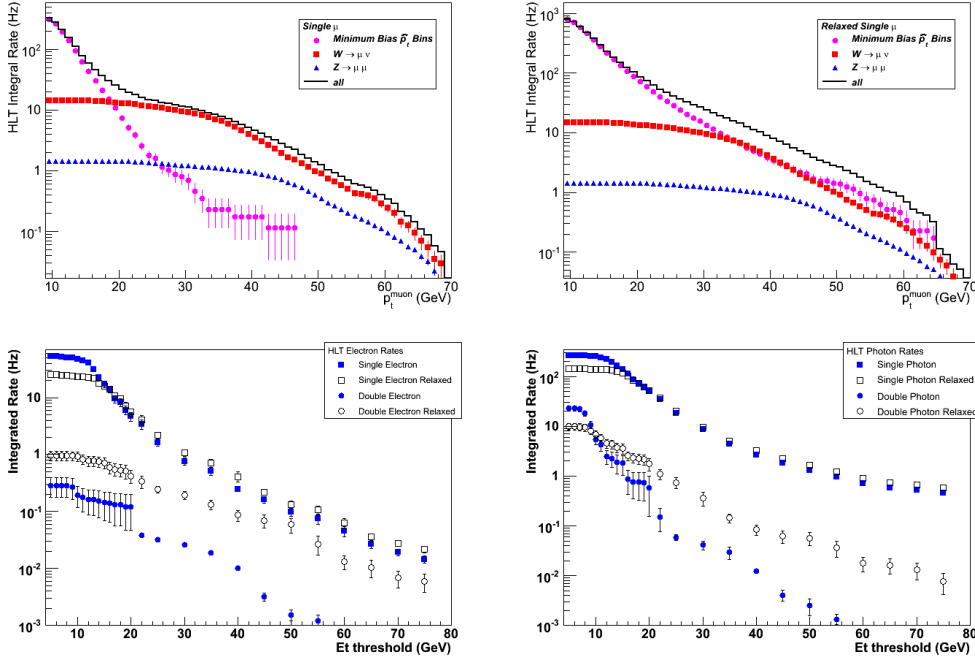


**Figure 5.1:** Integral rate of single muon (*Top-Left*) relaxed single muon (*Top-Right*), electrons (*Bottom-left*) and photons (*Bottom-Right*), as a function of the muon  $p_T$  threshold, and electron/photon  $E_T$  threshold [26]

As an example, in fig. 5.1 plots of electron and muon rates as a function of HLT  $p_T$  or  $E_T$  thresholds are shown.

On the basis of these rate studies, the  $p_T$  thresholds for the different trigger streams are chosen. In particular the L1 and HLT thresholds are chosen to guarantee the 90% efficiency. These thresholds are reported in tables 5.1, 5.2 and 5.3 together with the corresponding output rates. These results also include the isolation requirements described in chapter 3, which are set to 97% nominal efficiency.

	Start-up	Low Lumi		High Lumi	
	single- $\mu$	single- $\mu$	double- $\mu$	single- $\mu$	double- $\mu$
L1 [GeV]	7	14	3	20	5
HLT [GeV]	11	19	7	31	10
Rate [Hz]	$\sim 20$	29	6	53	7

**Table 5.1:** Muon HLT:  $p_T$  thresholds and output rates.[26]

	Start-up		Low Lumi	
	single- $e$	double- $e$	single- $e$	double- $e$
L1 [GeV]	12	8	20	10
HLT [GeV]	15	10	26	12
Rate [Hz]	16.9	0.1	-	-

**Table 5.2:** Electron HLT:  $E_T$  thresholds and output rates.[26]

	Start-up		Low Lumi	
	single- $\gamma$	double- $\gamma$	single- $\gamma$	double- $\gamma$
L1 [GeV]	12	8	20	10
HLT [GeV]	30	20,20	80	20,30
Rate [Hz]	8.3	0.5	-	-

**Table 5.3:** Photon HLT:  $E_T$  thresholds and output rates.

## 5.2 Trigger implementation in CMSSW

The HLT contains many *trigger paths*, each corresponding to a dedicated trigger. In the CMSSW implementation, a path consists of several software *modules*<sup>1</sup>, each one performing a well-defined task such as *unpacking* (RAW to DIGI), *reconstruction* of physics objects (electrons, muons, jets, MET, etc.), making *intermediate decisions* (triggering more refined reconstructions in subsequent modules) or calculating the *final decision* for a trigger path, which is then written into the Event as a *trigger bit*. Each module, therefore, is either an EDProducer (reconstruction modules) or an EDFilter (filter on trigger conditions): both receive data from the Event as input with the EDProducers putting their output (which is an *EDProduct*) into the Event. For accepted events, all intermediate and final EDProducts of all trigger paths are written out. It is also possible to trace back from intermediate and final HLT decisions to the individual reconstructed objects used by that particular filter to take its decision. During the data taking, HLT software modules will be run *online*, so the EDProducers performing reconstruction tasks must be as fast as possible, giving their results closer to those of the *offline* reconstruction used for physics analyses. Therefore, these EDProducers should ideally be taken from the standard offline reconstruction with parameters configured for HLT whenever this can be done, but replacing slower algorithms if time optimisation is needed.

Each HLT path starts with a filter module which looks for a suitable L1 *seed* (consisting of L1 bits and L1 objects), so that only trigger-paths

<sup>1</sup>For a complete description of CMS software framework see Appendix B

with a corresponding L1 seed are executed for an event. The Framework also ensures that if an intermediate decision is negative, the rest of that path is not executed and the event will not be processed as rejected by that specific trigger. Anyway, for these preliminary analysis, the default settings are such that, at each HLT level, reconstruction and filtering are always performed, independently on previous filters and levels, to allow complete efficiency studies. The final accept/reject decision, however, is the *logical “AND”* of all previous filter decisions, to reproduce the actual trigger result as it will be during the data taking.

In general, it is expected that all HLT triggers are run, even if the event is already accepted. In case this turns out to be too time-consuming, a *truncated mode* should be foreseen where the HLT stops running after the first accept and skips the rest of the triggers (which could be run anyway in the offline reconstruction step, in order to compute all trigger bits and insert the event in all the appropriate streams).

As an example, in fig. 5.2 the logical structure of muon HLT is represented.

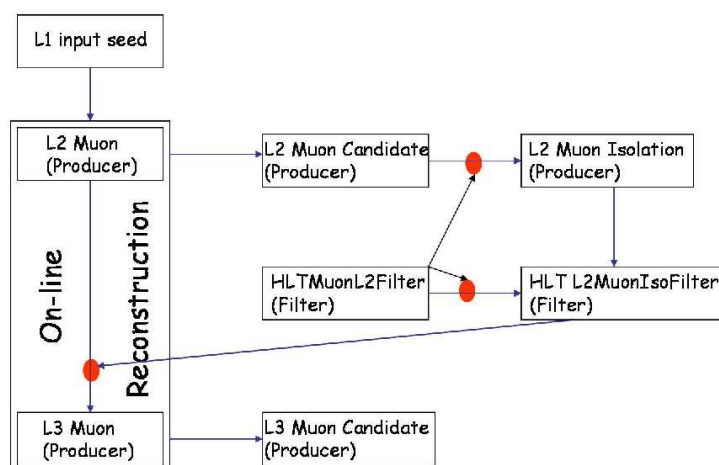


Figure 5.2: Muon HLT logical structure.

### 5.3 Electron/photon and muon HLT paths

In this section, the different HLT electron, photon and muon paths analyzed for this thesis are described in more detail. Though no photons are present in the signal channel, the corresponding triggers are considered anyway, since an electron can also be accepted by photon triggers.

### 5.3.1 Electron HLT path

A general description of the electron paths is provided below.

- **L1 bit:** filter on the L1 bit (`l1seedSingle`, `l1seedDouble` or `l1seedRelaxedDouble`, depending on the path).
- **ECAL clustering:** ECAL local reconstruction and regional clustering to produce corrected SuperClusters (SC).
- **SC to RecoEcal:** SC's converted to RecoEcal candidates.
- **L1 match:**  $\eta - \phi$  match of SC's and L1 seeds.
- **$E_T$  filter:**  $E_T$  threshold on corrected SC energy.
- **HCAL isolation:** HCAL local reconstruction and sum of  $E_T$  of HCAL hits in a cone around Egamma candidate.
- **HCAL isolation filter:** cut on the  $\sum E_T$  computed in the previous step.
- **Pixel seed match:** Pixel local reconstruction and pixel seeds for electrons from SC's.
- **Pixel match filter:** filter on the presence pixel seeds (from previous step).
- **Electron reconstruction:** local reconstruction in the strips of the Tracker and electron tracking.
- **Electron  $E/p$  filter:** cut on SC energy over track momentum.
- **Regional RecoTracker:** regional electron tracking.
- **Track isolation:** sum of  $p_T$  of tracks/number of tracks in a cone around the candidate.
- **Track isolation filter:** cut on the  $\sum p_T$  computed in the previous step.

### 5.3.2 Photon HLT path

A general description of the photon paths is provided below.

- **L1 bit:** filter on L1 bits (`l1seedSingle`, `l1seedDouble` or `l1seed-RelaxedDouble`), which are the same as for electrons (since  $e$  and  $\gamma$  are treated as one physical object at L1).
- **ECAL clustering:** ECAL local reconstruction and regional clustering to produce corrected SC's.
- **SC to RecoEcal:** SC's converted to RecoEcal candidates.
- **L1 match:**  $\eta - \phi$  match of SC's and L1 seeds.
- **$E_T$  filter:**  $E_T$  threshold on corrected SC energy.
- **ECAL isolation:** sum of  $E_T$  of all island basic clusters in a cone around the candidate.
- **ECAL isolation filter:** cut on the  $\sum E_T$  computed in the previous step.
- **HCAL isolation:** HCAL local reconstruction and sum of  $E_T$  of HCAL hits in a cone around Egamma candidate.
- **HCAL isolation filter:** cut on the  $\sum E_T$  computed in the previous step.
- **Regional RecoTracker:** tracker local reconstruction and regional tracking.
- **Track isolation:** number of tracks in the region in a cone around the candidate.
- **Track isolation filter:** cut on the  $\sum p_T$  computed in the previous step.

### 5.3.3 Muon HLT path

A general description of the muon paths is provided below.

- **L1 filter:** filtering L1 candidates, according to their quality,  $p_T$ , etc.
- **L1 seeds:** L1 provides seeds for L2 reconstruction.

- **L2 reconstruction:** it is performed using a common sequence, only if not done yet by a previous path.
- **L2 filter:** filter on the L2 output (mainly  $p_T$  thresholds).
- **Calorimetric isolation:** reconstruction of information from both ECAL and HCAL, only if not yet done by a previous path.
- **L2 isolation filter:** request for one or more (depending on the specific path) L2 isolated muon.
- **L3 reconstruction:** it uses a common sequence, performed only if not done yet by a previous path.
- **L3 filter:** filter on the L3 output (mainly  $p_T$  thresholds).
- **Track isolation:** reconstruction of information from the Tracker, only if not yet done by a previous path.
- **L3 isolation filter:** request for one or more (depending on the specific path) L3 isolated muon.

### 5.3.4 Detailed thresholds for low luminosity

As the study of HLT efficiencies has been carried out for low luminosity ( $\mathcal{L} = 2 \cdot 10^{33} \text{ cm}^{-2}\text{s}^{-1}$ ), a more detailed list of the thresholds used for the different electrons and muon paths is presented.

As far as electrons are concerned, the HLT exercise carried out considered six main trigger-paths: *single electron*, *double electron*, *relaxed double electron*, *single photon*, *double photon* and *relaxed double photon*.

The list of the corresponding  $E_T$  thresholds in the HLT is shown in Tab. 5.4.

L1 Trigger	Trigger	HLT $E_T$ Threshold (GeV)
SingleIsoEG20	Single Electron	26
DoubleIsoEG10	Double Electron	12
DoubleEG15	Relaxed Double Electron	19
SingleIsoEG20	Single Photon	80
DoubleIsoEG10	Double Photon	20,30
DoubleEG15	Relaxed Double Photon	20,30

**Table 5.4:**  $E_T$  HLT thresholds for *Egamma* trigger-paths. Relaxed means non isolated [27]

A more detailed list of *Egamma* trigger paths which requires isolation is shown in Tab. 5.5. Isolation cuts in the calorimeters are performed on  $\sum E_T(\Delta R)$ , sum of transverse energy of HCAL/ECAL deposits in a cone  $\Delta R = \sqrt{\Delta\phi^2 + \Delta\eta^2}$  around *Egamma* candidate. Isolation cuts in the tracker are performed on  $\sum p_T(\Delta R)/(p_T)_{tk}$ , sum of the measured transverse momenta of the tracks in a cone  $\Delta R$  normalized to the transverse momentum of the candidate electron track  $(p_T)_{tk}$ .

	Single $e$	Double $e$	Single $\gamma$	Double $\gamma$
$ \eta $	$< 2.5$	$< 2.5$	$< 2.5$	$< 2.5$
$E_T$ (GeV)	$> 26$	$> 12$	$> 80$	$> 30, 20$
TK isolation	$< 0.06$	$< 0.4$	$< 1$	$< 3$
HCAL isol. barrel (GeV)	$< 3$	$< 9$	$< 6$	$< 8$
HCAL isol. endcaps (GeV)	$< 3$	$< 9$	$< 4$	$< 6$
ECAL isolation (GeV)	-	-	$< 1.5$	$< 2.5$
E/P barrel	$< 1.5$	-	-	-
E/P endcaps	$< 2.45$	-	-	-

**Table 5.5:** Detailed thresholds for some selected *egamma* paths[27]

The considered muon trigger paths are: *single muon*, *di-muon*, *single muon non-isolated*, *di-muon non-isolated*

The list of the corresponding transverse momentum  $p_T$  thresholds in the HLT is shown in Tab. 5.6.

L1 Trigger	Trigger	HLT $E_T$ Threshold (GeV)
A_SingleMu15	Isolated Single Muon	19
A_SingleMu35	Relaxed Single Muon	37
A_DoubleMu7	Double Muon	7
A_DoubleMu10	Relaxed Double Muon	10

**Table 5.6:**  $p_T$  HLT thresholds for muon trigger-paths. Relaxed means non isolated [28]

A more detailed table for muon trigger-paths is presented in table 5.7

	Single muon	Single muon non-iso	Di-muon	Di-muon non-iso
$ \eta $	$< 2.5$	$< 2.5$	$< 2.5$	$< 2.5$
$Dr(\text{cm})$	$< 0.02$	$< 0.02$	$< 0.02$	$< 0.02$
$p_T$ (GeV)	19	37	7	10
L2 Isolation (GeV)	5.5	-	3.4	-
L3 Isolation (GeV)	3.1	-	2.3	-

**Table 5.7:** Thresholds for muon paths [28]

where  $Dr$  is the minimum distance between the vertex and the nominal interaction point in the transverse plane, and the isolation cut refers to  $\sum p_T(\Delta R)$  the sum on transverse momenta within a cone of  $\Delta R = 0.24$  from the candidate muon.

## 5.4 Efficiencies for Egamma trigger-paths

First of all the trigger efficiencies for  $H \rightarrow ZZ^* \rightarrow 2\mu 2e$  were studied for Egamma trigger paths only.

The  $10^4$  signal events (a Higgs mass  $M_H = 150 \text{ GeV}$  is assumed), were generated at the Bari Tier 2 Site and processed via GRID using the the HLT algorithms currently implemented in the CMS software framework<sup>2</sup>. The considered trigger-paths were *single electron*, *double electron*, *relaxed double electron*, *single photon*, *double photon* and *relaxed double photon*.

Generation cuts on leptons four-momenta are ( $|\eta_e| < 2.7$ ,  $|\eta_\mu| < 2.5$ ,  $p_T^e > 10 \text{ GeV}$ ,  $p_T^\mu > 3 \text{ GeV}$ ).

HLT routines need to access the DIGI data collection. These will be available in the RAW data actually taken in the real data taking but not in these samples which contain only the collection of HITS, i.e. the simulated response of the detector to the passage of the generated particles. Therefore the L1 objects which are the seeds for the HLT routines have to be simulated by the HLT code itself. So all efficiencies reported in the following are meant as an overall trigger efficiency L1+HLT.

The obtained signal efficiencies are reported in Tab. 5.8, where the uncertainty on the efficiency has been calculated according to a binomial distribution:

$$\sigma_\epsilon = \sqrt{\frac{\epsilon(1-\epsilon)}{N_{GEN}}}$$

<sup>2</sup>Events were produced with version CMSSW\_1.3.0 and processed with CMSSW\_1.3.1\_HLTX

Trigger path	Efficiency $\epsilon$
Single electron	$0.616 \pm 0.004$
Double electron	$0.496 \pm 0.005$
Double relaxed electron	$0.446 \pm 0.005$
Single photon	$0.002 \pm 0.0004$
Double photon	$0.263 \pm 0.004$
Double relaxed photon	$0.352 \pm 0.004$
Logical OR	$0.782 \pm 0.004$

**Table 5.8:** HLT efficiencies for Egamma paths. The events have not been refiltered

The events were then filtered at *RECO* level, requiring that there were still two reconstructed muons and two reconstructed electrons in the final state satisfying the same cuts on  $p_T$  and  $\eta$  performed at the generator level but now on the reconstruction variables.

In Tab. 5.9 the efficiencies for filtered events are presented.

Trigger path	Efficiency $\epsilon$
Single electron	$0.670 \pm 0.004$
Double electron	$0.598 \pm 0.004$
Double relaxed electron	$0.534 \pm 0.004$
Single photon	$0.005 \pm 0.001$
Double photon	$0.28 \pm 0.05$
Double relaxed photon	$0.379 \pm 0.004$
Logical OR	$0.839 \pm 0.003$

**Table 5.9:** HLT efficiencies for Egamma paths. The events have been re-filtered after reconstruction

The distributions of some of the variables used in the HLT algorithms are shown in Fig. 5.3, 5.4 and 5.5 for various trigger paths.

The different  $E_T$  thresholds for the various plots and the ECAL crack around  $|\eta| = 1.5$ , where there is a gap between EB (ECAL Barrel) and EE (ECAL Endcap), are clearly visible.

In these plots can be seen that the most performing Egamma trigger-path for our signal is the *single electron*, followed by the *double electron* and the *double relaxed electron*.

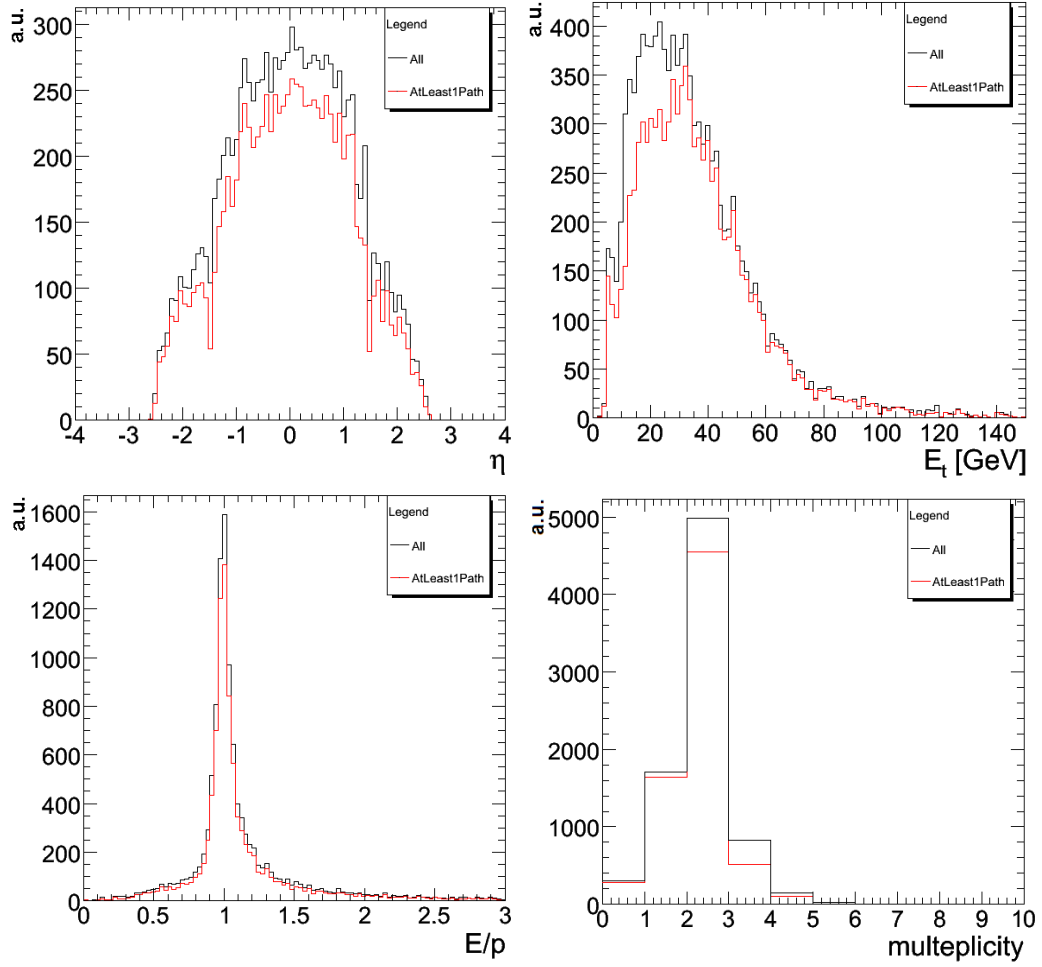


**Figure 5.3:** Comparison between all events and events passing at least one of the trigger paths (electron+photon). *Top-Left:* pseudorapidity  $\eta$  of Egamma object. *Top-Right:* transverse energy of Egamma objects  $E_T$ . *Bottom-left:*  $E/P$  of electrons. *Bottom-Right:* Egamma objects multiplicity

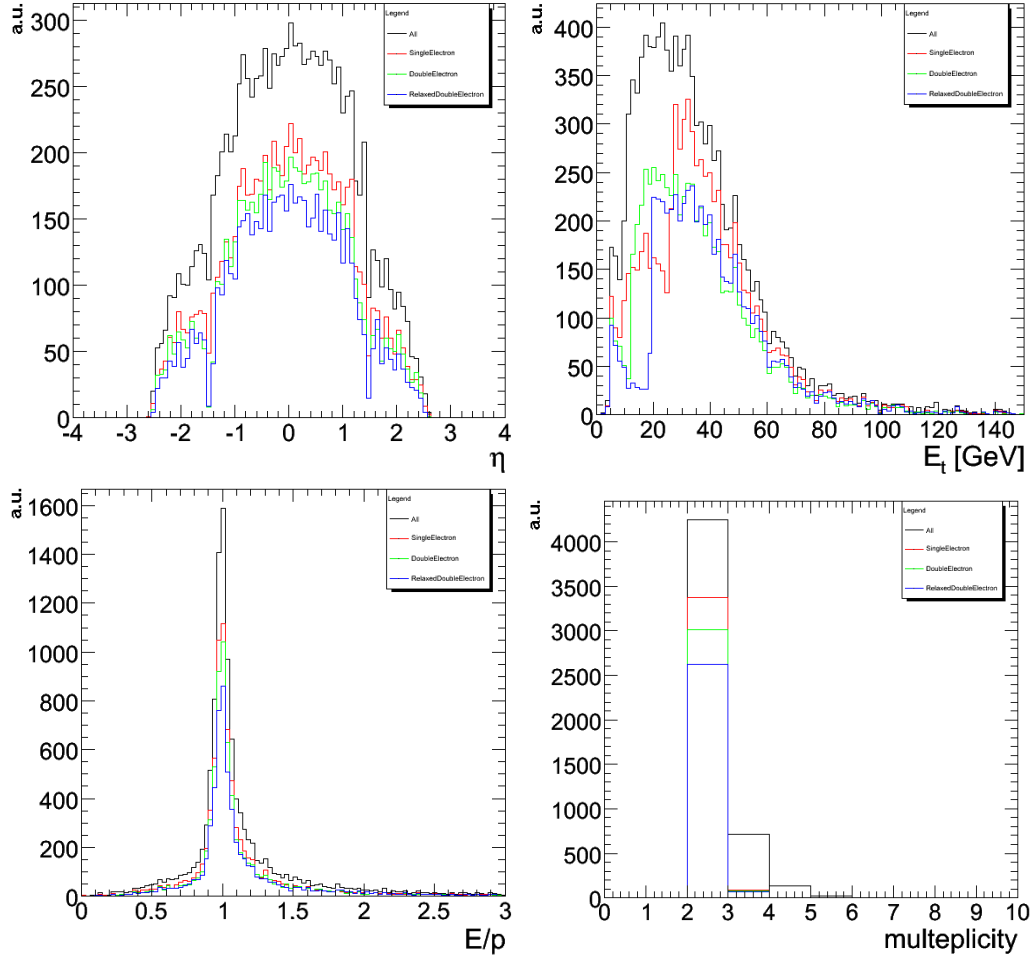


**Figure 5.4:** Comparisons between all events and events passing at least one of the electron trigger paths. *Top-Left:* pseudorapidity  $\eta$  of the Egamma object. *Top-Right:* transverse energy of Egamma objects  $E_T$ . *Bottom-left:*  $E/p$  of Egamma objects. *Bottom-Right:* Egamma objects multiplicity

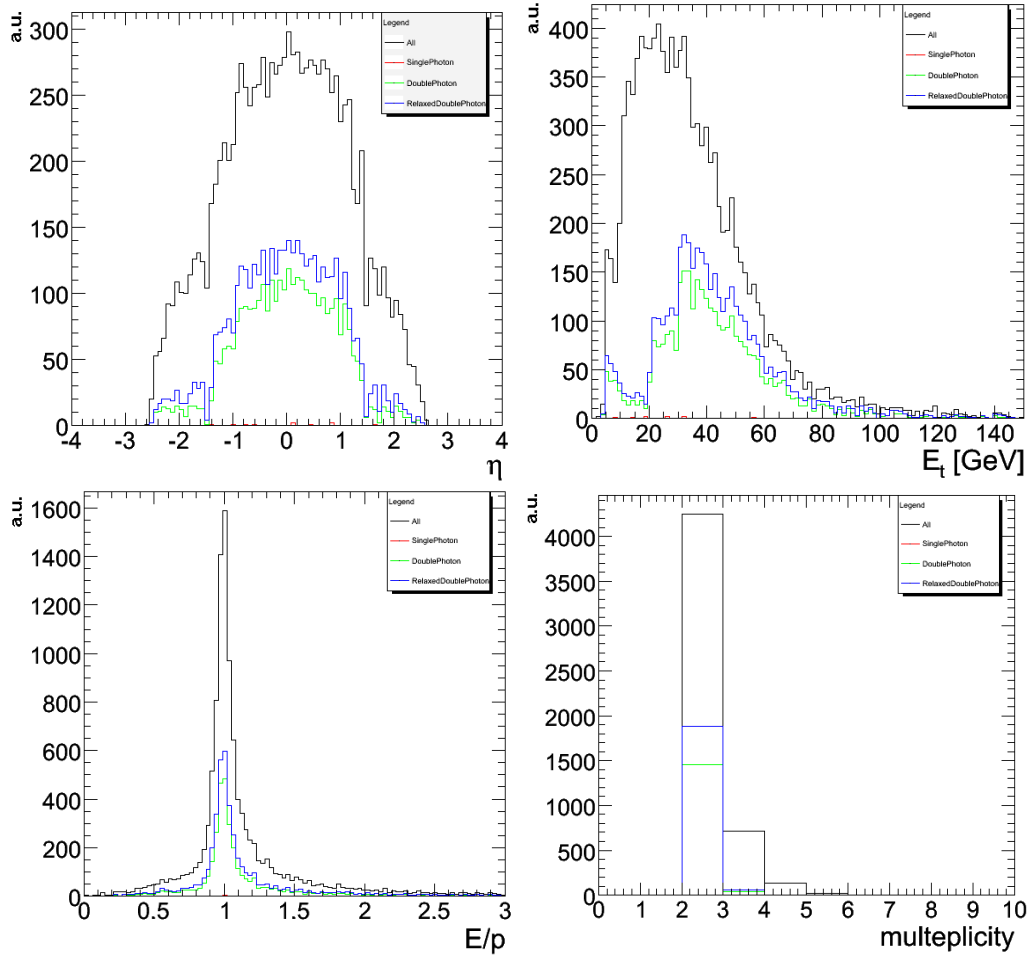


**Figure 5.5:** Comparisons between all events and events passing one of the photon trigger paths. *Top-Left:* pseudorapidity  $\eta$  of electron-like objects. *Top-Right:* transverse energy of electron-like objects  $E_T$ . *Bottom-left:*  $E/p$  of electron-like objects. *Bottom-Right:* electron's multiplicity

As expected the number of signal events passing the single photon trigger path is extremely low.

## 5.5 Trigger efficiencies for combined Egamma-muon paths

After the preliminary study on the Egamma trigger paths a more detailed study was carried out for a combination of muon and Egamma paths.

In order to minimize CPU computing time, since the access to data via GRID was not always possible, only combinations of the most performing Egamma/muon paths were considered: (*single muon-single electron, single muon-double electron, single muon-double photon, double muon-single electron, double muon-double electron, double muon-double photon, relaxed double muon-relaxed double electron, relaxed double muon-relaxed double photon*).

The combined absolute efficiencies (without re-filtering at reconstructed level) are presented in Tab. 5.10.

	Single $e$	Double $e$	Double $e$ no-Iso	Double $\gamma$	Double $\gamma$ no-Iso
Single $\mu$	0.929	0.900	-	0.860	-
Double $\mu$	0.863	0.823	-	0.742	-
Relaxed double $\mu$	-	-	0.795	-	0.753

**Table 5.10:** Trigger efficiencies for combined electron muon paths. Events were not re-filtered

After re-filtering, requiring at least two muons with  $p_T > 3 \text{ GeV}$  and  $|\eta| < 2.5$  and two electrons with  $p_T > 10 \text{ GeV}$  and  $|\eta| < 2.7$  the following efficiencies were found (Tab. 5.11).

	Single $e$	Double $e$	Double $e$ no-Iso	Double $\gamma$	Double $\gamma$ no-Iso
Single $\mu$	0.956	0.943	-	0.890	-
Double $\mu$	0.909	0.844	-	0.791	-
Relaxed double $\mu$	-	-	0.856	-	0.797

**Table 5.11:** Trigger efficiencies for combined electron muon paths. Events were re-filtered

The efficiency of the logical OR of all the single and double lepton paths (*single electron/muon OR double electron/muon*) is:

$$\epsilon(\cup paths) \pm \sigma_\epsilon = \frac{N_{HLT+L1}}{N_{filt}} \pm \sqrt{\frac{\epsilon(1-\epsilon)}{N_{filt}}} = 0.980 \pm 0.004$$

Where  $N_{HLT+L1}$  is the number of events passing the emulated L1 plus the HLT cuts for a given trigger path, while  $N_{filt}$  is the number of events satisfying the kinematical requirements on final state leptons.

The corresponding efficiency for all events ( before the filter ) is:

$$\epsilon(\cup paths) \pm \sigma_\epsilon = \frac{N_{HLT+L1}}{N} \pm \sqrt{\frac{\epsilon(1-\epsilon)}{N}} = 0.972 \pm 0.004$$

For the two most performing combined paths *single e-single  $\mu$*  and *double e-double  $\mu$*  a detailed study of signal efficiency was performed at each filtering step of the HLT routines (cf. Sec. 6.3).

The efficiencies presented are calculated as:

$$\epsilon_i = \frac{N(\text{after } \sum_n^i \text{ cuts})}{N_{filt}}$$

Results are presented in Tab. 5.12.

Trigger type	Cuts	$1\mu 1e$	$2\mu 2e$
e	L1seed	$0.921 \pm 0.004$	$0.803 \pm 0.004$
e	$E_T$	$0.785 \pm 0.004$	$0.704 \pm 0.004$
e	HCAL Iso	$0.779 \pm 0.004$	$0.701 \pm 0.004$
e	Pixel Match	$0.761 \pm 0.004$	$0.638 \pm 0.005$
e	E/P	$0.695 \pm 0.005$	$0.623 \pm 0.005$
e	Tk Iso	$0.673 \pm 0.005$	$0.599 \pm 0.005$
$\mu$	L1Seed	$0.963 \pm 0.004$	$0.960 \pm 0.004$
$\mu$	L2Pre	$0.924 \pm 0.004$	$0.778 \pm 0.004$
$\mu$	L2Iso	$0.903 \pm 0.004$	$0.775 \pm 0.004$
$\mu$	L3Pre	$0.861 \pm 0.004$	$0.685 \pm 0.005$
$\mu$	L3Iso	$0.837 \pm 0.004$	$0.684 \pm 0.005$

**Table 5.12:** Detailed HLT efficiencies for each cut for selected trigger paths

Distributions of kinematical variables after HLT-filtering are shown in fig. 5.6 for some of the combinations of  $\mu - e/\gamma$  trigger paths previously analyzed (at low luminosity).

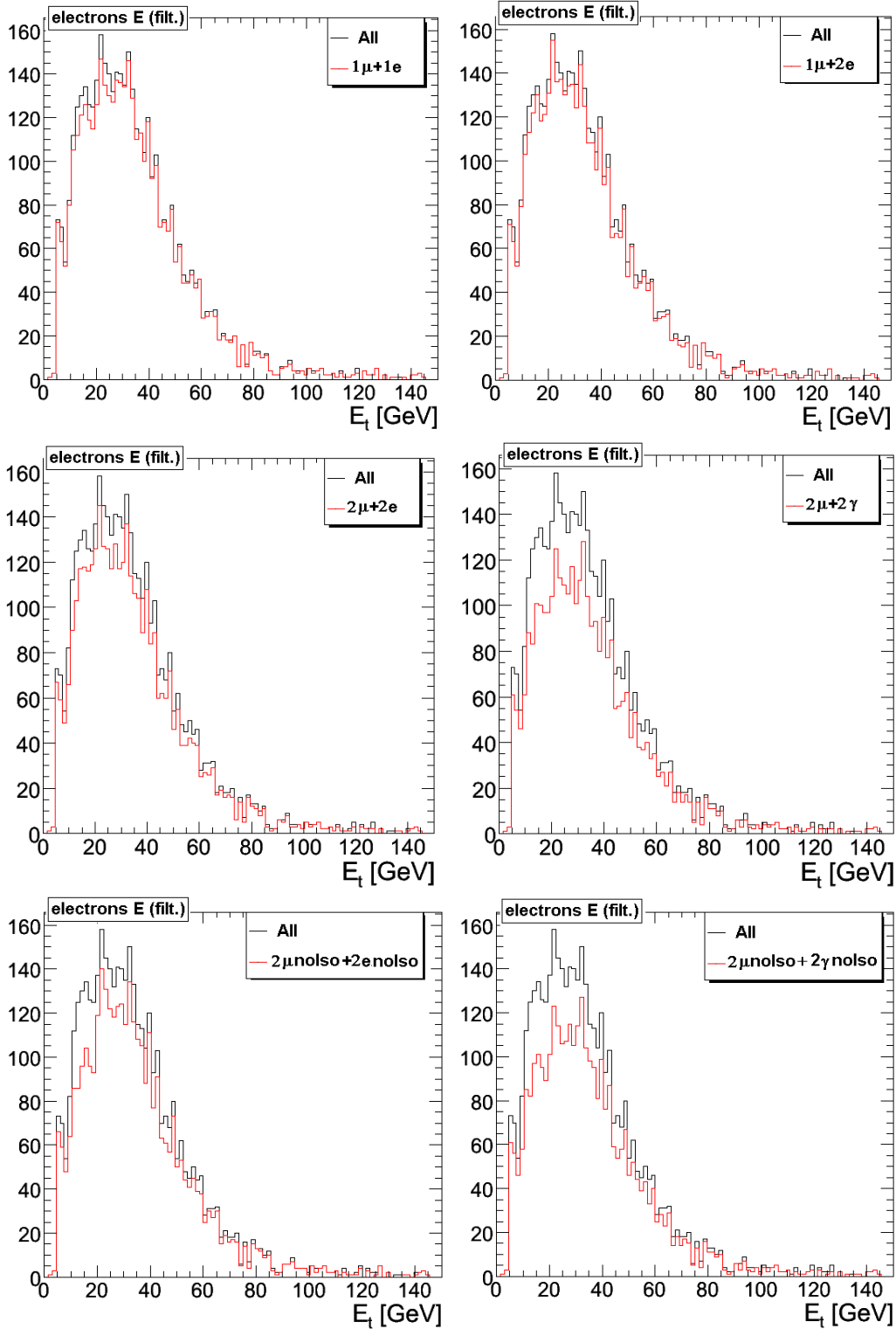


**Figure 5.6:** Distributions of electrons  $E_T$  for  $\mu - e/\gamma$  combined paths (low lumi): 1) single- $\mu$ -single- $e$  (left), single- $\mu$ -double- $e$  (right); 2) double- $\mu$ -double- $e$  (left), relaxed double- $\mu$ -relaxed double- $e$  (right); 3) double- $\mu$ -double- $\gamma$  (left), relaxed double- $\mu$ -relaxed double- $\gamma$  (right).

## 5.6 Resolution on selected observables

To fully qualify the performance of the HLT code, the same algorithms used for the signal should be studied on backgrounds as well.

Unfortunately this study could not be performed in this thesis as, because of the rapidly evolving CMS software, the digitization step needed by the HLT was not available in the background samples accessible via GRID.

Anyway one can assume that the most relevant variables for the rejection of the background are those based on the kinematics described in chapter 4:  $p_T$  of muons  $E_T$  of electrons, the invariant mass of the lepton pairs  $M(\ell\ell)$  and some simple angular variables, such as the angle between the two reconstructed Z bosons in the CMS reference frame.

The resolution on these variables as reconstructed by the current CMS algorithms is described below.

The resolution on muon  $p_T$  was obtained in the following way: for all the reconstructed muons in the event collection, a dedicate algorithm chose the closest generated muon (the one minimizing the separation variable:  $\Delta R_{rg} = \sqrt{(\phi_r - \phi_g)^2 + (\eta_r - \eta_g)^2}$ ).

Then the quantity  $r$  defined as:

$$\Delta_\mu = \Delta(1/p_T) = \frac{\frac{1}{p_T^{rec}} - \frac{1}{p_T^{gen}}}{\frac{1}{p_T^{gen}}}$$

was calculated and its r.m.s.  $\sigma_\Delta = \sqrt{\langle \Delta \rangle^2 - \langle \Delta^2 \rangle}$  derived for some different bins of transverse momentum.

In Fig.5.7-*left* is presented the the mean value of  $\Delta_\mu$  for 6 bins of transverse momentum with its relative r.m.s ( bins are defined such to contain the same number of events). The same was done for the electron transverse energy, defining in this case:

$$\Delta_e = \Delta(E_T) = \frac{E_T^{rec} - E_T^{gen}}{E_T^{gen}}$$

and the resulting plot of mean value in function of the transverse energy bin is presented in fig. 5.7-*right*.

The r.m.s of these two variables  $\Delta_\mu$  and  $\Delta_e$ , i.e. the experimental resolutions on the transverse momentum of muons and on the electrons transverse energy are plotted in function of the  $p_T$  and  $E_T$  bin in figure 5.8

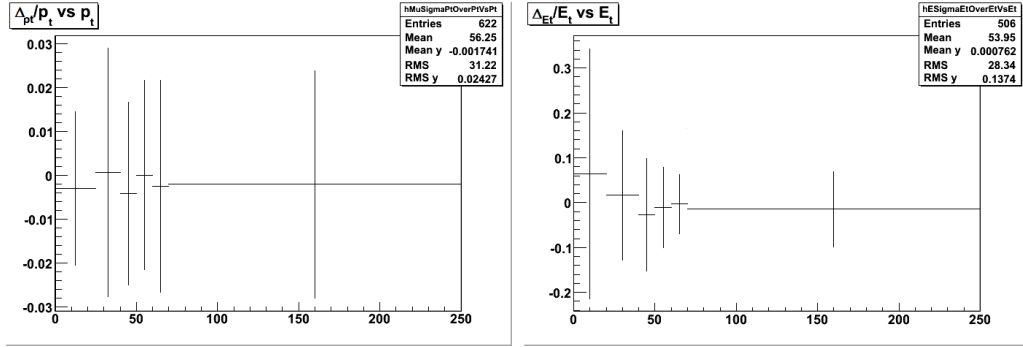


**Figure 5.7:** *Left:* Mean value of  $\Delta_\mu$  as a function of  $p_T$ . *Right:* mean value of  $\Delta_e$  as a function of  $E_T$ . See text

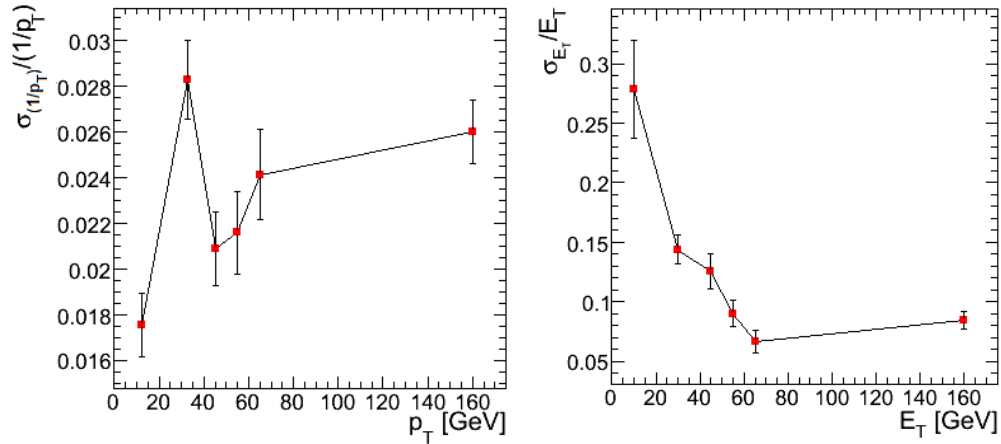


**Figure 5.8:** *Left*  $\sigma_r$  as a function of  $p_T$ . *Right*  $\sigma_{re}$  as a function of  $E_T$

From Fig. 5.8 it can be found the functional dependence on  $p_T$  and  $E_T$  for the muon transverse momentum and electron transverse energy resolutions.

As far as muon  $p_T$  is concerned the resolution grows with increasing  $p_T$  i.e., as anticipated

Resolution on the transverse energy of the electrons instead decreases with increasing  $p_T$

After the resolutions on energy and momentum, the angular resolution of the detector as to be taken into account in variables such as the invariant mass of a leptons pair:

$$M_{\ell^+\ell^-} \simeq 2\sqrt{E^+E^- - p^+p^- \cos \theta_{+,-}}$$

Angular resolution on the polar angle depends very slightly on the transverse energy of the muon or the electron as can be seen in Fig. 5.9

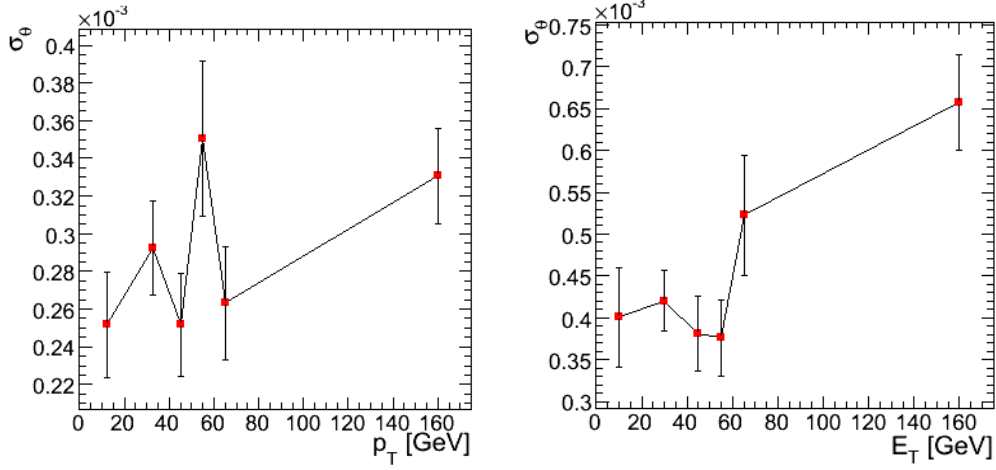


**Figure 5.9:** *Left* Angular resolution on  $\theta$  for muons as a function of  $p_T$ . *Right* Angular resolution in  $\theta$  for electrons as a function of  $E_T$

One can fit these distributions with a constant, yielding a mean value for muon polar angle of about  $\sigma_\theta^\mu \sim 3 \cdot 10^{-4}$  rad and for the electrons polar angle  $\sigma_\theta^e \sim 5 \cdot 10^{-4}$  rad.

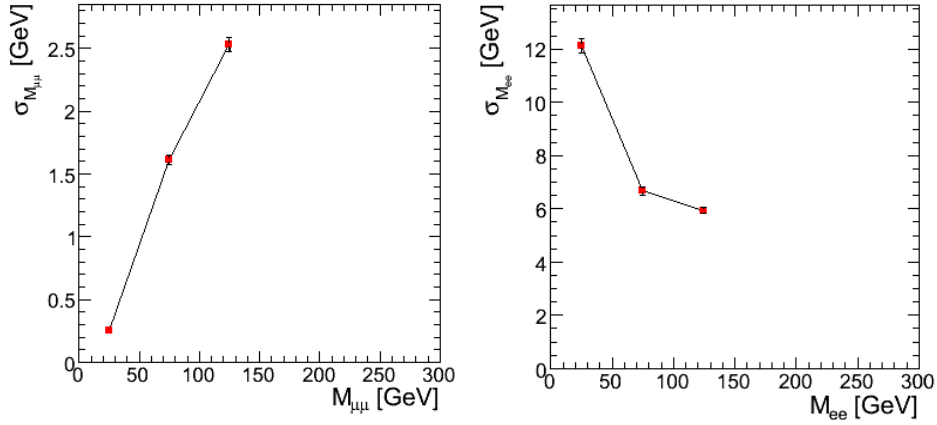


**Figure 5.10:** *Left*  $\sigma_{M(\mu\mu)}$  as a function of  $M_{\mu\mu}$ . *Right*  $\sigma_{M(ee)}$  as a function of  $M_{ee}$

In Fig. 5.10 the resolution on invariant masses for electrons and muons

pairs is presented.

One can notice that the muon pairs invariant mass resolution worsens as the invariant mass itself increases, while the analogue resolution for electrons pairs improves as the mass increases. However the resolution for lepton pairs around the  $Z$  peak for muons is at least twice better than for electrons.

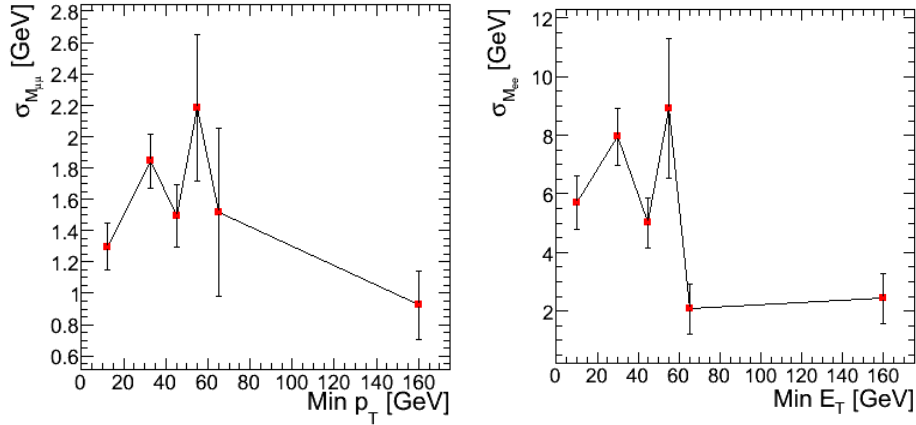


**Figure 5.11:** *Left*  $\sigma_{M(\mu\mu)}$  as a function of  $(p_T)_{min}$ . *Right*  $\sigma_{M(ee)}$  as a function of  $(E_T)_{min}$

Finally in fig.5.11 are presented the invariant mass resolutions for muons and electrons as a function of the softest  $p_T$  or  $E_T$  of the pair.

The trend for both resolutions is rather oscillating but significantly worse for the electrons, due the worse resolution on the energy measurement.

# Summary

The initial work of this thesis described in chapter 4, has dealt with the kinematic analysis of the signal  $H \rightarrow ZZ^* \rightarrow 2\mu 2e$  and backgrounds ( $ZZ^*, t\bar{t}, Zb\bar{b} \rightarrow 2\mu 2e + X$ ) at the generator level.

As far as the reducible backgrounds are concerned the most promising cut variables are the sorted leptons  $p_T$ , with the cut on the softest holding the highest rejective power and the invariant mass of the candidate  $Z$  boson: both in the case of completely non-resonating background  $t\bar{t}$ , on the second candidate  $Z$  for the  $Zb\bar{b}$ , for which at least one leptons pair resonates at the  $Z$  mass.

Then, a study of more refined angular variable in order to reject the reducible background was performed. The most promising variable  $\phi_D$ , angle of decay of Higgs boson, resulted losing most of its rejection power, after minimal preselection and acceptance cuts, in favour of the "simpler" variable  $\theta_{ZZ}$  angle between the the two decaying  $Z$  bosons.

In the last part of this work, a benchmark of the currently implemented CMS High Level Trigger algorithms on signal samples was performed.

The final efficiency for the combined muon and electron trigger paths is found to be at  $98.0 \pm 0.4\%$ , the largest inefficiencies coming mainly from the electron  $E_T$  (spectrum) and  $E/P$  (identification) cuts, and therefore hardly refinable.

# Appendix A

## Electroweak Lagrangian and spontaneous symmetry breaking

Experimental data from a vast number of purely leptonic and semileptonic processes, are consistent with the hypothesis that the leptonic matter field  $\psi_l(x)$  enters in the QFT Lagrangian describing flavour-changing weak interaction through a charged current of the type:<sup>1</sup>

$$J_\alpha(x) = \sum_l \overline{\psi_l(x)} \gamma_\alpha (1 - \gamma_5) \psi_{\nu_l}(x)$$

The corresponding interaction Hamiltonian could be written down as:

$$\mathcal{H}(x) = g_W (J^{\alpha\dagger}(x) W_\alpha(x) + J^\alpha(x) W_\alpha^\dagger(x)) \quad (\text{A.1})$$

where  $g_W$  is an a-dimensional coupling constant and the field  $W_\alpha(x)$  describes weak bosons W.

Interactions such as the one in 1.2 are known as V-A interactions being the charged current  $J_\alpha$  made up by two terms: a vector current term:

$$J_\alpha^V(x) = \sum_l \overline{\psi_l(x)} \gamma_\alpha \psi_{\nu_l}(x)$$

and an axial current term:

---

<sup>1</sup> $\overline{\psi} = \psi^\dagger \gamma_0$ . The operator  $\gamma_5$  is defined as  $\gamma_5 = \gamma^5 = i\gamma^0\gamma^1\gamma^2\gamma^3$ . The  $\gamma^\mu$  ( $\mu = 0, 1, 2, 3,$ ) are the Dirac matrixes defined trough anti-commutation relationship  $\{\gamma^\mu, \gamma^\nu\} = 2g^{\mu\nu}$ , where  $g^{\mu\nu}$  is Minkowski metric tensor  $g^{\mu\nu} = \text{diag}\{1, -1, -1, -1\}$ , being  $\gamma^0$  an hermitian matrix.  $\gamma^5$  hermiticity and unitarity are summarized in the relationships:  $\{\gamma^5, \gamma^\mu\} = 0, \gamma_5^\dagger = \gamma_5, (\gamma_5)^2 = 1$

$$J_\alpha^A(x) = \sum_l \overline{\psi_l(x)} \gamma_\alpha \gamma_5 \psi_l(x)$$

Under parity transformations ( $\mathbf{x} \rightarrow -\mathbf{x}$ )  $J_\alpha^V$  changes sign, while  $J_\alpha^A$  keeps its sign, so globally charged current weak interactions do not conserve parity, since weak hamiltonian does not commute with parity. This effect has been experimentally observed.

This feature carries its most important consequence for neutrinos. Actually, for mass-less particles, such as neutrinos, operator  $(1 - \gamma_5)/2$ , which enters the V-A current, coincides with the projector on left-handed states, i.e.:

$$\psi^L(x) = \frac{1 - \gamma_5}{2} \psi(x)$$

As a direct consequence right-handed neutrinos and left-handed antineutrinos do not interact weakly.

Even if the particle's mass is non-vanishing, the result of applying operator  $(1 - \gamma_5)/2$  on leptonic field is still an helicity eigenstate provided that the energy of the particle is far greater than its rest mass. For neutrinos this is true in very good approximation, even if their mass is non-zero; therefore in the following neutrinos will be considered as massless.

One can observe that for each leptonic family the electroweak interactions involve a left-handed doublet ( $\psi_L$ ) and a right-handed singlet ( $\psi_R$ ).

$$\Psi_L = \begin{pmatrix} \nu_l \\ l \end{pmatrix}_L = \frac{1 - \gamma_5}{2} \begin{pmatrix} \nu_l \\ l \end{pmatrix}$$

$$\Psi_R = (l)_R = \frac{1 + \gamma_5}{2} (l)$$

In this description right-handed neutrino singlet is not included for the above mentioned reasons. For quarks there are two right-handed singlets, one for up type quarks and one for down type quarks.

The EW phenomenology is described by a gauge theory based on  $SU(2)_L \otimes U(1)_Y$  symmetry. As in the SM the left- and right- handed fermions have different transformation properties under this gauge group, the mass terms (of type  $\overline{\psi}_L \psi_R + \text{h.c.}$ ) violate gauge invariance. Also the vector boson masses break the  $SU(2)_L \otimes U(1)_Y$  symmetry. To give masses to the particles, we have to invoke a mechanism that both explains the symmetry breaking and provides masses to fermions and weak bosons and *not* to the electromagnetic field.

Free Lagrangian density of  $SU(2)_L \otimes U(1)_Y$  for vector bosons may be written as the sum of a  $U(1)$  gauge field,  $B_\mu$  and three real gauge vector bosons of  $SU(2)_L$ ,  $W_\mu^A$  with  $A=1,2,3$ .

Requiring symmetry under the gauge group transformations, we obtain:

$$\mathcal{L}_{gauge}^F = -\frac{1}{4} \sum_{A=1}^3 F_{\mu\nu}^A F_A^{\mu\nu} - \frac{1}{4} B_{\mu\nu} B^{\mu\nu} \quad (\text{A.2})$$

where field strength tensors are defined as following equations 1.4 and 1.5:

$$B_{\mu\nu} = \partial_\mu B_\nu - \partial_\nu B_\mu \quad (\text{A.3})$$

$$F_{\mu\nu}^A = \partial_\mu W_\nu^A - \partial_\nu W_\mu^A - g \varepsilon_{ABC} W_\mu^B W_\nu^C \quad (\text{A.4})$$

where  $\varepsilon_{ABC}$  are the structure constants of the non-abelian gauge group  $SU(2)_L$ .

As far as fermion matter-fields are concerned the free Dirac Lagrangian should be:

$$\mathcal{L}_0 = \overline{\psi(x)} \gamma^\mu \partial_\mu \psi(x)$$

in order to obtain an object invariant under  $SU(2)_L \otimes U(1)_Y$  gauge transformations one has to replace ordinary derivatives with covariant derivatives, which for the considered gauge group are:

$$\partial_\mu \longrightarrow D_\mu = \partial_\mu + ig \sum_{A=1}^3 t_L^A W_\mu^A + ig' \frac{Y}{2} B_\mu \quad (\text{A.5})$$

where:

- $t_L^A$  are the  $SU(2)_L$  generators and  $g$  the corresponding coupling constant.
- $Y$  is the weak hypercharge and the generator of  $U(1)_Y$  and  $g'$  the corresponding coupling constant.
- $t_L^A$  obey angular momentum commutation laws:

$$t_L^A = \varepsilon_{ABC} [t_L^B, t_L^C] \quad (\text{A.6})$$

So one can write the SM Lagrangian for fermions as:

$$\mathcal{L}_{ferm} = \bar{\psi}_L \gamma^\mu \left[ i\partial_\mu - g \frac{t_L^A}{2} W_\mu^A - g' \frac{Y}{2} B_\mu \right] \psi_L + \bar{\psi}_R \gamma^\mu \left[ i\partial_\mu - g' \frac{Y}{2} B_\mu \right] \psi_R \quad (\text{A.7})$$

So the symmetric part with respect to  $SU(2)_L \otimes U(1)_Y$  of standard model lagrangian can be written as:<sup>2</sup>

$$\mathcal{L}_{symm} = -\frac{1}{4} \sum_{A=1}^3 F_{\mu\nu}^A F_A^{\mu\nu} - \frac{1}{4} B_{\mu\nu} B^{\mu\nu} + \bar{\psi}_L i\gamma^\mu \partial_\mu \psi_L + \bar{\psi}_R i\gamma^\mu \partial_\mu \psi_R \quad (\text{A.8})$$

One can notice that since  $\psi_R$  is an isosinglet of  $SU(2)_L$  then there is no term in its lagrangian proportional to  $g$ .

Instead  $\psi_L$  is an  $SU(2)_L$  isodoublet:  $\psi_L^{lept} = \begin{pmatrix} \nu_l \\ l \end{pmatrix}$  or  $\psi_L^{quark} = \begin{pmatrix} u^i \\ d^i \end{pmatrix}$

The relationship between  $Y$ ,  $t_L^3$  and  $Q$  (the  $U(1)_{EM}$  generator) is  $Q = t_L^3 + Y/2$ . Quantum numbers of all fermions are listed in Table A.1.

**Table A.1:** Fermions quantum numbers

Fermions	t	$t_L^3$	Q	Y
$\nu_{lL}$	$\frac{1}{2}$	$+\frac{1}{2}$	0	-1
$l_L$	$\frac{1}{2}$	$-\frac{1}{2}$	-1	-1
$l_R$	0	0	-1	-2
$u_L$	$\frac{1}{2}$	$+\frac{1}{2}$	$\frac{2}{3}$	$\frac{1}{3}$
$u_R$	0	0	$\frac{2}{3}$	$\frac{4}{3}$
$d_L$	$\frac{1}{2}$	$-\frac{1}{2}$	$-\frac{1}{3}$	$\frac{1}{3}$
$d_R$	0	0	$-\frac{1}{3}$	$-\frac{2}{3}$

The lagrangian  $\mathcal{L}_{symm}$  in Eq. 1.16 contains fields  $W_\mu^A$   $A=1,2,3$  and  $B_\mu$ . This fields are not the physical fields of electroweak interactions  $W_\mu^\pm$ ,  $Z_\mu$  and  $A_\mu$ . We can identify them correctly interpreting the associated currents. One obtain:

$$W_\mu^\pm = \frac{W_\mu^1 \mp iW_\mu^2}{\sqrt{2}} \quad (\text{A.9})$$

<sup>2</sup>for simplicity only one generic lepton family is discussed here, it is understood that the complete SM Lagrangian should comprehend the sum over all leptonic families and on quarks too, which have as previously discussed two  $SU(2)_L$  isosinglets:  $u_R^i$  and  $d_R^i$

$$\begin{cases} A_\mu = B_\mu \cos\theta_W + W_\mu^3 \sin\theta_W \\ Z_\mu = -B_\mu \sin\theta_W + W_\mu^3 \cos\theta_W \end{cases} \quad (\text{A.10})$$

where  $\theta_W$  is the Weinberg angle, that relates the electroweak coupling costants:

$$g \sin\theta_W = g' \cos\theta_W = e \quad (\text{A.11})$$

In terms of the physical fields Eq. 1.9 can be written as:

$$\mathcal{L}_{symm} = \mathcal{L}_{fermion} + \mathcal{L}_{A\bar{\psi}\psi} + \mathcal{L}_{W\bar{\psi}\psi} + \mathcal{L}_{Z\bar{\psi}\psi} + \mathcal{L}_{gauge} \quad (\text{A.12})$$

where:

- $\mathcal{L}_{fermion} = \bar{\psi} \gamma_\mu \partial_\mu \psi \equiv \bar{\psi}_L \gamma_\mu \partial_\mu \psi_L + \bar{\psi}_R \gamma_\mu \partial_\mu \psi_R$
- $\mathcal{L}_{A\bar{\psi}\psi} = -Q e \bar{\psi} \gamma^\mu \psi A_\mu \equiv -Q e \{ \bar{\psi}_L \gamma_\mu \psi_L + \bar{\psi}_R \gamma_\mu \psi_R \}$
- $\mathcal{L}_{W\bar{\psi}\psi} = -g \bar{\psi} \gamma^\mu \frac{1-\gamma_5}{2} \left[ \frac{t_L^+ W_\mu^-}{\sqrt{2}} + \frac{t_L^- W_\mu^+}{\sqrt{2}} \right] \psi \equiv -g \bar{\psi}_L \gamma^\mu \left[ \frac{t_L^+ W_\mu^-}{\sqrt{2}} + \frac{t_L^- W_\mu^+}{\sqrt{2}} \right] \psi_L$
- $\mathcal{L}_{Z\bar{\psi}\psi} = -\frac{g}{2 \cos\theta_w} \bar{\psi} \gamma_\mu \left[ \frac{1-\gamma_5}{2} t_L^3 - 2Q \sin^2\theta_w \right] \psi Z_\mu$   
 $= -\frac{g}{\cos\theta_w} [\bar{\psi}_L \gamma_\mu t_L^3 \psi_L - Q \sin^2\theta_w \bar{\psi} \gamma_\mu \psi] Z_\mu$
- $\mathcal{L}_{gauge} = -i g_{WWV} [W_{\mu\nu}^\dagger W^{\mu\nu} - W_\mu^\dagger V_\nu W^{\mu\nu} + W_\mu^\dagger W_\nu V^{\mu\nu}]$   
 $-i \frac{g^2}{4} [\varepsilon^{kij} \varepsilon^{klm} g^{\mu\alpha} g^{\nu\beta}] W_\mu^i W_\nu^j W_\alpha^l W_\beta^m$

where  $W_{\mu\nu} = \partial_\mu W_\nu - \partial_\nu W_\mu$ , and  $V_{\mu\nu} = \partial_\mu V_\nu - \partial_\nu V_\mu$   
 $g_{WW\gamma} = e$  and  $g_{WWZ} = e \cdot \cot\theta_W$ .

## A.1 Electroweak Simmetry Breaking

What is commonly called Higgs Mechanism is an extension of spontaneous symmetry breaking mechanism used to create massive vector bosons in a gauge-invariant theory. This procedure, developed by P.W. Higgs, breaks a local symmetry by introducing in the lagrangian density a new complex field of mass  $\mu$  with two components (Higgs doublet) together with an ad hoc potential. The interaction of the new Higgs field, expanded around its vacuum expectation value (v.e.v.), with the gauge field, originates mass terms for the three components of the latter.

The Higgs field apt to generate the described mechanism is a complex doublet  $\phi$  which belonging to the (2,1) representation<sup>3</sup> of  $SU(2)_L \otimes U(1)_Y$ , to be more precise:

$$\phi = \begin{pmatrix} \phi^+ \\ \phi^0 \end{pmatrix} = \begin{pmatrix} \phi^1 + i\phi^2 \\ \phi^3 + i\phi^4 \end{pmatrix}$$

which one has to insert in the Lagrangian density:

$$\mathcal{L}_{Higgs} = [D_\mu \phi]^\dagger D^\mu \phi - V(\phi^\dagger \phi)$$

with  $D_\mu$  the covariant derivative introduced in equation 1.6

$$\mathcal{L}_{Higgs} = \left[ \left( i\partial_\mu - g \frac{t_L^A}{2} W_\mu^A - g' \frac{Y}{2} B_\mu \right) \right]^\dagger \cdot \left[ \left( i\partial_\mu - g \frac{t_L^A}{2} W_\mu^A - g' \frac{Y}{2} B_\mu \right) \right] - V(\phi^\dagger \phi)$$

The usual choice for the Higgs potential, which itself has to be invariant under  $SU(2) \otimes U(1)_Y$  gauge transformations, is:

$$V(\phi^\dagger \phi) = \mu^2 (\phi^\dagger \phi) + \lambda (\phi^\dagger \phi)^2 \quad (\text{A.13})$$

where  $\mu^2 < 0$  and  $\lambda > 0$ . One has to limit Higgs potential self-interaction terms to the fourth power in order to ensure theory's renormalizability. The combination of signs is crucial for the model. If  $\mu^2 > 0$  this potential does not induce any symmetry breaking, while if  $\lambda < 0$  Higgs potential becomes unbounded below and the vacuum instable (no lower bound to minimum energy). Spontaneous symmetry breaking is induced if the minima of  $V(\phi)$ , which is the classical analogue of the quantum mechanical vacuum state, is obtained for non-vanishing  $\phi$  values. It is simple to verify that minimizing the Higgs potential as a function of  $\phi$ ,

$$\frac{\partial V(\phi)}{\partial \phi} = \frac{\partial}{\partial \phi} (\mu^2 (\phi^\dagger \phi) + \lambda (\phi^\dagger \phi)^2) = 0$$

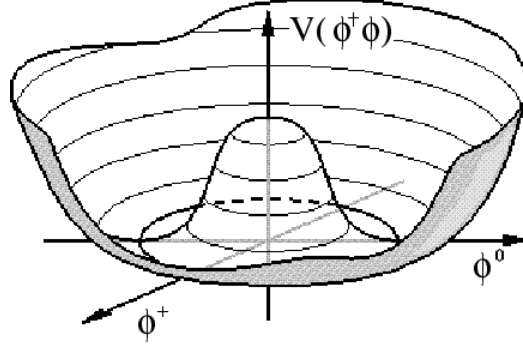
with the requested conditions on  $\mu^2$  and  $\lambda$ , the minimum is reached for:

$$\phi_{min}^{class} = \sqrt{\frac{-\mu^2}{2\lambda}} \quad (\text{A.14})$$

For the quantum vacuum state conventionally we define:

---

<sup>3</sup>That means simply that the Higgs field is an isodoublet of  $SU(2)_L$  and has  $Y=1$

**Figure A.1:** Shape of the Higgs potential for different signs of  $\mu^2$  and  $\lambda$ 

$$\langle 0|\phi(x)|0\rangle \equiv \frac{1}{\sqrt{2}} \begin{pmatrix} 0 \\ v \end{pmatrix} \quad (\text{A.15})$$

with  $v^2 = \frac{-\mu^2}{2\lambda}$ . Since at tree level  $m_H^2 \sim 2\lambda v^2$ , spontaneous symmetry breaking with Higgs mechanism implies  $m_H \neq 0$ . From experimental measurement  $v = (G_F)^{-\frac{1}{2}} \sim 246 \text{ GeV}$ .

It is possible to look at the Higgs mechanism as a perturbation of the vacuum introducing a field  $H(x)$  with v.e.v = 0:

$$\phi_{per} = \frac{1}{\sqrt{2}} \begin{pmatrix} 0 \\ v + H(x) \end{pmatrix} \quad (\text{A.16})$$

Actually one could rewrite Eq. (1.17) in a more convenient (but approximate) form:

$$\phi(x) \cong \frac{e^{i\xi(x)\cdot t_L}}{\sqrt{2}} \begin{pmatrix} 0 \\ v + H(x) \end{pmatrix} \quad (\text{A.17})$$

where  $\xi^{i=1,2,3}$  are the Goldstone bosons and  $H(x)$  is the field associated to Higgs boson. The exponential term is absorbed ("gauged away") by choosing a specific  $SU(2)_L \otimes U(1)_Y$  gauge. So  $SU(2)_L$  symmetry breaks down and the Goldstone bosons disappear.

The boson fields acquire their masses by coupling to the vacuum value of the Higgs field. Since the minimum for the Higgs field is invariant for  $U(1)$  transformation, the electromagnetic  $U(1)$  symmetry is therefore unbroken and the photon remains massless. This invariance is guaranteed by the condition:

$$Q\phi_0 = \left(t_L^3 + \frac{Y}{2}\right)\phi_0 = 0$$

and therefore:

$$\phi'_0 = e^{i\epsilon Q}\phi_0 = e^{i\epsilon(x)\left(t_L^3 + \frac{Y}{2}\right)}\phi_0 = \left[1 + \epsilon(x)\left(t_L^3 + \frac{Y}{2} + \dots\right)\right]\phi_0 = \phi_0 \quad \forall \epsilon(x)$$

and that guarantees  $U(1)_{EM}$  gauge invariance for vacuum state, provided the Higgs field has quantum numbers:  $T=\frac{1}{2}$ ,  $T_3 = -\frac{1}{2}$ ,  $Y=+1$ .

As one can notice the term in Eq. 1.20 that endows gauge bosons with mass is:

$$\mathcal{L}_{mass}^{bos} = \left[\left(-g\frac{t_i}{2}W_\mu^i - \frac{g'}{2}B_\mu\right)\phi_0\right]^\dagger \left[\left(-g\frac{t_i}{2}W^{i\mu} - \frac{g'}{2}B^\mu\right)\phi_0\right]$$

that writing explicitly  $\phi_0$  becoms

$$\mathcal{L}_{mass}^{bos} = \frac{1}{8}g^2v^2 [(W_\mu^1)^2 + (W_\mu^2)^2] + \frac{1}{8}v^2(g'B_\mu - gW_\mu^3)(g'B_\mu - gW_\mu^3) \quad (\text{A.18})$$

In order to interpret correctly in terms of physical fields the mass lagrangian, it is convenient to introduce the substitution:

$$W^\pm = \frac{W^1 \mp iW^2}{\sqrt{2}} \quad (\text{A.19})$$

and so, for what concerns the W boson mass lagrangian, one obtains:

$$\mathcal{L}_{mass}^W = \frac{1}{8}g^2v^2 [(W_\mu^1)^2 + (W_\mu^2)^2] = \left(\frac{1}{2}gv\right)^2 (W^+)_\mu(W^-)^\mu \quad (\text{A.20})$$

remembering that for a complex field a mass term is in the form  $M^2(W^+)_\mu(W^-)^\mu$  one can identify mass value of  $W^+$  and  $W^-$  with  $M_W = \frac{1}{2}gv$ .

The second term in Eq. 1.19 has to describe a massive vector boson (physically corresponding to  $Z^0$ 's field  $Z^\mu$ ) and the massless photon  $\gamma$  field ( $A^\mu(x)$ ). In order to obtain this one can rewrite the term in matrix form:

$$\mathcal{L}_{mass}^{neutral} = \frac{1}{8}v^2(g'B_\mu - gW_\mu^3)(g'B_\mu - gW_\mu^3) = \frac{1}{8}v^2(W_\mu^3 B_\mu) \begin{pmatrix} g^2 & -gg' \\ -gg' & g^2 \end{pmatrix} \begin{pmatrix} W_3^\mu \\ B^\mu \end{pmatrix} \quad (\text{A.21})$$

rotating the vector  $(W_\mu^3 \ B_\mu)$  in order to diagonalize the mass matrix:

$$\mathcal{M}_{mass} = \frac{1}{4}v^2 \begin{pmatrix} g^2 & -gg' \\ -gg' & g'^2 \end{pmatrix} \quad (\text{A.22})$$

diagonalization yields:

$$\mathcal{M}_{mass} - \lambda \mathbb{I} = \frac{1}{4}v^2 \begin{pmatrix} g^2 - \lambda & -gg' \\ -gg' & g'^2 - \lambda \end{pmatrix} = 0 \quad (\text{A.23})$$

Eigenvalues of Eq. (1.24) are:  $\lambda_1 = 0$  (as required in the hypothesis of a massless photon), and  $\lambda_2 = \frac{1}{4}v^2(g^2 + g'^2)$ ; this allows to identify mass eigenstates as in the relationship:

$$\begin{pmatrix} A_\mu \\ Z_\mu \end{pmatrix} = \frac{1}{\sqrt{g^2 + g'^2}} \begin{pmatrix} g & g' \\ -g' & g \end{pmatrix} \begin{pmatrix} B_\mu \\ W_\mu^3 \end{pmatrix}$$

The mass term for vector bosons lagrangian can be written then:

$$\mathcal{L}_{mass}^{bos} = M_W^2 (W^+)_\mu (W^-)^\mu + \frac{1}{2} M_Z^2 Z_\mu Z^\mu$$

and we have the identifications:

$$M_W = \frac{1}{2}gv \quad (\text{A.24})$$

$$M_Z = \frac{1}{2}v\sqrt{g^2 + g'^2} \quad (\text{A.25})$$

The inequality  $M_Z \neq M_W$  is due to the weak mixing between fields  $W_\mu^3$  and  $B_\mu$ , and actually in the limit  $\theta_W \rightarrow 0$ ,  $M_Z \rightarrow M_W$ .

We can also define a very important parameter in the theory, the Weinberg angle  $\theta_W$ :

$$\tan\theta_W = \frac{g'}{g} \quad (\text{A.26})$$

Implicitly we have also obtained  $M_A = 0$ , which is a control of theory self-consistency (not a prediction), since the model was built requiring not to break down the electromagnetic U(1) symmetry. Another important relationship is the following:

$$\frac{M_Z}{M_W} = \cos\theta_W \quad (\text{A.27})$$

This expression is fundamental since it links the theory parameter  $\theta_W$  with the observables  $M_W$  and  $M_Z$ .

Another very important result of Weinberg theory is the possibility to endow all fermions with masses, simply by adding an interaction Lagrangian with Yukawa-like couplings, without breaking explicitly the underlying  $SU(2)_L \otimes U(1)_Y$  symmetry as in mass terms like:

$$-m_l \bar{l}l = -m_l (\bar{l}_R l_L + \bar{l}_L l_R) \quad (\text{A.28})$$

Mass term Lagrangian for leptons can be written:

$$\mathcal{L}_{mass}^{ferm} = G_l [\bar{\Psi}_L \phi \Psi_R + \bar{\Psi}_R \phi \Psi_L] \quad (\text{A.29})$$

as:

$$\mathcal{L}_{mass}^{lept} = -\frac{G_l v}{\sqrt{2}} (\bar{l}_L l_R + \bar{l}_R l_L) - \frac{G_l}{\sqrt{2}} (\bar{l}_L l_R + \bar{l}_R l_L) H(x) \quad (\text{A.30})$$

where  $G_l$  is the leptonic Yukawa coupling constant.

We can immediately identify the lepton mass as:

$$m_l = \frac{G_l v}{\sqrt{2}}$$

that gives:

$$\mathcal{L}_{mass}^{lept} = -m_l \bar{l}l - \frac{1}{2} g \frac{m_l}{M_W} \bar{l}l H(x) \quad (\text{A.31})$$

Being  $G_l$  arbitrary, the lepton mass cannot be predicted, and rather it is its experimental value which determines the Yukawa coupling. The second term in Eq. 1.49 is the one associated with interaction vertex factor for fermion-antifermion current with Higgs field coupling:

$$vtx(H^0 f \bar{f}) \implies -\frac{1}{2} i g \frac{m_f}{M_W}$$

and this shows how Higgs field interactions involving heavier fermions are favoured.

As far as quarks are concerned the situation is more complicated because there are two weak isospin singlets for each family. Moreover weak interactions in general mix flavour eigenstates of quarks, so weak interactions eigenstates do not coincide with mass eigenstates. So the mass term lagrangian for quark families has to be written in the form:

$$\mathcal{L}_{mass}^q = -(G_d)^{ij} (\bar{u}_i \bar{d}'_i)_L \phi (d_j)_R - (G_u)^{ij} (\bar{u}_i \bar{d}'_i)_L \phi_c (u_j)_R + h.c.$$

where we have used the charged conjugate of the Higgs doublet in order to preserve  $SU(2)_L \otimes U(1)_Y$  gauge invariance:

$$C : \phi \longrightarrow \phi_c = \begin{pmatrix} -\bar{\phi}_0 \\ \phi_- \end{pmatrix} = \frac{1}{\sqrt{2}} \begin{pmatrix} v + H(x) \\ 0 \end{pmatrix}$$

It is understood that  $u_i$  and  $d'_i$  are weak interaction eigenstates:

$$\begin{cases} u_i & i = 1, 2, 3 \Rightarrow (u, c, t) \\ d'_i = \sum_{k=1}^3 U_{ik}^{CKM} d_k & d_i; i = 1, 2, 3 \Rightarrow (d, s, b) \end{cases}$$

where  $U^{CKM}$  is Cabibbo-Kobayashi-Maskawa mixing matrix. In the end mass lagrangian term for quarks assumes the form:

$$\mathcal{L}_{mass}^q = \sum_{k=1}^3 \left[ -\mathcal{M}_d^i \bar{d}_i d_i - \mathcal{M}_u^i \bar{u}_i u_i - \frac{1}{2} \frac{g}{M_W} \mathcal{M}_d^i \bar{d}_i d_i H(x) - \frac{1}{2} \frac{g}{M_W} \mathcal{M}_u^i \bar{u}_i u_i H(x) \right]$$

where:

$$\begin{cases} \mathcal{M}_d^i \delta_{ij} = \frac{(G_d)_{ik}^T U_{kj}^\dagger v}{\sqrt{2}} \\ \mathcal{M}_u^i \delta_{ij} = \frac{(G_u)_{ij} v}{\sqrt{2}} \end{cases}$$

As a consequence Higgs field coupling preserves flavour of quarks. Finally the Higgs Sector Lagrangian after symmetry breaking can be written as:

$$\mathcal{L}_{Higgs} = \mathcal{L}_H + \mathcal{L}_{HW} + \mathcal{L}_{HZ} + \mathcal{L}_{YC} \quad (\text{A.32})$$

where:

- $\mathcal{L}_H = \frac{1}{2} \partial_\mu H \partial^\mu H - \lambda v^2 H^2 - 2\lambda v H^3 - \lambda H^4$
- $\mathcal{L}_{HW} = \frac{1}{2} g^2 v^2 W^{\mu+} W_\mu^- + \frac{1}{2} g^2 v H W^{\mu+} W_\mu^- + \frac{1}{4} g^2 H^2 W^{\mu+} W_\mu^-$
- $\mathcal{L}_{HZ} = \frac{1}{8} \frac{g^2 v^2}{\cos^2 \theta_W} Z^\mu Z_\mu + \frac{1}{4} \frac{g^2 v}{\cos^2 \theta_W} H Z^\mu Z_\mu + \frac{1}{8} \frac{g^2}{\cos^2 \theta_W} H^2 Z_\mu Z^\mu$
- $\mathcal{L}_{YC} = -\frac{G_F}{2} v (g_d \bar{d} d + g_u \bar{u} u) - \frac{G_F}{2} H (g_d \bar{d} d + g_u \bar{u} u)$

The Higgs mechanism allows the incorporation of the weak boson masses while preserving the renormalizability of the theory. A theory based on a lagrangian density which does not respect the gauge symmetry is unrenormalizable and loses therefore all predictive power. Conversely, in a spontaneous broken gauge theory, the symmetry is in a sense still present; it is merely "hidden" by our choice of the ground state and the theory can be shown to

**Table A.2:** SM Higgs sector couplings with fermions and bosons

	Mass	Single Coupling	Double Coupling
H	$v\sqrt{2\lambda}$	$\frac{m_H^2}{v}$	$\frac{m_H^2}{2v^2}$
W	$\frac{1}{2}gv$	$2\frac{m_W^2}{v}$	$\frac{m_W^2}{v^2}$
Z	$\frac{1}{2}\frac{gv}{\cos\theta_W}$	$2\frac{m_Z^2}{v}$	$\frac{m_Z^2}{v^2}$
fermion	$\frac{G_F}{2}vg_f$	$\frac{m_f}{v}$	—

be renormalizable. The Higgs mechanism gives rise to three massive gauge bosons and a massless one, corresponding to a total of eleven degrees of freedom. Since the initial number of independent fields was twelve (four massless vector bosons with two polarization states each and four scalar fields), one additional scalar gauge boson should appear as a real particle. This particle is the Higgs Boson. When the gauge symmetry is spontaneously broken three massless real fields, the Goldstone bosons, disappear and the W and the Z acquire masses. The degree of freedom linked to the Goldstone boson becomes the longitudinal degree of freedom of the vector bosons.

We can summarize the SM couplings for the Higgs sector couplings in this table A.2:

## A.2 Standard Model Lagrangian and couplings

Now we have the complete Standard Model Lagrangian density which can be written:

- $\mathcal{L}_{SM} = -\frac{1}{4} \sum_{A=1}^3 W_{\mu\nu}^A W_A^{\mu\nu} - \frac{1}{4} B_{\mu\nu} B^{\mu\nu}$
- $+ \sum_L \bar{L} \gamma^\mu (i\partial_\mu - g \frac{1}{2} t_{LA} W_\mu^A - g' \frac{Y}{2} B_\mu) L$
- $+ \sum_R \bar{R} \gamma^\mu (i\partial_\mu - g' \frac{Y}{2} B_\mu) R$
- $+ |(i\partial_\mu - g \frac{1}{2} t_L^A W_\mu^A - g' \frac{Y}{2} B_\mu) \phi|^2 - \mu^2 \phi^\dagger \phi - \lambda (\phi^\dagger \phi)^2$
- $-(G_1 \bar{L} \phi R + G_2 \bar{L} \phi_c R + h.c.)$

After spontaneous symmetry breaking of  $SU(2)_L \otimes U(1)_Y$  down to  $U(1)_{EM}$ , the interactions between fermions and vector bosons are specified by the Lagrangian density:

$$\begin{aligned} \mathcal{L}_{int} = & \\ -\frac{g'}{e} J_{EM}^\mu [ & -\sin\theta_W Z_\mu(x) + \cos\theta_W A_\mu(x)] - J_3^\mu(x) \{g[Z_\mu(x) + \sin\theta_W A_\mu(x)] \\ & -g' [-\sin\theta_W Z_\mu(x) + \cos\theta_W A_\mu(x)]\} \end{aligned}$$

where  $J_{EM}^\mu = e\bar{\psi}\gamma^\mu\psi$  is the electromagnetic current and  $J_3^\mu = \bar{\psi}\gamma^\mu\frac{1-\gamma_5}{2}t_3\psi$

We want to identify gauge field  $A_\mu$  with the electromagnetic field, so it should couple with electric charge in the usual way, i.e. through the term  $-J_{EM}^\mu A_\mu(x)$  in the interaction lagrangian. This means that in the interaction lagrangian the coefficient before  $J_3^\mu A_\mu(x)$  should be vanishing and that the one before  $J_{EM}^\mu A_\mu(x)$  should be -1.

Therefore we require:

$$e = g\sin\theta_W = g' \cos\theta_W \quad (\text{A.33})$$

and using the definition of Fermi constant we obtain:

$$\frac{G_F}{\sqrt{2}} = \frac{g^2}{(2\sqrt{2})^2} \frac{1}{(M_W)^2} \quad (\text{A.34})$$

which permits to fix the electroweak symmetry break scale trough:

$$v^2 = \frac{1}{\sqrt{2}G_F} \simeq (246\text{GeV})^2 \quad (\text{A.35})$$

Another very important relationship that links the so-called precision observables ( $G_F, \theta_W, \alpha_{em}$ ):

$$M_Z^2 = \frac{\pi\alpha_{em}}{\sqrt{2}G_F \sin^2\theta_W \cos^2\theta_W} \quad (\text{A.36})$$

In this sense the so called Weinberg-Salam model represents a unification of weak and electromagnetic interactions, since  $e \sim g \sim g'$ . Only once the spontaneous symmetry breaking mechanism breaks down the original symmetry to U(1), since Z and W bosons acquire masses, real physical differences emerge.

# Appendix B

## CMS Software and computing tools

In a modern high-energy physics experiment, most of the data analysis is done using computers. When the data from LHC will be processed, only a very small fraction of the events selected will ever be directly examined by the physicists using visualization programs. Most tasks, such as monitoring, triggering, calibration, are computerized. To handle these data amounts efficiently and reliably, many software tools have been developed for physics processes simulation, detector simulation, event triggering and reconstruction, and data analysis, to name just a few.

For this study signal and background events were generated using PYHTIA and other Montecarlo generators (COMPHEP, PHANTOM, TOPREX). Then they were processed with a full simulation of particle interactions with matter, detector response, signal digitalization and reconstruction with CMSSW, CMS software framework.

This Chapter gives a brief overview of the most common software tools in use at the CMS experiment, especially of those related to this thesis.

### B.1 Priority and Challenges for CMS software

The major challenges for LHC software and computing today include:

- Event data storing demands huge amount of disk space (raw event is  $\mathcal{O}(2\text{ MB})$ )
- At design luminosity of  $10^{34}\text{ cm}^{-2}\text{ s}^{-1}$  approximately 17 minimum bias events per crossing are produced. With the bunch crossing time so

short (25ns) a realistic detector digitalization has to take into account the fact that events from different bunch crossings contribute to the digitization. At least 9 crossing contribute to calorimetry digitalization while muon digitization is affected by even more crossings. Typically, information from more than 150 ( $9 \times 17$ ) minimum bias events is needed for each signal event. Thus for one million signal events it would be required to generate more than 150 millions minimum bias events. This is impossible with the current available CPU, storage, etc. instead the minimum bias events are included in the digitization step and the simulated minimum bias events are recycled. For that a data set consisting of a few hundred thousands minimum bias events has been created. For each signal event the necessary minimum bias events are randomly selected in a straight-forward manner. Problems can arise when one single minimum bias by itself would trigger the detector, since this event would trigger many times. Therefore is necessary to filter the minimum bias events. The events removed have to be taken into account. The advantage of this approach is that is easy to study the same signal events at different luminosities and also with and without pile-up. The size of the 150 minimum bias events which have to be read in for each signal event is greater than 50 MB This results in a massive data movement problem.

- The CMS Tracker is immersed in a high magnetic field of 4 Tesla. The tracks of low momentum charged particles loop in the magnetic field and can persist for many crossings. This requires track finding in a very complex environment.
- The total tracker material adds up to 1 radiation length resulting in lots of bremsstrahlung for the electrons. This makes matching tracks to calorimeter clusters a non trivial task (see Figure 3.1).

## B.2 CMSSW Application Framework

The overall collection of software of the CMS experiment collaboration, referred to as CMSSW, is built around a Framework, an Event Data Model (EDM), and Services needed by the simulation, calibration and alignment, and reconstruction modules that process event data so that physicists can perform analysis. The primary goal of the Framework and EDM is to facilitate the development and deployment of reconstruction and analysis software.

The CMSSW framework implements a software bus model wherein there is one executable, called *cmsRun*, and many plug-in modules which run al-

gorithms. The same executable is used for both detector and Monte Carlo data. This framework is distinct from a more traditional approach in which several executables are used, one per task or set of tasks.

The CMSSW executable, *cmsRun*, is configured at run time by the user's job-specific configuration file. This file tells *cmsRun* which data to use, which modules to run, which parameter settings to use for each module, and in what order to run the modules. Required modules are dynamically loaded at the beginning of the job.

The CMS Event Data Model (EDM) is centered around the concept of an Event as a C++ object container for all RAW and reconstructed data pertaining to a physics event. During processing, data are passed from one module to the next via the Event, and are accessed only through the Event. All objects in the Event may be individually or collectively stored in ROOT files, and are thus directly browsable in ROOT. This allows tests to be run on individual modules in isolation. Auxiliary information needed to process an Event is accessed via the EventSetup. The CMSSW code is contained in a single CVS repository, under the project name CMSSW.

The Framework provides ways to guarantee reproducibility by automatically maintaining and recording sufficient provenance information for all application results.

### B.2.1 Modular Architecture

A module is a piece (or component) of CMSSW code that can be plugged into the CMSSW executable *cmsRun*. Each module encapsulates a unit of clearly defined event-processing functionality.

When preparing an analysis job, the user selects which modules to run, and specifies the parameters for his analysis via a configuration file. The module is called for every event according to the path statement in the configuration file.

There are six types of dynamically loadable processing modules, whose interface is specified by the framework:

- **Source** Reads in an Event from a ROOT file or generates an Event for Monte Carlo, gives the Event status information (such as Event number), and can add data directly or set up a call-back system to retrieve the data on the first request. Examples include the *DaqSource* which reads in Events from the global DAQ, and the *PoolSource* which reads Events from a ROOT file.
- **EDProducer** CMSSW uses the concept of producer modules and products, where producer modules (*EDProducers*) read in data from

the Event in one format, produce something from the data, and output the product, in a different format, into the Event. A succession of modules used in an analysis may produce a series of intermediate products, all stored in the Event.

- **EDFilter** reads data from the Event and returns a Boolean value that is used to determine if processing of that Event should continue for that path.
- **EDAnalyzer** Studies properties of the Event. An EDAnalyzer reads data from the Event but is neither allowed to add data to the Event nor effect the execution of the path. Typically an EDAnalyzer writes output, e.g., to a ROOT Histogram.
- **EDLooper** A module which can be used to control 'multi-pass' looping over an input sources data. It can also modify the EventSetup at well defined times. This type of module is used in the track based alignment procedure.
- **OutputModule** Reads data from the Event, and once all paths have been executed, stores the output to external media.

## B.2.2 Events

Physically, an event is the result of a single readout of the detector electronics and the signal that will (in general) have been generated by particles, tracks, energy deposits, present in a number of bunch crossings.

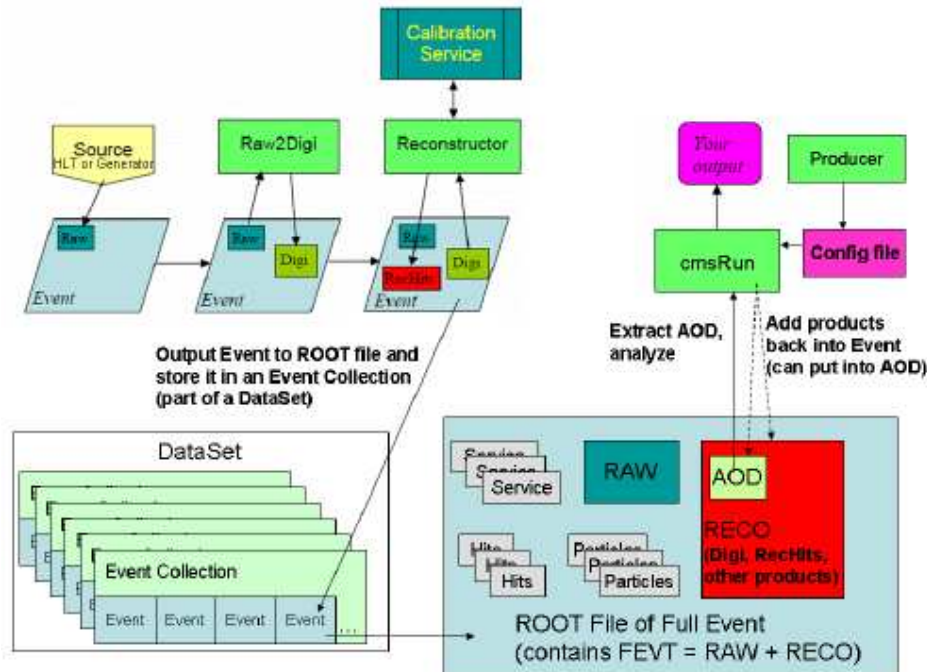
The task of the online Trigger and Data Acquisition System is to select, out of the millions of events recorded in the detector, the most interesting 100 or so per second, and then store them for further analysis. An event has to pass two independent sets of tests, or Trigger Levels, in order to qualify. The tests range from simple and of short duration (Level-1) to sophisticated ones requiring significantly more time to run (High Levels 2 and 3, called HLT). In the end, the HLT system creates RAW data events containing:

- the detector data,
- the level 1 trigger result
- the result of the HLT selections (HLT trigger bits)
- and some of the higher-level objects created during HLT processing

In software terms, an Event starts as a collection of the RAW data from a detector or MC event, stored as a single entity in memory. As the event data is processed, products (of producer modules) are stored in the Event as reconstructed (RECO) data objects. The Event thus holds all data that was taken during a triggered physics event as well as all data derived from the taken data. The Event also contains metadata describing the configuration of the software used for the reconstruction of each contained data object and the conditions and calibration data used for such reconstruction. The Event data is output to files browsable by ROOT. The event can be analyzed with ROOT and used as an n-tuple for final analysis.

Products in an Event are stored in separate containers, organizational units within an Event used to collect particular types of data separately. There are particle containers (one per particle), hit containers (one per sub-detector), and service containers for things like provenance tracking. The full event data (FEVT) in an Event is the RAW plus the RECO data. Analysis Object Data (AOD) is a subset of the RECO data in an event; AOD alone is sufficient for most kinds of physics analysis.

**Figure B.1:** CMSSW framework Event processing workflow



Event Format	Content	Purpose	Event size [MB]	Evts/yr [ $\times 10^9$ ]	Data volume [PB]
DAQ-RAW	Detector data in FED format and the L1 trigger result	Primary record of physics event. Input to online HLT	$1 \div 1.5$	1.5	-
RAW	Detector data after online formatting, L1 and HLT results (trigger bits)	Input to T0 reconstruction, primary archive of data at CERN	1.5	3.3	5.0
RECO	Reconstructed objects (tracks, vertices, jets, muons, etc., including hits/clusters)	Output of T0 reconstruction and subsequent rec. passes Refitting of tracks, etc.	0.25	8.3	2.1
AOD	Reconstructed objects (tracks, vertices, jets, muons, etc.): part of RECO	Physics analysis	0.05	53	2.6
TAG	Run/event number, high-level physics physics objects, e.g. used to index events	Rapid identification of events for further study (event directory)	0.01	-	-
FEVT	Term used for RAW + RECO		-	-	-

**Table B.1:** CMS event formats at LHC start-up, assuming a luminosity of  $\mathcal{L} = 2 \times 10^{33} \text{ cm}^{-2} \text{ s}^{-1}$

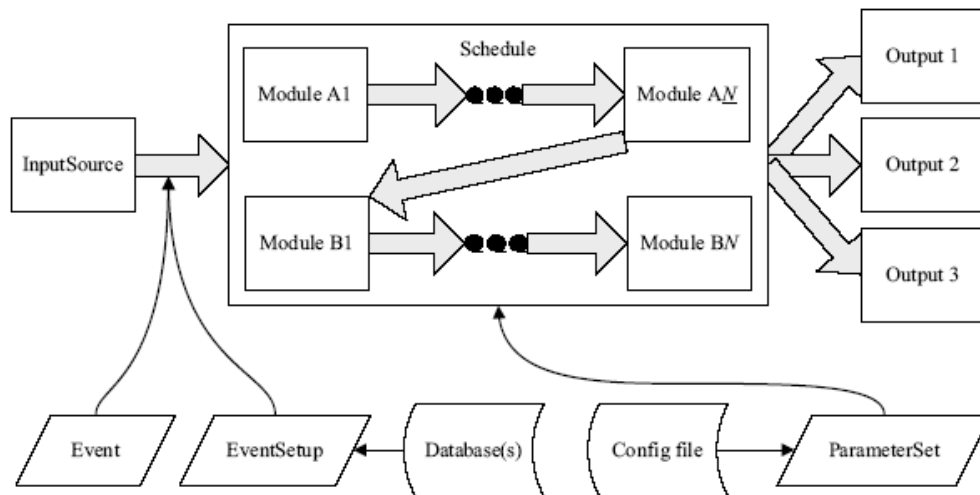
The tier-structured CMS Computing Model governs which portions of the Event data are available at a given tier. For event grouping, the model supports both physicist abstractions, such as dataset and event collection, as well as physical packaging concepts native to the underlying computing and Grid systems, such as files. Here is a framework diagram illustrating how an Event changes as data processing occurs:

## B.3 The Processing Model

Events are processed by passing the Event through a sequence of modules.

The exact sequence of modules is specified by the user via a path statement in a configuration file. A path is an ordered list of Producer/Filter/Analyzer modules which sets the exact execution order of all the modules. When an Event is passed to a module, that module can get data from the Event and put data back into the Event. When data is put into the Event, the provenance information about the module that created the data will be stored with the data in the Event. The components involved in the framework and EDM are shown here:

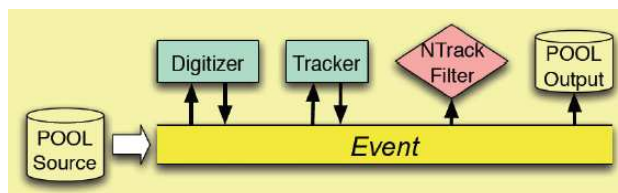
**Figure B.2:** Event Processing flowchart



In a second figure below, we see a Source that provides the Event to the framework. (The standard source which uses POOL is shown; it combines C++ Object streaming technology, such as ROOT I/O, with a transaction-safe relational database store.) The Event is then passed to the execution paths. The paths can then be ordered into a list that makes up the schedule for the process. Note that the same module may appear in multiple paths, but the framework will guarantee that a module is only executed once per Event. Since it will ask for exactly the same products from the event and produce the same result independent of which path it is in, it makes no sense to execute it twice. On the other hand a user designing a trigger path should not have to worry about the full schedule. Each path should be executable

by itself, in that modules within the path, only ask for things they know have been produced in a previous module in the same path or from the input source.

**Figure B.3:** Event processing



## B.4 CMS computing Model

CMS presents challenges not only in terms of the physics to discover and the detector to build and operate, but also in terms of the data volume and the necessary computing resources. Data sets and resource requirements are at least an order of magnitude larger than in previous experiments.

CMS computing and storage requirements would be difficult to fulfill at any one place, for both technical and funding reasons. Therefore, the CMS computing environment has been constructed as a distributed system of computing services and resources that interact with each other as Grid services. The set of services and their behaviour together comprise the computing, storage and connectivity resources that CMS uses to do data processing, data archiving, Monte Carlo event generation, and all kinds of computing-related activities.

The computational infrastructure is intended to be available to CMS collaborators, independently of their physical locations, and on a fair share basis.

### B.4.1 Tier architecture of computing resources

The computing centres available to CMS around the world are distributed and configured in a tiered architecture that functions as a single coherent system. Each of the three tier levels provides different resources and services:

### Tier-0 (T0)

The first tier in the CMS model, for which there is only one site, CERN, is known as Tier-0 (T0). The T0 performs several functions. The standard workflow is as follows:

- accepts RAW data from the CMS Online Data Acquisition and Trigger System (TriDAS)
- repacks the RAW data received from the DAQ into primary datasets based on physics attributes (e.g., their trigger path). The number of datasets is not set yet; it may be as high as 50.
- archives the repacked RAW data to tape.
- distributes RAW data sets among the next tier stage resources (Tier-1) so that two copies of every piece of RAW data is saved, one at CERN, another at a Tier-1.
- performs Prompt Calibration in order to get the calibration constant needed to run the reconstruction.
- feeds the RAW datasets to reconstruction.
- performs prompt first pass reconstruction which writes the RECO and Analysis Object Data (AOD) extraction.
- distributes the RECO datasets among Tier-1 centers, such that the RAW and RECO match up at each Tier-1
- distributes full AOD to all Tier-1centers

The T0 does not provide analysis resources. The T0 merges output files if they are too small. (This will affect RECO and AOD, and maybe AlcaReco; under certain repacker scenarios one could even imagine merging RAW data files but this will be avoided as much as possible.) The T0 also maintains the CMS-CAF (CERN Analysis Facility). The CAF integrates services associated with T1 and T2 centers and performs latency critical, non-automated activities. The CAF is not needed for normal Tier0 operation; it is intended for short-term, high priority, human-operated calibration, physics validation and analysis. For example, the CAF would be used for very fast physics validation and analysis of the *Express Stream* (a subset of the data that is tagged by Online and then processed as quickly as possible).

### Tier-1 (T1)

There is a set of (currently) seven Tier-1 (T1) sites, which are large centers in CMS collaborating countries. Tier-1 sites will in general be used for large-scale, centrally organized activities and can provide data to and receive data from all Tier-2 sites. Each T1 center:

- receives some subset of the 50 or so datasets from the T0
- provides tape archive of FEVT
- provides substantial CPU power for: re-reconstruction,skimming, calibration, AOD extraction
- distributes RECOs, skims and AOD to its (the T1's) associated group of next tier stage resources (Tier-2)
- provides custodial storage (second secure copy) of the RAW data that it receives (the subset of the datasets from T0)
- provides secure storage for MC events generated by the T2's (described below)

### Tier-2 (T2)

A more numerous set of smaller Tier-2 (T2) centres, but with substantial CPU resources, provide capacity for user analysis, calibration studies, and Monte Carlo production. T2 centers provide limited disk space, and no tape archiving. T2 centers rely upon T1s for access to large datasets and for secure storage of the new data (generally Monte Carlo) produced at the T2. The MC production in Tier-2's will in general be centrally organized, but all other activities will be user driven and organized by the Tier-2 responsables in collaboration with physics groups, regional associations and local communities.

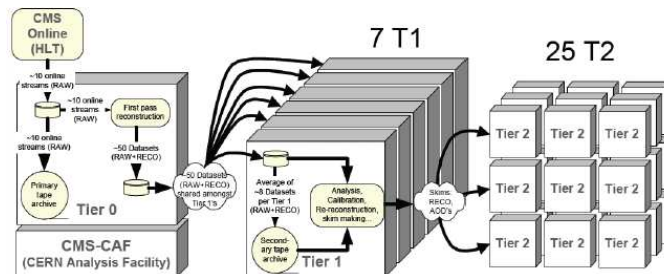
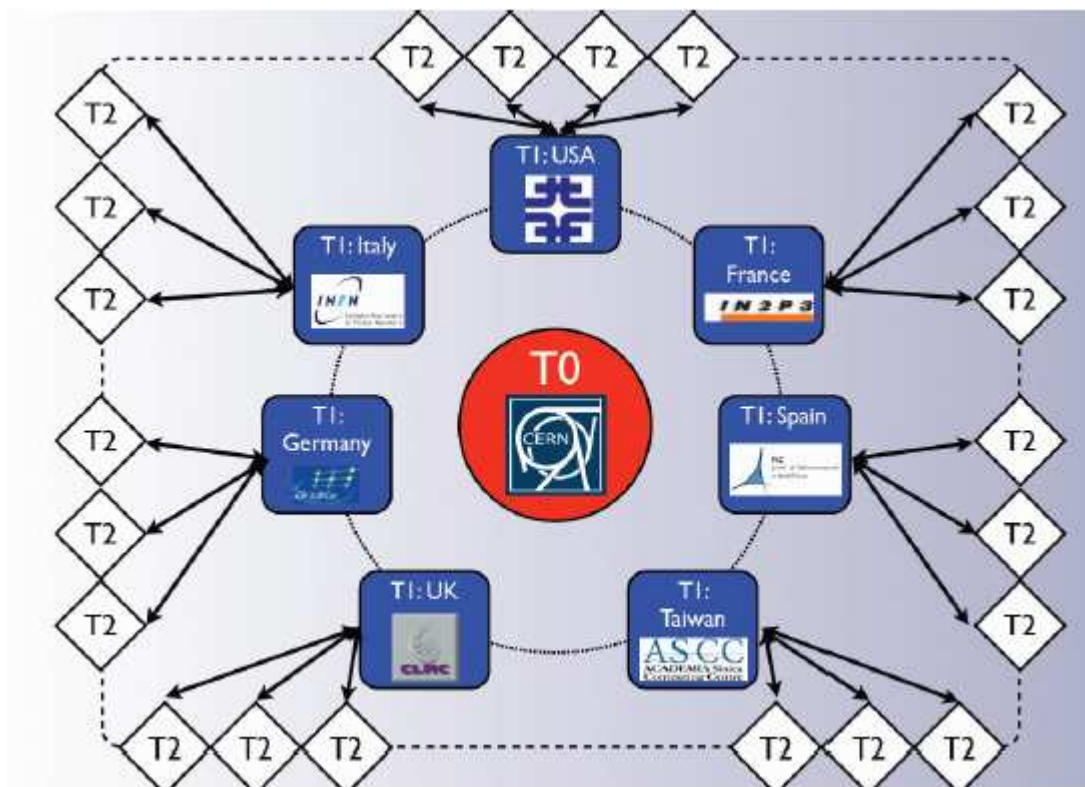


Figure B.4: Data flow through the CMS computing tiers

The previous diagram in fig. B.4 shows the flow of CMS detector data through the tiers:

**Figure B.5:** CMS computing tiers hierarchy



## B.4.2 Data Organization

To extract a physics message for a high energy physics analysis, a physicist has to combine a variety of information: reconstructed information from the recorded detector data, specified by a combination of trigger paths and possibly further selected by cuts on reconstructed quantities (e.g., two jets), MC samples which simulate the physics signal under investigation, and background samples (specified by the simulated physics process).

The physics abstractions physicists use to request these items are datasets and event collections. The datasets are split off at the T0 and distributed to the T1s, as described above. An event collection is the smallest unit within a dataset that a user can select. Typically, the reconstructed information

needed for the analysis, as in the first bullet above, would all be contained in one or a few event collections. Data are stored as ROOT files. The smallest unit in computing space is the file block which corresponds to a group of ROOT files likely to be accessed together. This requires a mapping from the physics abstraction (event collection) to the file location. CMS has a global data catalog called the Dataset Bookkeeping System (DBS) which provides mapping between the physics abstraction (dataset or event collection) and the list of fileblocks corresponding to this abstraction. It also gives the user an overview what is available for analysis, as it has the complete catalog. The locations of these fileblocks within the CMS grid (several centers can provide access to the same fileblock) are resolved by the Dataset Locator Service (DLS). The mapping thus occurs in two steps, at the DBS and the DLS.

## B.5 Event Simulation

Until the LHC start-up, no data will be taken by CMS. Nevertheless, software tools for physics reconstruction and data analysis are already being developed using *simulated data*.

A simulation chain starts with the generation of physics events with a *Monte Carlo generator*, such as PYTHIA, CompHEP, TopRex, etc. Interfaces to all of these generators are collected in a CMSSW package, called `IOMC/GeneratorInterface`, and are available for physics event generation as plugin modules, configurable by their `ParameterSets`.

The Monte Carlo chain must eventually lead to a simulation of the detector *response* to the passage of particles through it, which is used as input to the reconstruction and analysis tools.

Creating Monte Carlo event samples consists of three distinct steps, which give rise to three different kinds of event data.

- **Generation:** production of physics event by a Monte Carlo event generator (e.g. PYTHIA, particle gun, etc.). Data produced in this step is referred to as **GEN**.
- **Simulation:** *Geant4*-based simulation of the physics processes that accompany the passage of particles through the materials of the CMS detector, and of the subdetector responses (simulated hits or **SIM**).
- **Digitization:** simulation of the electronics response to the hits in the detector (**DIGI**).

### B.5.1 Monte Carlo event generators

Monte Carlo event generators are used to generate high energy physics events, i.e. sets of outgoing particles produced in the interactions between two incoming particles.

Several general-purpose event generators are interfaced to CMSSW (e.g. PYTHIA, Herwig, Sherpa), though the main workhorse used in CMS so far is PYTHIA. The goal of general-purpose event generators is to provide, as accurate as possible, a description of what happens in a particle collision. They contain theory and models for a number of physics aspects, such as hard and soft interactions, parton distributions, initial and final state parton showers, multiple interactions, fragmentation and decay.

#### PYTHIA

PYTHIA is a *leading order* (LO) MC generator and is frequently used in high energy physics simulations. It is able to produce a complete set of final states for a wide range of processes. In particular, it is used for the simulation of hard interactions in  $e^+e^-$ ,  $pp$  and  $ep$  colliders. PYTHIA provides a wide selection of fundamental electroweak and strong SM processes. It also generates *minimum bias* events and many non-SM processes. Most of these are produced using a combination of analytical results and various models instead of exact matrix element calculations.

Most of the samples used in this work were generated with PYTHIA. The resulting output can be dumped in ROOT files to be subsequently processed with CMSSW to obtain the full simulation chain. Otherwise, the event generation can be run in the same job with further processing, by including the PYTHIA interface module in the same configuration file with detector simulation.

#### Other Monte Carlo generators

Some of the samples used in this study have been produced with other LO event generators:

**PHANTOM** It's a dedicated six-fermion final state generator, used to produce samples of VV-fusion to be compared to PYTHIA samples.

**CompHEP** Samples of the background process  $pp \rightarrow Zb\bar{b} \rightarrow 4\ell + X$  used in this work were produced with CompHEP, which performs the exact matrix element calculation.

**TopRex** Some of the samples of background process  $pp \rightarrow t\bar{t} \rightarrow 4\ell + X$  (especially for reconstructed event analysis) were produced with TopRex generator.

### Vertex smearing

By default the nominal vertex of an event is (0,0,0). In order to simulate the IR spread, CMSSW provides the possibility to apply a smearing on this vertex, for which a specific module, **VertexGenerator**, has to be used. The smearing can be simulated according to various distributions (such as gaussian or flat).

Vertex smearing can be applied in the same chain with generating events or reading previously generated events from an external file.

## B.5.2 Detector simulation

Full-scale simulation of the CMS detector is based on the Geant4 toolkit. It relies on a fairly detailed description of the hierarchy of volumes and materials, and knowing which parts are “sensitive detector” (i.e., furnished with a readout) as opposed to “dead materials”.

As the input, detector simulation takes GEN data (generated particles, in a standard format called **HepMCProduct**). The generated particles are traced through the materials that compose the detector and the physics processes that accompany particle passage through matter are modeled. Results of each particle’s interactions with matter are recorded in the form of simulated hits (SIM data). Particles can be either “*primary*” (generated particle) or “*secondary*” (a result of Geant4-modeled interactions of a primary particle with matter).

The CMSSW detector simulation software is, in fact, a port of an old package, *OSCAR*, into the new framework. As a software component, it’s organized as a single module, **OscarProducer**, which plugs directly into the **cmsRun** framework executable. Information about the detector geometry and the magnetic field map must be included in the configuration file as well.

## B.5.3 Digitization

The next step in the process is reproducing the response of the detector readout electronics, i.e., the digitization step, which results in the DIGI data.

The digitization is performed separately on a sub-detector basis: SIM data from each subdetector is taken as the input by the corresponding dig-

itizer. The geometry reconstruction service is also needed to identify the sensitive volumes of each subdetector.

The output of the GEN+SIM+DIGI chain can be saved in a ROOT file containing all the persistent objects produced and stored in the event (optionally, the user can drop some of them).

### B.5.4 Pile-up simulation

The *pile-up* is the effect of more than one physics interaction per beam crossing, due to high concentration of particles in a bunch, and/or the effect of the electronics signal spill-over from the previous bunch crossings into the current crossing, due to the fact that the bunch spacing (time between collisions) is often shorter than the duration of an electronic signal in some subdetector.

The pile-up can be optionally simulated by a dedicated module, the `MixingModule`. For the digitization of ECAL, HCAL and the three Muon subdetector, the `MixingModule` must be present in the chain before the corresponding digitizers, at least in the *zero pile-up mode*, because those digitizers explicitly require at least an “empty” product of the `MixingModule` in the Event.

### B.5.5 Reconstruction

RECO is the name of the data-tier which contains conveniently formatted objects created by the event reconstruction. These objects are derived from RAW data. The normal completion of the reconstruction task results in a full set of these reconstructed objects useable for physics analysis. Reconstruction is expensive in terms of CPU, so several “official” samples of RECO data are available to CMS physicists and are normally used for analysis, thus avoiding RAW data altogether. Anyway, it is necessary to rerun reconstruction algorithms for analysis requiring to take into account new calibrations, novel algorithms, and so on.

Event reconstruction is structured in several hierarchical steps:

**Detector-specific processing** Starting from detector data unpacking and decoding, detector calibration constants are applied and cluster or hit objects are reconstructed.

**Tracking** Hits in the silicon and muon detectors are used to reconstruct global tracks. Pattern recognition in the tracker is the most CPU-intensive task.

**Vertexing** Reconstructs primary and secondary vertex candidates.

**Particle identification** Using a wide variety of sophisticated algorithms, standard physics object candidates are created (*high-level physics objects*, such as electrons, photons, muons, missing transverse energy, jets, heavy-quarks,  $\tau$  decay). These objects are mostly used in physics analyses.

## B.6 CRAB

**CRAB**(CMS Remote Analysis Builder) is the computing tool used in CMS to manage the data analysis workflow.

It is still at a development stage and it is responsible for data analysis job preparation, splitting and submission. This software is meant to simplify CMS physics analysis by means of officially processing data, concealing to the final user the intrinsic complexity of GRID infrastructure, so that one can access remote data with the same ease of locally stored data.

CRAB allows to send final user's analysis code to the site in which data are stored. Here a distributed analysis is performed, subdividing the *task* (which can encompass an entire *dataset*) in smaller jobs, depending on user's necessity.

### B.6.1 CRAB Workflow

CRAB is developed in PYTHON language and is installed in the **UI** (User Interface), i.e. the user's access point to the GRID. Users develop their analysis code in an interactive environment and decide which stored data process. It is therefore necessary to specify to CRAB the following input:

- Data Parameter: keywords to select particular *dataset*, the number of events for each job, and the number of analysis jobs
- Analysis code developed by the final user with its parameters
- Output file name and how it is meant to be managed: returned back to the UI or stored in a SE (Storage Element)

The search for sites containing the requested data, inspection of resources' availability, submitted jobs status control and retrieval of the output are operations completely managed by CRAB and concealed to the final user. This last works on a UI, prepares analysis code and execute the analysis job directly from there, specifying the settings by means of a configuration file.

The software providing the necessary infrastructure to keep track in real-time of GRID submitted jobs, by controlling the progress and resource

consumption is BOSS (Batch Object Submission System). As one can see in Fig. B.6, BOSS becomes part of CMS workflow, entering as an interface between the WorkLoad Management System (WMS) which regulates access to distributed resources and the application tool to submit jobs on the GRID (CRAB).

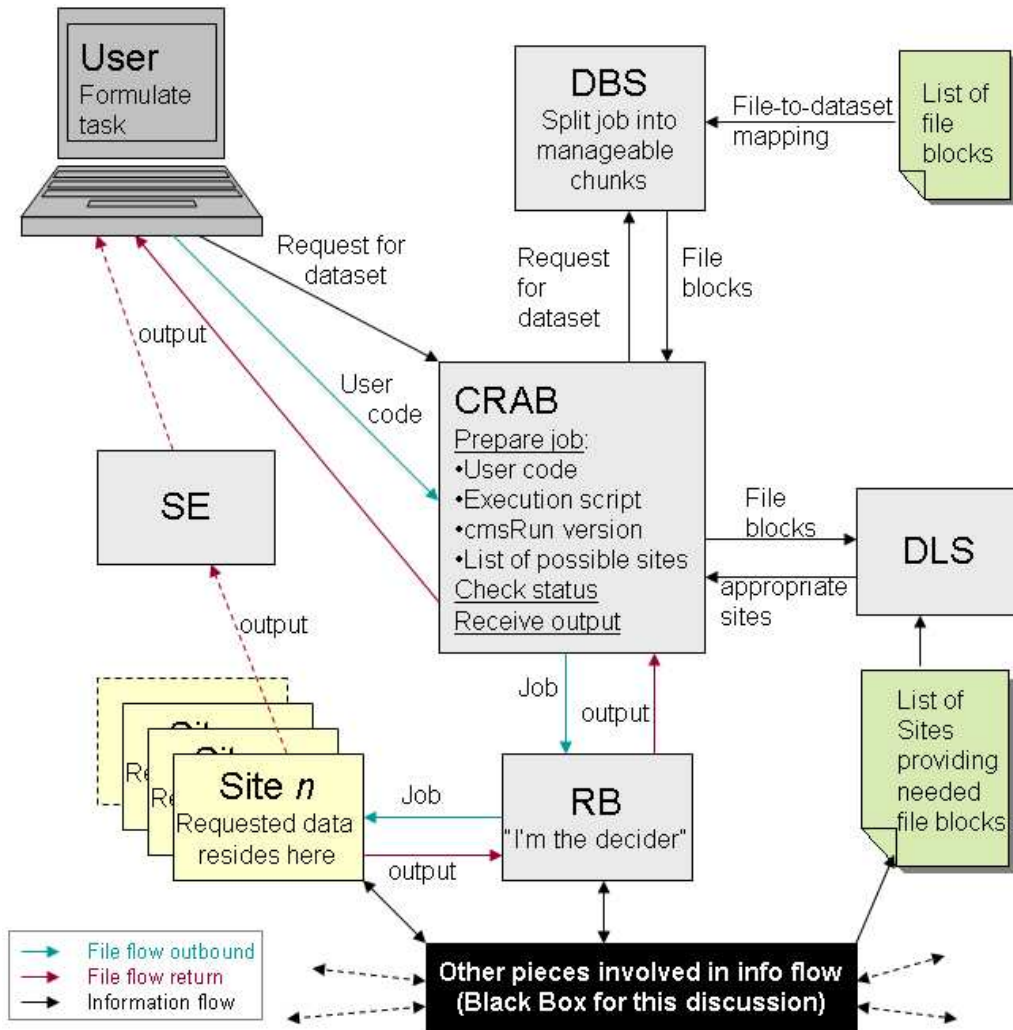


**Figure B.6:** BOSS entering CMS workflow between the User Interface (CRAB) and the WMS which regulates access to GRID

In CMS dataflow, through the use of BOSS and CRAB, it is possible to tell apart the principal phases of interaction with LCG GRID elements. After

the configuration of the work area environment on the UI in order to execute the analysis, the user creates the jobs through CRAB which contacts the DBS and DLS database in order to get information needed on the requested data and subsequently prepares the jobs via BOSS. Then, the user asks to submit a certain number of created jobs and CRAB, after having verified the presence of a valid proxy, through BOSS submit them to the Resource Broker (RB) which is the GRID module that receives users requests. It is therefore BOSS that interacts directly with the GRID in order to submit the jobs. So the jobs are submitted from the RB to the site(s) having the needed features for the analysis requested by the user. Afterwards CRAB controls, always via BOSS, the processing state of the submitted jobs. Finally, in the case the analysis is finished successfully, CRAB requires the output retrieval from the RB.

Almost all of this process is concealed to the the user, who interacts only with CRAB for the processing of the physics analysis. In conclusion the only operations whereof the user has to handle to use the GRID are:

- **Job Creation:** this operation corresponds to prepare the files necessary for job submission. CRAB creates all the jobs (*tasks*) desired by the user for the particular considered *dataset* and according to splitting specifics
- **Submission:** created jobs are submitted to the GRID
- **Job Status:** the user can require to CRAB information about job processing status. It can be Submitted, Waiting,Ready,Scheduled, Running, Aborted and Done
- **Outut retrieval:** in the case the job status is *Done* is possible to retrieve the output of the analysis job

# Bibliography

- [1] S.L. Glashow, Nucl. Phys. **22** (1961) 579;  
S. Weinberg, Phys. Rev. Lett. **19** (1967) 1246;  
A. Salam, *Elementary Particle Theory*, Almquist & Wiskells, Stockholm (1968) p. 367.
- [2] S. Dawson, *Introduction to Electroweak Symmetry Breaking*, hep-ph/9901280.
- [3] A. Djouadi, J. Kalinowski and M. Spira. HDECAY: a program for Higgs boson decays in the Standard Model and its supersymmetric extensions. *Comp. Phys. Commun.*, 108:56-74, 1998.
- [4] S.Dawson, *The Standard Model intermediate mass Higgs boson, Perspectives on Higgs Physics II* ed. Gordon L. Kane, World Scientific, 1997.
- [5] G. Altarelli and G. Isidori *Phys. Lett.* B337 (1994), J. A. Casas, J. R. Espinosa and M. Quiròs, *Phys. Lett.* B342 (1995) 171, B382 (1996) 374, T. Hambye and K. Riesselmann, *Phys. Rev.* D55 (1997) 7255.
- [6] T. Applequist and C.W. Bernard, *Phys. Rev.*,D22 (1980) 200, *Strongly Interacting Higgs Boson*,  
A. Longhitano, *Nucl. Phys.*, B118 (1981) 118, *Low-Energy Impact of a Higgs Boson Sector*
- [7] M.J.G. Veltman, *Acta Phys. Polon.*, B8 (1977) 475, *Second Threshold in Weak Interactions*.
- [8] The LEP Working Group for Higgs Boson Searches, *Search for the Standard Model Higgs boson at LEP*, CERN-EP/2003-11.
- [9] The LEP Collaborations ALEPH, DELPHI, L3, OPAL, the LEP Electroweak Working Group and the SLD Heavy Flavour Group, hep-ex/0312023 *Combination of Preliminary Electroweak Measurements and Constraints on the Standard Model*.

- 
- [10] CDF and D0 collaboration *FERMILAB-PUB-03/320-E Results of the Tevatron Higgs Sensivity Study*
- [11] *LHC Design Report*, CERN-2004-003.
- [12] ALICE Collaboration, *Technical Proposal for A Large Ion Collider Experiment at the CERN LHC*, CERN/LHCC 95-71.
- [13] LHCb Collaboration, *Technical Proposal*, CERN/LHCC 98-4.
- [14] ATLAS Collaboration, *Technical Proposal*, CERN/LHCC 94-43.
- [15] CMS Collaboration, *Technical Proposal*, CERN/LHCC 94-38.
- [16] CMS Collaboration, *The Tracker Project, CMS Tracker Technical Design Report*, CERN/LHCC98-6 (1998)
- [17] CMS Collaboration, *The Electromagnetic Calorimeter, CMS ECAL Technical Design Report*, CERN/LHCC97-33 (1997)
- [18] CMS Collaboration, *The Hadronic Calorimeter, CMS HCAL Technical Design Report*, CERN/LHCC97-31 (1997)
- [19] CMS Collaboration, *The Muon Project, Technical Design Report*, CERN/LHCC97-32 (1997)
- [20] The CMS Trigger and Data Acquisition Group, *The CMS High Level Trigger*.
- [21] T. Sjöstrand, P. Edén, C. Friberg, L. Lönnbald, G. Miu, S. Mrenna and E. Norrbin, *High-Energy-Physics Event Generation with PYTHIA* hep-ph/010017
- [22] A. Pukhova, E. Boss, M. Dubinin, V. Edneral, V. Ilyin, D. Kovalenko, A. Kryukov, V. Savrin, S. Shichanin and A. Semenov. *CompHEP- a package for evaluation of Feynman diagrams and integration over multi-particle phase space* pre-print in msu 98-41/542 edition (1999) hep-ph/9908288
- [23] M. Spira, *HIGLU: A Program for the Calculation of the Total Higgs Production Cross Section at Hadron Collider via Gluon Fusion Including QCD Corrections* DESY T-95-05, hep-ph/9510347
- [24] R. Rainwater, M. Spira and D. Zeppenfeld *Higgs Boson Production at Hadron Collider*, hep-ph/0203187

- 
- [25] The CMS Physics Group, *Physics Technical Design Report, vol II - Physics Performance*.
- [26] The CMS Trigger And Data Acquisition Group, *Online Selection Software Guide*  
<https://twiki.cern.ch/twiki/bin/view/CMS/SWGuideOnSel>
- [27] CMS Egamma HLT Group Twiki page,  
<https://twiki.cern.ch/twiki/bin/view/CMS/SWGuideEgamaHLT>
- [28] CMS Muon HLT Group Twiki page,  
<https://twiki.cern.ch/twiki/bin/view/CMS/SWGuideMuonHLT>

# List of Tables

1.1	Fermion features . . . . .	4
1.2	Gauge Bosons features . . . . .	6
1.3	Event rates for some processes at LHC . . . . .	30
2.1	LHC design parameters . . . . .	41
3.1	L1 trigger table at low luminosity . . . . .	70
3.2	L1 trigger table at high luminosity . . . . .	70
4.1	Cross sections for the Higgs boson production, branching ratio into $ZZ^*$ and preselection efficiencies for different values of the Higgs mass. The cross section and branching ratios are obtained from Spira[23] . . . . .	83
4.2	Cross-section, branching ratio and preselection efficiency for the different backgrounds. A mass of 175 GeV for the top quark has been assumed . . . . .	105
4.3	$Z$ selection algorithm efficiencies. . . . .	107
4.4	Number of generated events and efficiencies for signal and background . . . . .	117
5.1	Muon HLT: $p_T$ thresholds and output rates.[26] . . . . .	124
5.2	Electron HLT: $E_T$ thresholds and output rates.[26] . . . . .	125
5.3	Photon HLT: $E_T$ thresholds and output rates. . . . .	125
5.4	$E_T$ HLT thresholds for $E_{\gamma}$ trigger-paths. Relaxed means non isolated [27] . . . . .	129
5.5	Detailed thresholds for some selected $e_{\gamma}$ paths[27] . . . . .	130
5.6	$p_T$ HLT thresholds for muon trigger-paths. Relaxed means non isolated [28] . . . . .	130
5.7	Thresholds for muon paths [28] . . . . .	131
5.8	HLT efficiencies for $E_{\gamma}$ paths. The events have not been refiltered . . . . .	132

---

5.9	HLT efficiencies for Egamma paths. The events have been re-filtered after reconstruction . . . . .	132
5.10	Trigger efficiencies for combined electron muon paths. Events were not re-filtered . . . . .	136
5.11	Trigger efficiencies for combined electron muon paths. Events were re-filtered . . . . .	136
5.12	Detailed HLT efficiencies for each cut for selected trigger paths	137
A.1	Fermions quantum numbers . . . . .	147
A.2	SM Higgs sector couplings with fermions and bosons . . . . .	155
B.1	CMS event formats at LHC start-up, assuming a luminosity of $\mathcal{L} = 2 \times 10^{33} \text{ cm}^{-2}\text{s}^{-1}$ . . . . .	163

# List of Figures

1.1	Gauge Couplings . . . . .	6
1.2	Functional form of Higgs potential . . . . .	10
1.3	Total decay width $\Gamma_H$ of Standard Model Higgs Boson in function of its mass . . . . .	14
1.4	Decay branching ratios of the Standard Model Higgs boson as a function of the mass. Decays into fermion-antifermion pairs are represented by solid lines, decays into vector bosons with dashed lines . . . . .	15
1.5	Theoretical limits on Standard Model Higgs . . . . .	17
1.6	Theoretical limits on Standard Model Higgs . . . . .	19
1.7	Lowest order Feynman diagram for Higgs decay into two fermions	20
1.8	Lowest order Feynman diagram of Higgs decay into a vector boson pair . . . . .	21
1.9	Trend of function $R(x)$ in the interval $(\frac{1}{4} < x < 1)$ $x = \left(\frac{M_Z}{M_H}\right)^2$ , corresponding to $(M_Z < M_H < 2M_Z)$ . . . . .	22
1.10	Typical lowest order diagrams contributing to $H^0 \rightarrow \gamma\gamma$ . . . . .	23
1.11	The Blue Band Plot . . . . .	24
1.12	Lep Likelihood . . . . .	26
1.13	Parton density function for a proton with $Q^2 = 10GeV^2$ (left) and $Q^2 = m_W^2$ (right) . . . . .	28
1.14	A proton proton interaction, at partonic level . . . . .	29
1.15	Leading order Feynman diagram for gluon fusion . . . . .	31
1.16	Leading order Feynman diagram for vector boson fusion . . . . .	32
1.17	Leading order Feynman diagram for <i>Higgs-strahlung</i> . . . . .	33
1.18	Leading order Feynman diagram for associated top production	33
1.19	Cross sections for all Higgs production channels . . . . .	37
2.1	Cross sections for different processes as a function of the center of mass energy in p-p collisions . . . . .	39

2.2	Overview of the accelerator complex at CERN. Protons will be accelerated up to 50 MeV by a linear accelerator LINAC. A Booster raises the beam energy up to 1.4 GeV injecting proton beam in the old circular protosynchrotron PS. The 25 GeV energy beams extracted at PS are injected into a bigger circular accelerator SPS, which introduces 450 GeV proton beams in the LHC ring . . . . .	41
2.3	Map of LHC and related experiments . . . . .	43
2.4	Schematic picture of CMS experiment at LHC . . . . .	44
2.5	One quarter of CMS . . . . .	45
2.6	Transverse view of CMS . . . . .	46
2.7	One quarter of CMS . . . . .	49
2.8	One quarter of CMS tracker . . . . .	50
2.9	Pixel Detector . . . . .	51
2.10	Tracker Resolutions . . . . .	52
2.11	ECAL longitudinal view . . . . .	54
2.12	ECAL energy resolution . . . . .	54
2.13	HCAL . . . . .	55
2.14	Muon System . . . . .	56
2.15	DT Station . . . . .	57
2.16	Drift cell . . . . .	58
3.1	Cross sections and event rates at high luminosity ( $10^{34}; cm^{-2}s^{-1}$ ) as a function of particle masses. . . . .	61
3.2	Components of the L1 trigger system and their relationships. . . . .	63
3.3	Structure of the L1 Muon Trigger system . . . . .	67
3.4	Schematic picture of Muon Isolation . . . . .	78
4.1	Expected number of signal events after one year of LHC running with an integrated luminosity of $20 fb^{-1}$ . . . . .	83
4.2	The mass distribution of the on-shell Z boson (the Z closer to the nominal Z boson mass) for three different Higgs masses. . . . .	84
4.3	The mass distribution of the off-shell $Z^*$ boson for three different Higgs masses. . . . .	85
4.4	<i>Left</i> : Cross section for 2 off shell Z (see text) in function of $M_H$ . <i>Right</i> : Fraction of events with two off-shell Z . . . . .	85
4.5	The $p_T$ distributions of the four leptons in signal events for three different Higgs boson masses. In each event leptons are sorted according to $p_T$ value. Distributions are normalized to unit area . . . . .	86
4.6	Leading order Feynman diagrams for gluon-gluon fusion and vector boson fusion. . . . .	87

4.7	Transverse momentum distribution for final state leptons. <i>Top-Left</i> : leading muon $p_T$ . <i>Top-Right</i> : softest muon $p_T$ . <i>Bottom-Left</i> : leading electron $p_T$ . <i>Bottom-Right</i> : softest electron $p_T$ . . . . .	88
4.8	<i>Left</i> Pseudorapidity and ( <i>right</i> ) transverse momentum (right) of the reconstructed $Z$ . . . . .	89
4.9	<i>Left</i> : Invariant mass of reconstructed $Z$ . <i>Right</i> : Pseudorapidity of $ZZ^*$ system . . . . .	89
4.10	Top left: angle between two leptons from the same $Z$ . Top right: angle between the highest $p_T$ muon and the highest $p_T$ electron. Bottom left: angle between two like-sign leptons. Bottom right: angle between the two reconstructed $Z$ . . . . .	90
4.11	Feynman diagram showing the internal bremsstrahlung process.	91
4.12	Transverse energy distribution of the final state radiation photons (left) and angular separation between the photon and the muon (right) in signal events for $M_H = 150 \text{ GeV}$ . . . . .	92
4.13	Effect on neglecting internal bremsstrahlung photons in the invariant mass computation: on the abscissa the normalized difference between the four leptons invariant mass computed with and without considering photons in the final state . . . . .	92
4.14	Leading order Feynman diagrams for the $t\bar{t}$ production in hadronic collisions . . . . .	93
4.15	$t\bar{t}$ production rates. <i>Left</i> : scale dependence at fixed order (NLO, dashed line in lower insert), and NLO+NLL (solid lines). <i>Right</i> : PDF dependence . . . . .	94
4.16	Typical decay chain of a $t\bar{t}$ pair. Two leptons come from the $W$ bosons decays, the other two come from the b-jet hadronization.	94
4.17	Sources of final state muons/electrons in the top quark decay chain . . . . .	95
4.18	$p_T$ distribution of the four leptons in $t\bar{t}$ events. The muons are sorted by decreasing $p_T$ . . . . .	96
4.19	Invariant mass distributions of the two $\ell^+\ell^-$ pairs in $t\bar{t}$ background. The first lepton pair (left) is chosen as the one with the invariant mass closest to the nominal $Z$ mass. The invariant mass of the remaining leptons is shown on the right . . . . .	97
4.20	<i>Left</i> : Invariant mass distribution of the four leptons coming from $t\bar{t}$ events. <i>Right</i> : Comparison between first and second candidate $Z$ spectra . . . . .	97
4.21	Comparison of the $\eta$ (left) and $p_T$ (right) distributions of the b quarks in $Zb\bar{b}$ events generated by PYTHIA and CompHEP, distributions are normalized to the same integrated luminosity.	98

4.22	Leading order diagrams corresponding to the possible initial states producing $Zb\bar{b}$ . . . . .	99
4.23	Invariant mass distribution of the the two $\ell^+\ell^-$ pairs in $Zb\bar{b}$ events. <i>Left</i> : Invariant mass of the best $Z$ candidate. <i>Right</i> : invariant mass of the remaining two leptons . . . . .	100
4.24	<i>Left</i> Invariant mass distribution of the four leptons coming from the $Zb\bar{b}$ events. <i>Right</i> invariant mass of the two reconstructed "Z". . . . .	101
4.25	$p_T$ distribution of the four leptons in $Zb\bar{b}$ events. The muons are sorted by decreasing $p_T$ . . . . .	101
4.26	Leading order processes for the $t$ -channel $ZZ^*$ production in hadronic collisions . . . . .	102
4.27	The $Z$ and $Z^{(*)}$ boson mass distribution as produced by PYTHIA. . . . .	103
4.28	Transverse momentum (left) and invariant mass distribution (right) of the $ZZ^{(*)}$ system. . . . .	104
4.29	The $p_T$ distributions of the four leptons in $ZZ^*$ events. In each event leptons are sorted according to $p_T$ value. . . . .	104
4.30	$p_T$ distributions for muons and $Z$ s. <i>Top left(right)</i> : weighted (normalized) distribution of all muon momenta. <i>Center left(right)</i> : Hardest (softest) muon $p_T$ spectrum (normalized to the unit area). <i>Bottom-left</i> : weighted $p_T$ distribution for $Z$ . <i>Bottom-right</i> : normalized $Z P_T$ distributions . . . . .	110
4.31	Invariant mass distributions. <i>Top</i> : muon-pairs (all combinations and selected pairs). <i>Center</i> : $Z$ candidate invariant mass (weighted and normalized). <i>Bottom</i> : on-shell and off-shell $Z$ . . . . .	111
4.32	Angular variables distributions: angles between $\mu^+\mu^-$ and $e^+e^-$ pairs (from the same $Z$ decay), between $\mu - e$ pairs with higher and lower $p_T$ , between $\mu^+ - e^+$ and between two $Z$ 's . . . . .	112
4.33	Pseudorapidity distributions. <i>Left</i> : Normalized distribution for electrons. <i>Right</i> : Normalized distribution for $Z$ s from electrons . . . . .	113
4.34	Muons collinearity in $p_z$ for signal and backgrounds . . . . .	113
4.35	<i>Top-Left</i> : $p_T$ of two candidate $Z$ . <i>Top-Right</i> Pseudorapidity of two candidate $Z$ . <i>Center-Left</i> : $p_T$ of leading lepton. <i>Center-Right</i> : $p_T$ of second lepton. <i>Bottom-Left</i> : $p_T$ of third lepton. <i>Bottom-Right</i> : $p_T$ of softest lepton . . . . .	114
4.36	<i>Left</i> : muons $p_T$ for different Higgs mass values. <i>Right</i> : lepton pairs invariant mass (i.e. $Z$ boson mass) for different Higgs mass values) . . . . .	115
4.37	Distributions of $\mu^+\mu^-$ -angle and $ZZ$ angle for different Higgs mass values . . . . .	115

4.38	Leading order Feynman graphs for $ZZ^*$ irreducible background and Higgs boson signal . . . . .	116
4.39	Distribution of $\cos\phi_D$ , for signal and backgrounds . . . . .	117
4.40	Distribution of $\phi_D$ decay angle and $\cos\phi_D$ , its cosine . . . . .	118
4.41	Sketch of considered angular variables . . . . .	119
4.42	Angular distributions and cosine of considered angles. At the left $\theta_{ls}$ distribution of like-sign muons. At the centre distribution of opposite sign muons $\theta_{os}$ and at the right distribution of angle between $Z$ $\theta_{ZZ}$ . . . . .	119
4.43	Angular distributions and cosine of considered angles. On the left the largest $\theta_{ls}$ , on the right the smallest $\theta_{ls}$ . . . . .	120
4.44	Top-left: Efficiency vs Purity for each cut position. Top-right: Efficiency times Purity Vs the cut cosine. Bottom-Left: Signal to Background ratio vs the cut cosine. Bottom-right: Signal to Signal plus Background ratio vs the cut cosine . . . . .	122
5.1	Integral rate of single muon ( <i>Top-Left</i> ) relaxed single muon ( <i>Top-Right</i> ), electrons ( <i>Bottom-left</i> ) and photons ( <i>Bottom-Right</i> ), as a function of the muon $p_T$ threshold, and electron/photon $E_T$ threshold [26] . . . . .	124
5.2	Muon HLT logical structure. . . . .	126
5.3	Comparison between all events and events passing at least one of the trigger paths (electron+photon). <i>Top-Left</i> : pseudorapidity $\eta$ of Egamma object. <i>Top-Right</i> : transverse energy of Egamma objects $E_T$ . <i>Bottom-left</i> : $E/P$ of electrons. <i>Bottom-Right</i> : Egamma objects multiplicity . . . . .	133
5.4	Comparisons between all events and events passing at least one of the electron trigger paths. <i>Top-Left</i> : pseudorapidity $\eta$ of the Egamma object. <i>Top-Right</i> : transverse energy of Egamma objects $E_T$ . <i>Bottom-left</i> : $E/P$ of Egamma objects. <i>Bottom-Right</i> : Egamma objects multiplicity . . . . .	134
5.5	Comparisons between all events and events passing one of the photon trigger paths. <i>Top-Left</i> : pseudorapidity $\eta$ of electron-like objects. <i>Top-Right</i> : transverse energy of electron-like objects $E_T$ . <i>Bottom-left</i> : $E/P$ of electron-like objects. <i>Bottom-Right</i> : electron's multiplicity . . . . .	135
5.6	Distributions of electrons $E_T$ for $\mu - e/\gamma$ combined paths (low lumi): 1) single- $\mu$ -single- $e$ ( <i>left</i> ), single- $\mu$ -double- $e$ ( <i>right</i> ); 2) double- $\mu$ -double- $e$ ( <i>left</i> ), relaxed double- $\mu$ -relaxed double- $e$ ( <i>right</i> ); 3) double- $\mu$ -double- $\gamma$ ( <i>left</i> ), relaxed double- $\mu$ -relaxed double- $\gamma$ ( <i>right</i> ). . . . .	138

5.7	<i>Left</i> : Mean value of $\Delta_\mu$ as a function of $p_T$ . <i>Right</i> : mean value of $\Delta_e$ as a function of $E_T$ . See text . . . . .	140
5.8	<i>Left</i> $\sigma_r$ as a function of $p_T$ . <i>Right</i> $\sigma_{r_e}$ as a function of $E_T$ . . . . .	140
5.9	<i>Left</i> Angular resolution on $\theta$ for muons as a function of $p_T$ . <i>Right</i> Angular resolution in $\theta$ for electrons as a function of $E_T$	141
5.10	<i>Left</i> $\sigma_{M(\mu\mu)}$ as a function of $M_{\mu\mu}$ . <i>Right</i> $\sigma_{M(ee)}$ as a function of $M_{ee}$ . . . . .	141
5.11	<i>Left</i> $\sigma_{M(\mu\mu)}$ as a function of $(p_T)_{min}$ . <i>Right</i> $\sigma_{M(ee)}$ as a function of $(E_T)_{min}$ . . . . .	142
A.1	Shape of the Higgs potential for different signs of $\mu^2$ and $\lambda$ . . . . .	150
B.1	CMSSW framework Event processing workflow . . . . .	162
B.2	Event Processing flowchart . . . . .	164
B.3	Event processing . . . . .	165
B.4	Data flow through the CMS computing tiers . . . . .	167
B.5	CMS computing tiers hierarchy . . . . .	168
B.6	BOSS entering CMS workflow between the User Interface (CRAB) and the WMS which regulates access to GRID . . . . .	174

# Acknowledgements

Non è facile ringraziare adeguatamente tutti coloro i quali sono stati in qualche maniera importanti per portare a termine questo lavoro e il mio percorso di studi. Proverò ugualmente, confidando che tutti mi perdoneranno per la semplicità con cui lo farò.

Ci terrei in primo luogo a ringraziare il Dott. Ernesto Migliore per la quantità di tempo dedicatomi e per gli insegnamenti e il supporto che da lui ho ricevuto e la Dott.ssa Chiara Mariotti, oltre che per i preziosi consigli, per l'entusiasmo che ha saputo trasmettermi.

Un ringraziamento generale va all'intero gruppo CMS di Torino, a tutti coloro con cui ho collaborato e non; è stato importante lavorare all'interno di questa grande "famiglia", che mi ha dato la possibilità di imparare molto in un ambiente coinvolgente e stimolante. Un sentito ringraziamento va alla Prof.ssa Alessandra Romero per avermi seguito costantemente dall'alto e aver provveduto all'organizzazione del lavoro nella sua interezza.

In questi mesi ho avuto modo di conoscere e collaborare con un gruppo di persone che sono state i miei "compagni di avventura", senza di loro tutto questo non sarebbe stato possibile. Grazie (rigorosamente in ordine alfabetico) ad Alessandro, per la sua allegria e la sua competenza, Cristina per la sua determinazione e organizzazione e a Daniele per la sua pazienza e spirito di collaborazione: è stato bello condividere questi mesi e questa avventura con voi.

Un ringraziamento particolare va ai giovani del gruppo, a Giorgia e a Sara per l'aiuto tecnico, il sostegno e la fiducia che hanno saputo infonderci, a Susy e Roberto per l'aiuto e per aver tollerato una turbolenta massa di lauerandi nel "loro" ufficio.

Ci tengo a ringraziare tutta la compagnia dei "fisici" che è stata così importante per rendere più divertente in questi anni la vita all'Università e fuori: Francesco, Edoardo, Thanu, Leonardo, Roberto, Sandro; insieme a loro si sono sempre trascorse ore piacevoli, parlando di Fisica e non.

Come non ringraziare poi Paolo e Alessandro, i miei due compagni di viaggio, dell'estenuante odissea quotidiana per raggiungere Via Pietro Giuria

I, che in questi anni hanno rallegrato le nostre mattine e i nostri pranzi a Fisica; un ringraziamento particolare ad Ale per le ore piacevoli trascorse a discutere di scienza e di montagna.

Un grazie veramente sentito alla compagnia di amici "storici": Alessandro, amico di una vita e di mille avventure, per il cammino compiuto assieme in montagna e non, per il suo entusiasmo nell'ascoltarmi parlare di quanto apprendevo; Achille, per la sua simpatia e la sua schietta sincerità, per i momenti di ilarità che ha saputo regalarci; i due Andrea per le serate trascorse davanti ad una birra, a parlare di musica e di "fatti della vita"; un abbraccio particolare ad Anna, che è ormai lontana, per essere stata una buona amica tutti questi anni; a Tomeck per la sua sconfinata saggezza e cultura musicale, Enrico che ha sempre una parola buona; a Viviana, Stefano, Alessia, Carola, Marina, Domenico, i due Andrea, per le occasioni di "staccare la spina" in questi anni e in questa estate "particolare"; a tutti gli altri amici e a coloro che mi hanno voluto bene.

Ringrazio poi mio zio Ezio e la sua famiglia, sempre presente con il suo sostegno; i miei zii Aldo e Giovannina e mio zio Giovanni con la sua famiglia, per tutto l'aiuto e l'incoraggiamento ricevuto in questi anni. Mia nonna Elsa, che è stata una seconda mamma e mi ha insegnato col suo esempio di vita cosa significa "stare al mondo".

E infine ai miei genitori Angela e Domenico grazie ai quali io esisto e ai quali debbo la maggior parte di quello che so, a loro dedico questo mio lavoro e qualsiasi altro traguardo potrò raggiungere, sintesi dei loro sacrifici.